Tampere University

ROOSA-MARIA SALLINEN

Broadband Methods in Dynamic Analysis and Control of Battery Energy Storage Systems

Tampere University Dissertations 816

Tampere University Dissertations 816

ROOSA-MARIA SALLINEN

Broadband Methods in Dynamic Analysis and Control of Battery Energy Storage Systems

ACADEMIC DISSERTATION
To be presented, with the permission of
the Faculty of Information Technology and Communication Sciences
of Tampere University,
for public discussion in the TB109
of Tietotalo, Korkeakoulunkatu 1, Tampere,
on 9 June 2023, at 12 o'clock.

ACADEMIC DISSERTATION
Tampere University, Faculty of Information Technology and Communication Sciences
Finland

Responsible supervisor and Custos	Associate Professor Tomi Roinila Tampere University Finland	
Pre-examiners	Ph.D. Silvia Arrua Proterra Inc. United States	Ph.D. Arash Khoshkbar-Sadigh TAE Technologies United States
Opponents	Dr.Sc. Juha Huusari ABB Oy Finland	

Cover design: Roihu Inc.

ISBN 978-952-03-2939-6 (print)
ISBN 978-952-03-2940-2 (pdf)
ISSN 2489-9860 (print)
ISSN 2490-0028 (pdf)
http://urn.fi/URN:ISBN:978-952-03-2940-2

Carbon dioxide emissions from printing Tampere University dissertations have been compensated.

PunaMusta Oy – Yliopistopaino
Joensuu 2023

ACKNOWLEDGEMENTS

This Ph.D. research was conducted between 2018 and 2022; first at Tampere University of Technology and later at Tampere University under the Doctoral Program of Electrical Engineering, in the Faculty of Information Technology and Communication Sciences. During this time, my research has been financially supported by the Tampere University Doctoral Program and public research projects from Business of Finland, for which I am deeply grateful. I also highly appreciate a personal grant from the Emil Aaltonen Foundation.

Above all, I am deeply grateful to my supervisor, Professor Tomi Roinila, for providing guidance and feedback throughout my Ph.D. project and for his invaluable supervision, support, and belief in me. Similarly, I extend my sincere thanks to Dr. Tuomas Messo for his guidance at the beginning of my doctoral studies. I would also like to thank Professor Teuvo Suntio and Professor Seppo Valkealahti for their support and contributions, as well as Professor Tamas Kerekes from Aalborg University, who made my research exchange possible.

I also wish to extend my sincere thanks to my current and former colleagues: Dr. Matias Berg, Dr. Aapo Aapro, Dr. Jyri Kivimäki, Dr. Jukka Viinamäki, Dr. Jenni Rekola, M.Sc. Markku Järvelä, Dr. Roni Luhtala, M.Sc. Tommi Reinikka, Dr. Jussi Sihvo, Dr. Henrik Alenius, M.Sc. Minh Tran, and M.Sc. Hikmat Basnet. I will always cherish their company and support. I would also like to thank my other friends, lab mates, and colleagues for the precious time together in the lab and social settings, especially Dr. Maija Ylinen and M.Sc. Jay Panchal. Moreover, special thanks go to the laboratory engineers Lasse Söderlund and others for their help in building the laboratory prototypes.

Lastly, my appreciation goes out to my husband, family, and friends for their neverending encouragement and support throughout my studies. Thank you all.

Tampere, May 2023

ABSTRACT

Battery energy storage systems have become essential in the operation of many modern power-distribution systems, such as dc microgrids, electric ships, and electric aircraft. Energy storage systems often rely on the operation of bidirectional converters to control the power flow. In modern power systems, these bidirectional converters are typically a part of an extensive converter system, a multi-converter system that consists of several electrical converter-based sources and loads. Even though each converter in a multi-converter system is standalone stable, adverse interactions between the interconnected converters can present issues to the system's performance and stability.

Assessing the stability of multi-converter systems is usually challenging, given that the systems are complex, and the dynamics are affected by various operating modes and points. Recent studies have presented methods for assessing the stability of interconnected converters through impedance-based stability criterion. Impedance-based analysis is particularly advantageous for complex multi-converter systems as this method does not require the knowledge of intricate details of the system's parameters. The method can also facilitate adaptive stabilizing control schemes using reliable and fast identification implementations. However, impedance identification of multi-converter systems is typically challenging due to the coupled nature of the interconnected converters and potential non-linear behavior. Moreover, the bidirectional power flow of battery energy storage systems further complicates the stability assessment.

This thesis presents small-signal modeling methods, online stability assessment methods, and adaptive stabilizing control strategies for multi-converter systems that have bidirectional converters. The accuracy of traditional, small-signal-model-based converter control design is enhanced with a procedure that extends a converter's small-signal model with given load and source dynamics. In addition, frequency response identification methods are used to assess the system stability under varying operating conditions. The presented identification methods offer reliable and quick impedance measurements and stability assessment among several converters. The design aims to minimize the interference on the system, which allows the identification during the system's regular operation. The stability assessment provides a platform for adaptive stabilizing control methods, and two such techniques are implemented on a bidirectional converter. Several experimental results confirm the effectiveness of the proposed methods.

CONTENTS

ORIGINAL PUBLICATIONS

The thesis is based on the following original publications, which are referred to as [P1], [P2], [P3], [P4], [P5] and [P6] in the text.

Publication I R.-M. Sallinen, A. Aapro, M. Berg, and T. Messo, Complete Small-Signal Model of Three-Phase Photovoltaic Inverter Considering the Source and Load Effects, in *Proc. Annual Conference of the IEEE Industrial Electronics Society*, pp. 2237–2244, 2018.

Publication II R.-M. Sallinen and T. Messo, The Combined Source-Effect of Photovoltaic Generator and Bi-Directional DC-DC Battery Charger on Inverter Control Dynamics, *The Journal of Engineering*, pp. 5197–5201, 2018.

Publication III R.-M. Sallinen, T. Messo and T. Roinila, Mitigating Voltage Fluctuations in Battery Energy Storage Systems, in *Proc. IEEE Workshop on Control and Modeling for Power Electronics*, 6 pages, 2019.

Publication IV R.-M. Sallinen, T. Roinila and H. Abdollahi, Stability Analysis and Adaptive Resonance Damping of Multi-Converter System Applying Bidirectional Converter, in *Proc. IEEE Workshop on Control and Modeling for Power Electronics*, 7 pages, 2020.

Publication V R.-M. Sallinen and T. Roinila, Broadband Impedance-Measurement Methods in Dynamic Analysis of Dual Active Bridge Converters, in *Proc. IEEE Workshop on Control and Modelling of Power Electronics*, 6 pages, 2021.

Publication VI R.-M. Sallinen and T. Roinila, Adaptive Bus-Impedance-Damping Control of Multi-Converter System Applying Bidirectional Converters, *IEEE Journal of Emerging and Selected Topics in Power Electronics*, vol. 11, no. 1, pp. 567–575, 2023.

SUMMARY OF PUBLICATIONS

Publication I

This article outlines a generalized method for including the effects of load and source to the dynamic model of a power electronic converter, such as a photovoltaic (PV) inverter. Specifically, the article derives a full-order small-signal model for a grid-connected PV inverter that includes both the load and source effects. The model can be used to assess the effect of an arbitrary non-ideal current-type source and a voltage-type load on the inverter dynamics. The full-order dynamic analysis enables accurate prediction of the control and impedance dynamics. The model is verified from a switching model, as well as using HIL simulations.

Publication II

This article offers a small-signal model for a PV inverter that takes the effect of a PV source and a battery energy storage system (BESS) into account. The outlined method can be used for deriving an accurate model of the PV-BESS-inverter input and output impedances. The article shows that PV sources may introduce a right-hand plane (RHP) pole in the inverter dc bus voltage control loop, which may lead to instability. However, connecting BESS in parallel with the PV source lowers the pole frequency, which enhances the stability.

Publication III

DC bus voltage fluctuation can be dampened using a BESS to emulate a capacitor so that the voltage variations are mitigated and attenuation increased. This article uses a control method to increase the bus capacitance by introducing a virtual capacitance with a bidirectional converter interfacing a BESS. As a result, the method improves the output current THD of an inverter system connected to the DC bus. The control strategy can function as a supplementary control algorithm in BESS applications with a DC bus.

Publication IV

This article utilizes a bidirectional converter to provide adaptive damping in the dc bus of a multi-converter system. In this control strategy, the controller has an adaptive resonance damping gain. The resonance damping gain is tuned based on bus impedance measurements that estimate the system's small-signal stability and performance. The controller effectively makes the bidirectional converter operate as a virtual impedance, damping resonances in the bus impedance. The analysis shows that the bidirectional converter can efficiently dampen the resonances in the bus impedance. As a result, regardless of possible network or operating

mode changes, the network is reliable and stable without hardware updates or controller retuning.

Publication V
Broadband methods can be used to provide frequency response measurements in real-time. While the other articles have focused on taking advantage of the frequency response measurements, this article focuses on possible limitations and challenges in the measurement methods. The publication contributes to a more critical understanding of the challenges the frequency response measurements may face, especially on some bidirectional converter types. The publication compares different perturbation methods on a DAB converter. It demonstrates that it is vital to consider the system dynamics at the chosen set-point before choosing the perturbation method. For DAB converters, the measurement implementation may be unfeasible at certain set-points due to nonlinear behavior if the perturbation signal perturbs the converter duty ratio. On the other hand, if the perturbation signal perturbs the phase shift, an accurate measurement implementation can be more straightforward.

Publication VI
This article implements an adaptive stabilizing controller on a BESS. The resonance-damping-gain-based stabilizing control scheme is implemented on a bidirectional converter. The controller's gain is tuned based on identifying the multi-converter system's performance with bus impedance measurements. The tuning modifies the converter's impedance, damping undesired resonances in the bus impedance. The experimental results show that the bus impedance identification is sufficient, and the BESS efficiently dampens its resonances. As a result, the multi-converter system's damping is adjusted to the desired level, averting adverse impedance-based interactions.

Author's contribution

The author was the main contributor for implementing and developing the methods presented in [P1] – [P6] and writing the manuscripts. The author was also responsible for the design, building, and configuration of the experimental bidirectional dc-dc converter setup used in Publications [P4] – [P6]. [P1] was the most collaborative work, where Dr. Aapo Aapro helped with the analysis of the system dynamics, Dr. Matias Berg assisted with the simulation results, and Dr. Tuomas Messo commented on the manuscript. Dr. Messo continued to offer his advice in [P2] – [P3], particularly in topics related to control and dynamic analysis of power electronics. In [P4], Dr. Hessamaldin Abdollahi assisted with the impedance-based stability analysis and identification process. The thesis supervisor, Professor Dr. Tomi Roinila, provided counsel and insights during the doctoral work, particularly in aspects related to system identification.

SYMBOLS

Scalar variables

A	Excitation signal time-domain amplitude
C_{b}	Converter input-side capacitance
C_{dc}	DC-bus capacitance
C_{hv}	Converter high-voltage-side capacitance
C_{em}	Emulated capacitance
C_{f}	CL-filter capacitance
d	Duty ratio
d_{d}	Duty cycle d-component
d_{q}	Duty cycle q-component
θ	Angle between the d-axis of the dq-frame and the a-axis of the abc frame
f_{bw}	Bandwidth of pseudo-random perturbation
$f_{\mathrm{c\text{-}c}}$	Current control loop cross-over frequency
$f_{\mathrm{c\text{-}inner\ loop}}$	Inner (current) control loop cross-over frequency
$f_{\mathrm{c\text{-}v}}$	Voltage control loop cross-over frequency
f_{g}	Grid frequency
f_{gen}	Generation frequency of pseudo-random perturbation
f_{res}	Frequency resolution
$f_{\mathrm{rhp\text{-}zero}}$	Frequency of a right-half-plane zero
f_{sw}	Converter switching frequency

ϕ	Phase shift (delay) between the modulating signals of the high-voltage-side bridge and the low-voltage-side bridge of a dual active converter
$\phi_{\mathrm{hv}}^{\mathrm{DAB}}$	Phase shift of the high-voltage-side bridge of a dual active converter
$\phi_{\mathrm{lv}}^{\mathrm{DAB}}$	Phase shift of the low-voltage-side bridge of a dual active converter
$\varphi_{\mathrm{m-c}}$	Current loop phase margin
$\varphi_{\mathrm{m-v}}$	Voltage loop phase margin
i_{in}	Converter input current
i_{L}	Current through the inductor L
i_{od}	Output current d-component
i_{oq}	Output current q-component
i_{out}	Converter output current
j	Imaginary unit
k	A non-negative integer
K_{m}	Separation margin
K_{r}	Damping at a resonance frequency
L	L-filter inductance, LCL-filter converter-side inductance
L_2	LCL-filter grid-side inductance
L_{tot}	Equivalent (total) inductance
m	Number of bus-connected converters
N	Sequence length
n	Shift register length for maximum-length binary sequence generation
N_{P}	Number of averaged periods
n_{tf}	Transformer turns ratio ($n_{\mathrm{hv}}/n_{\mathrm{lv}}$)
n_{u}	Number of system inputs
n_{y}	Number of system outputs
P	Active power
Q	Quality factor
Q_{d}	Quality factor of a virtual impedance
r_{Cb}	Parasitic resistance of a converter input-side capacitor C_{b}
r_{Cdc}	Parasitic resistance of a dc-bus capacitor

$R_{\text{eq1}}, R_{\text{eq2}}$	Equivalent representations of resistance values for mathematical simplification
r_{L}	Parasitic resistance of an inductor L
$r_{\text{sw1}}, r_{\text{sw2}}$	Internal on-time resistances of the switches S_1 and S_2
R_{load}	Load resistance
r_{pv}	Photovoltaic source dynamic resistance
s	Laplace variable
t	Time
t_{d}	Deadtime
T_{s}	Switching/sampling interval
u	Input signal
v_{Cb}	Voltage over the capacitor C_{b}
v_{in}	Converter input voltage
V_{eq}	Equivalent representation of a voltage for mathematical simplification
v_{out}	Converter output voltage
v_{od}	Converter output voltage d-component
v_{oq}	Converter output voltage q-component
$V_{\text{lv}}, V_{\text{hv}}$	DC voltages on converter low- and high-voltage side
y	Output signal
$Z_{\text{o-bus}}$	Characteristic impedance of bus impedance transfer function
ζ_{abc}	A variable in the abc-frame
ζ_{dq}	A variable in the dq-frame
ω	Angular frequency
ω_{o}	Resonance frequency
ω_{r}	Resonance bandwidth
ω_{ζ}	Angular frequency from phase-locked-loop (PLL)

Transfer functions

$G_{\text{Cem-v}}$	Capacitance emulating controller transfer function

G_{ci}	Control-to-input transfer function
G_{co}	Control-to-output transfer function
G_{io}	Input-to-output transfer function
G_{PI}	Proportional-integral controller transfer function
$G_{PI\text{-}v}$	Proportional-integral voltage controller transfer function
$G_{PIR\text{-}v}$	Proportional-integral voltage controller transfer function with a resonance-damping controller
G_{R}	Resonance-damping controller transfer function
$L_{Cem\text{-}v}$	Control loop gain of capacitance emulating controller
L_{ci}	Control loop gain of input current feedback controller
L_{cd}	Control loop gain of output current d-component feedback controller
L_{co}	Control loop gain of output current feedback controller
L_{v}	Control loop gain of output voltage feedback controller
T_{oi}	Reverse transfer function
Y_{in}	Input admittance transfer function
Y_{o}	Output admittance transfer function
Z_{bus}	Bus impedance transfer function
Z_{load}	Load impedance transfer function
Z_{o}	Output impedance transfer function

Vector and matrix variables

$\mathbf{A}$	State matrix of a state-space representation
$\mathbf{B}$	Input matrix of a state-space representation
$\mathbf{C}$	Output matrix of a state-space representation
$\mathbf{D}$	Feed-through matrix of a state-space representation
$\mathbf{G}_{tf}$	A general representation of a transfer function matrix
$\mathbf{H}$	Hadamard matrix
$\mathbf{I}$	Identity matrix
$\mathbf{M}$	Closed-loop transfer function matrix

P	Park's transformation matrix from *abc*-frame to *dq*-frame
u	Input variable vector
x	State variable vector
y	Output variable vector

Superscripts

^	Linearized variable
B	Variable mapped into an alternative state-space representation form
bess	Bidirectional dc-dc converter variable
DAB	Dual active bridge converter variable
casc	Closed-loop dynamics of a system with cascaded control loop
inv	Inverter variable
pv	Photovoltaic source variable
S	Source-affected variable

Subscripts

1	First component of a vector
2	Second component of a vector
11	First direct component of a matrix
12	First cross-coupling component of a matrix
21	Second cross-coupling component of a matrix
22	Second direct component of a matrix
a	Phase a component
abc	Three-phase phase-domain variable
b	Phase b component
bus	Variables related to bus impedance transfer function
c	Phase c component
Cem	Capacitance emulation variable

CPL	Constant-power-load variable
d	D component
hv	High-voltage-side variable
load	Load variable
lv	Low-voltage-side variable
max	Maximum value
meas	Measurement implementation variable
min	Minimum value
mlbs	Variable related to a maximum-length binary sequence
mpp	Variable related to a photovoltaic source maximum power point
N	Normalized variable
o	Open-loop variable
q	Q component
ref	Reference variable
source	Source-related variable

ABBREVIATIONS

AC	Alternating current
AIR	Allowable impedance region
BESS	Battery energy storage system
CPL	Constant power load
DAB	Dual active bridge
DC	Direct current
HV	High voltage
Im	Imaginary part of a value
LV	Low voltage
MIMO	Multiple-input and multiple-output
MLBS	Maximum-length binary sequence
MPP	Maximum power point
PI	Proportional-integral
PLL	Phase-locked loop
PRS	Pseudo-random sequence
PV	Photovoltaic
PWM	Pulse-width-modulation
RHP	Right-hand plane
Re	Real part of a value
SISO	Single-input and single-output
SNR	Signal-to-noise ratio
STC	Standard test conditions
THD	Total harmonic distortion
VSC	Voltage source converter
XOR	Exclusive-or operation

1 INTRODUCTION

1.1 Background

Climate change is among the most significant challenges of the 21st century, and an overwhelming body of evidence has presented considerable ecological and economic threats driven by the change [7], [8]. The scientific community has widely acknowledged the influence of human actions in progressing climate change and recognized greenhouse gas emissions as the main contributor to the increasing global temperatures [9]. Accordingly, authorities have established and adopted various environmental policies to halt global warming. Significantly, in the Paris Agreement of 2015, 196 nations signed an agreement to confine the increase of global average temperature to below 2°C and pursue a limit of 1.5°C [10]. Even though the signatories accounted for 97 percent of global greenhouse gas emissions and other additional measures taken since then, the established policies are still assessed as insufficient [11]–[13]. Increasing the number of renewable energy sources such as wind and solar power is considered one of the most critical factors in achieving the climate goals [14]. However, despite significant renewable energy additions in 2021, global CO_2 emissions rose to a record high due to adverse weather and energy market conditions and rapid economic recovery after the COVID-19 pandemic [15].

To utilize the full potential of renewable energy generation, energy storage systems are deemed essential [16]. Energy storage systems, such as battery energy storage systems (BESS), provide flexibility to the intermittent renewable energy production and to improve the efficiency, practicality, and reliability of renewable energy sources, thus advancing their adoption and furthering their usability and potential [17]. Additionally, BESS can strengthen and improve power system stability through various grid-supporting control solutions and provide flexibility for the balance between generation and demand [16], [18]–[20]. In effect, energy storage systems are becoming increasingly prevalent in modern power systems. Global battery storage capacity increased by 5 GW in 2020, which is almost twice as high as the increase in 2019 [21]. The importance of BESS is also gradually recognized on a societal level. For example, California officials will require new commercial buildings to install battery energy storage starting from 2023 [22].

The efficient use of most BESS relies on power-electronics-based converters. In fact, mod-

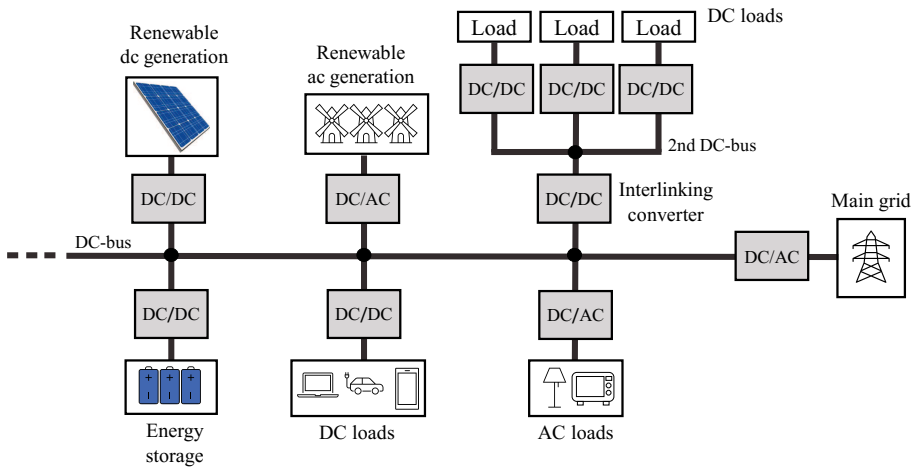

Figure 1.1 Illustration of a modern electric power system.

ern power systems with BESS applications typically consist of several interconnected converters, some of which can have bidirectional power flow. Such power-electronics-based converters are dominated by fast, semiconductor-induced electromagnetic dynamics rather than conventional, slow electromechanical dynamics. Therefore, the converter systems allow for robust converter output regulation. However, the dynamic behavior of the converter systems introduces new challenges to the power system stability [23]–[25]. For example, a lack of system inertia and the risk of improper converter control introduce design challenges and make the converter systems inherently more prone to instability compared to traditional power systems [26], [27]. Moreover, the stability issues in converter-driven systems are often complex to analyze, and their specific root causes are challenging to identify and predict [28].

Due to the increasing demand for applications facilitated by power-electronic converters, the modern power grid is transforming toward a decentralized, converter-penetrated system where various types of production and consumption intermesh [29]. Fig. 1.1 illustrates an electric power system that uses power-electronic converters to bring together several types of energy production, consumption, and storage. In fact, such multi-terminal dc systems have become an attractive alternative for enabling the efficient integration of renewable energy sources and storage solutions [30], [31]. However, securing stability at each bus becomes difficult due to complex interactions between the interconnected converters [32]. Conclusively, robust and reliable power converters capable of operating under various operating conditions and as a part of complex power systems are critical for the successful facilitation of modern power systems.

Stability Issues in Multi-Converter Systems

A system consisting of many converters and various sources and loads can exhibit degraded stability due to interactions between the interconnected devices, even though each converter in the system is standalone stable. For example, distributed energy sources, such as photovoltaic (PV) and wind, have been found to have a considerable effect on the system's damping performance, which can lead to oscillation and instability [33], [34]. On the load side, a major challenge is the constant power load (CPL) instability problem that occurs in multi-converter systems with power-electronic loads when the load converter dynamic response is faster than the source converter dynamic response. The high control bandwidth of the load converters introduces a negative incremental impedance at the point of coupling with the dc bus: input current increases when input voltage decreases, and vice versa. The negative incremental impedance of CPLs has a destabilizing effect on the system [35]–[42] and is the main reason for interaction dynamics in dc multi-converter systems [43], [44]. In particular, when a CPL is connected in parallel with a source converter, their impedances may cause underdamped or unstable oscillation. To avoid such interaction-based stability issues, the control systems of the converters are often designed to ensure robustness, even for interfaces with low damping. However, ensuring robustness can easily lead to overly conservative controller design and the controllers may be designed based on the worst-case scenario, leading to decreased system performance in some operating points.

Multi-converter systems typically experience many changes in their system dynamics during their operation, which complicates the stability analysis. The dynamics of the multi-converter system may vary drastically and unpredictably due to factors such as changes in the devices' control modes, operating modes, or the network's topology. For example, a change in power flow direction can cause loss of stability even though the system is stable with the initial power flow direction [45]. Furthermore, each of the converters' control loops poses a risk to the multi-converter system's performance, and variations in a converter's controller parameters can have a detrimental effect on the system's small-signal stability [46]. Similarly, adding a new device to a multi-converter system can cause the system to become unstable if the system's dynamic performance, such as damping, degrades. Since the multi-converter system's structure can also change over time with new devices or hardware upgrades, for example, it becomes more and more challenging to keep track of the changes and form an accurate and reliable model of the system.

Traditional stability analysis methods are insufficient for addressing the stability issues of modern power systems where multiple power-electronics converters are connected together. The stability analysis of a power grid is conventionally performed by considering the large-signal stability of the system through an analysis of the voltage stability, rotor angle stability, and frequency stability [47]–[49]. In multi-converter systems, however, the stability can be lost due to the dynamic interactions between the converter and the other devices [28], [50].

The small-signal stability can be assessed by considering the impact of the source or load on the controller dynamics or by examining the compatibility of the terminal impedances of the converter and the interfacing bus [51]. Although the former method provides insights into multi-converter interactions through the participation factor and sensitivity analysis, it relies on the complicated full-state small-signal model, where the model order will increase as the number of converters increases [52]. Moreover, the approach needs complete knowledge of the system model that could be hard to obtain due to unknown parameters and variables. The other small-signal stability-assessment method is known as impedance-based stability analysis. This method describes the relationship of the voltage and current at the converter terminals and the analysis is performed in frequency domain. The main advantage of such impedance-based analysis is that, rather than relying on dynamic modeling, the terminal impedances can be extracted by measurements without having detailed information on the system parameters. However, the impedance-based stability analysis is typically interface-specific and provides analysis only in the local scope [51], [53]. Thus, its use for multi-converter systems may become problematic, requiring more general and efficient stability analysis methods.

Broadband Methods in Stability Analysis of Multi-Converter Systems

Nonparametric frequency-response measurements provide an efficient tool with which to apply the impedance-based approach in the stability analysis of multi-converter systems. In the method, the system is excited with an external voltage or current perturbation. The impedance is then identified by measuring the resulting output voltage and current and transforming the measurement data to the frequency domain. Typically, the perturbation should be designed in such a way that it interferes with the regular operation of the system as little as possible. One of the most basic perturbation signals is a sine signal, which facilitates the frequency-response identification at the chosen frequency. However, such a measurement may take a long time when the frequency response is measured at a wide frequency band. Moreover, the practical implementation of a sine signal is not straightforward due to the infinite number of signal levels.

Broadband methods offer attractive attributes to the perturbation signal design of online frequency-response measurements. A broadband perturbation excites multiple frequencies simultaneously, thus decreasing the required measurement time significantly rather than measuring each frequency component individually [54]. Specifically, a class of periodic and deterministic perturbations known as maximum-length binary sequence (MLBS) has favorable characteristics for the online identification of converter systems. The main advantage of the MLBS is its largely controllable spectral-energy content. Another advantage is the signal binary form; only two levels of data points are required. Therefore, the signal can

be implemented even with a low-cost signal generator, the output of which can only cope with a small number of signal levels. The MLBS perturbations have a low crest factor, which means that the signal energy is high in relation to the signal amplitude in the time domain [54]. Additionally, unlike typical multi-sine signals, MLBS signals do not include large peaks in their time-domain waveforms.

In a typical multi-converter system, the individual converters are coupled. This complicates the bus impedance identification process. For example, in the case of two converters, the source converter output impedance must be identified with a perturbation only from the source converter. Similarly, the load converter input impedance must be identified with a perturbation only from the load converter. The bus impedance can then be constructed based on the two separately identified impedances. In essence, the impedance identifications of coupled systems must be performed sequentially to avoid interference between the different perturbations. As the amount of converters increases, the bus identification process becomes challenging as many individual input/output identifications have to be performed. Such a procedure accumulates the required measurement time and may yield unreliable results if the operating point changes between the individual impedance measurements. A more beneficial approach is to use multiple-input multiple-output (MIMO) techniques with uncorrelated perturbation signals [55]. In this method, several orthogonal perturbation signals are fed into the system simultaneously. This simultaneous identification is possible since each of the orthogonal perturbation signals has energy at different frequencies. Thus, the identification can be performed during a single identification cycle. In effect, the approach guarantees the same operating conditions for each identified impedance. The method is especially advantageous for systems that include renewable energy sources, as they tend to shift the converters' operating conditions, making the results inaccurate if the measurement takes a long time.

1.2 Aim and Scope of the Thesis

The goal of this work is to provide modeling methods and adaptive control techniques for enhancing the stability of BESS. The methods enable a more robust and reliable design of systems with high penetration of converters, which advances the deployment of modern power systems and expands renewable energy production capacity. The methods can be employed online during the system's regular operation, allowing for performance regulation even under changing operating conditions. Moreover, the methods can be applied both in local and global scope, providing comprehensive surveillance and regulation of the stability and performance of the BESS's power-electronic converter and the whole multi-converter system.

This thesis presents identification and control methods that monitor and enhance the

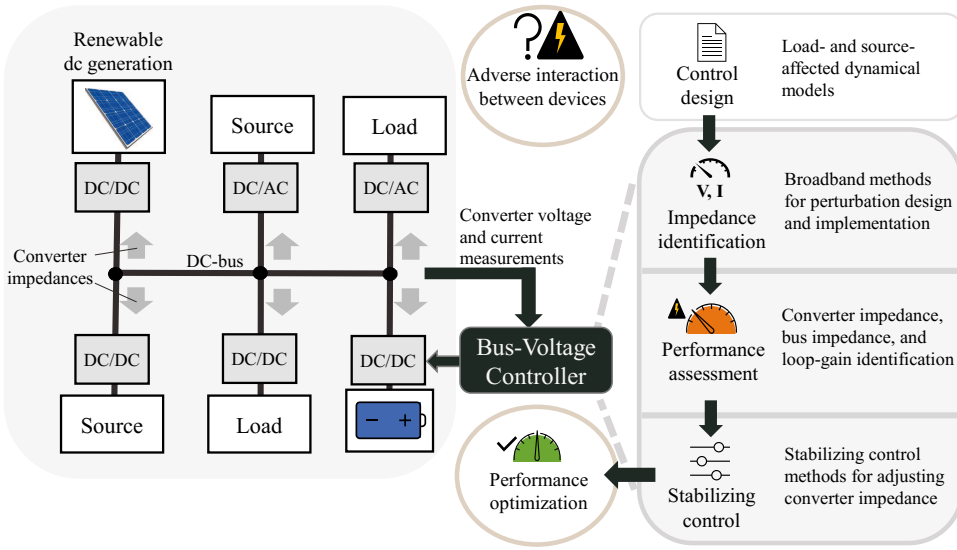

Figure 1.2 Graphical abstract of the thesis.

stability of renewable-energy-penetrated multi-converter systems. The identification methods are based on broadband methods, such as periodic pseudo-random sequences, and allow rapid identification of multivariable systems. Procedures for efficient utilization of such broadband identification methods are provided, focusing on their reliability in modern bidirectional converters and multi-converter systems. The presented identification methods provide performance evaluation without requiring detailed knowledge of the devices or separate communication channels.

The introduced control methods further utilize the performance metrics provided by the identification methods. The stabilizing control methods utilize a BESS to enhance the multi-converter system's dynamic performance. The BESS is employed to introduce a virtual impedance into the multi-converter system dynamics to acquire the desired performance and stability conditions. The introduced stabilizing control methods provide stability and performance enhancement for different applications, and their effects on the regular converter control are considered and restricted.

Fig. 1.2 presents a graphical abstract of this work. The illustration presents a modern multi-converter system with several sources and loads, including solar panels and a BESS. The detailed device parameters and operating modes may be unknown, posing a risk of adverse interactions between the interconnected devices. Therefore, the BESS controller is set to employ algorithms that adaptively enhance the system's stability. First, the system's dynamic performance is identified from the resulting currents and voltage with broadband-based frequency response measurements. Based on the identified performance metrics, the BESS converter control is adjusted to achieve the desired virtual impedance that prevents

stability degradation and optimizes the multi-converter system's performance.

The main contributions of this thesis can be summarized as follows:

- A procedure for selecting design criteria and identifying limitations for broadband impedance measurements of multi-converter systems with bidirectional converters
- Real-time implementation of stability and performance assessment for multi-converter systems with bidirectional converters
- A stabilizing controller that offers adaptive virtual capacitance with a bidirectional converter
- A stabilizing controller that optimizes damping of dc multi-converter systems with a bidirectional converter

1.2.1 Research Challenges

The modeling and stability assessment of multi-converter systems involves multiple challenges. Although many of the obstacles are general for dynamic analysis and system identification, some challenges are particularly present in multi-converter systems with bidirectional converters. The main challenge in assessing such systems is their innate complexity and versatility. The variable nature of power flows, loads, and other phenomena cause the power system dynamics to vary constantly. Due to the complex structure of these systems, it may be challenging to identify the interfaces suitable for reliable stability assessment. In addition, adverse interactions between the various sources and loads, especially constant power loads, pose risks to the system's stability and further complicate the analysis. Accordingly, the unknown effects of the sources and loads make the converter control design demanding, and sufficient safety margins may be difficult to determine.

Another challenge for the stability assessment of multi-converter systems is the limited and inaccessible information of the system parameters. Some of the subsystems, such as load or source converters, may have entirely unspecified internal dynamics since the detailed controller structure of each subsystem is typically unknown. Additionally, the parameters of passive components (and their parasitic components) typically have uncertainties and their values may be strongly operating-point-dependent. Consequently, parametric methods are typically impractical and highly demanding for multi-converter systems. The lack of accurate and reliable models may jeopardize the system's stability and problematize the analysis, so measurement-based approaches are more favorable than modeling-based approaches. Such measurement methods should also be capable of performing a fast re-assessment of the system stability to keep up with the varying operating conditions.

Several difficulties challenge the identification process required for the measurement-based stability analysis. As the measurements typically require the introduction of a perturbation to the system, an inherent trade-off exists between the measurement accuracy and the

interference to the system's regular operation and power quality. In effect, the perturbation signal's time-domain amplitude and frequency-domain spectrum must be carefully designed for the system under study [56]. This is particularly problematic in multi-converter systems since each perturbing device affects each other one, leading to cross-effects and interaction due to their coupled nature through the shared bus connection. Furthermore, nonlinear operating points and other phenomena can introduce additional challenges as the identification methods are typically designed for linear systems.

Lastly, there are several challenges related to the practical implementation of the system identification. Preferably, the measurements should be implemented by applying the existing devices so that external instruments or hardware are not required. In effect, the perturbation signal is typically introduced into the converter via the control feedback path (such as the modulation signal or the reference voltage) or directly into the duty cycle. Therefore, the method should be straightforward to perform on a digital controller, or a separate measurement instrument is required. In addition, the point of perturbation introduction must be considered carefully to guarantee meaningful results since stability analysis is typically interface-specific, providing analysis only in the local scope.

1.2.2 Research Questions

The research questions in this thesis can be summarized as follows:

- How can a virtual impedance be applied to enhance the stability of a BESS-connected power-distribution system?
- How can a bidirectional converter be applied to emulate a virtual capacitor?
- What are the design criteria for a virtual-impedance-based controller in a power-distribution system that has bidirectional power flow?
- What are the design criteria for an adaptive virtual-impedance-based controller in a power-distribution system with bidirectional power flow?
- What are the limitations in applying virtual-impedance-based controllers in multi-converter systems?
- What are the design criteria and limitations for a broadband frequency-response measurement of a multi-converter system that has bidirectional converters?

1.3 Literature Review

The first invention of electric battery cells dates to the early 19th century, when they were applied as small electric generators [57]. By the end of that century, BESS were increasingly applied in industrial plants, railways, and commercial lighting to improve the process procedures and enhance economics [58], [59]. Technological advancements in power-electronic converters after the development of commercial semiconductor switches in the 1950s have allowed BESS to be used in more advanced applications such as in renewable energy systems, railway, automotive, ships, aerospace, elevators, dc microgrids, uninterruptable power supplies, distribution networks, and smart grid applications [16], [60]–[70]. In particular, BESS has become an integral part of new PV applications [71] and dc micro-grids [72]–[74], and the use of large-scale BESS is becoming increasingly popular [75].

The dynamic behavior of BESS is typically mainly dominated by the dynamics of their designated power-electronic converters. Appropriately, small-signal dynamical models have been derived for various dc-dc converters of BESS applications, such as bidirectional buck-boost, flyback, dual-Cuk, and dual active bridge (DAB) converters, have been analyzed [76]–[82]. Likewise, dynamical models exist for grid-connected applications, such as electric vehicle chargers [83], [84]. For such applications, the BESS is typically connected to the grid either through an inverter or via a combination of a dc-dc converter and an inverter. Rather than focusing only on the converter small-signal models, some models have been extended to include the effect of various non-ideal sources and loads, such as battery impedance [84], [85], PV source [86], [87], and load impedance/resistance [86], [88]–[90]. Such models are particularly useful for converter design as they provide the converter's source- and load-affected control dynamics. Additionally, the dynamical models can facilitate stability analysis, such as impedance-based stability analysis. Introduced by Middlebrook in 1976 [91], the impedance-based stability analysis studies the closed-loop stability between two cascaded power-electronic devices by assessing the ratio of the equivalent impedances of both subsystems [84], [92]. This ratio is called the minor-loop gain.

In modern power systems, BESS is typically a part of a multi-converter system that consists of several electrical, converter-based sources and loads with unpredictable and varying dynamical behavior. Therefore, measurement-based stability assessment is preferable to relying solely on analytical models. The impedance-based stability analysis of cascaded systems has offered a valuable foundation for developing such methods, and it has been extended to consider multi-converter systems through several approaches. Various impedance-based stability criteria have been presented [53], [93], and impedance-based stability analysis has been recently applied for dc microgrids and other modern power systems [94]–[96]. A supplementary approach was taken in [97], where the impedance ratio was chosen based on the converters' role in contributing to the current and voltage control instead of their role as

load and source converters. Alternatively, a passivity-based stability criterion, introduced in [98], uses an approach in which the stability is analyzed based on the passivity of the bus impedance. The bus impedance is defined as the equivalent impedance of all the interconnected sources and loads, which simplifies the analysis to one parameter (bus impedance) instead of a ratio of two (source and load impedance). In [99], the passivity-based stability criterion is extended to converter systems with multiple bus connections. The stability analysis of bus impedance is especially advantageous for systems with bidirectional power flow as it does not require the converters to be categorized as loads or sources.

The recent interest in impedance-based stability analysis has advanced research on impedance shaping and other stabilizing control features. One approach is to add passive or active circuit components to the existing system to alter the operating conditions to more favorable ones [43], [100]. Alternatively, several stabilizing control methods have been proposed that reshape the converter output impedance with a specific control feature, such as virtual resistor [41], [101], virtual capacitor [102], virtual negative inductor [103], and virtual impedance [104]–[106]. Moreover, following the introduction of bus impedance analysis, several methods have been proposed to damp undesired resonances in the bus impedance, such as a specific adjustment of the source-converter controller [107], additional damping term in the source-converter controller [108], and a positive feed-forward controller in the load-converter controller [109]. In [46], the stabilizing methods have been found to be more effective on source converters than load converters. Alternatively, rather than adding new control features, another approach for stability enhancement is to utilize the system identification for implementing auto-tuning of the regular converter controller [107].

Fast, measurement-based impedance identification is required to facilitate the online impedance-based stability analysis and the associated stabilizing control features. Early implementations of impedance identification were typically performed by introducing severe transients to the system [110], [111]. Such impulse-like transients may disturb the system operation and provide results only at limited frequencies. An improved identification method was used in [112], where the system was perturbed by controllable sinusoidal signals, and in [113], multi-sine signals were introduced for impedance identification. In [114], the identification procedures were further improved by utilizing the converter itself in the perturbation injection, which removed the need for an additional measurement instrument, although some high-power applications still require it [115], [116]. Recently, binary-sequence-based broadband methods, such as MLBS, have been used for impedance identification to analyze system stability and facilitate advanced control and protection features [109], [117]–[120]. In [55], similar methods were considered for MIMO systems as orthogonal binary sequences were introduced for impedance identification. In [121], binary orthogonal sequences were used to identify the d- and q-components of grid impedance simultaneously, and in [122], orthogonal binary injections were used to perform bus-impedance identification in a multi-converter system.

1.4 Summary of Scientific Contributions

The scientific contributions of this thesis can be summarized as follows.

- A method to obtain a small-signal model for a grid-connected inverter that includes the effect of an arbitrary non-ideal current-type source (or sources) on the inverter dynamics
- A method to obtain a small-signal model for a grid-connected inverter that includes the effect of PV and BESS sources on the inverter dynamics
- A method to identify limitations and selecting a perturbation for broadband impedance measurements on bidirectional DAB converters
- A design method for broadband impedance measurements on multi-converter systems.
- A real-time method that assesses stability and level of damping of multi-converter systems with bidirectional converters
- A design method for a virtual-capacitance-based stabilizing controller on a bidirectional converter to enhance system stability
- A design method for a resonance-damping impedance-based stabilizing controller on a bidirectional converter to enhance multi-converter system stability

1.5 Structure of the Thesis

This thesis consists of five chapters and six publications [P1–P6]. The contents of the chapters can be summarized as follows.

Chapter 2 introduces the theoretical background for the dynamical analysis and identification of multi-converter systems with bidirectional converters. First, individual bidirectional converters are discussed: dynamic models of a bidirectional buck-boost converter, a bidirectional DAB converter, and an inverter are presented. Then the stability and dynamic performance of a multi-converter system are analyzed with bus impedance transfer function. Finally, broadband identification methods are discussed in detail.

Chapter 3 briefly describes the main methods used in this thesis. The chapter is divided into three sections. The first section outlines broadband identification implementation methods on bidirectional converters; the second presents converter control design methods with source and load effect; and the third suggests two different methods for stabilizing control design with virtual impedance.

In Chapter 4, the methods proposed in this thesis are implemented on experimental setups. This chapter summarizes the experiments performed in the original publications that

form the foundation of this thesis. The experimental results verify the performance and applicability of the proposed methods.

Finally, Chapter 5 draws conclusions that summarize the thesis. The presented methods are given a critical review, where limitations and potential challenges in the presented methods are discussed. Moreover, the discussion considers the general challenges in the stability assessment of complex systems that have a high penetration power-electronic converters. The last section discusses the potential future research topics based on the results of this thesis.

2 THEORY

This chapter introduces the theoretical background for a dynamic analysis and stability assessment of multi-converter power-electronics systems that have bidirectional converters. First, the control principles of bidirectional converters are discussed briefly and several dynamical models are presented for different converter topologies: a buck-boost converter, a DAB converter, and a three-phase two-level inverter. After this, the impedance-based stability analysis is presented to assess the stability and dynamical performance of a multi-converter system. The adverse effect on system stability caused by a CPL will be discussed and demonstrated.

2.1 Dynamic Modeling of Bidirectional Converters

The small-signal dynamics of a BESS mainly depends on the chosen control scheme and converter topology. Accurate converter small-signal models are essential for designing converter control parameters such that the necessary safety margins are met and the system is standalone stable. Moreover, the models provides information on the converter impedance, thus facilitating compatibility studies between the BESS and its sources and loads, which will lead to a more comprehensive stability assessment being made.

2.1.1 Control of Bidirectional Converters

The control design of bidirectional converters is typically limited by various requirements. For example, specific considerations may relate to the desired converter topology or application-related control functions. Primarily, the bidirectional converters of a BESS require control schemes that adjust the circuit to produce an appropriate power flow in and out of the energy storage. These charging and discharging processes are typically achieved by controlling the energy storage current or voltage depending on the application and battery type. The executed control scheme can also vary depending on such factors as the battery state of charge or the power-flow direction.

In this thesis, the converters are typically controlled with conventional proportional-integral (PI) controllers using either current control or cascaded control with a current-controlling inner loop and voltage-controlling outer loop. Fig. 2.1 presents block diagrams

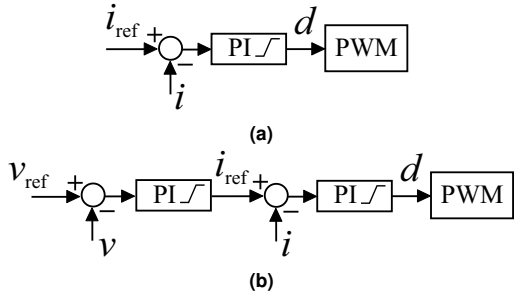

Figure 2.1 Typical power-electronic converter control block diagrams of a) current control, and b) cascaded control.

of such control schemes. However, the presented methods are valid with any control type as long as the converter's frequency responses, such as loop gain and output impedance, can be assessed or measured. In general, the crossover frequencies of control loops are restricted by possible zeros and poles in the converter dynamics, as well as the switching dynamics. For example, the crossover frequency should typically be at least two times higher than the frequency of a right-hand plane (RHP) pole [123]. Such considerations can be especially important with bidirectional converters, as the system dynamics may change profoundly depending on the power direction (compare, for example, buck and boost converters). Additionally, in the cascaded control scheme, the inner and outer control loop should be decoupled.

Converters with ac variables, such as three-phase inverters, require additional tools if linear (PI) controllers are employed. For balanced three-phase systems, a rotating orthogonal reference frame (dq-frame) can be adopted along with the Park transformation to transform the ac variables into dc. Thereby, a variable ζ_{abc} in the abc-frame is transformed into a variable ζ_{dq} in the dq-frame via the operation $\zeta_{\text{dq}} = \mathbf{P}(\theta)\zeta_{\text{abc}}$, where θ is the angle between the perpendicular (i.e., d) axis of the dq-frame and the a axis of the abc frame. Note that ζ_{dq} and the dq-frame should rotate with the same angular frequency to ensure their synchronous rotation. To this end, with grid-connected converters, it is common practice to use the angular frequency ω_ζ provided by a phase-locked-loop (PLL) for the angular frequency of the dq-frame.

One of the fundamental aims of converter control design is to modify the converter's output impedance to the desired shape. In the case of a current-controlled converter, the impedance can be described as a CPL since the converter has a negative incremental impedance within the feedback control loop bandwidth, i.e., the impedance magnitude is resistive with a $-180°$ phase. In contrast, the impedance of a voltage-controlled converter has a relatively small magnitude, except for a resonance peak around the voltage control cross-over frequency. Similarly, droop-controlled converters have the same impedance characteristics as voltage-controlled converters except for very low frequencies, in which the impedance magnitude is affected by the droop coefficient [124]. Thus, the chosen controller determines the

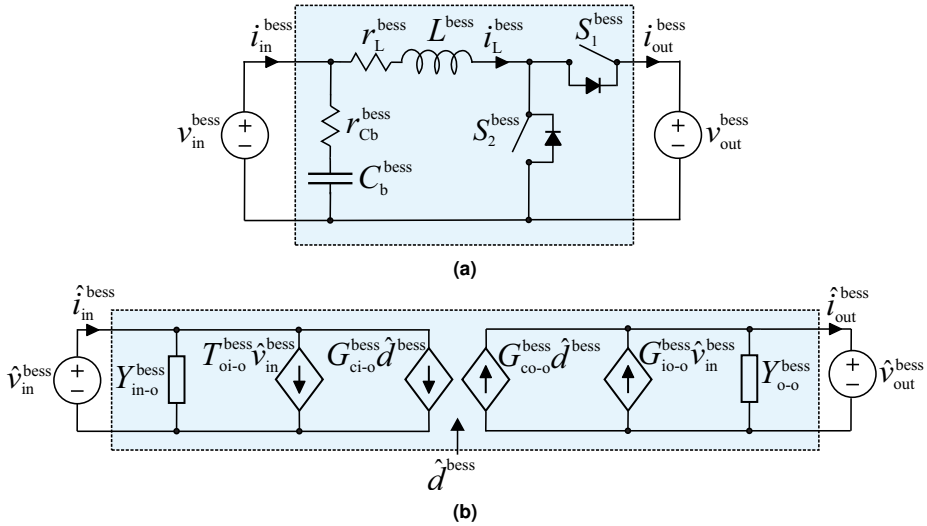

Figure 2.2 A bi-directional buck-boost dc-dc converter a) schematic, and b) linear equivalent circuit in open-loop.

shape of the BESS output impedance.

Additionally, appropriate safety measures pose a critical perspective to the control design of energy storage applications due to their high energy levels. Energy storages are very sensitive to over-current and over-voltage, and the controller should limit the operation through means such as appropriate saturation limits to avoid placing excessive stress on the energy storage at its terminals. The converter also provides short circuit protection and allows the disconnection of the BESS to perform maintenance upstream etc. Energy storages are also susceptible to over- and under-charge. For example, extended periods of undercharging a battery can lead to excessive sulphation and stratification, whereas overcharging can cause gassing and grid corrosion. In fact, specific battery management systems are typically applied at the cell, module, and string levels to protect the system against imbalance as well as over-voltage, over-current, and overheating.

2.1.2 Bidirectional Buck-Boost Converter

A bidirectional buck-boost converter is a typical example of a traditional dc-dc converter that can be used in battery applications. Its main advantages are simplicity, small size, and low price. These converters are particularly beneficial for battery systems where the battery voltage varies widely due to variations in the battery state of charge. The main disadvantage of utilizing a buck-boost converter in battery applications is the lack of galvanic isolation, which makes it unsuitable for some applications. In such cases, the isolation would have to be acquired by other means, such as through a separate transformer. Moreover, the buck-boost converter's ability to boost voltage may not be enough for larger battery applications, and the efficiency may be poor depending on the operating point.

Fig. 2.2a presents a schematic diagram of a bidirectional buck-boost converter for connecting the battery storage to the common dc bus. Only one of the switches is active at a time: S_2^{bess} when discharging (boost mode) and S_1^{bess} when charging (buck mode). Here, the output current $i_{\text{out}}^{\text{bess}}$ is defined as an output variable. Thus, the dc bus can be modeled as a constant voltage source. Note that the positive current direction is as it is in discharging mode, and in charging mode, the current is defined as negative.

In order to derive a small-signal model for the system, the state vector and input and output vectors are defined as

$$\hat{\mathbf{x}}(t) = \begin{bmatrix} \hat{v}_{\text{Cb}}^{\text{bess}} \\ \hat{i}_{\text{L}}^{\text{bess}} \end{bmatrix}, \hat{\mathbf{u}}(t) = \begin{bmatrix} \hat{v}_{\text{in}}^{\text{bess}} \\ \hat{v}_{\text{out}}^{\text{bess}} \\ \hat{d}^{\text{bess}} \end{bmatrix}, \hat{\mathbf{y}}(t) = \begin{bmatrix} \hat{i}_{\text{in}}^{\text{bess}} \\ \hat{i}_{\text{out}}^{\text{bess}} \end{bmatrix}, \tag{2.1}$$

respectively, where $\hat{v}_{\text{Cb}}^{\text{bess}}$ is the voltage over the capacitor and $\hat{i}_{\text{L}}^{\text{bess}}$ is the current through the inductor. The hat above the variables implies a small-signal (ac) variable. The switch S_2^{bess} is controlled by duty cycle d^{bess} and switch S_1^{bess} by its opposite, $1 - d^{\text{bess}}$. The linearized state-space representation can be presented in a matrix form as

$$\frac{d\hat{\mathbf{x}}(t)}{dt} = \mathbf{A}\hat{\mathbf{x}}(t) + \mathbf{B}\hat{\mathbf{u}}(t) \tag{2.2}$$

$$\hat{\mathbf{y}}(t) = \mathbf{C}\hat{\mathbf{x}}(t) + \mathbf{D}\hat{\mathbf{u}}(t), \tag{2.3}$$

where the state, input, output, and feed-through matrices **A**, **B**, **C**, and **D**, respectively, are defined as [P3]

$$\begin{aligned} \mathbf{A} &= \begin{bmatrix} -\dfrac{1}{C_{\text{b}}^{\text{bess}} r_{\text{Cb}}^{\text{bess}}} & 0 \\ 0 & \dfrac{R_{\text{eq1}}}{L^{\text{bess}}} \end{bmatrix}, \ \mathbf{B} = \begin{bmatrix} \dfrac{1}{C_{\text{b}}^{\text{bess}} r_{\text{Cb}}^{\text{bess}}} & 0 & 0 \\ \dfrac{1}{L^{\text{bess}}} & \dfrac{D^{\text{bess}} - 1}{L^{\text{bess}}} & \dfrac{V_{\text{eq}}}{L^{\text{bess}} R_{\text{eq2}}} \end{bmatrix}, \\ \mathbf{C} &= \begin{bmatrix} -\dfrac{1}{r_{\text{Cb}}^{\text{bess}}} & 1 \\ 0 & 1 - D^{\text{bess}} \end{bmatrix}, \quad \mathbf{D} = \begin{bmatrix} \dfrac{1}{r_{\text{Cb}}^{\text{bess}}} & 0 & 0 \\ 0 & 0 & -\dfrac{V_{\text{in}}^{\text{bess}} + \left(D^{\text{bess}} - 1\right) V_{\text{out}}^{\text{bess}}}{R_{\text{eq2}}} \end{bmatrix}, \end{aligned} \tag{2.4}$$

where

$$\begin{aligned} R_{\text{eq1}} &= \left(r_{\text{L}}^{\text{bess}} + r_{\text{sw1}}\right) \left(D^{\text{bess}} - 1\right) - D^{\text{bess}} \left(r_{\text{L}}^{\text{bess}} + r_{\text{sw2}}\right), \\ R_{\text{eq2}} &= r_{\text{L}}^{\text{bess}} + r_{\text{sw1}} + D^{\text{bess}} \left(r_{\text{sw2}} - r_{\text{sw1}}\right), \\ V_{\text{eq}} &= \left(r_{\text{L}}^{\text{bess}} + r_{\text{sw2}}\right) V_{\text{out}}^{\text{bess}} + \left(r_{\text{sw1}} - r_{\text{sw2}}\right) V_{\text{in}}^{\text{bess}}. \end{aligned} \tag{2.5}$$

The variables correspond to Fig. 2.2a, except for r_{sw1} and r_{sw2}, which are the internal on-time resistances of the switches S_1^{bess} and S_2^{bess}, respectively. Moreover, the capital letters represent the steady-state values.

Based on the state-space representation, the transfer functions from the input variables to the output variables at open loop can be solved in the s-domain by noting that

$$\hat{\mathbf{y}}(s) = \left(\mathbf{C}(s\mathbf{I} - \mathbf{A})^{-1}\mathbf{B} + \mathbf{D}\right)\hat{\mathbf{u}}(s), \tag{2.6}$$

where $\mathbf{I}$ is the identity matrix [125]. As a result, the converter open-loop dynamics can be presented in a matrix-form as

$$\begin{bmatrix} \hat{i}_{\text{in}}^{\text{bess}} \\ \hat{i}_{\text{out}}^{\text{bess}} \end{bmatrix} = \begin{bmatrix} Y_{\text{in-o}}^{\text{bess}} & T_{\text{oi-o}}^{\text{bess}} & G_{\text{ci-o}}^{\text{bess}} \\ G_{\text{io-o}}^{\text{bess}} & -Y_{\text{o-o}}^{\text{bess}} & G_{\text{co-o}}^{\text{bess}} \end{bmatrix} \begin{bmatrix} \hat{v}_{\text{in}}^{\text{bess}} \\ \hat{v}_{\text{out}}^{\text{bess}} \\ \hat{d}^{\text{bess}} \end{bmatrix}, \tag{2.7}$$

where the 2x3 matrix consists of the open-loop transfer functions between the input and the output variables, denoted as follows: the input admittance $Y_{\text{in-o}}^{\text{bess}}$, the reverse transfer function $T_{\text{oi-o}}^{\text{bess}}$, the control-to-input transfer function $G_{\text{ci-o}}^{\text{bess}}$, the input-to-output transfer function $G_{\text{io-o}}^{\text{bess}}$, the output admittance transfer function $Y_{\text{o-o}}^{\text{bess}}$, and the control-to-output transfer function $G_{\text{co-o}}^{\text{bess}}$. Note that the output impedance has a minus-sign to comply with positive current direction. Fig. 2.2b illustrates the converter linear equivalent model in open-loop. Note that (2.7) is a general presentation for the small-signal dynamics and can be applied to any type of dc-dc converter.

The converter open-loop model in (2.7) can be applied for control design. The closed-loop dynamics can be presented as

$$\begin{bmatrix} \hat{i}_{\text{in}}^{\text{bess}} \\ \hat{i}_{\text{out}}^{\text{bess}} \end{bmatrix} = \overbrace{\begin{bmatrix} Y_{\text{in}}^{\text{bess}} & T_{\text{oi}}^{\text{bess}} & G_{\text{ci}}^{\text{bess}} \\ G_{\text{io}}^{\text{bess}} & -Y_{\text{o}}^{\text{bess}} & G_{\text{co}}^{\text{bess}} \end{bmatrix}}^{\mathbf{M}_{\text{bess}}} \begin{bmatrix} \hat{v}_{\text{in}}^{\text{bess}} \\ \hat{v}_{\text{out}}^{\text{bess}} \\ \hat{i}_{\text{ref}} \end{bmatrix}, \tag{2.8}$$

where $\mathbf{M}_{\text{bess}}$ denotes a matrix of the closed-loop transfer functions and the reference signal is used as a system input. By utilizing feedback control from the output current, the transfer function matrix can be presented as

$$\mathbf{M}_{\text{bess}} = \begin{bmatrix} Y_{\text{in-o}}^{\text{bess}} - \dfrac{G_{\text{PI}} G_{\text{ci-o}}^{\text{bess}} G_{\text{io-o}}^{\text{bess}}}{1 + L_{\text{co}}} & T_{\text{oi-o}}^{\text{bess}} + \dfrac{G_{\text{PI}} G_{\text{ci-o}}^{\text{bess}} Y_{\text{o-o}}^{\text{bess}}}{1 + L_{\text{co}}} & \dfrac{G_{\text{PI}} G_{\text{ci-o}}^{\text{bess}}}{1 + L_{\text{co}}} \\ \dfrac{G_{\text{io-o}}^{\text{bess}}}{1 + L_{\text{co}}} & -\dfrac{Y_{\text{o-o}}^{\text{bess}}}{1 + L_{\text{co}}} & \dfrac{L_{\text{co}}}{1 + L_{\text{co}}} \end{bmatrix}, \tag{2.9}$$

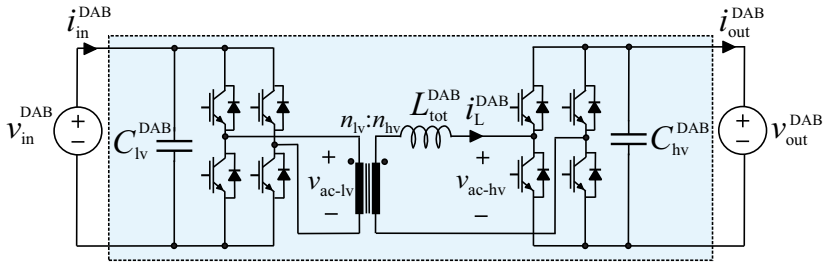

Figure 2.3 DAB converter with a battery energy storage.

where the control loop gain is defined as $L_{\text{co}} = G_{\text{PI}} G_{\text{co-o}}^{\text{bess}}$ with a PI controller G_{PI}. Similarly, if the input current is controlled, the transfer function matrix can be presented as [P2]

$$\mathbf{M}_{\text{bess}} = \begin{bmatrix} \dfrac{Y_{\text{in-o}}^{\text{bess}}}{1+L_{\text{ci}}} & \dfrac{T_{\text{oi-o}}^{\text{bess}}}{1+L_{\text{ci}}} & \dfrac{L_{\text{ci}}}{1+L_{\text{ci}}} \\ G_{\text{io-o}}^{\text{bess}} - \dfrac{G_{\text{PI}} G_{\text{co-o}}^{\text{bess}} Y_{\text{in-o}}^{\text{bess}}}{1+L_{\text{ci}}} & -\left(Y_{\text{o-o}}^{\text{bess}} - \dfrac{G_{\text{PI}} G_{\text{co-o}}^{\text{bess}} T_{\text{oi-o}}^{\text{bess}}}{1+L_{\text{ci}}} \right) & \dfrac{G_{\text{PI}} G_{\text{co-o}}^{\text{bess}}}{1+L_{\text{ci}}} \end{bmatrix}, \tag{2.10}$$

where the control loop gain is defined as $L_{\text{ci}} = G_{\text{PI}} G_{\text{ci-o}}^{\text{bess}}$.

2.1.3 Dual Active Bridge Converter

A dual active bridge (DAB) converter is a modern dc-dc converter suitable for various battery applications. The converter was originally proposed by de Doncker *et al.* [79] and has gained prominence in battery applications due to its flexible power flow control, zero voltage-switching, high efficiency, galvanic isolation, and modular structure [65], [79], [126]. An example of a DAB converter schematic is shown in Fig. 2.3, where the high voltage (HV) side is defined as the output side and low voltage (LV) side as the input side. The converter consists of two filtering capacitors, two full-bridges, a high-frequency transformer, and an energy-transferring inductance. The inductance $L_{\text{tot}}^{\text{DAB}}$ denotes the (total) equivalent inductance, which is associated with the transformer's leakage inductance and possible additional inductive components.

The ac stage between the two full bridges differentiates the DAB converters from the more traditional dc-dc converters that do not have an ac stage and can therefore be controlled only by the duty ratio. In contrast, the DAB converters can be controlled not only by the pulse-width-modulated duty ratios of the HV-side and LV-side full bridges but also by the phase shift between those modulating signals [79]. In fact, one of the most popular modulation techniques for DAB converters is phase-shift modulation, in which the phase shift is varied to control the transferred power, and the duty ratios are kept constant. This modulation method is simple and allows for high power and efficiency, especially if soft-

switching can be used. The control manages the power transfer between the two dc buses as the leading bridge delivers power to the lagging bridge. For example, if the modulating signal of the HV-side bridge is delayed by a phase shift ϕ in comparison with the modulating signal of the LV-side bridge, the achieved power transfer can be given as

$$P_{\mathrm{DAB}} = \frac{n_{\mathrm{tf}} V_{\mathrm{lv}} V_{\mathrm{hv}}}{2\pi f_{\mathrm{sw}} L_{\mathrm{tot}}} \phi \left(1 - \frac{|\phi|}{\pi}\right) \tag{2.11}$$

where n_{tf} is the transformer turns ratio ($n_{\mathrm{hv}}/n_{\mathrm{lv}}$), V_{lv} and V_{hv} are the dc voltages of the LV and HV side, f_{sw} is the switching frequency, and L_{tot} is the (total) equivalent inductance.

The small-signal dynamics of a DAB converter depend on the chosen passive and active components as well as the chosen control scheme and the load dynamics. If the system output variables are defined as the HV-side voltage and the LV-side current, the open-loop control-related transfer functions of the DAB converter in Fig. 2.3 can be given as

$$\begin{aligned} G_{\mathrm{co\text{-}o}}^{\mathrm{DAB}} &= \frac{V_{\mathrm{hv}}}{n_{\mathrm{tf}} 2\pi f_{\mathrm{sw}} L_{\mathrm{tot}}} \left(1 - \frac{2|\phi|}{\pi}\right) \frac{Z_{\mathrm{load}}}{1 + sC_{\mathrm{hv}} Z_{\mathrm{load}}}, \\ G_{\mathrm{ci\text{-}o}}^{\mathrm{DAB}} &= \frac{V_{\mathrm{hv}}}{n_{\mathrm{tf}}^{-1} 2\pi f_{\mathrm{sw}} L_{\mathrm{tot}}} \left(1 - \frac{2|\phi|}{\pi}\right), \end{aligned} \tag{2.12}$$

where Z_{load} is the load impedance and C_{hv} the HV-side capacitance. The open-loop output impedance of a DAB converter connected to a load can be given as

$$Z_{\mathrm{o\text{-}o}}^{\mathrm{DAB}} = -\frac{Z_{\mathrm{load}}}{1 + sC_{\mathrm{hv}} Z_{\mathrm{load}}}, \tag{2.13}$$

and by utilizing feedback control from the input current, the closed-loop output impedance can be given (as in (2.10)) as

$$Z_{\mathrm{o}}^{\mathrm{DAB\text{-}cc}} = -\left(Z_{\mathrm{o\text{-}o}}^{\mathrm{DAB}} - \frac{G_{\mathrm{PI\text{-}c}} G_{\mathrm{co\text{-}o}}^{\mathrm{DAB}} T_{\mathrm{oi\text{-}o}}^{\mathrm{DAB}}}{1 + L_{\mathrm{ci}}}\right), \tag{2.14}$$

where $L_{\mathrm{ci}} = G_{\mathrm{PI\text{-}c}} G_{\mathrm{ci\text{-}o}}^{\mathrm{DAB}}$ is the control loop gain of the input current controller. Then, if cascaded control is used such that the current control operates as the inner control loop and an outer control loop regulates the output voltage, the output impedance can be given as

$$Z_{\mathrm{o}}^{\mathrm{DAB\text{-}casc}} = -\frac{Z_{\mathrm{o\text{-}o}}^{\mathrm{DAB}} + L_{\mathrm{ci}} \left(Z_{\mathrm{o\text{-}o}}^{\mathrm{DAB}} + T_{\mathrm{oi\text{-}o}}^{\mathrm{DAB}} \dfrac{G_{\mathrm{co\text{-}o}}^{\mathrm{DAB}}}{G_{\mathrm{ci\text{-}o}}^{\mathrm{DAB}}}\right)}{\left(1 + L_{\mathrm{v}}\right)\left(1 + L_{\mathrm{ci}}\right)}, \tag{2.15}$$

where $L_\mathrm{v} = G_\mathrm{PI\text{-}v}\dfrac{L_\mathrm{ci}}{1+L_\mathrm{ci}}\dfrac{G^\mathrm{DAB}_\mathrm{co\text{-}o}}{G^\mathrm{DAB}_\mathrm{ci\text{-}o}}$ is the control loop gain of the outer voltage controller. Note that similar representations can be achieved regardless of the chosen converter topology.

Cascaded control scheme can also control variables on the same side; for example, control of output current in the inner loop and output voltage in the outer loop. For the inner loop dynamics, the output current is an output signal, and the current-control-affected dynamics can be given as in (2.9). Then, these dynamics have to be mapped such that output voltage becomes the output signal and output current an input signal [127] as

$$\begin{aligned}\begin{bmatrix}\hat{i}^\mathrm{DAB}_\mathrm{in}\\ \hat{v}^\mathrm{DAB}_\mathrm{out}\end{bmatrix} &= \begin{bmatrix}Y^\mathrm{DAB\text{-}B}_\mathrm{in} & T^\mathrm{DAB\text{-}B}_\mathrm{oi} & G^\mathrm{DAB\text{-}B}_\mathrm{ci}\\ G^\mathrm{DAB\text{-}B}_\mathrm{io} & -Z^\mathrm{DAB\text{-}B}_\mathrm{o} & G^\mathrm{DAB\text{-}B}_\mathrm{co}\end{bmatrix}\begin{bmatrix}\hat{v}^\mathrm{DAB}_\mathrm{in}\\ \hat{i}^\mathrm{DAB}_\mathrm{out}\\ \hat{i}_\mathrm{ref}\end{bmatrix}\\ &= \begin{bmatrix}Y^\mathrm{DAB}_\mathrm{in}+\dfrac{G^\mathrm{DAB}_\mathrm{io}T^\mathrm{DAB}_\mathrm{oi}}{Y^\mathrm{DAB}_\mathrm{o}} & -\dfrac{T^\mathrm{DAB}_\mathrm{oi}}{Y^\mathrm{DAB}_\mathrm{o}} & G^\mathrm{DAB}_\mathrm{ci}+\dfrac{G^\mathrm{DAB}_\mathrm{co}T^\mathrm{DAB}_\mathrm{oi}}{Y^\mathrm{DAB}_\mathrm{o}}\\ \dfrac{G^\mathrm{DAB}_\mathrm{io}}{Y^\mathrm{DAB}_\mathrm{o}} & -\dfrac{1}{Y^\mathrm{DAB}_\mathrm{o}} & \dfrac{G^\mathrm{DAB}_\mathrm{co}}{Y^\mathrm{DAB}_\mathrm{o}}\end{bmatrix}\begin{bmatrix}\hat{v}^\mathrm{DAB}_\mathrm{in}\\ \hat{i}^\mathrm{DAB}_\mathrm{out}\\ \hat{i}_\mathrm{ref}\end{bmatrix},\end{aligned} \tag{2.16}$$

where the superscript DAB denotes the current-control-affected dynamics with output current as the output signal and the superscript DAB-B denotes the same dynamics with output voltage as the output signal. The output-side-cascaded-control-affected closed-loop output impedance can then be given by plugging the DAB-B denoted dynamics in (2.15) as

$$Z^\mathrm{DAB\text{-}casc\text{-}o}_\mathrm{o} = -\frac{\dfrac{1}{Y^\mathrm{DAB}_\mathrm{o\text{-}o}}+L_\mathrm{ci}\left(\dfrac{1}{Y^\mathrm{DAB}_\mathrm{o\text{-}o}}-\dfrac{T^\mathrm{DAB}_\mathrm{oi\text{-}o}}{Y^\mathrm{DAB}_\mathrm{o\text{-}o}}\dfrac{G^\mathrm{DAB}_\mathrm{co\text{-}o}/Y^\mathrm{DAB}_\mathrm{o\text{-}o}}{G^\mathrm{DAB}_\mathrm{ci\text{-}o}+\dfrac{G^\mathrm{DAB}_\mathrm{co\text{-}o}T^\mathrm{DAB}_\mathrm{oi\text{-}o}}{Y^\mathrm{DAB}_\mathrm{o\text{-}o}}}\right)}{\left(1+L^\mathrm{B}_\mathrm{v}\right)\left(1+L_\mathrm{ci}\right)}, \tag{2.17}$$

where the mapped control loop gain of the outer voltage controller is

$$L^\mathrm{B}_\mathrm{v} = G_\mathrm{PI\text{-}v}\frac{L_\mathrm{ci}}{1+L_\mathrm{ci}}\frac{G^\mathrm{DAB}_\mathrm{co\text{-}o}/Y^\mathrm{DAB}_\mathrm{o\text{-}o}}{G^\mathrm{DAB}_\mathrm{ci\text{-}o}+\dfrac{G^\mathrm{DAB}_\mathrm{co\text{-}o}T^\mathrm{DAB}_\mathrm{oi\text{-}o}}{Y^\mathrm{DAB}_\mathrm{o\text{-}o}}}. \tag{2.18}$$

Note that such a control scheme does not directly limit the input side variables through saturation limits so additional protection features should be implemented.

Accurate modeling of the power and dynamics of a practical DAB converter can be challenging. If methods other than the phase-shift modulation are used, the relationship between

the power transfer, phase shift(s), and duty ratio(s) is more complicated and operating-point dependent [5], [128]–[132]. In addition, the presence of deadtime can further complicate the DAB converter power transfer characteristics. The deadtime is a necessary time during which all the switches of an H-bridge are turned off to avoid short circuit through the low-resistance paths of simultaneously conducting switches. The presence of deadtime is a fundamental requirement in most power electronic converters, and it is present in DAB converters regardless of the chosen modulation and control strategy. The deadtime affects the power transfer characteristics of DAB converters through various voltage distortion phenomena, such as voltage polarity reversal, voltage sag, phase drift, and duty-cycle abnormity [133]. In fact, the presence of deadtime can lead to a false interpretation of the system stability margins if not considered properly [134]. While various methods to avoid or mitigate deadtime effects in DAB converters have been suggested [135]–[138], the applicability of these methods depends strongly on the chosen application, such as the modulation and control method, and should therefore be considered based on the specific application.

2.1.4 Three-Phase Inverter

Inverters are required to connect dc sources, such as batteries and PV sources, to the electric grid. Three-phase, two-level converters are typical examples of inverters. Fig. 2.4a shows a schematic of a three-phase current-fed inverter. In the literature, the inverter dc side is often modeled with a voltage-type source (i.e., a voltage source converter, or VSC). However, if the inverter controls the dc bus voltage, the dc side must be considered with a current-type source. Such a current-fed model is required, for example, when the inverter is connected directly to a battery or a PV source and dc voltage control is needed. The dynamics of VSC are well established, and small-signal models can be found, for example, in [127]. In this section, the focus is on the current-fed inverter model.

Using the *dq* reference frame, the dynamic open-loop behavior of the current-fed inverter shown in Fig. 2.4a can be presented in a matrix form as [P2]

$$\begin{bmatrix} \hat{v}_{\text{in}}^{\text{inv}} \\ \hat{i}_{\text{od}}^{\text{inv}} \\ \hat{i}_{\text{oq}}^{\text{inv}} \end{bmatrix} = \begin{bmatrix} Z_{\text{in-o}}^{\text{inv}} & T_{\text{oid-o}}^{\text{inv}} & T_{\text{oiq-o}}^{\text{inv}} & G_{\text{cid-o}}^{\text{inv}} & G_{\text{ciq-o}}^{\text{inv}} \\ G_{\text{iod-o}}^{\text{inv}} & -Y_{\text{od-o}}^{\text{inv}} & G_{\text{crqd-o}}^{\text{inv}} & G_{\text{cod-o}}^{\text{inv}} & G_{\text{coqd-o}}^{\text{inv}} \\ G_{\text{ioq-o}}^{\text{inv}} & G_{\text{crdq-o}}^{\text{inv}} & -Y_{\text{oq-o}}^{\text{inv}} & G_{\text{codq-o}}^{\text{inv}} & G_{\text{oq-o}}^{\text{inv}} \end{bmatrix} \begin{bmatrix} \hat{i}_{\text{in}}^{\text{inv}} \\ \hat{v}_{\text{od}}^{\text{inv}} \\ \hat{v}_{\text{oq}}^{\text{inv}} \\ \hat{d}_{\text{d}}^{\text{inv}} \\ \hat{d}_{\text{q}}^{\text{inv}} \end{bmatrix}, \tag{2.19}$$

where the 3 x 5 matrix consists of the transfer functions between the input and output variables. The derivation of the transfer functions can be found, for example, in [139]. Fig. 2.4b illustrates the linear equivalent model in open-loop. Note that (2.19) can be considered a general presentation of inverter small-signal dynamics that applies to any type of inverter

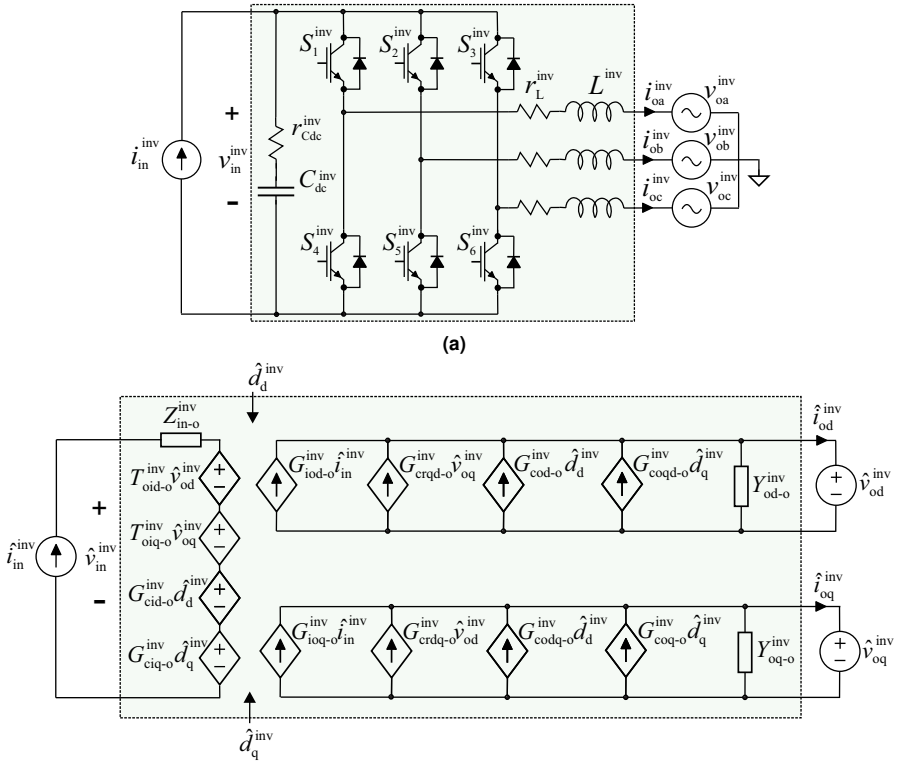

Figure 2.4 A two-level three-phase inverter a) schematic, and b) linear equivalent circuit presented in dq reference frame.

with similar system input and output variables.

A conventional, cascaded control scheme can be implemented on the current-fed inverter. The outer dc-voltage controller provides the reference for the inner d-current controller. Assuming that no reactive power support is desired (unity power factor), the q-current reference is set to zero. Alternatively, the q-current reference can be given by an outer control loop, such as an ac voltage controller. The closed-loop input impedance during cascaded control can be given as

$$Z_{\text{in}}^{\text{inv}} = \frac{1}{1+L_{\text{v}}}\left(-Z_{\text{in-o}}^{\text{inv}} + \frac{G_{\text{PI-cd}}G_{\text{cid-o}}^{\text{inv}}G_{\text{iod-o}}^{\text{inv}}}{1+L_{\text{cd}}}\right), \tag{2.20}$$

where $L_{\text{cd}} = G_{\text{PI-cd}}G_{\text{cid-o}}^{\text{inv}}$ is the control loop gain of the inner d-current controller and $L_{\text{v}} = G_{\text{PI-v}}\dfrac{L_{\text{cd}}}{1+L_{\text{cd}}}\dfrac{G_{\text{cod-o}}^{\text{inv}}}{G_{\text{cid-o}}^{\text{inv}}}$ is the control loop gain of the outer voltage controller.

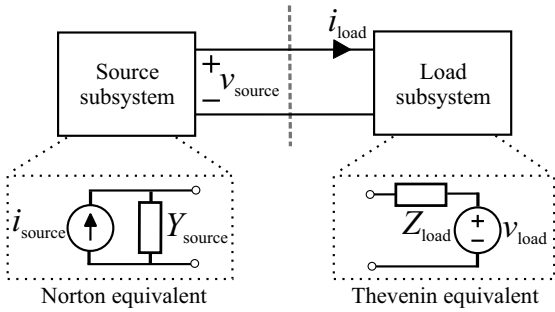

Figure 2.5 Equivalent source-load system based on Norton and Thevenin equivalents.

2.2 Impedance-Based Stability Analysis

Impedance-based stability analysis is a common method for the stability analysis of interconnected power-electronics systems. The method assesses the system stability by examining the ratio of the subsystem's terminal impedances or admittances. Since no other information on the system details is required, the analysis offers a straightforward and general procedure for the stability analysis at the interface between the two systems assuming that the required admittance and impedance terms can be identified.

The source and load subsystems can be represented by small-signal equivalent models using either a Norton or a Thevenin equivalent. Fig. 2.5 shows an example of such a system with current-type source and voltage-type load. Using Kirchhoff's current law, the current flowing to the load can be obtained as

$$i_{\text{load}} = \frac{i_{\text{source}} - Y_{\text{source}} v_{\text{source}}}{1 + Y_{\text{source}} Z_{\text{load}}}, \tag{2.21}$$

where i_{source} is the source current, Y_{source} the source equivalent admittance, v_{source} the output voltage of the source subsystem, and Z_{load} the load equivalent impedance. According to basic control theory, the system is stable if the poles of (2.21) have a negative real part. Hence, the impedance-based stability can be defined through the poles of the term

$$\frac{1}{1 + Y_{\text{source}} Z_{\text{load}}}. \tag{2.22}$$

Assuming the subsystems are stand-alone stable, examining the term in (2.22) is both a necessary and a sufficient condition for the system stability. Note that the term in (2.22) is also analogical to the transfer function of a closed-loop system with a negative-feedback $L = Y_{\text{source}} Z_{\text{load}}$. This term is also known as the minor loop gain. Thus, the system stability can be examined similarly to a conventional feedback system using the Nyquist criterion [127].

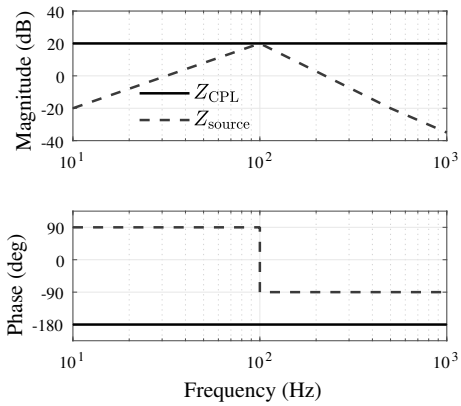

Figure 2.6 Bode diagram of an exemplary source impedance and CPL impedance.

The impedance-based stability analysis is an effective tool for analyzing the effect of a CPL. Such load converters typically have a high control bandwidth that introduces a negative incremental (small-signal) impedance at the converter's source-side bus: the input current increases when the input voltage decreases, and vice versa. Meanwhile, the source converter's impedance has a peak magnitude around the voltage control bandwidth. This magnitude peak is caused by the control dynamics. Within the current control bandwidth, the current control gain is high and the closed loop impedance is similar to the open loop impedance. Yet, within the voltage control bandwidth, the voltage control gain becomes more prominent and lowers the magnitude at frequencies lower than the control bandwidth. If the load and the source impedances are of equal magnitude and opposite phases, the denominator in (2.22) becomes very small and the system exhibits significant resonance. Essentially, the resonance is caused by a resonant pole that occurs close to the voltage control cross-over frequency. Fig. 2.6 shows exemplary source and load impedances that demonstrate the phenomena. In summary, when a CPL is connected in parallel with a source converter, their impedances may cause under-damped or unstable oscillation around the frequency of the voltage control bandwidth.

2.3 Discussion

This chapter has established the theoretical background for the small-signal assessment of various converters and their control loops essential in BESS applications. It has been shown that the converter output impedance plays an important role in the converter control design and in assessing the system stability. A theoretical method for dynamically analyzing the interactions between a source converter and a load converter using their impedances and admittances was presented, and the adverse effect of CPL was demonstrated. The presented

theory lays the basis for the stability analysis, identification, and enhancement methods presented later in this thesis. The next chapter extends the converter models and analysis to multi-converter systems and presents stabilizing control methods suitable for bidirectional converters.

3 METHODS

This chapter presents the methods applied in the thesis. The chapter is divided into four sections. The first section presents the derivation of source-affected dynamic models and studies the effect of a BESS on PV-inverter control dynamics. The second section presents impedance-based stability analysis for multi-converter systems. The third section utilizes broadband methods for impedance identification, and in the fourth section, stabilizing control methods are implemented on bidirectional converters.

3.1 Source Dynamics

Most electric sources and loads, such as a PV source or the electric grid, have non-ideal characteristics compared to a pure voltage or current source, which can affect the converter's internal dynamics [140]. One method for analyzing such systems is to extend the converter models so that the converter transfer functions incorporate the sources (and loads) [P1]. This section presents a general method to include source dynamics into a converter model. Specifically, the method extends the small-signal model of an inverter with the impedances of a PV source and a dc-dc converter. The derived model is used to study the effects of a BESS on the PV-inverter's stability.

Fig. 3.1a shows a grid-connected system consisting of a PV-inverter and a BESS. The linear small-signal model of the three-phase inverter was given in (2.19) at open loop, but lacks the effect of the PV source and the BESS. The dc-dc converter closed-loop dynamics were given in (2.9), and the non-ideal characteristics of the PV source — i.e., the dynamic resistance — can be presented using an admittance term of

$$Y_{\mathrm{o}}^{\mathrm{pv}} = \frac{1}{r_{\mathrm{pv}}} \tag{3.1}$$

in parallel with the current source. Fig. 3.1b presents the corresponding linear equivalent model.

Based on Fig. 3.1a and Kirchhoff's current law, the BESS and PV source dynamics can be included to the inverter dynamics (2.19) by replacing the input current with $i_{\mathrm{in}}^{\mathrm{inv}} = i_{\mathrm{o}}^{\mathrm{pv}} + i_{\mathrm{o}}^{\mathrm{bess}}$.

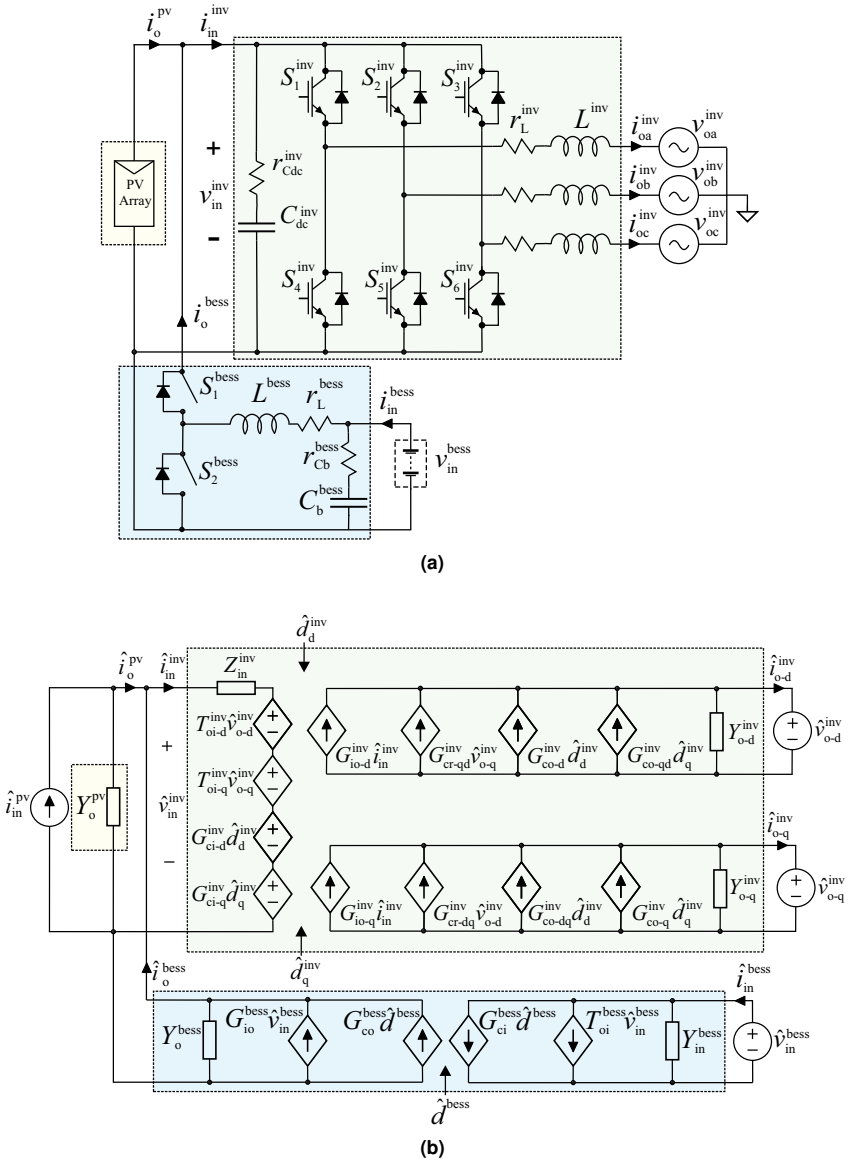

Figure 3.1 A BESS-PV-inverter a) schematic, and b) linear equivalent circuit.

Thus, the d-component of the source-affected control-to-output-current inverter transfer function can be given as [P2]

$$G_{\text{co-d}}^{\text{inv-S}} = G_{\text{co-d}}^{\text{inv}} - \frac{G_{\text{io-d}}^{\text{inv}} G_{\text{ci-d}}^{\text{inv}} Y_{\text{o}}^{\text{S}}}{1 + Z_{\text{in}}^{\text{inv}} Y_{\text{o}}^{\text{S}}}, \tag{3.2}$$

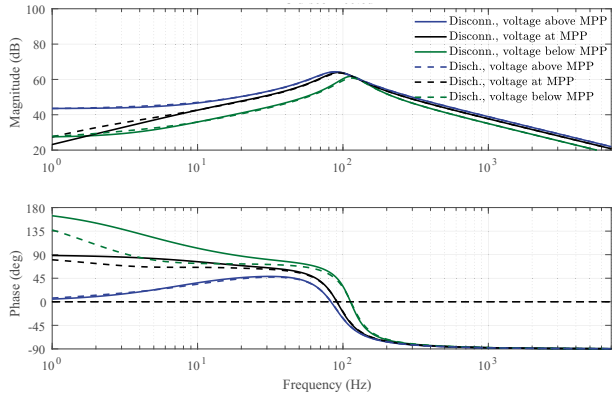

Figure 3.2 Frequency response of $G_{\text{co-d}}^{\text{inv-S}}$ for different PV operating points when BESS is a) disconnected, or b) discharging.

where $Y_{\text{o}}^{\text{S}} = Y_{\text{o}}^{\text{pv}} + Y_{\text{o}}^{\text{bess}}$. The full closed-loop source-affected small-signal model can be found in Appendix A. Note that the poles of the source-affected small-signal model (e.g., (3.2)) correspond to the poles of the system obtained through the impedance-based modeling (2.22).

The effect of a BESS on PV-inverter dynamics can be analyzed with the derived source-affected transfer functions [P2]. Fig. 3.2 compares the source-affected control-to-output-current frequency responses (3.2) in different scenarios: the BESS is either disconnected or discharging, and the voltage over the PV ($v_{\text{in}}^{\text{inv}}$ in Fig. 3.1) is

i) Above the maximum power point (MPP) voltage (PV operates in the constant voltage region),

ii) Equal to the PV source's MPP voltage, or

iii) Below the MPP voltage (PV operates in the constant current region).

The operating point of the PV source clearly has a strong effect on the dynamics at low frequencies. Particularly, when the PV source is operated below the MPP voltage, the transfer function includes a low-frequency RHP zero that increases the phase at low frequencies to 180° instead of 0°. However, when the BESS is connected and discharging, both the PV and the BESS have an effect on the frequency response. The BESS shifts the RHP zero to a lower frequency compared to a situation without the BESS. Fig. 3.3 compares the root-loci plots of the zero with and without BESS at several PV voltages in a range of voltages around the MPP voltage (at MPP the zero is at 0 rad/s). Note that a similar result applies when charging the BESS [P2].

The location of the low-frequency RHP zero in the source-affected control-to-output-current frequency responses (3.2) can limit the control design. Since the inverter is operated using a feedback-based cascaded control scheme in which the outer loop controls the dc-bus voltage and the inner loop the inverter current, the RHP zero of the inner control loop becomes an RHP pole in the outer control loop. As discussed in Section 2.1.1, the location

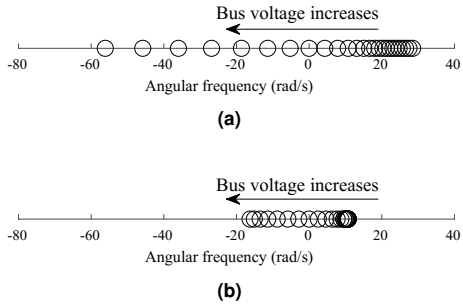

Figure 3.3 The low-frequency zero of the PV- and BESS-affected $G_{\text{co-d}}^{\text{inv-S}}$ for varying dc bus voltages when the BESS is a) disconnected, or b) discharging.

of an RHP pole can be a critical factor for reliable control design, and the crossover frequency should be at least twice as high as the RHP pole frequency. However, the dc-voltage control should be tuned for a low crossover frequency due to the limitations set by the cascaded control scheme and to mitigate second harmonic ripple caused by unbalanced grid voltages. Since the BESS lowers the RHP zero (and pole) frequency, the inverter dc-voltage control is less likely to become unstable than when it is disconnected. Therefore, the BESS has a stabilizing effect on the PV-inverter.

The source-affected models allow the detailed analysis of the converter transfer functions and can be useful for control design and stability analysis. The source can be considered as an input filter, dc-dc converter, long dc cabling, a PV generator, and so on. However, such methods might not be suitable for all situations. The derivation of source-affected models becomes challenging as the system complexity increases. For example, the control structures can be complex and can vary depending on the control mode. Additionally, detailed information on the system might not be available to form the models. Rather, adaptive and nonparametric stability assessment methods that do not require detailed information about the system variables can be beneficial.

3.2 Stability Analysis of Multi-Converter Systems

A bidirectional converter can often be considered as part of a more complicated multi-converter system in which several converters are connected to a common dc bus. Fig. 3.4 demonstrates such a system of m bus-connected converters. Such a system, consisting of many converters and various sources and loads, can exhibit degraded stability due to interactions between the interconnected devices even though each converter in the system is standalone stable.

Several stability assessment methods have been proposed in the literature to consider the stability of such multi-converter systems. For systems that adopt adaptive controllers,

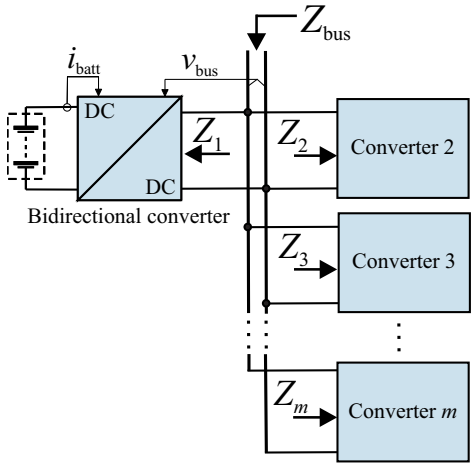

Figure 3.4 Multi-converter system with a bidirectional converter. [P6]

the impedance-based approaches are especially suitable as they can benefit from online frequency response identification. The stability of multi-converter systems can be assessed by considering the multi-converter system as a single-port impedance, bus impedance. For a multi-converter system of m bus-connected converters, the system's bus impedance Z_{bus} can be given as a parallel connection of the bus-connected impedance, i.e., [98]

$$Z_{\text{bus}}(s) = \frac{1}{Z_1^{-1} + Z_2^{-1} + \ldots + Z_m^{-1}}, \tag{3.3}$$

where m impedances are identified at the bus-side of the corresponding subsystem (as shown in Fig. 3.4). The positive current directions are defined as from the common dc bus into the converters. The interconnected multi-converter system can be shown to be passive, and thus also stable, if the following requirements are met [98].

1. $Z_{\text{bus}}(s)$ does not have RHP poles
2. $\text{Re}\{Z_{\text{bus}}(j\omega)\} \geq 0, \forall \omega > 0$

Passivity is a sufficient but not a necessary condition for stability. Additional concepts are required to assess other performance metrics of the multi-converter system (e.g., the level of damping), such as the allowable impedance region (AIR) introduced in [99]. Whereas passivity limits the bus impedance to the RHP, the AIR is defined within the RHP as a semicircle with a radius that limits the maximum damping to a desired value, $Q_{\max}$.

Similar to adverse impedance-based interactions within a source-load system, degrading interactions within a multi-converter system can occur between CPLs and voltage controlling converters: The resonance peak in the voltage-controlling converter's impedance can cause the denominator in (3.3) to become very small if the converter impedances have equal

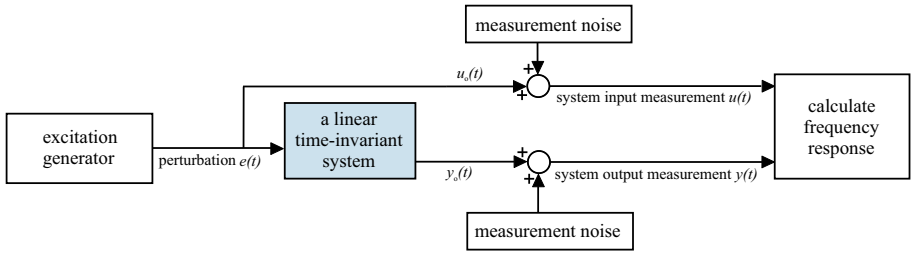

Figure 3.5 Typical setup for frequency response measurement.

magnitudes with opposite phase, leading to a resonance. In such a case, the bus impedance is typically characterized by a single prominent resonance peak that can be expressed as a second-order system as [99]

$$Z_{\text{bus}}(j\omega) = Z_{\text{o-bus}} \frac{s\omega_{\text{o}}}{s^2 + s\omega_{\text{o}}/Q_{\text{bus}} + \omega_{\text{o}}^2}, \tag{3.4}$$

where $Z_{\text{o-bus}}$ is the characteristic impedance, ω_{o} is the resonance frequency, and the quality factor Q_{bus} specifies the level of damping. The bus impedance magnitude peaks at the resonance frequency to a real value, $Z_{\text{bus}}(j\omega_{\text{o}}) = Z_{\text{o-bus}}Q_{\text{bus}}$. Now, the AIR can be defined in the complex plane as a semicircle with a radius of $Z_{\text{o-bus}}Q_{\max}$. This condition can be normalized by dividing the bus impedance and the AIR radius by $Z_{\text{o-bus}}$. Thus, the normalized AIR radius equals to the desired quality factor $Q_{\max}$. Accordingly, the chosen bus impedance attenuation is achieved if the normalized bus impedance $Z_{\text{bus-N}}(j\omega)$ remains within the corresponding AIR.

3.3 Broadband Methods in Bus-Impedance Identification

Power-electronic converters can be regarded as linear, time-invariant systems up to half their switching frequency. The converter dynamics can be studied nonparametrically in the time domain using impulse response functions and in the frequency domain through Fourier transformation; i.e., using frequency response functions [141]. In fact, frequency response functions are a valuable tool for examining the dynamics of switched-mode converters, such as their output impedance or control-related transfer functions, and impedance identification through measurement-based techniques can benefit the control and design of power converter systems.

Fig. 3.5 shows a generic measurement setup for obtaining the system frequency response. In the setup, a perturbation $e(t)$ is introduced to the system. For example, in power-electronic converters, the excitation signal is typically added to the converter controller's reference value, duty cycle, or other variables. Then the input and output signals are measured and

the frequency-response function is computed as

$$G(j\omega) = \frac{Y(\mathrm{j}\omega)}{U(\mathrm{j}\omega)}, \tag{3.5}$$

where $U(\mathrm{j}\omega)$ and $Y(\mathrm{j}\omega)$ are the Fourier-transformed measured input and output signals, respectively.

The selection of an appropriate excitation signal is critical for identifying the system frequency response. The excitation should result in the desired frequency content in the input and output signals while causing minimal degradations in the system's regular operation and avoiding any significant corruptive distortions caused by the noise and the plant itself. A single-tone sine wave is a trivial excitation signal, where all the excitation energy occurs at a single frequency, resulting in a maximal signal-to-noise (SNR) ratio [142]. However, when using the single-tone sine, multiple sequential measurements are required to obtain the frequency response in a wide band, thus increasing the measurement time unsuitable for applications requiring more rapid identification. Instead, broadband methods are desired where multiple frequency points are excited simultaneously.

3.3.1 Broadband Identification with Pseudo-Random Binary Sequences

Pseudo-random sequences (PRS) are a class of deterministic and periodic broadband signals. PRS signals have a largely controllable bandwidth and frequency resolution and a small number of signal levels, making them easy to implement on a digital controller [142]. Consequently, these sequences have been used as excitation signals to identify various power-electronic systems and their frequency responses [118], [143], [144].

One of the most popular PRS is the maximum-length binary sequence (MLBS). The MLBS signal has a low peak factor [54], which means that the signal has a very high total energy in relation to its time-domain amplitude. Owing to this characteristic, the MLBS is suitable for exciting sensitive systems requiring minimized perturbation on their regular operation during the identification process. The MLBS signal has only two signal levels, and it can be generated with shift registers that consist of bits 0 and 1 and an exclusive-or (XOR) operation [145]. The resulting binary signal can then be mapped to $-A$ and A, creating a symmetric excitation signal with an amplitude of A and an average value close to zero.

In the design procedure of an MLBS signal, the following application-dependent specification variables are established first: [54]

- Desired frequency resolution
- Required measurement time
- Measurable bandwidth in the frequency domain
- Desired SNR in the time domain

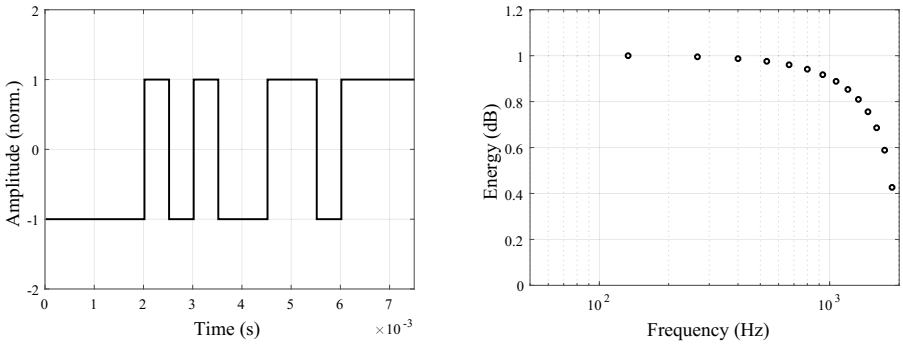

Figure 3.6 An MLBS signal a) in time-domain and b) its energy spectrum.

Then, the design variables can be adjusted to meet and optimize these criteria:

- Sequence length
- Generation frequency
- Amplitude
- Number of periods for averaging

The MLBS power spectrum is evenly spaced with a constant frequency resolution of $f_{\text{res}} = f_{\text{gen}}/N$, where N is the sequence length and f_{gen} is the sequence generation frequency and the frequency at which the signal energy decreases to zero. The MLBS sequence length is always $N = 2^n - 1$, where n is a positive integer. Hence, the available sequence lengths are limited and each available sequence is approximately twice as long as the previous one. The sequence time is always inherently inversely linked with the frequency resolution and can be given as $t_{\text{mlbs}} = 1/f_{\text{res}} = N/f_{\text{gen}}$. Since the sequence exists only in specific, doubly increasing lengths, unnecessarily long sequences should be avoided as it considerably increases the measurement time. Fig. 3.6 presents an exemplary MLBS signal in the time and frequency domain ($N = 15$ and $f_{\text{gen}} = 2$ kHz). The energy spectrum is constant at low frequencies, but decreases to zero at the generation frequency due to the discrete, zero-order-hold dynamic behavior of the sequence. The measurable bandwidth is typically considered to be the frequency at which the spectral energy has dropped to half of its maximum power; approximately, $f_{\text{bw}} \approx 0.44 f_{\text{gen}}$. Thus, the generation frequency should be designed to be high enough to obtain accurate identification results for the desired frequency range.

In the frequency-response measurement, the excitation amplitude A should be high enough to reach the desired SNR level, but low enough not to disturb the system's normal operation more than necessary. For example, in power-electronic systems, the excitation signal amplitude should be high enough to increase SNR and the identification accuracy, but low enough to guarantee that the system variables, such as currents and voltages, remain within

the allowable limits and that the perturbations do not excessively degrade the power quality [56]. When implementing the broadband identifications on power-electronic converters, the excitation signal is typically added to the converter controller's reference value, duty cycle, or other variables. In case the excitation signal is added to the controller references, the controller takes care of the accurate perturbation within the control bandwidth. If the perturbation is added to another variable, such as the duty ratio, the amplitude requires more careful design to ensure that the perturbation produces high enough spectral energy to the whole frequency band of interest. Depending on the effects of noise and other distortions, the amplitude is typically chosen so that the excited variables deviate no more than 5 percent from their nominal values.

The desired SNR may be difficult to achieve if the system has high levels of noise and disturbances, and several methods can be used to increase the measurement accuracy. For example, the excitation sequence can be repeated and the measurements averaged over these periods. Averaging the measurements mitigates the effect of nonsystematic noise, such as white noise and other random errors, which are typical in power-electronic systems. However, this averaging process leads to an increased measurement time $t_{\mathrm{meas}} = N_{\mathrm{P}} t_{\mathrm{mlbs}}$, where N_{P} is the number of periods. Moreover, systematic noise cannot be mitigated using averaging, and other methods may be required.

In addition to averaging, the SNR can be increased with methods that mitigate the effects of system distortions. For example, the system distortions can cause steady-state variation in the input and output signals, degrading the identification accuracy. Depending on the noise type, the mitigation methods can include careful selection of the excitation signal parameters (such as the measurement time or the excited frequencies), or the source of the corruptive noise can be mitigated, avoided, or eliminated through filtering, control design, etc. For example, converter systems typically include harmonics that disturb the system identification, and the impact of such periodic oscillations on the identification accuracy can be mitigated with an appropriate excitation signal that has a measurement time equal to a multiple of the harmonic signal's period length [146]. Thus, the spectral leakage of the harmonic is mitigated, and the measurement is less corrupted by the critical harmonic(s).

Another issue for the identification accuracy is nonlinear system behavior. In fact, in the presence of nonlinear behavior or when operating close to system limits, increasing the amplitude may not improve the accuracy, but may yield unreliable results [P5]. Typical sources of nonlinear behavior in converter systems include switching dynamics, nonlinear parameters (for example, nonlinear inductances, capacitances, and couplings between components), and nonlinear dynamics, such as saturation and deadtime. If the relationship between the excitation signal and the perturbed variable(s) is nonlinear, the excitation energy at a specific frequency may not translate to the same frequency in the perturbed variable(s), degrading the measurement accuracy. Thus, nonlinear operating points should be identified to avoid or mitigate their effects. For example, identifying the output impedance of a DAB converter

using the duty ratio as the excitation variable may be unfeasible at some set points due to a strong nonlinear relationship between the duty ratio and the output power [P5]. On the other hand, the same identification can yield a much more accurate result using the phase shift as the excitation variable since the nonlinear effects are then avoided [P5]. Therefore, it is vital to consider the effect of nonlinear system dynamics at the selected set point such that any necessary mitigation actions can be taken.

3.3.2 Multivariable Identification with Orthogonal Sequences

Identifying the relevant dynamics of complex MIMO systems may require the identification of several transfer functions. For example, based on the bus-impedance definition (3.3), the bus-impedance-based stability assessment of multi-converter systems requires the identification of several impedances, as shown in Fig. 3.4. The dynamical behavior of MIMO systems can be generally characterized by a n_u x n_y matrix of transfer functions, where n_u is the number of system inputs and n_y is the number of system outputs. For example, for a system of two interacting single-input and single-output (SISO) subsystems where the two outputs are dependent on the inputs of both subsystems, a transfer function matrix $\mathbf{G}_\mathrm{tf}$ can be given as

$$\begin{bmatrix} y_1 \\ y_2 \end{bmatrix} = \overbrace{\begin{bmatrix} G_{11} & G_{12} \\ G_{21} & G_{22} \end{bmatrix}}^{\mathbf{G}_\mathrm{tf}} \begin{bmatrix} u_1 \\ u_2 \end{bmatrix}. \tag{3.6}$$

The transfer functions G_{11} and G_{22} represent the direct relationships between the input and output variables of the same subsystem, and the transfer functions G_{12} and G_{21} represent the cross-couplings between the two different subsystems. The MLBS signals can be used to identify the transfer function matrix of a MIMO system by using a sequential identification approach: each subsystem is excited sequentially, and the output responses are measured separately for each input. However, such an approach multiplies the required measurement time, and variations in the operating conditions between the separate identification cycles can corrupt the results.

Orthogonal sequences offer an approach for identifying multiple transfer functions simultaneously. In this method, a set of excitation sequences are used that are orthogonal with each other and therefore do not excite the same frequencies [54]. The first sequence can be chosen as any MLBS, and the orthogonal sequences are generated in a recursive manner based on the values of the previous one. Since the sequences do not share energy on the same frequencies, multiple orthogonal sequences can be employed simultaneously to identify multiple different transfer functions without the risk of them interfering with each other. As a result, the overall measurement time becomes much shorter than when using

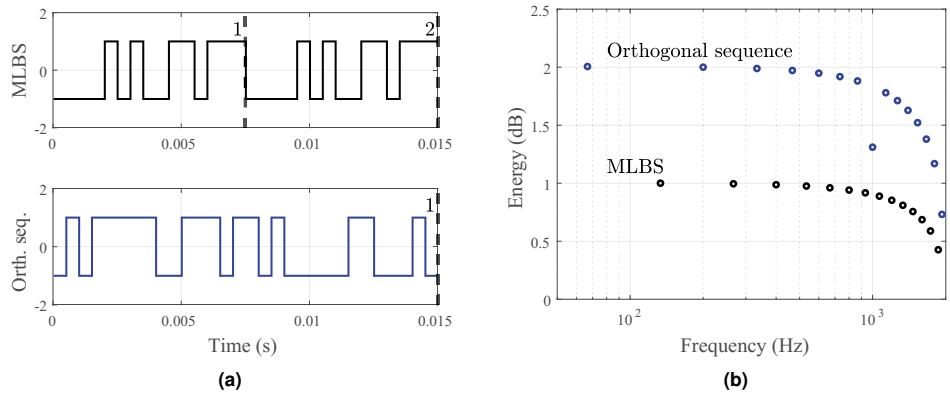

Figure 3.7 An MLBS and its orthogonal sequence a) in time-domain, and b) the energy spectrum. The vertical dashed lines in the time-domain figure mark the repeating sequences (periods).

the sequential approach for the identification of multiple transfer functions. Additionally, applying orthogonal sequences ensures that each response is identified under the same system operating conditions, which may not be the case if sequential perturbations are applied. Therefore, orthogonal excitation signals are particularly advantageous for bus impedance identification of multi-converter systems: all the interconnected terminal impedances can be identified simultaneously by adding each orthogonal sequence to the corresponding converter and performing Fourier techniques on the resulting currents and bus voltage [98].

One method for generating orthogonal sequences utilizes a Sylvester construction in which different Hadamard matrices are constructed recursively [147]. The Hadamard matrix is a 2^k x 2^k matrix, where k is a non-negative integer, and it consists of values +1 and -1 such that the matrix rows are mutually orthogonal (i.e., each row represents a perpendicular vector). The Hadamard matrix with $k = 0$ is defined as $\mathbf{H}_1 = [1]$, from which each consequent Hadamard matrix can be constructed recursively following a sequence of

$$\mathbf{H}_{2^k} = \begin{bmatrix} \mathbf{H}_{2^{k-1}} & \mathbf{H}_{2^{k-1}} \\ \mathbf{H}_{2^{k-1}} & -\mathbf{H}_{2^{k-1}} \end{bmatrix}. \tag{3.7}$$

Then, the orthogonal sequence $(k + 1)$ can be generated by concatenating the previous orthogonal sequence (k) with itself, transforming this sequence into a vector form, and multiplying this vector with another vector that contains the repeated k^{th} row of the Hadamard matrix $\mathbf{H}_k$ using element-wise multiplication [54]. Thus, the second orthogonal sequence is equivalent to repeating the previous sequence twice and inverting every second bit.

Fig. 3.7 demonstrates the time-domain signals and frequency spectra of a 15-bit-long MLBS and its 30-bit-long orthogonal sequence (f_{gen} = 2 kHz). The energy values are scaled

to clarify the illustration. The energies of both sequences drop to zero at the generation frequency. The signals are orthogonal as they do not have energy at the same frequencies. Therefore, assuming the system is linear, transfer functions with different inputs can be identified simultaneously without interference between the individual identifications.

The length of each orthogonal sequence is always doubled compared to the previous sequence. In fact, the desired identification time typically sets limitations on how many orthogonal sequences can be employed. However, in a case where averaging is desired to improve the measurement SNR, the total identification time may be less affected by carefully allotting which sequence is used with which identification: the shortest sequence (i.e., the first sequence) should be employed for the measurement with the highest noise because the shortest sequence is repeated, and thus averaged, more than the longer sequences. Similarly, the longest sequence should be employed for the measurement with the lowest noise level. This way, fewer additional periods are required for accurate results compared to allotting the sequences differently. Moreover, the second sequence can be assigned for the most sensitive identification as it cancels out the effect of even-order nonlinearities due to its inverse-repeat binary sequence characteristics [148]. In fact, nonlinear system dynamics may cause the orthogonal excitation signals to correlate with each other, corrupting the identification results. Thus, the application-dependent nonlinear operating points should be identified and their effects mitigated or avoided appropriately.

Since the converters might employ different switching frequencies, the available sequence generation frequencies may be limited as each of the converter switching frequencies has to be a multiple of the chosen generation frequency; i.e., $f_{\text{gen}} = n f_{\text{sw-}m}$, where n is a positive integer. This requirement can limit the available resolution and measurement time, and a balance should be found for the most suitable identification design. Additionally, to decrease the identification time, it is essential to carefully choose the desired frequency range and consider whether unnecessarily low frequencies could be excluded. For example, in the case of bus impedance identification, the frequencies that are much lower than the voltage control crossover frequency are not critical for the analysis and can be excluded from the desired frequency range [P6].

3.4 Stabilizing Control with Bidirectional Converters

The stability of multi-converter systems can be enhanced through stabilizing control schemes that utilize the concept of virtual impedance. These control schemes reshape the impedance of one of the converters, thus achieving the desired attenuation level. Such stabilizing control methods offer a straightforward way of increasing system damping and mitigating resonances caused by, for example, adverse impedance-based interactions. If the virtual-impedance-based methods are adaptive and continuous, the impedance reshaping can prevent

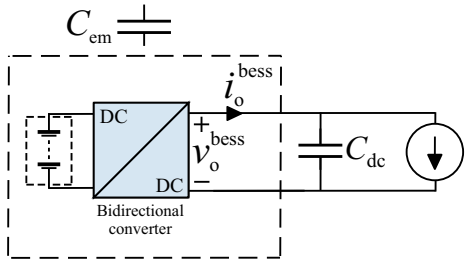

Figure 3.8 Illustration of the capacitance emulation within the current control bandwidth.

impedance-based interactions from degrading the multi-converter system's performance.

With a BESS, impedance reshaping can be achieved by modifying the converter control to offer additional damping to the converter's closed-loop impedance at the desired frequency range. Based on the bus impedance characteristics presented in Section 3.2, resonances caused by impedance-based interactions typically occur close to the voltage control cross-over frequency. Thus, the BESS converter voltage/current controllers typically offer high enough bandwidth to introduce an appropriate virtual impedance. In this section, two different stabilizing control methods are considered: capacitance emulation and resonance-damping gain.

3.4.1 Capacitance Emulation

Capacitors are vital parts of electric systems because they limit changes in their voltage by storing and releasing energy in their magnetic fields. One method of introducing a stabilizing effect with a BESS is to assign it to emulate a capacitance. This method increases damping within the whole control bandwidth, which mitigates voltage fluctuations and enhances stability.

The idea of capacitance emulation utilizing a BESS is illustrated in Fig. 3.8. To emulate the capacitance within the current control bandwidth, the BESS output current i_o^{bess} is controlled according to

$$i_{o\text{-ref}}^{bess} = -C_{em}\frac{dv_o^{bess}}{dt} = -C_{em}sv_o^{bess}, \tag{3.8}$$

where C_{em} represents the emulated capacitance and v_o^{bess} the BESS output voltage **article3**, [149]. Accordingly, within the control loop, the resulting closed-loop output impedance of the BESS becomes

$$Z_{o\text{-Cem}}^{bess} = \frac{1}{C_{em}s}. \tag{3.9}$$

The control algorithm (3.8) can be presented in discrete-time using the Euler discretization

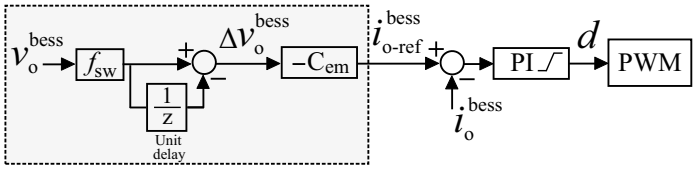

Figure 3.9 Control block diagram of a BESS with the capacitance emulation algorithm.

method as

$$\begin{aligned} i_{\text{o-ref}}^{\text{bess}}(z) &= -C_{\text{em}} \frac{z-1}{T_{\text{s}}} v_{\text{o}}^{\text{bess}} \\ &= -C_{\text{em}} (z-1) f_{\text{sw}} v_{\text{o}}^{\text{bess}}, \end{aligned} \tag{3.10}$$

where T_{s} is the switching/sampling interval and f_{sw} switching frequency. Fig. 3.9 illustrates the discretized control structure, where a regular PI controller regulates the current. The control algorithm was validated in [P3].

The closed-loop output impedance of the capacitance-emulating converter can be given as in (2.17) by replacing the voltage control gain $G_{\text{PI-v}}$ with $G_{\text{Cem-v}} = -C_{\text{em}}s$. Within the control bandwidth, the voltage and current loop gains are high ($L_{\text{Cem-v}} \gg 1$ and $L_{\text{co}} \gg 1$), so the closed loop output impedance becomes equal to $1/(C_{\text{em}}s)$, as desired. The closed-loop output impedance can be used to evaluate the effect of the capacitance-emulating BESS on other parts of the converter system and to initiate impedance-based stability analysis.

3.4.2 Resonance-Damping Gain

A stabilizing control method that increases damping at a specific (resonance) frequency rather than within the whole control bandwidth can be advantageous in multi-converter systems with CPLs. An adaptive, resonance-damping gain can be used to do this. Such a method offers an efficient, direct, and targeted approach for the resonance mitigation as the achieved damping enhancement is focused on the identified resonance frequency rather than within the whole control bandwidth. This adaptive stabilizing control method is facilitated by the bus-impedance-based stability assessment presented in Section 3.2 and the online identification methods presented in Section 3.3.

In this control strategy, the controller has an adaptive resonance-damping gain, R-gain, in parallel with the regular voltage controller. This R-gain is tuned adaptively based on an online bus impedance identification to optimize the bus impedance damping around the identified resonance frequency. The R-gain is chosen as [150]

$$G_{\text{R}}(s) = \frac{2K_{\text{r}}\omega_{\text{r}}s}{s^2 + 2\omega_{\text{r}}s + \omega_{\text{o}}^2}, \tag{3.11}$$

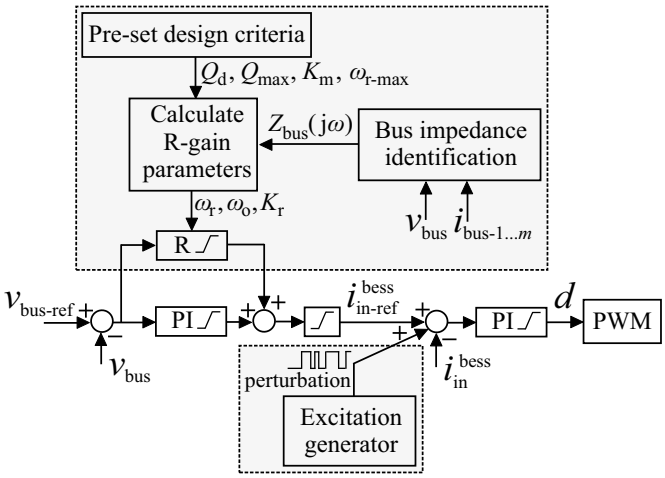

Figure 3.10 Block diagram of the converter controller with a resonance gain.

where K_r determines the damping at the resonance frequency ω_o, and ω_r is the resonance bandwidth. The following design criteria are used:

- The resonance bandwidth ω_r is limited below a chosen frequency $\omega_{r\text{-}max}$
- The added virtual impedance has a damping level of a chosen quality factor Q_d
- The resulting normalized bus impedance $Z_{bus\text{-}N}(j\omega)$ remains within an AIR specified by a chosen quality factor Q_{max}, and, at the resonance frequency ($Z_{bus\text{-}N}(j\omega_o)$), is separated from the quality factor by a chosen separation margin K_m

Typical ranges for these parameters are $Q_{max} = 0.7...1$, $K_m = 0...1$, and $Q_d = 0.7...1$. Fig. 3.10 presents a control block diagram, in which the converter employs the R-gain with a cascaded control scheme. With the R-gain, the voltage control gain is $G_{PIR\text{-}v}(s) = G_{PI\text{-}v}(s) + G_R(s)$.

The R-gain parameters can be determined in an adaptive manner using online bus impedance identification. In this way, the resonance frequency ω_o, the characteristic impedance $Z_{o\text{-}bus}$, and the bus impedance quality factor Q_{bus} are determined from the identified bus impedance according to (3.4). Then, K_r and ω_r are selected based on the chosen design criteria as [108]

$$K_r = \frac{Q_d}{Z_{o\text{-}damp}}; \quad \omega_r = \frac{\omega_o}{2Q_d}, \tag{3.12}$$

where

$$Z_{o\text{-}damp} = Z_{o\text{-}bus}\frac{Q_d Q_{bus}\left(Q_{max} - K_m\right)}{Q_{bus} - \left(Q_{max} - K_m\right)}. \tag{3.13}$$

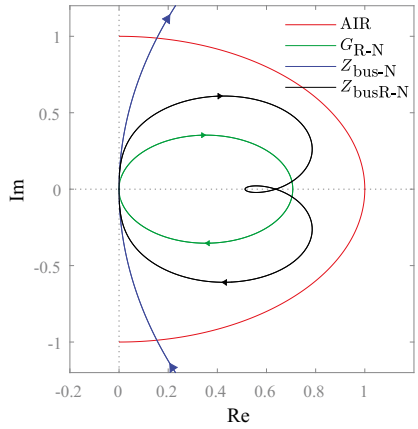

Figure 3.11 The normalized R-gain (green line), and the normalized bus impedance without (blue line) and with (black line) the R-gain.

The resonance bandwidth is limited with [P6]

$$\omega_{\text{r-max}} < \frac{2\pi f_{\text{c-inner loop-min}}}{10} < \frac{2\pi f_{\text{sw}}}{10}; \quad \omega_{\text{r-max}} < \frac{2\pi f_{\text{rhp-zero}}}{2}, \tag{3.14}$$

where f_{sw} is the converter switching frequency, $f_{\text{c-inner loop}}$ is the inner (current) control loop cross-over frequency, and $f_{\text{rhp-zero}}$ is the frequency of a possible right-half-plane zero in the control-to-output voltage transfer function. This limitation verifies that the R-gain does not increase the voltage control crossover frequency beyond the limits of stable operation, which is restricted by the inner control loop (as the control loops should be decoupled in a cascaded control scheme) and possible zeros and poles in the converter dynamics [P6]. Fig. 3.11 demonstrates the effect of an R-gain (with $Q_{\text{d}} = 0.7$, $Q_{\text{max}} = 1$, and $K_{\text{m}} = 0.5$) on the normalized bus impedance when the bus impedance is as given in (3.4) with $Z_{\text{o-bus}} = 9$, $\omega_{\text{o}} = 477$ rad/s, and $Q_{\text{bus}} = 6.5$. The R-gain decreases the normalized bus impedance quality factor from the maximum of 6 (out of scale) to values within the AIR, and to $Q_{\text{max}} - K_{\text{m}}$ at the resonance frequency. The virtual impedance (R-gain) has a damping that corresponds to the chosen quality factor Q_{d}.

3.4.3 Discussion

Stabilizing control methods can enhance system stability and mitigate resonances using BESS applications. Since the energy required for the mitigation is typically oscillatory in nature, the state of charge of the BESS is not affected by such control features. The presented sta-

bilizing control methods are particularly suitable for BESS applications as they are independent of the power-flow directions, the converter operation modes, and the system grouping. Moreover, the methods are well-suited for multi-converter systems. Even though adverse resonances could also be smoothed with hardware changes, an adaptive and control-oriented solution can offer a more optimized solution.

The capacitance-emulating stabilizing control method can optimize the system dynamics within the control bandwidth by introducing a virtual capacitance. This method is straightforward to implement as it does not necessarily require additional measurements or communication channels between the converters. However, the algorithm utilizes a numerical derivative sensitive to noise, and thus an appropriate low-pass filter should be used. Moreover, this control scheme can slow down the voltage response during transients, leading to sluggish behavior if the control feature is not tuned properly.

The resonance-damping-gain-based stabilizing control method that increases damping at a specific (resonance) frequency rather than within the whole control bandwidth can be particularly advantageous in multi-converter systems with CPLs. This method requires more current measurements than the capacitance emulation, but the effect on the impedance stability is more targeted and only affects a limited part of the voltage response during transients. While the capacitance emulation modifies the impedance within the control bandwidth, the resonance-damping gain affects only a short frequency range around the identified resonance frequency.

The presented stabilizing control features can benefit significantly from broadband identification methods, as the system dynamics are identified quickly to provide input to the controller, which allows the controller to adapt to changes. The identification time is particularly critical in multi-converter systems where the system conditions may be challenging to predict, and the operating conditions might change frequently. Orthogonal sequences are advantageous perturbation signals in such multi-converter systems since they allow the simultaneous identification of several separate transfer functions without interference between the measurements, which shortens the identification time.

4 EXPERIMENTAL RESULTS

This chapter presents the experimental verifications of the proposed methods. The methods are verified through experimental tests and simulations. This chapter is divided into three sections. The first section introduces the experimental setups; the second section presents the experimental results related to broadband impedance identifications on a bidirectional converter and broadband stability assessments on multi-converter systems; and the third section presents results related to two stabilizing control algorithms employed on a bidirectional converter and validates the effectiveness of the applied algorithms and their design. The experiments can be summarized as follows.

Experiment Set 1: Design of Broadband Identification for Impedance and Stability Analysis [P5–P6]

The first set of experiments focuses on the characteristics, performance, and challenges of broadband frequency-response measurements performed on a bidirectional DAB converter and on a multi-converter system. The experiments present validation for the design methods introduced in Section 3.3. Additionally, the experiments validate the bus-impedance-based multi-converter system stability identification method. This set of experiments include the following:

Experiment a): Design of Impedance Identification on DAB Converters

This experiment compares different broadband impedance identification implementations on a bidirectional DAB converter. The results are verified with a comparison to a theoretical result. Issues related to nonlinear operating points are identified. Design guidelines are suggested for selecting the most suitable implementation method. The performance of the methods is compared and verified by several experimental impedance identifications at different operating points. [P5]

Experiment b): Design of Online Bus-Impedance-based Stability Analysis

This experiment verifies the design and implementation of a bus-impedance-based multi-converter system stability assessment employing online broadband identification. [P6]

Experiment Set 2: Stabilizing Control Schemes [P3, P5–P6]

The second set of experiments validates the performance of the proposed stabilizing control methods. This set of experiments include the following:

Experiment i): Design of Virtual Capacitance Stabilizing Control

This experiment employs the capacitance-emulating stabilizing controller on a bidirectional dc-dc converter and validates its effectiveness through simulations. [P3]

Experiment ii): Design of Resonance Damping Virtual Impedance Stabilizing Control

This experiment implements the resonance-damping-gain-based stabilizing controller on a DAB converter based on the online bus-impedance assessment. [P6]

4.1 Experimental Setups

The experiments in this thesis were conducted with two different experimental setups, as described below. Additionally, one simulation model was implemented using MATLAB software.

Experimental Setup 1 is a custom-built bidirectional DAB converter with a resistive load. The converter is supplied by a battery emulator. This setup is used to study the implementation of broadband frequency response identification on the DAB converter.

Experimental Setup 2 is a multi-converter system that consists of a battery-emulator-supplied DAB converter and two three-phase inverters. The inverters are connected to a grid-emulator or a three-phase resistive load. All three of these converters share the same dc bus. This setup is used to study the online stability analysis of multi-converter systems and the implementation of a resonance damping virtual-impedance-based stabilizing controller on a bidirectional converter.

Simulation Model is a MATLAB Simulink model of a grid-connected BESS-PV-inverter system. The BESS consists of a bidirectional dc-dc converter and a constant voltage source and the inverter is a three-phase two-level PV-inverter with L-type filters. This simulation model is used to validate the capacitance-emulating stabilizing control algorithm during a grid imbalance.

The experimental setups utilize grid- and battery-emulators to enable the system study at varying operating points. Further details on the experimental setups and the simulation model such as schematics and parameter values are given in the following subsections.

4.1.1 Experimental Setup 1

The first experimental setup facilitates several broadband identification methods on a bidirectional DAB converter to identify the terminal impedance of a resistive load. A power-converter system depicted in Fig. 4.1 was constructed in the laboratory. The system consisted of a custom-built bidirectional DAB converter, a battery emulator, and a resistive load. The battery emulator operated as a constant voltage source. The DAB converter consisted of four Imperix PEB 8024 half-bridge SiC power modules and the passive components. The DAB converter topology was equivalent to the one presented in Fig. 2.3. The detailed system parameters are given in Table 4.1.

The DAB converter controller and the phase-shifted PWM were implemented on a rapid prototyping controller by Imperix, which provided the switching commands. In the exper-

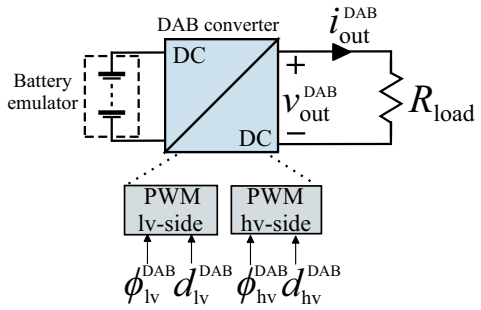

Figure 4.1 Simplified schematic of Experimental Setup 1.

Table 4.1 Parameters used in Experimental Setup 1.

Parameter	Value	Description
V_{lv}	100 V	dc voltage on low-voltage (battery) side
R_{load}	150 Ω	resistive load
$C_{\text{lv}}^{\text{DAB}}$, $C_{\text{hv}}^{\text{DAB}}$	520 μF	capacitance on low- and high-voltage side
$L_{\text{tot}}^{\text{DAB}}$	300 μH	equivalent inductance on high-voltage side
n_{tf}	2.6	transformer turns ratio ($n_{\text{hv}}/n_{\text{lv}}$)
$f_{\text{sw}}^{\text{DAB}}$, $t_{\text{d}}^{\text{DAB}}$	50 kHz, 2 μs	switching frequency and deadtime
$d_{\text{lv}}^{\text{DAB}}$	0.5	duty ratio for low-voltage-side bridge
$d_{\text{hv}}^{\text{DAB}}$	0.5 (range 0.3–0.9)	duty ratio for high-voltage-side bridge
$\phi_{\text{lv}}^{\text{DAB}}$	0 deg	phase shift for low-voltage-side bridge
$\phi_{\text{hv}}^{\text{DAB}}$	60 deg (range 30–90 deg)	phase shift for high-voltage-side bridge

iment, the converter was operated at open-loop to bypass the effect of the controller and the high-voltage-side duty ratio and high-voltage-side phase-shift were varied. The low-voltage-side phase shift was set to 0 deg and the low-voltage-side duty ratio was kept at constant 0.5. The deadtime was selected as 2 μs. The measured signals were recorded directly on PC connected to the controller platform.

4.1.2 Experimental Setup 2

The second experimental setup facilitates experiments on a multi-converter system. A power -converter system depicted in Fig. 4.2 was constructed in the laboratory. The system consisted of three custom-built power converters that together form a dc multi-converter system. A DAB converter was connected to two inverters through a common dc bus. The DAB converter was the same one as used in Experimental Setup 1 (and its topology was as in Fig. 2.3). Inverter #1 was built with insulated-gate bipolar-transistor switches (Myway Plus MWINV-9R144) and Inverter #2 consisted of three Imperix PEB 8024 half-bridge SiC power modules. The inverter topologies were typical three-phase two-level inverters as in Fig. 2.4 with grid-side filters; Inverter #1 was loaded with a star-connected resistive load and Inverter #2 was connected to the grid through an isolation transformer. The detailed system parameters are given in Table 4.2 for all the three converters.

As shown in Fig. 4.2 through the control-related voltage and current measurements, the DAB converter and Inverter #1 operate under cascaded control, and Inverter #2 controls the grid-side current. The DAB controller and Inverter #2 controller were implemented using rapid prototyping controllers by Imperix, whereas Inverter #1 controller was implemented on dSPACE platform. In the experiment, the DAB converter and Inverter #2 were bidirectional and operated either as a load or as a source, depending on the chosen operating point. All the converters were standalone stable such that a degradation in the system performance

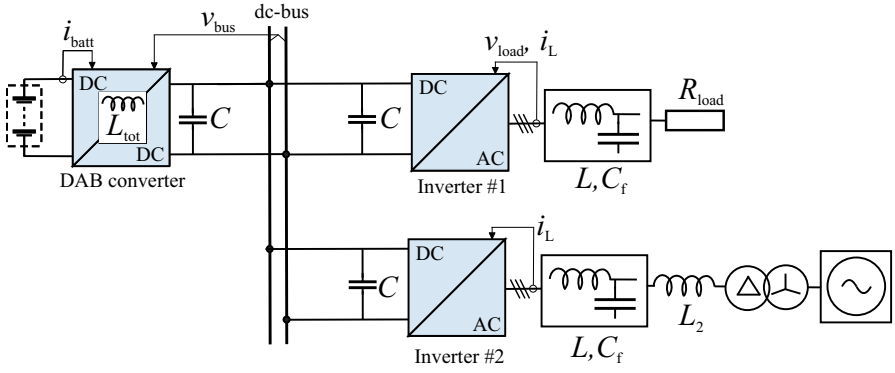

Figure 4.2 Simplified schematic of Experimental Setup 2.

Table 4.2 Parameters used in Experimental Setup 2.

Parameter	Value (DAB / Inv. #1 / Inv. #2)	Description
V_{bus}	400 V	bus voltage
V_{in}	200 V (dc) / 120 V_{rms} (ac) / 120 V_{rms} (ac)	source- or load-side voltage
R_{load}	25 Ω	load of Inv. #1 (star-conn.)
f_{sw}	50 kHz / 8 kHz / 20 kHz	switching frequency
C	1.5 mF / 1.5 mF / 1.95 mF	bus-side capacitance
C_{f}	none / 25 μF / 10 μF	inv. ac-side filter capacitance
L_{tot}	300 μH	DAB total inductance
L	none / 2.2 mH / 2.5 mH	inv. ac-side filter inductance
L_2	none / none / 0.6 mH	inv. grid-side filter inductance
$f_{\text{c-c}}$	1 kHz / 500 Hz / 450 Hz	current loop cross-over freq.
$\varphi_{\text{m-c}}$	65^o / 65^o / 60^o	current loop phase margin
$f_{\text{c-v}}$	20 Hz / 6 Hz / none	voltage loop cross-over freq.
$\varphi_{\text{m-v}}$	55^o / 60^o / none	voltage loop phase margin

would originate from the interactions between the single converters. The measured signals were recorded directly on PC connected to the controller platforms.

4.1.3 Simulation Model

The simulation model was used to validate the capacitance-emulating stabilizing control algorithm. A simulation model of the power-converter system depicted in Fig. 4.3 was built on MATLAB Simulink. The system consisted of a bidirectional dc-dc converter with a constant voltage source and a three-phase two-level grid-connected PV-inverter with L-type grid-side filters. The dc-dc converter topology was equivalent to the one presented in Fig. 2.2 and the inverter topology equivalent to the one presented in Fig. 2.4. The detailed system parameters are given in Table 4.3.

The dc-dc converter employs the capacitance-emulating control scheme shown in Fig. 3.9 with a crossover frequency of 800 Hz. The PV-inverter uses a cascaded control structure that controls the grid-side current and PV-side voltage, where the dc-bus voltage is controlled to match the MPP operating point. In the simulation, a resonance was introduced to the dc-bus voltage through grid imbalance by setting phase A voltage magnitude to 70 percent of the nominal value.

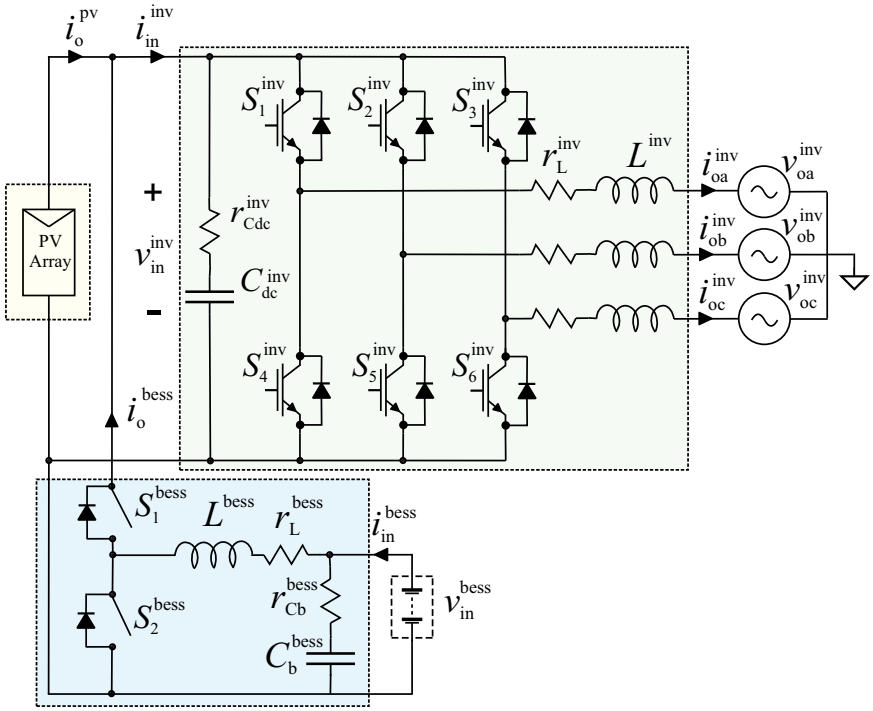

Figure 4.3 A schematic of the Simulation Model.

Table 4.3 Parameters used in Simulation Model.

Parameter	Value	Description
$V_{\text{in}}^{\text{inv}}$	480 V	dc-bus voltage
$V_{\text{in}}^{\text{bess}}$	200 V	battery terminal voltage
$C_{\text{dc}}^{\text{inv}}$, $r_{\text{Cdc}}^{\text{inv}}$	1 mF, 90 mΩ	dc-bus capacitor
L^{inv}, $r_{\text{L}}^{\text{inv}}$	1 mH, 1 mΩ	inverter L-filter
$C_{\text{b}}^{\text{bess}}$, $r_{\text{Cb}}^{\text{bess}}$	1 μF, 10 mΩ	battery-side capacitor
L^{bess}, $r_{\text{L}}^{\text{bess}}$	1.3 mH, 70 mΩ	battery-side inductor
$V_{\text{pv-mpp}}$, $I_{\text{pv-mpp}}$	480 V, 8 A	MPP conditions (STC)
$V_{\text{a,b,c}}$	240 V	grid voltage (RMS)
f_{g}	60 Hz	grid frequency
f_{sw}	20 kHz	switching frequency

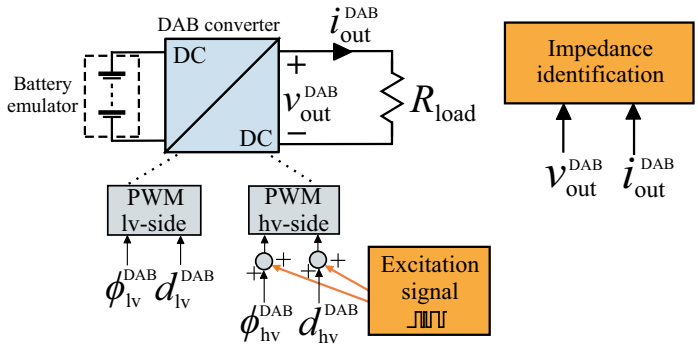

Figure 4.4 Simplified schematic of the experimental setup with the impedance identification. The excitation signal is added either to the phase shift or duty ratio of the high-voltage-side bridge.

4.2 Broadband Impedance Identification and Stability Analysis

4.2.1 Experiment a): Broadband Impedance Identification on a DAB Converter [P5]

This experiment applies Experimental Setup 1. In this experiment, several implementations of broadband impedance identification on a DAB converter are compared. The results are compared to identify measurement and identification challenges and to establish the most efficient method for impedance identification on DAB converters.

Fig. 4.4 presents the experimental setup with the broadband identification configuration. The orange parts depict the implemented broadband identification configurations. The excitation signal was introduced to the system through two different variables:

- Excitation was added to the high-voltage-side phase shift (with a high-voltage-side duty ratio of 0.5)
- Excitation was added to the high-voltage-side duty ratio (with a high-voltage-side phase shift of 60 deg)

This allowed for straightforward comparison between the impedance-identification-implementation methods as well as a basis for observing the deadtime effects.

The excitation signal design was done with a desired frequency range of 10 Hz to 200 Hz. A 63-bit-long MLBS signal with a generation frequency of 500 Hz was applied. Three averaging periods were used to mitigate non-systematic noise, which allowed for a measurement time less than 0.4 s. The injection amplitude was selected so that the converter output voltage and current deviated less than 2 percent of their nominal (average) values. Fig. 4.5 shows

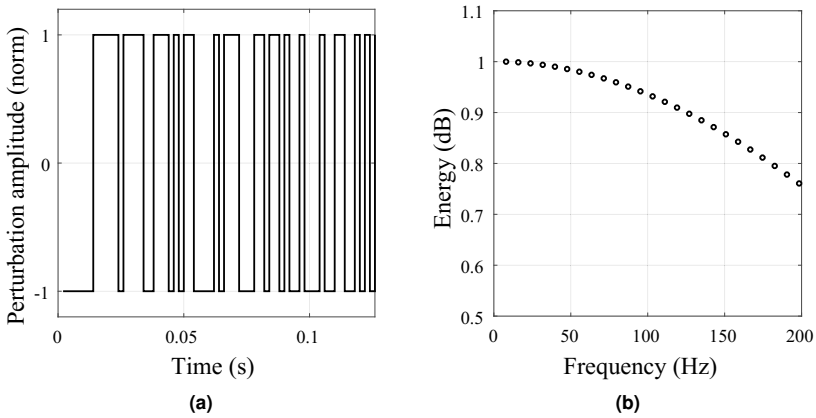

Figure 4.5 The MLBS signal used for perturbation a) in time-domain, and b) its energy spectrum. [P5]

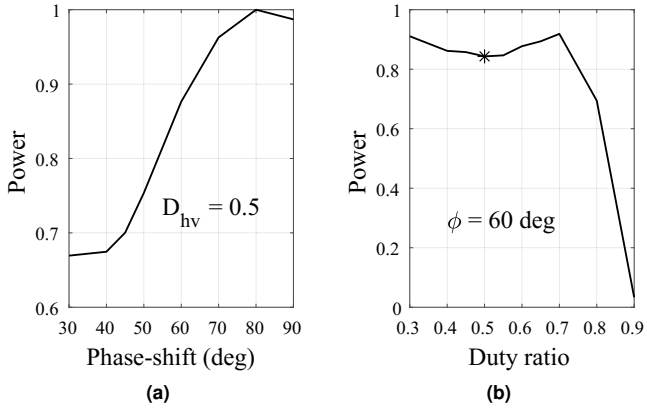

Figure 4.6 Measured transferred power (normalized) a) as a function of the phase shift (with $D_{\mathrm{hv}}^{\mathrm{DAB}} = 0.5$), and b) as a function of the high-voltage side duty ratio (with $\phi_{\mathrm{hv}}^{\mathrm{DAB}} = 60$ degrees). The marker highlights the nonlinear point ($D_{\mathrm{hv}}^{\mathrm{DAB}} = 0.5$).

the designed MLBS both in the time and frequency domain.

Before the impedance identification, the relationship between the power transfer and phase shift and duty ratio was studied by measuring the output power at different set-points as shown in Fig. 4.6. In Fig. 4.6a, the relationship between the phase shift and power is linear around the phase shift of 60 degrees. On the other hand, Fig. 4.6b shows strong nonlinearity between the duty ratio and power around the duty ratio of 0.5: the power increases regardless of how the duty ratio changes (see the marker in Fig. 4.6b). The employed identification method is based on the assumption of linearity between the perturbed parameter and con-

Table 4.4 Perturbations used in the experimental results and their effect on voltage and current (as percentage of average).

Perturbed variable	Average	Injection amplitude	Perturbation amplitude in current	Perturbation amplitude in voltage
Phase shift	60 degrees	6 degrees	1.9 %	1.7 %
Duty ratio without offset	0.50	0.10	1.1 %	0.9 %
Duty ratio with offset	0.60	0.05	1.1 %	1.0 %

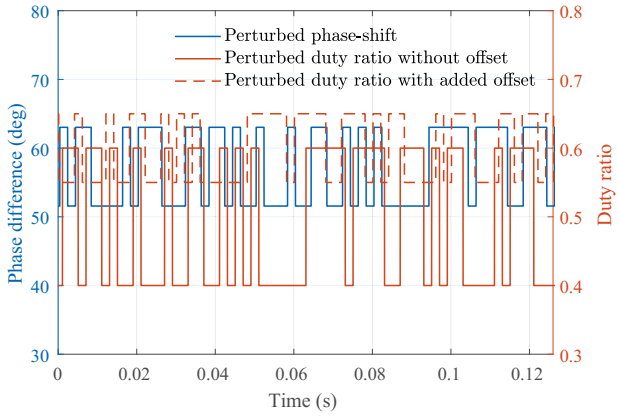

Figure 4.7 Samples of the perturbed variables.

verter output power. Therefore, at the set-point with a duty ratio of 0.5, the impedance measurement implementation with an excitation to the duty ratio yields unreliable results. To verify the accuracy-degrading effects of the nonlinear set point, an additional impedance identification was performed with an added offset to the duty ratio. This slightly increased the converter currents and voltages (i.e., changed the set-point), but allowed for greatly improved identification accuracy as the relationship between the power and duty ratio was more linear.

After the relationships between the output variables and the perturbed variables had been studied, the impedance identifications were carried out. The designed MLBS-based excitation signal was introduced to the system by applying three different injection methods. In the first case, the phase shift was perturbed. In the second and third cases, the duty ratio was perturbed without and with an added offset, respectively. More details of the perturbation parameters are given in Table 4.4, and Fig. 4.7 shows a sample of the perturbed variables. Fig. 4.8a compares the resulting converter output impedances, and Fig. 4.8b shows the corresponding errors in comparison to an ideal measurement (45 dB in magnitude and zero degrees in phase). With the phase shift excitation, the result is more accurate having less

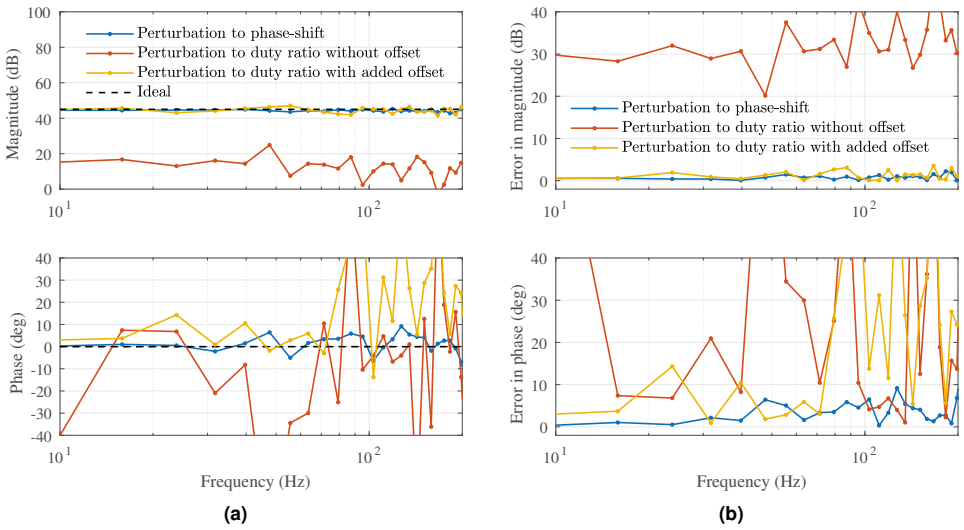

Figure 4.8 a) The identified output impedances for the three cases and an ideal result, and b) the corresponding errors compared to the ideal measurement. [P5]

than 2.5 dB (5.5 percent) error in magnitude and 10 degrees in phase. On the other hand, with the duty ratio excitation (without the offset), the result is not accurate at all, even if the perturbation amplitude is increased. This degradation in accuracy was expected based on the nonlinear relationship between the power and duty ratio of the DAB converter at the applied set-point. However, with the small dc-offset that slightly increases the power, the impedance is obtained more accurately, giving a maximum of 3.5 dB (7.8 percent) error in the magnitude response. In the phase response, however, the maximum error is higher and becomes significant at frequencies above 70 Hz. This phase response accuracy cannot be improved by increasing the amplitude as the relationship between the duty ratio and output power is nonlinear at both set-points $D_{\mathrm{hv}} = 0.5$ and $D_{\mathrm{hv}} = 0.7$.

The results show that a nonlinear relationship between the output variable and the perturbed variable strongly affects the impedance measurements on DAB converters. This applies especially when injecting the perturbation to the duty ratio due to the strongly nonlinear characteristics at certain set-points. Therefore, under such nonlinear behavior, the perturbation should be applied to the phase shift rather than to the duty ratio. However, if the nonlinear set-points are avoided or their effects are mitigated, sufficient measurements could be achieved using both perturbation methods.

As a summary, three different injection methods can be applied when implementing a broadband impedance identification on a DAB converter, and the following guidelines should be considered in the identification implementation design:

Method 1—*Injection to output voltage or current reference*: In this method, the amplitude

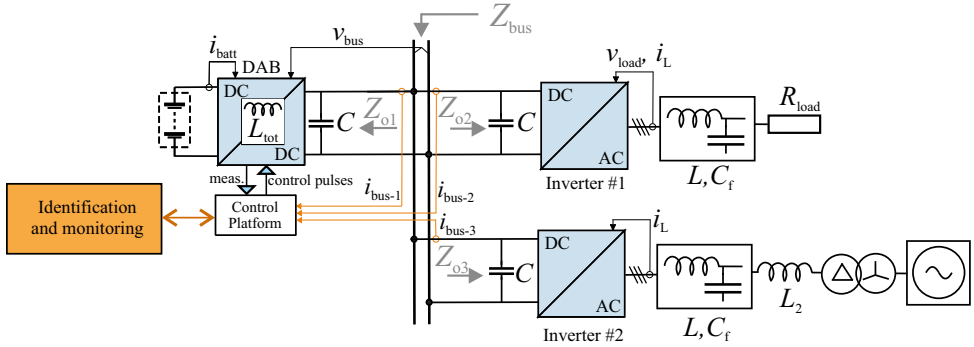

Figure 4.9 Simplified schematic of the experimental setup with the bus-impedance identification.

design of the excitation is less sensitive than in the other methods because the injection is affected by the controller dynamics. The amplitude value, as well as other parameters of the injection, can be designed by general guidelines [54].

Methods 2 and 3—*Injection to duty ratio or phase-shift*: In this method the amplitude design is sensitive and set-point-dependent due to nonlinear behavior between the perturbed parameter and output power. Hence, it is recommended to identify the nonlinear operating points and use the variable that produces the most linear behavior around the chosen set-point. The perturbation amplitude can then be increased so that the desired SNR is reached without violating interference requirements. It is emphasized that, under strong nonlinearities, the measured impedance accuracy cannot be improved by increasing the injection amplitude. Instead, strategies to mitigate or to avoid nonlinear effects should be considered. The other injection parameters can be designed by general guidelines [54].

4.2.2 Experiment b): Online Bus-Impedance-Based Stability Assessment [P6]

This experiment applies Experimental Setup 2. In this experiment, a MIMO-based frequency-response identification is implemented on a multi-converter system to identify its bus impedance using the broadband identification techniques. The bus-side impedances of the three parallel-connected converters are identified, from which the bus impedance is calculated. Each of the three converters is perturbed with an orthogonal MLBS signal and the three impedances are derived from the resulting voltage and current measurements. The results facilitate the stabilizing controller used in Experiment ii).

Fig. 4.9 presents the experimental setup with the broadband identification configuration. The orange parts depict the implemented broadband identification configuration, where the orange arrows relate to the current measurements required for the impedance identifications.

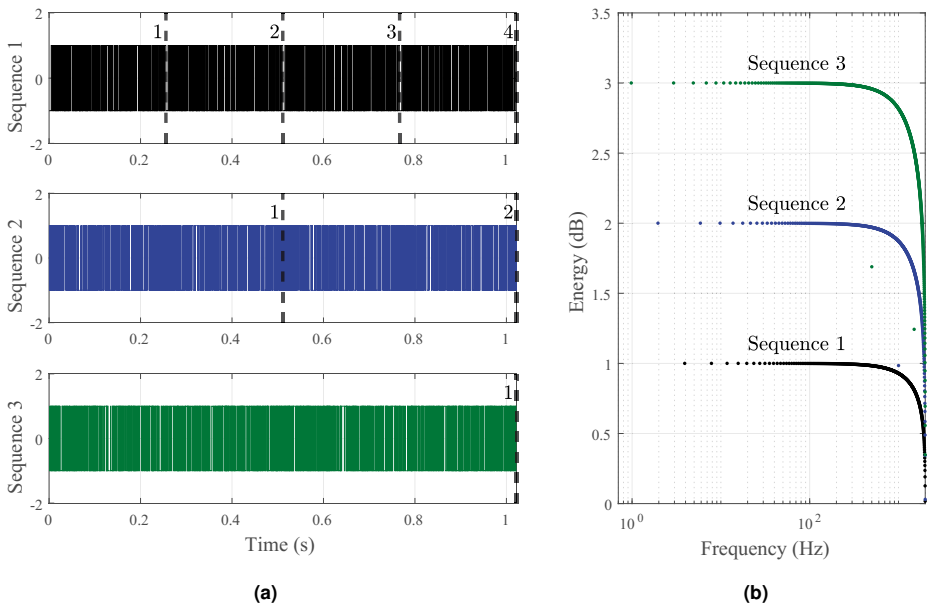

Figure 4.10 The orthogonal signals used for perturbation a) in time domain and b) the energy spectrum. The vertical dashed lines in the time-domain figure mark the repeating sequences (periods). The sequence 1 and 2 spectrums have been multiplied by two and three to improve readability.

The experiments were conducted at two different operating points: the DAB converter either fed the dc bus with 500 W while discharging the battery, or consumed 350 W while charging the battery. This change in the operating point was achieved by changing Inverter #2 from feeding the grid with 150 W to feeding the dc bus with 700 W.

The perturbation sequences are implemented in all the three control platforms. Three orthogonal MLBS sequences are used: Sequence 1 for DAB converter, Sequence 2 for Inverter #1, and Sequence 3 for Inverter #2. Sequence 1 is of length $N = 2^9 - 1$. Since the sequences are orthogonal, the length of Sequence 2 is $2N$, and the length of Sequence 3 is $4N$. Fig. 4.10 shows the three sequences in both the time and frequency domain. The frequency range of interest is around the voltage control cross-over frequency, which is well within the chosen energy spectrum. The selected spectrum does not identify unnecessarily low frequencies, which shortens the required measurement time. The sequences are generated at $f_{\text{gen}} = 2$ kHz, which provides an 800 Hz bandwidth for the measured frequency responses. Each of the converter switching frequencies is a multiple of the chosen generation frequency. As demonstrated in Fig. 4.10, Sequence 3 has a period length of 1.022 s, during which the other sequences are repeated periodically. The actual injection amplitudes are selected such that their values are 5–7 percent of the nominal voltage or current reference

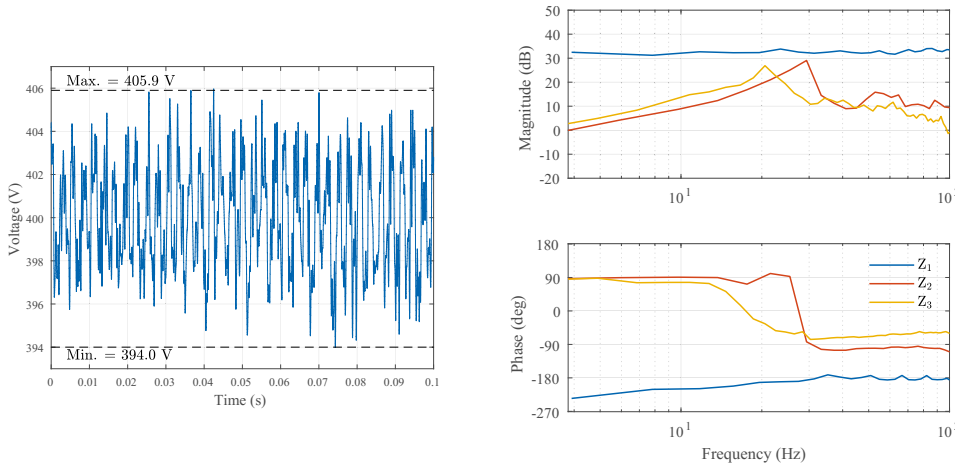

Figure 4.11 a) The low-pass filtered (500 Hz) bus voltage while discharging the battery, and b) the identified impedances.

values.

The designed perturbations were simultaneously added to the controller reference voltages and/or currents of each converter. The first perturbation was applied with three periods, the second with six periods, and the third with 12 periods (because each perturbation length is twice that of the previous one). The resulting bus voltage and output current of each converter were then measured using a sampling rate of 50 kHz. The measurements were averaged over the applied periods and Fourier transform was used to obtain the output impedances of each converter. The bus impedance was then computed based on (3.3).

First, the discharging mode was considered. Fig. 4.11a shows the bus voltage when the battery is discharging. The minimum (394.0 V) and maximum (405.09 V) values are also marked, meaning a voltage deviation of 2.77 percent. Fig. 4.11b shows the identified impedances, and the resulting bus impedance is shown in Fig. 4.12a with a blue line. The bus impedance has a magnitude of 37 dB at 21 Hz, highlighted with a marker in Fig. 4.12a.

Next, a similar study is performed while charging the battery. The voltages are comparable to Fig. 4.11a. The identified bus impedance is shown in Fig. 4.12a with a purple line, and the bus impedance has a magnitude of 23 dB at 13 Hz that is highlighted with a marker in the figure. The resonance peak in the bus impedance magnitude is 14 dB higher while discharging the battery than while charging the battery. Fig. 4.12b presents the corresponding normalized bus impedances in a complex plane. The AIR is also presented, and neither of the bus impedances stays within this area. A stabilizing controller is implemented in Experiment ii) to improve the damping to the desired level.

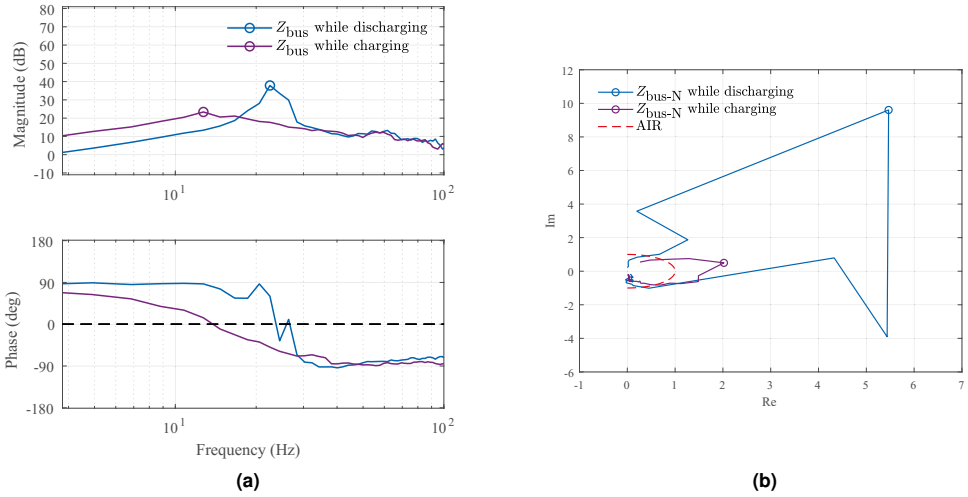

Figure 4.12 a) The identified bus impedances while discharging or charging the battery (the markers highlight the identified resonance), and b) the corresponding Nyquist contour of the normalized bus impedance (AIR boundary indicated with the red line, marker highlights the identified resonance).

4.3 Stabilizing Control Schemes

4.3.1 Experiment i): Capacitance-Emulation-Based Stabilizing Control [P3]

This experiment applies the simulation model given in Fig. 4.3. In this experiment, the capacitance-emulating stabilizing control algorithm is validated and its resonance-damping effect demonstrated. The BESS-PV-inverter system with the capacitance-emulating bidirectional converter is illustrated in Fig. 4.13.

First, the impedances of an ideal and a virtual capacitance were compared. Fig. 4.14a presents the impedance of three different systems: 1-mF dc-bus capacitor C_{dc} (with parasitic resistance of 90 mΩ), the same capacitor in parallel with a 1-mF ideal capacitance, and the same capacitor in parallel with a 1-mF emulated capacitance. The increase of capacitance decreases the impedance magnitude and, thus, increases damping of voltage fluctuations. The emulated capacitance has a similar impedance with the ideal capacitance within the control bandwidth.

The resonance-damping effect of the implemented virtual capacitance was then demonstrated. The BESS-PV-inverter with the capacitance-emulating bidirectional converter was simulated under grid imbalance by setting phase *A* voltage magnitude to 70 percent of the nominal value. This imbalance caused a second-order harmonic component (120 Hz) to

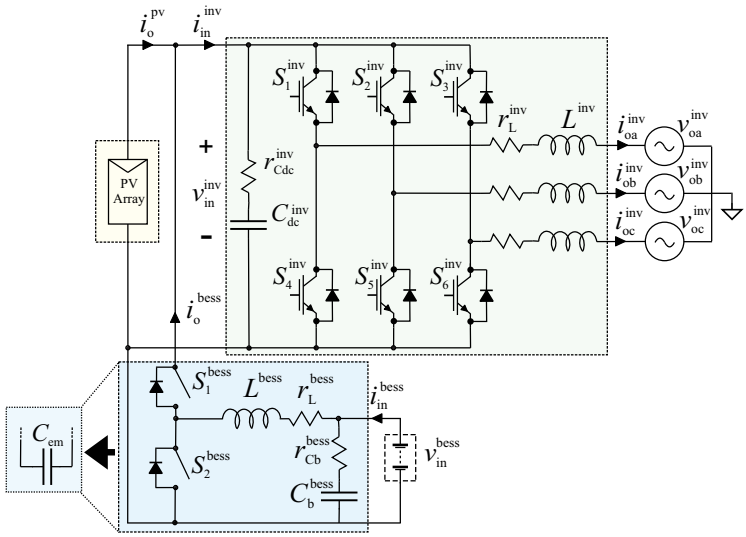

Figure 4.13 A BESS with a capacitance-emulating bidirectional dc-dc converter connected to the dc-bus of a PV inverter.

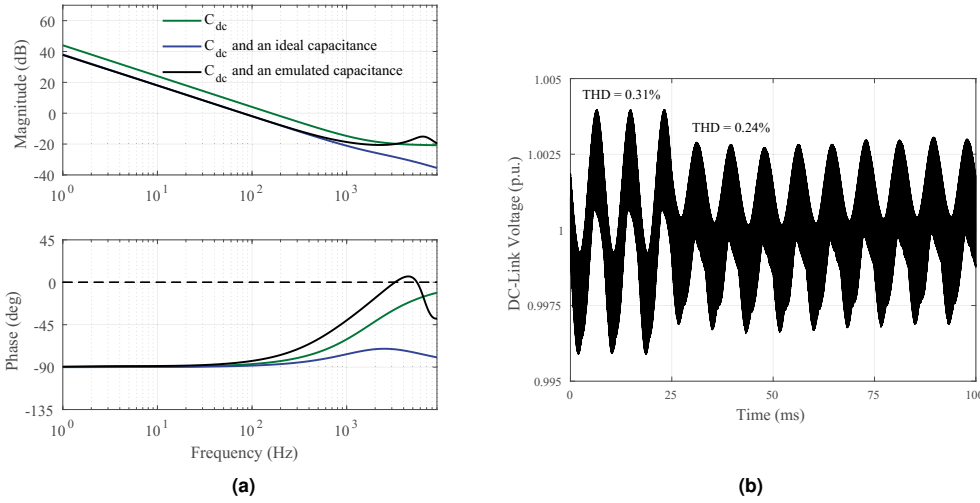

Figure 4.14 a) Impedance of a dc-bus capacitor C_{dc} with and without an ideal and an emulated capacitance. b) Simulated dc-bus voltage during grid imbalance; The capacitance emulation algorithm is activated at 25 ms. [P3]

the dc-bus voltage, and the capacitance emulation algorithm was used to lower its amplitude, as shown in Fig. 4.14b. As a result, the second harmonic component decreased from 0.24 percent to 0.13 percent and the total harmonic distortion (THD) from 0.31 percent to 0.24 percent. Thus, the capacitance-emulating stabilizing control mitigated the resonance.

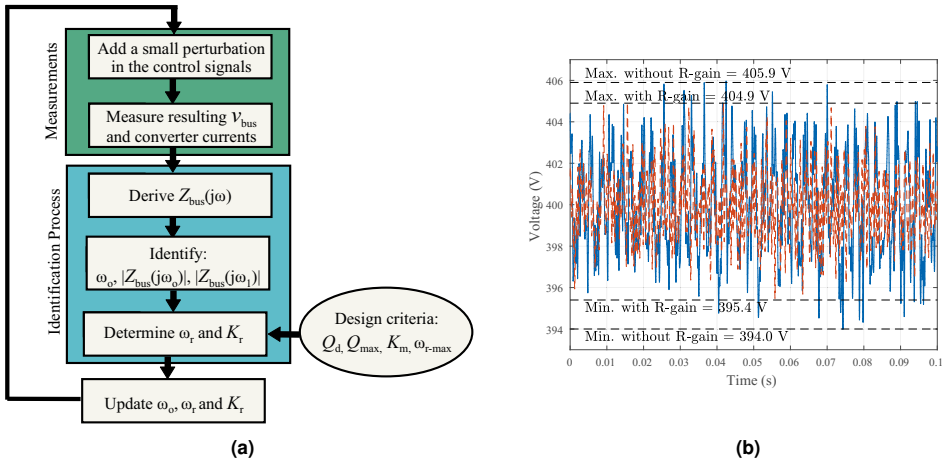

Figure 4.15 a) A flowchart representing the adaptive resonance-damping algorithm with the chosen design criteria, and b) the low-pass filtered (500 Hz) bus voltage without (blue) and with (orange) damping R-gain while discharging the battery

4.3.2 Experiment ii): Virtual-Impedance-Based Stabilizing Control [P5–P6]

This experiment applies Experimental Setup 2. In this experiment, a stabilizing controller is implemented on the DAB converter, optimizing the bus impedance damping of the multi-converter system. The stabilizing controller utilizes the bus-impedance identification of Experiment b) and tunes the stabilizing resonance damping gain of the DAB converter voltage controller such that the converter's own impedance is adjusted to optimize the resulting bus impedance around the identified resonance frequency. The identified bus impedances are compared, both with and without the stabilizing control algorithm, to validate the effectiveness of the controller.

After establishing the identification process presented in Experiment b), the resonance-damping R-gain is employed on the DAB controller. The R-gain parameters were assigned based on the identified bus impedance and (3.12) with $Q_d = 0.7$, $Q_{max} = 1$, and $K_m = 0.5$. Fig. 4.15a outlines the bus impedance identification and the controller update process. The experiments were conducted at the same two operating points as in Experiment b): the DAB converter was either feeding the dc bus with 500 W while discharging the battery, or consuming 350 W while charging the battery. This change in the operating point was achieved by changing Inverter #2 from feeding the grid with 150 W to feeding the dc bus with 700 W. To improve stability, the proposed PI-R controller was used so that an enhanced damping was achieved around the chosen frequency.

First, the discharging mode is considered. Following the design procedure and the identified bus impedance, the values of $K_r = 0.17$ and $\omega_r = 18$ Hz are obtained for the R-gain. The orange line in Fig. 4.15b shows the resulting bus voltage. The minimum (395.4 V) and maxi-

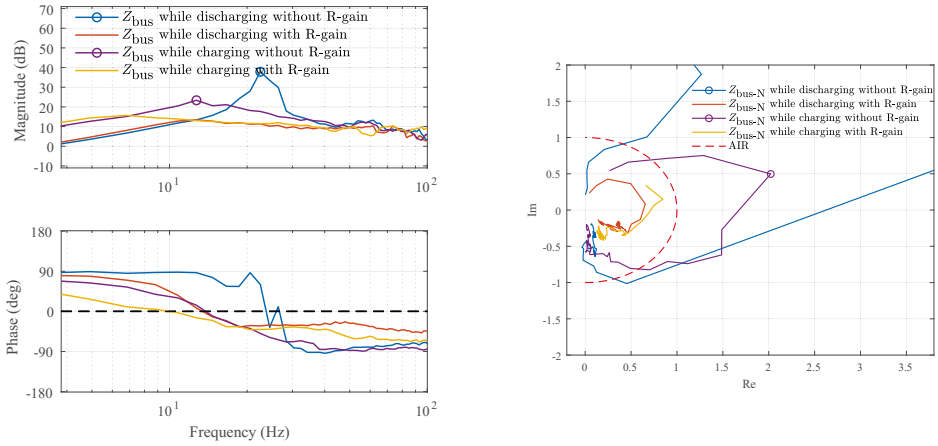

Figure 4.16 a) The identified bus impedances with and without damping R-gain while discharging or charging the battery (the markers highlight the identified resonance), and b) The Nyquist contour of the normalized bus impedance with and without damping R-gain (AIR boundary indicated with the red line, marker highlights the identified resonance).

mum (404.9 V) values are shown, resulting in 2.38 percent voltage deviation. The R-gain has decreased the deviation by 0.4 percent. The red line in Fig. 4.16a shows the resulting bus impedance. The R-gain increases the bus impedance damping around the identified resonance frequency (21 Hz) by 26 dB, lowering it to 11 dB and thus improving the system damping.

Next, a similar study is performed while charging the battery. The R-gain parameter values are calculated as $K_r = 0.25$, $\omega_r = 7$ Hz. The resulting bus impedance is shown in Fig. 4.16a with the yellow line. The R-gain increases the bus impedance damping around 13 Hz, lowering it by 11 dB to 12 dB.

In both the discharging and charging experiments, the R-gain controller enhanced the system stability and damping around the identified resonance frequency. The R-gain controllers optimized the identified bus impedances, which were well-stabilized. Fig. 4.16b presents the identified normalized bus impedances in a complex plane in both discharging and charging mode. Compared to the cases without the R-gain, the R-gain-affected normalized bus impedances have more damping and are well-confined within the AIR boundary. The Nyquist contour of the R-gain affected normalized bus impedances intersects with the real axis around the requested magnitude, indicating the achievement of the desired damping level. With the R-gain, the system damping is within the desired limits. The experimental results confirm the effectiveness of the proposed adaptive stabilization method. The BESS can efficiently dampen the resonances in the bus impedance in both charging and discharging modes. Therefore, despite possible network or operating mode changes, the system reliability and stability can be enhanced in an adaptive manner without hardware updates or controller re-tuning.

5 CONCLUSIONS

Battery energy storage systems (BESS) have become an essential technology in modern power systems. BESSs offer fast-acting energy storage and advanced power processing capabilities, and they can strengthen and improve power system stability through various grid-supporting control solutions and provide flexibility for the balance between generation and demand. These characteristics have made them essential components in many power-distribution systems, such as renewable power generation, dc micro-grids, and electric transportation. Such applications are often complex and consist of various types of converter-based sources and loads, forming a multi-converter system.

Bidirectional power electronic converters facilitate the operation of BESSs by controlling the power flow. The widespread usage of power electronic converters has introduced challenges to the power system's stability and quality, and bidirectional devices further complicate the system design and stability analysis. Consequently, the stability analysis of power electronics has become essential. Previous studies have offered methods for evaluating the stability of such systems by applying state-space modeling or impedance-based stability criteria, where the stability is analyzed based on terminal impedance at the interface. However, the detailed dynamics and parameters of some subsystems may not be known, making model-based approaches impractical. Additionally, the small-signal dynamics depend on the system's operating conditions, which may vary over time, making such analysis insufficient in many cases.

This thesis has presented broadband stability analysis methods that can be applied in the assessment of multi-converter systems with bidirectional converters. The methods utilize frequency-response identification based on pseudo-random broadband sequences. Additionally, stabilizing control algorithms were presented for enhancing stability and optimizing the system dynamics as desired. The contributions of this thesis can be summarized into three categories:

- A modeling method for including the effect of a BESS into other dynamical small-signal models that is used to analyze the behavior of a BESS-PV-inverter under different operating conditions. The analysis showed that PV sources can introduce sources of instability into the inverter control loop, but adding a converter-controlled BESS in parallel with the PV source enhances the stability and alleviates control design limitations.

- Broadband methods for identifying the impedance of bidirectional converters and multi-converter systems. Challenges related to nonlinear operating points were examined and guidelines were suggested to avoid such issues on DAB converters. The identification methods for multi-converter systems utilize orthogonal perturbation signals that allow the identification of several impedances simultaneously rather than sequentially. The presented broadband methods can be used to rapidly obtain the system-characterizing frequency responses, thus facilitating various adaptive control methods.
- Stabilizing controllers are proposed that can be employed on bidirectional converters to enhance stability and optimize system dynamics. The stabilizing control methods enhance the system stability and mitigate resonances using BESS applications. The controllers reshape the impedance of the converter to better match the desired dynamics. The capacitance-emulating controller affects the dynamics within the whole control bandwidth by introducing a virtual capacitance, while the resonance-damping-gain-based stabilizing controller increases damping at a specific (resonance) frequency. The presented stabilizing control methods are particularly suitable for BESS applications as they are independent of the power-flow directions, the converter operation modes, and the system grouping. Since the energy required for the mitigation is typically oscillatory in nature, such control features affect the BESS energy level to a relatively minor degree, making the applications very practical. The methods are also well-suited for multi-converter systems.

The presented measurement and analysis methods were validated through experiments by applying a bidirectional DAB converter and a multi-converter hardware setup. In the experiments, several broadband impedance identifications were applied and optimized and the presented stabilizing control features were verified. It was shown that the presented broadband identification techniques and guidelines enabled short identification times while achieving accurate results. The stability analysis methods were shown to accurately predict the system stability and stability margins in different configurations.

Discussion and Criticism

The stability analysis and control design of modern converter-based power systems have become challenging due to the ever-increasing complexity of such systems. The system configurations may vary drastically and unpredictably due to factors such as changes in the devices' control modes, operating modes, and the network's topology. For example, a change in power flow direction can cause a loss of stability even though the system is stable with the initial power flow direction. In fact, the increase of converters applying bidirectional power flow further challenges the system analysis. As a result, the stability analysis methods may have to be applied without detailed knowledge of the system configurations and operating

modes. Consequently, the stability analysis of converter-based power systems can benefit from measurement-based approaches. Broadband methods perform well in online applications due to their fast identification time and can facilitate adaptive control designs capable of responding to variations in the system dynamics.

The applicability of the presented methods depends heavily on the efficiency of identifying the subsystems' terminal impedances. The identification typically requires either special hardware or access to the control structure of the existing hardware. The presented methods allow the converters to implement the perturbation such that no additional hardware is required. Accordingly, the converter control structure must facilitate the perturbation implementation, which is typically not the case in commercial devices. Additionally, because the employed broadband perturbations are sensitive to nonlinear relationships between the perturbed variable and the variables used for the identification, it may be challenging to make accurate identifications in applications that have such characteristics. As the issues related to nonlinear behavior are typically highly application-dependent, this thesis presents only general guidelines for the identification implementation in such situations with a focus on a DAB converter, and further analysis may be required in other applications.

Another important aspect in the identification of converter systems is the generated interference to the system. The created perturbation acts as a disturbance to the system, so the system requirements and specifications limit its design. The perturbation signal's time-domain amplitude and frequency-domain spectrum must be designed carefully to guarantee that the system variables, such as currents and voltages, stay within allowable limits and that the perturbations does not excessively degrade the power quality. Even though this thesis has presented design methods for minimizing the interference, the degrading effects cannot be completely neglected and may become a limiting factor in sensitive applications.

Future Work

Several challenges remain in the efficient stability assessment of multi-converter systems. Even though the broadband identification methods, particularly the orthogonal perturbation signals, shorten the identification time, each identified system impedance doubles the required time. Methods for providing faster identifications or identifying only the critical identifications could allow the identification of more complex systems within a sufficient identification time. Moreover, even though the utilization of orthogonal sequences makes communication between the different devices unnecessary, a communication network is still required for analyzing the multi-converter system stability through the bus impedance. Additionally, the systems require logic for deciding when the stability assessment is performed. For example, an instability detector could be used to initiate the stability analysis procedure.

Another objective for future research is to improve broadband identification procedures. Operating points with a strong nonlinear relationship between the perturbed variable and

the identification-related variables were found to be challenging, if not impossible, for frequency response identification. Rather than avoiding such operating points, mitigation methods could be used to alleviate the nonlinear effects, or a perturbation signal could be used that is more suitable for identifying nonlinear systems. Moreover, methods to further speed up the impedance identification processes would benefit the designs and allow more reliable adaptive controllers and extend the number of suitable applications.

The stability enhancement techniques are also an important topic for future work. The variety of multi-converter systems creates a variety of possible challenges. In this thesis, the resonance-damping algorithm was utilized to dampen only a single resonance frequency. However, several resonance frequencies might exist simultaneously in a higher-order system. For such situations, the control algorithm could be altered to dampen several frequencies. Moreover, a possible collaboration between several stabilizing converters could be beneficial, but such a scheme creates challenges due to even more varying dynamics, and such designs have to be well developed such that the converters may not work against each other under any circumstances.

REFERENCES

[1] R.-M. Sallinen, A. Aapro, M. Berg, and T. Messo, Complete Small-Signal Model of Three-Phase Photovoltaic Inverter Considering the Source and Load Effects, in *Proc. Annual Conference of the IEEE Industrial Electronics Society*, pp. 2237–2244, 2018.

[2] R.-M. Sallinen and T. Messo, The Combined Source-Effect of Photovoltaic Generator and Bi-Directional DC-DC Battery Charger on Inverter Control Dynamics, *The Journal of Engineering*, pp. 5197–5201, 2018.

[3] R.-M. Sallinen, T. Messo and T. Roinila, Mitigating Voltage Fluctuations in Battery Energy Storage Systems, in *Proc. IEEE Workshop on Control and Modeling for Power Electronics*, 6 pages, 2019.

[4] R.-M. Sallinen, T. Roinila and H. Abdollahi, Stability Analysis and Adaptive Resonance Damping of Multi-Converter System Applying Bidirectional Converter, in *Proc. IEEE Workshop on Control and Modeling for Power Electronics*, 7 pages, 2020.

[5] R.-M. Sallinen and T. Roinila, Broadband Impedance-Measurement Methods in Dynamic Analysis of Dual Active Bridge Converters, in *Proc. IEEE Workshop on Control and Modelling of Power Electronics*, 6 pages, 2021.

[6] R.-M. Sallinen and T. Roinila, Adaptive Bus-Impedance-Damping Control of Multi-Converter System Applying Bidirectional Converters, *IEEE Journal of Emerging and Selected Topics in Power Electronics*, vol. 11, no. 1, pp. 567–575, 2023.

[7] Institute for Economics & Peace, *Ecological Threat Report 2021: Understanding Ecological Threats, Resilience and Peace*, Sydney, Australia, 2021.

[8] World Economic Forum, *The Global Risks Report 2021: Insight Report*, 2021.

[9] J. Cook, N. Oreskes, P. T. Doran *et al.*, Consensus on consensus: A synthesis of consensus estimates on human-caused global warming, *Environmental Research Letters*, vol. 11, no. 4, 2016.

[10] United Nations, *Paris Agreement*, United Nations Treaty Collection, Chapter XXVII 7 D, Paris, France, 2015.

[11] M. Roelfsema, H. L. van Soest, M. Harmsen *et al.*, Taking stock of national climate policies to evaluate implementation of the Paris Agreement, *Nat. Commun.*, vol. 11, no. 2096, 2020.

[12] Y.-M. Wei, R. Han, C. Wang *et al.*, Self-preservation strategy for approaching global warming targets in the post-Paris Agreement era, *Nat. Commun.*, vol. 11, no. 1624, 2020.

[13] D. L. McCollum, W. Zhou, C. Bertram *et al.*, Energy investment needs for fulfilling the Paris Agreement and achieving the Sustainable Development Goals, *Nat. Energy*, vol. 3, pp. 589–599, 2018.

[14] International Panel on Climate Change, *Climate Change 2022: Impacts, Adaptation and Vulnerability*, 2022.

[15] International Energy Agency, *Global Energy Review: CO2 Emissions in 2021*, IEA, Paris, France, 2021.

[16] M. Stecca, L. R. Elizondo, T. B. Soeiro *et al.*, A Comprehensive Review of the Integration of Battery Energy Storage Systems Into Distribution Networks, *IEEE Open Journal of the Industrial Electronics Society*, vol. 1, pp. 46–65, 2020.

[17] I. Batarseh and K. Alluhaybi, Emerging Opportunities in Distributed Power Electronics and Battery Integration: Setting the Stage for an Energy Storage Revolution, *IEEE Power Electronics Magazine*, vol. 7, no. 2, pp. 22–32, 2020.

[18] J. Alshehri and M. Khalid, Power Quality Improvement in Microgrids Under Critical Disturbances Using an Intelligent Decoupled Control Strategy Based on Battery Energy Storage System, *IEEE Access*, vol. 7, pp. 147314–147326, 2019.

[19] Y. Tan, K. M. Muttaqi, P. Ciufo *et al.*, Enhanced Frequency Regulation Using Multilevel Energy Storage in Remote Area Power Supply Systems, *IEEE Transactions on Power Systems*, vol. 34, no. 1, pp. 163–170, 2019.

[20] L. Meng, J. Zafar, S. K. Khadem *et al.*, Fast frequency response from energy storage systems—a review of grid standards, projects and technical issues, *IEEE Transactions on Smart Grid*, vol. 11, no. 2, pp. 1566–1581, 2020.

[21] International Energy Agency, *Energy Storage*, IEA, Paris, France, 2021.

[22] The California Energy Commission, *Energy Code*, California, USA, 2022.

[23] Q. Peng, Q. Jiang, Y. Yang *et al.*, On the Stability of Power Electronics-Dominated Systems: Challenges and Potential Solutions, *IEEE Transactions on Industry Applications*, vol. 55, no. 6, pp. 7657–7670, 2019.

[24] A. Khan, M. Hosseinzadehtaher, M. B. Shadmand *et al.*, On the Stability of the Power Electronics-Dominated Grid: A New Energy Paradigm, *IEEE Industrial Electronics Magazine*, vol. 14, no. 4, pp. 65–78, 2020.

[25] C. K. Tse, M. Huang, X. Zhang *et al.*, Circuits and Systems Issues in Power Electronics Penetrated Power Grid, *IEEE Open Journal of Circuits and Systems*, vol. 1, pp. 140–156, 2020.

[26] L. Kong, Y. Xue, L. Qiao *et al.*, Review of Small-Signal Converter-Driven Stability Issues in Power Systems, *IEEE Open Access Journal of Power and Energy*, vol. 9, pp. 29–41, 2022.

[27] J. Fang, H. Li, Y. Tang *et al.*, On the Inertia of Future More-Electronics Power Systems, *IEEE Journal of Emerging and Selected Topics in Power Electronics*, vol. 7, no. 4, pp. 2130–2146, 2019.

[28] N. Hatziargyriou, J. Milanovic, C. Rahmann *et al.*, Definition and Classification of Power System Stability – Revisited & Extended, *IEEE Transactions on Power Systems*, vol. 36, no. 4, pp. 3271–3281, 2021.

[29] F. Blaabjerg, Y. Yang, K. Ma *et al.*, Power electronics – the key technology for renewable energy system integration, in *Proc. International Conference on Renewable Energy Research and Applications*, 2015, pp. 1618–1626.

[30] T. Hakala, T. Lähdeaho and P. Järventausta, Low-Voltage DC Distribution – Utilization Potential in a Large Distribution Network Company, *IEEE Transactions on Power Delivery*, vol. 30, no. 4, pp. 1694–1701, 2015.

[31] T. Dragičević, X. Lu, J. C. Vasquez *et al.*, DC Microgrids—Part II: A Review of Power Architectures, Applications, and Standardization Issues, *IEEE Transactions on Power Electronics*, vol. 31, no. 5, pp. 3528–3549, 2016.

[32] L. Xiong, X. Liu, Y. Liu *et al.*, Modeling and stability issues of voltage-source converter dominated power systems: A review, *CSEE Journal of Power and Energy Systems*, 18 pages, 2020.

[33] R. Shah, N. Mithulananthan, A. Sode-Yome *et al.*, Impact of large-scale PV penetration on power system oscillatory stability, in *Proc. IEEE PES General Meeting*, 2010, 7 pages.

[34] S. Lamichhane and N. Mithulananthan, Possible impact of large scale wind energy integration on small signal stability, in *Proc. IEEE PES Asia-Pacific Power and Energy Engineering Conference*, 2015, 5 pages.

[35] X. Feng, J. Liu and F. C. Lee, Impedance specifications for stable DC distributed power systems, *IEEE Transactions on Power Electronics*, vol. 17, no. 2, pp. 157–162, 2002.

[36] E. Hossain, R. Perez, A. Nasiri *et al.*, A Comprehensive Review on Constant Power Loads Compensation Techniques, *IEEE Access*, vol. 6, pp. 33285–33305, 2018.

[37] M. A. Hassan, C.-L. Su, J. Pou *et al.*, DC Shipboard Microgrids With Constant Power Loads: A Review of Advanced Nonlinear Control Strategies and Stabilization Techniques, *IEEE Transactions on Smart Grid*, vol. 13, no. 5, pp. 3422–3438, 2022.

[38] K. E. L. Marcillo, D. A. P. Guingla, W. Barra *et al.*, Interval Robust Controller to Minimize Oscillations Effects Caused by Constant Power Load in a DC Multi-Converter Buck-Buck System, *IEEE Access*, vol. 7, pp. 26324–26342, 2019.

[39] A. Kwasinski and C. N. Onwuchekwa, Dynamic Behavior and Stabilization of DC Microgrids With Instantaneous Constant-Power Loads, *IEEE Transactions on Power Electronics*, vol. 26, no. 3, pp. 822–834, 2011.

[40] X. Lu, K. Sun, J. M. Guerrero *et al.*, Stability Enhancement Based on Virtual Impedance for DC Microgrids With Constant Power Loads, *IEEE Transactions on Smart Grid*, vol. 6, no. 6, pp. 2770–2783, 2015.

[41] M. Wu and D. D.-C. Lu, A Novel Stabilization Method of LC Input Filter With Constant Power Loads Without Load Performance Compromise in DC Microgrids, *IEEE Transactions on Industrial Electronics*, vol. 62, no. 7, pp. 4552–4562, 2015.

[42] J. Beerten, S. D'Arco and J. A. Suul, Identification and Small-Signal Analysis of Interaction Modes in VSC MTDC Systems, *IEEE Transactions on Power Delivery*, vol. 31, no. 2, pp. 888–897, 2016.

[43] L. Herrera, W. Zhang and J. Wang, Stability Analysis and Controller Design of DC Microgrids With Constant Power Loads, *IEEE Transactions on Smart Grid*, vol. 8, no. 2, pp. 881–888, 2017.

[44] X. Lu, K. Sun, J. M. Guerrero *et al.*, Stability Enhancement Based on Virtual Impedance for DC Microgrids With Constant Power Loads, *IEEE Transactions on Smart Grid*, vol. 6, no. 6, pp. 2770–2783, 2015.

[45] M. Amin, M. Molinas, J. Lyu *et al.*, Impact of Power Flow Direction on the Stability of VSC-HVDC Seen From the Impedance Nyquist Plot, *IEEE Transactions on Power Electronics*, vol. 32, no. 10, pp. 8204–8217, 2017.

[46] M. Habibullah, N. Mithulananthan, K. N. Bhumkittipich *et al.*, A Comprehensive Investigation on High-Frequency Oscillation in DC Microgrid, *IEEE Access*, vol. 9, pp. 54850–54861, 2021.

[47] P. Kundur, *Power System Stability and Control*. McGraw-Hill, 1994, pp. 1176.

[48] P. Kundur, J. Paserba, V. Ajjarapu *et al.*, Definition and classification of power system stability IEEE/CIGRE joint task force on stability terms and definitions, *IEEE Transactions on Power Systems*, vol. 19, no. 3, pp. 1387–1401, 2004.

[49] J. Machowski, Z. Lubosny, J. W. Bialek *et al.*, *Power System Dynamics: Stability and Control*. Wiley, 2020, 888 pages.

[50] X. Wang, F. Blaabjerg and W. Wu, Modeling and Analysis of Harmonic Stability in an AC Power-Electronics-Based Power System, *IEEE Transactions on Power Electronics*, vol. 29, no. 12, pp. 6421–6432, 2014.

[51] M. Amin and M. Molinas, Small-Signal Stability Assessment of Power Electronics Based Power Systems: A Discussion of Impedance- and Eigenvalue-Based Methods, *IEEE Transactions on Industry Applications*, vol. 53, no. 5, pp. 5014–5030, 2017.

[52] C. E. Ugalde-Loo, J. B. Ekanayake and N. Jenkins, State-Space Modeling of Wind Turbine Generators for Power System Studies, *IEEE Transactions on Industry Applications*, vol. 49, no. 1, pp. 223–232, 2013.

[53] A. Riccobono and E. Santi, Comprehensive Review of Stability Criteria for DC Power Distribution Systems, *IEEE Transactions on Industry Applications*, vol. 50, no. 5, pp. 3525–3535, 2014.

[54] A. H. Tan and K. R. Godfrey, *Industrial Process Identification*. Cham, Switzerland: Springer, 2019.

[55] T. Roinila, J. Huusari and M. Vilkko, On frequency-response measurements of power-electronic systems applying mimo identification techniques, *IEEE Transactions on Industrial Electronics*, vol. 60, no. 11, pp. 5270–5276, 2013.

[56] R. Pintelon and J. Schoukens, *System Identification - A Frequency Domain Approach*. New Jersey, US: Institute of Electrical and Electronics Engineers, Inc., 2001.

[57] P. Brenni, R. Galdi, F. Pietra *et al.*, From Volta onwards: A variety of electrical batteries in the Pavia Museum of Electrical Technology, in *Proc. IEEE History of Electro-Technology Conference*, 2012, 6 pages.

[58] J. L. Woodbridge, Application of storage batteries to regulation of alternating-current systems, in *Proc. American Institute of Electrical Engineers*, vol. 27, 1908, pp. 949–983.

[59] E. P. Roberts, Description of a Large Secondary Battery Plant for General Commercial Distribution, *Transactions of the American Institute of Electrical Engineers*, vol. II, no. 1, pp. 65–84, 1885.

[60] Y.-M. Chen, A. Q. Huang and X. Yu, A High Step-Up Three-Port DC-DC Converter for Stand-Alone PV/Battery Power Systems, *IEEE Transactions on Power Electronics*, vol. 28, no. 11, pp. 5049–5062, 2013.

[61] Z. Li, S. Hoshina, N. Satake *et al.*, Development of DC/DC Converter for Battery Energy Storage Supporting Railway DC Feeder Systems, *IEEE Transactions on Industry Applications*, vol. 52, no. 5, pp. 4218–4224, 2016.

[62] W. Qian, H. Cha, F. Z. Peng *et al.*, 55-kW Variable 3X DC-DC Converter for Plug-in Hybrid Electric Vehicles, *IEEE Transactions on Power Electronics*, vol. 27, no. 4, pp. 1668–1678, 2012.

[63] Z. Jin, L. Meng, J. M. Guerrero *et al.*, Hierarchical control design for a shipboard power system with dc distribution and energy storage aboard future more-electric ships, *IEEE Transactions on Industrial Informatics*, vol. 14, no. 2, pp. 703–714, 2018.

[64] H. Zhang, F. Mollet, C. Saudemont *et al.*, Experimental validation of energy storage system management strategies for a local dc distribution system of more electric aircraft, *IEEE Transactions on Industrial Electronics*, vol. 57, no. 12, pp. 3905–3916, 2010.

[65] F. Krismer and J. W. Kolar, Efficiency-Optimized High-Current Dual Active Bridge Converter for Automotive Applications, *IEEE Transactions on Industrial Electronics*, vol. 59, no. 7, pp. 2745–2760, 2012.

[66] R. T. Naayagi, A. J. Forsyth and R. Shuttleworth, High-Power Bidirectional DC-DC Converter for Aerospace Applications, *IEEE Transactions on Power Electronics*, vol. 27, no. 11, pp. 4366–4379, 2012.

[67] N. Jabbour and C. Mademlis, Improved Control Strategy of a Supercapacitor-Based Energy Recovery System for Elevator Applications, *IEEE Transactions on Power Electronics*, vol. 31, no. 12, pp. 8398–8408, 2016.

[68] T. K. Roy, M. A. Mahmud, A. M. T. Oo *et al.*, Nonlinear adaptive backstepping controller design for islanded dc microgrids, *IEEE Transactions on Industry Applications*, vol. 54, no. 3, pp. 2857–2873, 2018.

[69] Z. Zhang, O. C. Thomsen, M. A. E. Andersen *et al.*, Analysis and Design of Bidirectional DC-DC Converter in Extended Run Time DC UPS System Based on Fuel Cell and Supercapacitor, in *Proc. IEEE Applied Power Electronics Conference and Exposition*, 2009, pp. 714–719.

[70] X. Li and S. Wang, Energy management and operational control methods for grid battery energy storage systems, *CSEE Journal of Power and Energy Systems*, vol. 7, no. 5, pp. 1026–1040, 2021.

[71] S. Chiang, K. Chang and C. Yen, Residential photovoltaic energy storage system, *IEEE Transactions on Industrial Electronics*, vol. 45, no. 3, pp. 385–394, 1998.

[72] F. S. Al-Ismail, DC Microgrid Planning, Operation, and Control: A Comprehensive Review, *IEEE Access*, vol. 9, pp. 36154–36172, 2021.

[73] L. Roggia, L. Schuch, J. E. Baggio *et al.*, Integrated Full-Bridge-Forward DC-DC Converter for a Residential Microgrid Application, *IEEE Transactions on Power Electronics*, vol. 28, no. 4, pp. 1728–1740, 2013.

[74] B. Zhao, Q. Yu and W. Sun, Extended-Phase-Shift Control of Isolated Bidirectional DC-DC Converter for Power Distribution in Microgrid, *IEEE Transactions on Power Electronics*, vol. 27, no. 11, pp. 4667–4680, 2012.

[75] B. Guo, M. Niu, X. Lai *et al.*, Application research on large-scale battery energy storage system under Global Energy Interconnection framework, *Global Energy Interconnection*, vol. 1, no. 1, pp. 79–86, 2018.

[76] N. Kondrath, Bidirectional DC-DC converter topologies and control strategies for interfacing energy storage systems in microgrids: An overview, in *Proc. IEEE International Conference on Smart Energy Grid Engineering*, 2017, pp. 341–345.

[77] M. Kashif, Bidirectional flyback DC-DC converter for hybrid electric vehicle: Utility, working and PSPICE computer model, in *Proc. Asia Pacific Conference on Postgraduate Research in Microelectronics and Electronics*, 2012, pp. 61–66.

[78] A. Aboulnaga and A. Emadi, Performance evaluation of the isolated bidirectional Cuk converter with integrated magnetics, in *Proc. IEEE Annual Power Electronics Specialists Conference*, vol. 2, 2004, pp. 1557–1562.

[79] R. De Doncker, D. Divan and M. Kheraluwala, A three-phase soft-switched high-power-density DC/DC converter for high-power applications, *IEEE Transactions on Industry Applications*, vol. 27, no. 1, pp. 63–73, 1991.

[80] S. Shao, L. Chen, Z. Shan *et al.*, Modeling and Advanced Control of Dual-Active-Bridge DC-DC Converters: A Review, *IEEE Transactions on Power Electronics*, vol. 37, no. 2, pp. 1524–1547, 2022.

[81] M. Forouzesh, Y. P. Siwakoti, S. A. Gorji *et al.*, Step-Up DC-DC Converters: A Comprehensive Review of Voltage-Boosting Techniques, Topologies, and Applications, *IEEE Transactions on Power Electronics*, vol. 32, no. 12, pp. 9143–9178, 2017.

[82] Q. Xu, N. Vafamand, L. Chen *et al.*, Review on Advanced Control Technologies for Bidirectional DC/DC Converters in DC Microgrids, *IEEE Journal of Emerging and Selected Topics in Power Electronics*, vol. 9, no. 2, pp. 1205–1221, 2021.

[83] M. Yilmaz and P. T. Krein, Review of Battery Charger Topologies, Charging Power Levels, and Infrastructure for Plug-In Electric and Hybrid Vehicles, *IEEE Transactions on Power Electronics*, vol. 28, no. 5, pp. 2151–2169, 2013.

[84] V. M. Iyer, S. Gulur and S. Bhattacharya, Small-Signal Stability Assessment and Active Stabilization of a Bidirectional Battery Charger, *IEEE Transactions on Industry Applications*, vol. 55, no. 1, pp. 563–574, 2019.

[85] Y. Yao, F. Fassinou and T. Hu, Stability and Robust Regulation of Battery-Driven Boost Converter With Simple Feedback, *IEEE Transactions on Power Electronics*, vol. 26, no. 9, pp. 2614–2626, 2011.

[86] E. Figueres, G. Garcera, J. Sandia *et al.*, Sensitivity Study of the Dynamics of Three-Phase Photovoltaic Inverters With an LCL Grid Filter, *IEEE Transactions on Industrial Electronics*, vol. 56, no. 3, pp. 706–717, 2009.

[87] D. Venkatramanan and V. John, Dynamic Modeling and Analysis of Buck Converter Based Solar PV Charge Controller for Improved MPPT Performance, *IEEE Transactions on Industry Applications*, vol. 55, no. 6, pp. 6234–6246, 2019.

[88] S. Kurm and V. Agarwal, Dual Active Bridge Based Reduced Stage Multiport DC/AC Converter for PV-Battery Systems, *IEEE Transactions on Industry Applications*, vol. 58, no. 2, pp. 2341–2351, 2022.

[89] P. Xuewei and A. K. Rathore, Small-Signal Analysis of Naturally Commutated Current-Fed Dual Active Bridge Converter and Control Implementation Using Cypress PSoC, *IEEE Transactions on Vehicular Technology*, vol. 64, no. 11, pp. 4996–5005, 2015.

[90] T. L. Nguyen, G. Griepentrog and V. T. Phung, Modeling and control of dual active bridge converter with two control loops and output filter, in *Proc. Annual Conference of the IEEE Industrial Electronics Society*, 2017, pp. 4683–4689.

[91] R. D. Middlebrook, Input filter considerations in design and application of switching regulators, in *Proc. IEEE Industry Applications Society Annual Meeting*, Chicago, IL, USA, 1976, pp. 366–382.

[92] D. Wang, B. Nahid-Mobarakeh and A. Emadi, Second Harmonic Current Reduction for a Battery-Driven Grid Interface With Three-Phase Dual Active Bridge DC-DC Converter, *IEEE Transactions on Industrial Electronics*, vol. 66, no. 11, pp. 9056–9064, 2019.

[93] C. Wildrick, F. Lee, B. Cho *et al.*, A method of defining the load impedance specification for a stable distributed power system, *IEEE Transactions on Power Electronics*, vol. 10, no. 3, pp. 280–285, 1995.

[94] J.-S. Lee, G.-Y. Lee, S.-S. Park *et al.*, Impedance-Based Modeling and Common Bus Stability Enhancement Control Algorithm in DC Microgrid, *IEEE Access*, vol. 8, pp. 211224–211234, 2020.

[95] Y. Hu, S. Bu, B. Zhou *et al.*, Impedance-Based Oscillatory Stability Analysis of High Power Electronics-Penetrated Power Systems—A Survey, *IEEE Access*, vol. 7, pp. 120774–120787, 2019.

[96] M. Amin and M. Molinas, A Gray-Box Method for Stability and Controller Parameter Estimation in HVDC-Connected Wind Farms Based on Nonparametric Impedance, *IEEE Transactions on Industrial Electronics*, vol. 66, no. 3, pp. 1872–1882, 2019.

[97] X. Zhang, X. Ruan and C. K. Tse, Impedance-Based Local Stability Criterion for DC Distributed Power Systems, *IEEE Transactions on Circuits and Systems I: Regular Papers*, vol. 62, no. 3, pp. 916–925, 2015.

[98] A. Riccobono and E. Santi, A novel Passivity-Based Stability Criterion (PBSC) for switching converter DC distribution systems, in *Proc. Annual IEEE Applied Power Electronics Conference and Exposition*, 2012, pp. 2560–2567.

[99] J. Siegers, S. Arrua and E. Santi, Stabilizing Controller Design for Multibus MVdc Distribution Systems Using a Passivity-Based Stability Criterion and Positive Feedforward Control, *IEEE Journal of Emerging and Selected Topics in Power Electronics*, vol. 5, no. 1, pp. 14–27, 2017.

[100] M. Cespedes, L. Xing and J. Sun, Constant-Power Load System Stabilization by Passive Damping, *IEEE Transactions on Power Electronics*, vol. 26, no. 7, pp. 1832–1836, 2011.

[101] A. M. Rahimi and A. Emadi, Active Damping in DC/DC Power Electronic Converters: A Novel Method to Overcome the Problems of Constant Power Loads, *IEEE Transactions on Industrial Electronics*, vol. 56, no. 5, pp. 1428–1439, 2009.

[102] P. Magne, D. Marx, B. Nahid-Mobarakeh *et al.*, Large-Signal Stabilization of a DC-Link Supplying a Constant Power Load Using a Virtual Capacitor: Impact on the Domain of Attraction, *IEEE Transactions on Industry Applications*, vol. 48, no. 3, pp. 878–887, 2012.

[103] S. Liu, P. Su and L. Zhang, A Virtual Negative Inductor Stabilizing Strategy for DC Microgrid With Constant Power Loads, *IEEE Access*, vol. 6, pp. 59728–59741, 2018.

[104] X. Zhang, X. Ruan and Q.-C. Zhong, Improving the Stability of Cascaded DC/DC Converter Systems via Shaping the Input Impedance of the Load Converter With a Parallel or Series Virtual Impedance, *IEEE Transactions on Industrial Electronics*, vol. 62, no. 12, pp. 7499–7512, 2015.

[105] P. Yang, M. Yu, Q. Wu *et al.*, Decentralized Bidirectional Voltage Supporting Control for Multi-Mode Hybrid AC/DC Microgrid, *IEEE Transactions on Smart Grid*, vol. 11, no. 3, pp. 2615–2626, 2020.

[106] J. He, L. Du, B. Liang *et al.*, A Coupled Virtual Impedance for Parallel AC/DC Converter Based Power Electronics System, *IEEE Transactions on Smart Grid*, vol. 10, no. 3, pp. 3387–3400, 2019.

[107] M. Kanzian, H. Gietler, C. Unterrieder *et al.*, Low-Complexity State-Space-Based System Identification and Controller Auto-Tuning Method for Multi-Phase DC-DC Converters, *IEEE Transactions on Industry Applications*, vol. 55, no. 2, pp. 2076–2087, 2019.

[108] H. Abdollahi, S. Arrua, T. Roinila *et al.*, A Novel DC Power Distribution System Stabilization Method Based on Adaptive Resonance-Enhanced Voltage Controller, *IEEE Transactions on Industrial Electronics*, vol. 66, no. 7, pp. 5653–5662, 2019.

[109] J. Siegers, S. Arrua and E. Santi, Allowable bus impedance region for MVDC distribution systems and stabilizing controller design using positive feed-forward control, in *Proc. IEEE Energy Conversion Congress and Exposition*, 2016, 8 pages.

[110] A. S. Morched and P. Kundur, Identification and Modelling of Load Characteristics at High Frequencies, *IEEE Transactions on Power Systems*, vol. 2, no. 1, pp. 153–159, 1987.

[111] P. Aronhime and G. Cecil, A new method of capacitance measurement, in *Proc. Midwest Symposium on Circuits and Systems*, vol. 1, 1992, pp. 718–721.

[112] M. Harris, A. Kelley, J. Rhode *et al.*, Instrumentation for measurement of line impedance, in *Proc. IEEE Applied Power Electronics Conference and Exposition*, vol. 2, 1994, pp. 887–893.

[113] W. Evans, The design of a multi-sine LCR component meter, in *Proc. IEE Colloquium on Digital Signal Processing in Instrumentation*, 1992, 11 pages.

[114] B. Palethorpe, M. Sumner and D. Thomas, Power system impedance measurement using a power electronic converter, in *Proc. International Conference on Harmonics and Quality of Power*, vol. 1, 2000, pp. 208–213.

[115] K. Yomura, T. Kato and K. Inoue, Versatile measurement method for three-phase impedance in a two-phase domain, in *Proc. IEEE Workshop on Control and Modelling of Power Electronics*, 2021, 6 pages.

[116] P. Pan, H. Hu, X. Yang *et al.*, Impedance measurement of traction network and electric train for stability analysis in high-speed railways, *IEEE Transactions on Power Electronics*, vol. 33, no. 12, pp. 10086–10100, 2018.

[117] A. Riccobono, M. Mirz and A. Monti, Noninvasive Online Parametric Identification of Three-Phase AC Power Impedances to Assess the Stability of Grid-Tied Power Electronic Inverters in LV Networks, *IEEE Journal of Emerging and Selected Topics in Power Electronics*, vol. 6, no. 2, pp. 629–647, 2018.

[118] H. Gong, D. Yang and X. Wang, Parametric Identification of DQ Impedance Model for Three-Phase Voltage-Source Converters, in *Proc. IEEE International Power Electronics and Application Conference and Exposition*, 2018, 6 pages.

[119] R. Luhtala, T. Roinila and T. Messo, Implementation of Real-Time Impedance-Based Stability Assessment of Grid-Connected Systems Using MIMO-Identification Techniques, *IEEE Transactions on Industry Applications*, vol. 54, no. 5, pp. 5054–5063, 2018.

[120] R. Luhtala, Real-time identification and adaptive control of grid-connected three-phase inverters, Ph.D. dissertation, Tampere, Finland, 2020.

[121] T. Roinila, T. Messo and E. Santi, Mimo-identification techniques for rapid impedance-based stability assessment of three-phase systems in dq domain, *IEEE Transactions on Power Electronics*, vol. 33, no. 5, pp. 4015–4022, 2018.

[122] T. Roinila, H. Abdollahi, S. Arrua *et al.*, Real-Time Stability Analysis and Control of Multiconverter Systems by Using MIMO-Identification Techniques, *IEEE Transactions on Power Electronics*, vol. 34, no. 4, pp. 3948–3957, 2019.

[123] S. Skogestad and I. Postlethwaite, *Multivariable feedback control: Analysis and Design*. West Sussex, England: John Wiley & Sons Ltd, 1996.

[124] G. Liu, P. Mattavelli and S. Saggini, Design of droop controllers for converters in dc microgrids towards reducing bus capacitance, in *Proc. European Conference on Power Electronics and Applications*, 2018, 9 pages.

[125] H. H. Rosenbrock, *State-Space and Multivariable Theory*. Nelson, 1970.

[126] I. Alhurayyis, A. Elkhateb and J. Morrow, Isolated and nonisolated dc-to-dc converters for medium-voltage dc networks: A review, *IEEE Journal of Emerging and Selected Topics in Power Electronics*, vol. 9, no. 6, pp. 7486–7500, 2021.

[127] T. Suntio, T. Messo and J. Puukko, *Power Electronic Converters: Dynamics and Control in Conventional and Renewable Energy Applications*. Weinheim, Germany: Wiley, 2017.

[128] H. Bai and C. Mi, Eliminate reactive power and increase system efficiency of isolated bidirectional dual-active-bridge dc-dc converters using novel dual-phase-shift control, *IEEE Transactions on Power Electronics*, vol. 23, no. 6, pp. 2905–2914, 2008.

[129] F. Krismer and J. W. Kolar, Closed form solution for minimum conduction loss modulation of dab converters, *IEEE Transactions on Power Electronics*, vol. 27, no. 1, pp. 174–188, 2012.

[130] F. Krismer, Modeling and optimization of bidirectional dual active bridge dc-dc converter topologies, Ph.D. dissertation, Zürich, Switzerland, 2010.

[131] M. Jafari, Z. Malekjamshidi and J. G. Zhu, Analysis of operation modes and limitations of dual active bridge phase shift converter, in *Proc. IEEE International Conference on Power Electronics and Drive Systems*, 2015, pp. 393–398.

[132] H. Shi, K. Sun, H. Wu *et al.*, A unified state-space modeling method for a phase-shift controlled bidirectional dual-active half-bridge converter, *IEEE Transactions on Power Electronics*, vol. 35, no. 3, pp. 3254–3265, 2020.

[133] B. Zhao, Q. Song, W. Liu *et al.*, Dead-time effect of the high-frequency isolated bidirectional full-bridge dc-dc converter: Comprehensive theoretical analysis and experimental verification, *IEEE Transactions on Power Electronics*, vol. 29, no. 4, pp. 1667–1680, 2014.

[134] M. Berg, Deadtime effect and impedance coupling in dynamic analysis of grid-connected inverters, Ph.D. dissertation, Tampere, Finland, 2021.

[135] K. Takagi and H. Fujita, Dynamic control and dead-time compensation method of an isolated dual-active-bridge dc-dc converter, in *Proc. European Conference on Power Electronics and Applications*, 2015, 10 pages.

[136] C. Song, A. Chen, J. Chen *et al.*, Dead-time effect analysis of dual active bridge dc-dc converter with dual-phase-shift control, in *Proc. Chinese Automation Congress*, 2017, pp. 6545–6550.

[137] J.-i. Itoh, K. Kawauchi and H. Watanabe, Non-linear dead-time error compensation method of dual active bridge dc-dc converter for variable dc-bus voltage, in *Proc. International Conference on Smart Grid*, 2018, pp. 208–213.

[138] S. Luo, F. Wu and G. Wang, Effect of dead band and transient actions on ctps modulation for dab dc-dc converter and solutions, *IEEE Transactions on Transportation Electrification*, vol. 7, no. 3, pp. 949–957, 2021.

[139] T. Messo, J. Jokipii, J. Puukko *et al.*, Determining the value of dc-link capacitance to ensure stable operation of a three-phase photovoltaic inverter, *IEEE Transactions on Power Electronics*, vol. 29, no. 2, pp. 665–673, 2014.

[140] J. Puukko and T. Suntio, Modelling the effect of non-ideal load in three-phase converter dynamics, *Electronics Letters*, vol. 48, no. 7, pp. 402–404, 2012.

[141] J. Schoukens, K. Godfrey and M. Schoukens, Nonparametric Data-Driven Modeling of Linear Systems: Estimating the Frequency Response and Impulse Response Function, *IEEE Control Systems Magazine*, vol. 38, no. 4, pp. 49–88, 2018.

[142] K. Godfrey, *Perturbation Signals for System Identification*. Hemel Hempstead, UK: Prentice Hall, 1993.

[143] C. Fernandez, L. Ortega, M. Granda *et al.*, Online impedance measurement of the batteries and loads connected to a modular multi-active bridge converter, in *Proc. IEEE Workshop on Control and Modeling for Power Electronics*, 2019, 6 pages.

[144] T. Roinila, T. Messo, R. Luhtala *et al.*, Hardware-in-the-loop methods for real-time frequency-response measurements of on-board power distribution systems, *IEEE Transactions on Industrial Electronics*, vol. 66, no. 7, pp. 5769–5777, 2019.

[145] W. Davies, Using the binary maximum length sequence for the identification of system dynamics, *Proceedings of the Institution of Electrical Engineers*, vol. 114, no. 10, pp. 1582–1584, 1967.

[146] R. Luhtala, H. Alenius, T. Messo *et al.*, Online frequency response measurements of grid-connected systems in presence of grid harmonics and unbalance, *IEEE Transactions on Power Electronics*, vol. 35, no. 4, pp. 3343–3347, 2020.

[147] A. Ziani and A. Medouri, Analysis of different pseudo-random and orthogonal spreading sequences in ds-cdma, *International Conference on Multimedia Computing and Systems*, 2012, 558–564.

[148] T. Roinila, M. Vilkko and T. Suntio, Frequency-response measurement of switched-mode power supplies in the presence of nonlinear distortions, *IEEE Transactions on Power Electronics*, vol. 25, no. 8, 2179–2187, 2010.

[149] E. Shoubaki, S. Essakiappan, M. Manjrekar *et al.*, Synthetic inertia for bess integrated on the dc-link of grid-tied pv inverters, in *Proc. IEEE International Symposium on Power Electronics for Distributed Generation Systems*, 2017, 5 pages.

[150] D. N. Zmood and D. G. Holmes, Stationary frame current regulation of pwm inverters with zero steady-state error, *IEEE Transactions on Power Electronics*, vol. 18, no. 3, pp. 814–822, 2003.

A

The source-affected inverter dynamics of a PV-inverter with a BESS were derived in Chapter 3.1 and can be given as

$$\begin{bmatrix} v_{\text{in}}^{\text{inv}} \\ i_{\text{o-d}}^{\text{inv}} \\ i_{\text{o-q}}^{\text{inv}} \end{bmatrix} = \frac{1}{\sigma} \begin{bmatrix} Z_{\text{pv-in}}^{\text{inv-S}} & G_{\text{bess-in}}^{\text{inv-S}} & T_{\text{oi-d}}^{\text{inv-S}} & T_{\text{oi-q}}^{\text{inv-S}} & G_{\text{ci-d}}^{\text{inv-S}} & G_{\text{ci-q}}^{\text{inv-S}} \\ G_{\text{pv-io-d}}^{\text{inv-S}} & G_{\text{bess-io-d}}^{\text{inv-S}} & -Y_{\text{o-d}}^{\text{inv-S}} & G_{\text{cr-qd}}^{\text{inv-S}} & G_{\text{co-d}}^{\text{inv-S}} & G_{\text{co-qd}}^{\text{inv-S}} \\ G_{\text{pv-io-q}}^{\text{inv-S}} & G_{\text{bess-io-q}}^{\text{inv-S}} & G_{\text{cr-dq}}^{\text{inv-S}} & -Y_{\text{o-q}}^{\text{inv-S}} & G_{\text{co-dq}}^{\text{inv-S}} & G_{\text{co-q}}^{\text{inv-S}} \end{bmatrix} \begin{bmatrix} i_{\text{in}}^{\text{pv}} \\ v_{\text{in}}^{\text{bess}} \\ v_{\text{o-d}}^{\text{inv}} \\ v_{\text{o-q}}^{\text{inv}} \\ d_{\text{d}}^{\text{inv}} \\ d_{\text{q}}^{\text{inv}} \end{bmatrix} \tag{A.1}$$

$$= \frac{1}{\sigma} \begin{bmatrix} \mathbf{Z}_{\text{in-1x2}}^{\text{inv-S}} & \mathbf{T}_{\text{oi-1x2}}^{\text{inv-S}} & \mathbf{G}_{\text{ci-1x2}}^{\text{inv-S}} \\ \mathbf{G}_{\text{io-2x2}}^{\text{inv-S}} & \mathbf{Y}_{\text{o-2x2}}^{\text{inv-S}} & \mathbf{G}_{\text{co-2x2}}^{\text{inv-S}} \end{bmatrix} \begin{bmatrix} i_{\text{in}}^{\text{pv}} \\ v_{\text{in}}^{\text{bess}} \\ v_{\text{o-d}}^{\text{inv}} \\ v_{\text{o-q}}^{\text{inv}} \\ d_{\text{d}}^{\text{inv}} \\ d_{\text{q}}^{\text{inv}} \end{bmatrix},$$

where the matrix variables are derived as

$$\mathbf{Z}_{\text{in-1x2}}^{\text{inv-S}} = \begin{bmatrix} Z_{\text{in}}^{\text{inv}} & G_{\text{io-c}}^{\text{inv}} Z_{\text{in}}^{\text{inv}} \end{bmatrix}, \tag{A.2}$$

$$\mathbf{T}_{\text{oi-1x2}}^{\text{inv-S}} = \begin{bmatrix} T_{\text{oi-d}}^{\text{inv}} & T_{\text{oi-q}}^{\text{inv}} \end{bmatrix}, \tag{A.3}$$

$$\mathbf{G}_{\text{ci-1x2}}^{\text{inv-S}} = \begin{bmatrix} G_{\text{ci-d}}^{\text{inv}} & G_{\text{ci-q}}^{\text{inv}} \end{bmatrix}, \tag{A.4}$$

$$\mathbf{G}_{\text{io-2x2}}^{\text{inv-S}} = \begin{bmatrix} G_{\text{io-d}}^{\text{inv}} & G_{\text{io-c}}^{\text{bess}} G_{\text{io-d}}^{\text{inv}} \\ G_{\text{io-q}}^{\text{inv}} & G_{\text{io-c}}^{\text{bess}} G_{\text{io-q}}^{\text{inv}} \end{bmatrix}, \tag{A.5}$$

$$\mathbf{Y}_{\text{o-2x2}}^{\text{inv-S}} = \begin{bmatrix} -\left(Y_{\text{o-d}}^{\text{inv}}\sigma + G_{\text{io-d}}^{\text{inv}} T_{\text{oi-d}}^{\text{inv}} Y_{\text{o}}^{\text{S}}\right) & Y_{\text{o-qd}}^{\text{inv}}\sigma + G_{\text{io-d}}^{\text{inv}} T_{\text{oi-q}}^{\text{inv}} Y_{\text{o}}^{\text{S}} \\ Y_{\text{o-dq}}^{\text{inv}}\sigma + G_{\text{io-q}}^{\text{inv}} T_{\text{oi-d}}^{\text{inv}} Y_{\text{o}}^{\text{S}} & -\left(Y_{\text{o-q}}^{\text{inv}}\sigma + G_{\text{io-q}}^{\text{inv}} T_{\text{oi-q}}^{\text{inv}} Y_{\text{o}}^{\text{S}}\right) \end{bmatrix}, \tag{A.6}$$

$$\mathbf{G}_{\text{co-2x2}}^{\text{inv-S}} = \begin{bmatrix} G_{\text{co-d}}^{\text{inv}}\sigma - G_{\text{io-d}}^{\text{inv}} G_{\text{ci-d}}^{\text{inv}} Y_{\text{o}}^{\text{S}} & G_{\text{co-qd}}^{\text{inv}}\sigma - G_{\text{io-d}}^{\text{inv}} G_{\text{ci-q}}^{\text{inv}} Y_{\text{o}}^{\text{S}} \\ G_{\text{co-dq}}^{\text{inv}}\sigma - G_{\text{io-q}}^{\text{inv}} G_{\text{ci-d}}^{\text{inv}} Y_{\text{o}}^{\text{S}} & G_{\text{co-q}}^{\text{inv}}\sigma - G_{\text{io-q}}^{\text{inv}} G_{\text{ci-q}}^{\text{inv}} Y_{\text{o}}^{\text{S}} \end{bmatrix}, \tag{A.7}$$

and where

$$Y_{\text{o}}^{\text{S}} = Y_{\text{pv}} + Y_{\text{o-c}}^{\text{bess}}, \tag{A.8}$$

$$\sigma = 1 + Z_{\text{in}}^{\text{inv}} Y_{\text{o}}^{\text{S}}. \tag{A.9}$$

PUBLICATIONS

PUBLICATION

I

Complete Small-Signal Model of Three-Phase Photovoltaic Inverter Considering the Source and Load Effects

R.-M. Sallinen, A. Aapro, M. Berg, and T. Messo

in *Proc. Annual Conference of the IEEE Industrial Electronics Society*, pp. 2237–2244, 2018.

Complete Small-Signal Model of Three-Phase Photovoltaic Inverter Considering the Source and Load Effects

Roosa-Maria Sallinen, Aapo Aapro, Matias Berg, Tuomas Messo
Laboratory of Electrical Energy Engineering,
Tampere University of Technology, Tampere, Finland
Email: roosa-maria.sallinen@tut.fi, aapo.aapro@gmail.com, matias.berg@tut.fi, tuomas.messo@tut.fi

***Abstract*—The amount of photovoltaic inverters connected to the electrical grid is increasing. In order to control the power fed to the grid, the inverter must be controlled, and many different approaches for small-signal modeling have been proposed to facilitate the controller design. However, a solar panel cannot be modeled by an ideal current source and the photovoltaic inverter is not connected to an ideal grid on the load side. This paper proposes a generalized method to include the load and source effects to the dynamic model of a photovoltaic inverter. The method can be used to include the source impedance of the photovoltaic generator and impedance of the distribution line in the small-signal model of the photovoltaic inverter.**

I. Introduction

Renewable energy is revolutionizing the energy production by becoming more and more competitive in terms of price and small environmental effect [1], [2]. Accordingly, the amount of grid-connected inverters is increasing to ramp-up the share of renewable energy in the power system. Three-phase inverters are commonly selected for the power conversion due to their good and well-known performance [3], [4].

However, as a result, the power generation becomes more and more scattered due to the distributed nature of the renewable energy production, and the grid is constructed by various subsystems exhibiting different impedance characteristics depending on the topology of the grid [5]. Generally, a grid with high impedance is considered a weak grid if its short circuit ratio (SCR) is smaller than 10 [6]. This finite grid impedance may cause stability issues in photovoltaic (PV) power plants, such as, harmonic resonances and instability [7]. In order to analyze these phenomena, accurate mathematical models are necessary, which capture the internal dynamic behavior of the converters.

Small-signal modeling is widely utilized to perform reliable and deterministic control design of three-phase power inverters [8]–[12]. Moreover, recent interest toward impedance-based stability analysis has encouraged research on the output impedance characteristics and impedance shaping [5], [13]–[17]. Generally, non-ideal sources and loads affect the formulation of small-signal models by changing the internal behavior (e.g., control performance) of the inverter profoundly [18]. Analysis on the effect of source and load subsystems is always required when connecting the converter power stage to a non-ideal source or load. Practically, this is always the case and, therefore, the inverter cannot be analyzed separately from the source or load dynamics.

Although literature exists around the topic of small-signal modeling with PV and weak grid, the literature partly lacks the full-order or accurate representation of the system dynamics with both source and load subsystems. For example, small-signal modeling of grid-connected PV system was presented in [10], which characterized only the control dynamics of the converter. Similar small-signal analysis was performed in [19], [20], which both lacked the recognition of the effect of a PV generator (PVG) on the system dynamics. Also, no transfer functions in the frequency domain were presented in the paper in [19]. Small-signal analysis was also performed in [8] and [21], yet system transfer functions were not presented and only the time-domain behavior was analyzed. Reduced-order model with load-effect is presented in [18], where all the cross-couplings and dynamics related to q-components are neglected. Thus, the model gives over-simplified and inaccurate results, when the inverter does not operate at unity power factor or the effect of cross-couplings is significant. In [22], the full-order dynamical assessment of all system dynamics were not presented as it concentrated on the proper stability evaluation of the output interface, i.e., only the impedances were analyzed. Thus, the assessment of the load impedance e.g. on the control design was not presented.

Considering the aforementioned factors, this paper presents the full-order small-signal model which can be used to assess the effect of an arbitrary non-ideal current-type source (e.g. PV generator or PV generator with a boost converter) as well as a voltage-type load (e.g. utility grid or grid-forming inverter) on the inverter dynamics in the dq-domain. The model is developed with the multiple-input-multiple-output modeling technique lacked e.g. in [10], [18], [19], [23], which simplifies significantly the derivation of the closed-loop model and improves accuracy of the model [9]. The main contribution of this paper is the full-order small-signal model which considers both the load and source effects. Furthermore, the accuracy of the model is verified from a switching model as well as HIL simulations.

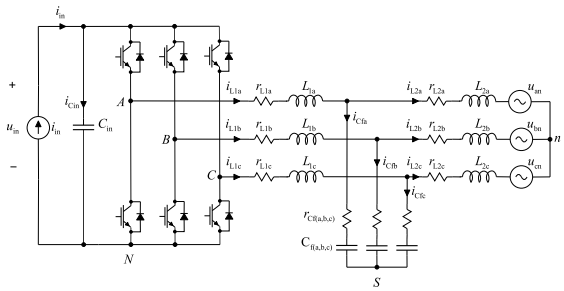

Fig. 1. Power stage of a three-phase grid-connected PV inverter.

II. Small-Signal Modeling

The power stage of a typical grid connected photovoltaic inverter is shown in Fig. 1. By performing averaging and linearization according to technique developed by Middlebrook [24], the linearized state space can be given as in (4). Note that the state matrices **A**, **B**, **C**, and **D** are given in Appendix A. The state variable, input variable, and output variable vectors are defined as (1), (2), and (3), respectively.

$$\begin{aligned}\mathbf{X}(s) &= \left[\hat{i}_{\mathrm{L1d}}, \hat{i}_{\mathrm{L1q}}, \hat{i}_{\mathrm{L2d}}, \hat{i}_{\mathrm{L2q}}, \hat{u}_{\mathrm{Cd}}, \hat{u}_{\mathrm{Cq}}, \hat{u}_{\mathrm{Cin}}\right]^{\mathrm{T}} \\ &= \left[\underline{\hat{i}}_{\mathrm{L1}}, \underline{\hat{i}}_{\mathrm{L2}}, \underline{\hat{u}}_{\mathrm{C}}, \hat{u}_{\mathrm{Cin}}\right]^{\mathrm{T}} \end{aligned} \tag{1}$$

$$\mathbf{U}(s) = \left[\hat{i}_{\mathrm{in}}, \hat{u}_{\mathrm{od}}, \hat{u}_{\mathrm{oq}}, \hat{d}_{\mathrm{d}}, \hat{d}_{\mathrm{q}}\right]^{\mathrm{T}} = \left[\hat{i}_{\mathrm{in}}, \underline{\hat{u}}_{\mathrm{o}}, \underline{\hat{d}}\right]^{\mathrm{T}} \tag{2}$$

$$\mathbf{Y}(s) = \left[\hat{u}_{\mathrm{in}}, \hat{i}_{\mathrm{L1d}}, \hat{i}_{\mathrm{L1q}}, \hat{i}_{\mathrm{L2d}}, \hat{i}_{\mathrm{L2q}}\right]^{\mathrm{T}} = \left[\hat{u}_{\mathrm{in}}, \underline{\hat{i}}_{\mathrm{L1}}, \underline{\hat{i}}_{\mathrm{L2}}\right]^{\mathrm{T}} \tag{3}$$

$$\begin{aligned} s\mathbf{X}(s) &= \mathbf{A}\mathbf{X}(s) + \mathbf{B}\mathbf{U}(s) \\ \mathbf{Y}(s) &= \mathbf{C}\mathbf{X}(s) + \mathbf{D}\mathbf{U}(s). \end{aligned} \tag{4}$$

With minor algebraic manipulation, the equation above can be rearranged and solved with respect to the input and output variables as in (5) and (6).

$$\mathbf{Y}(s) = \left[\mathbf{C}(s\mathbf{I} - \mathbf{A})^{-1}\mathbf{B} + \mathbf{D}\right]\mathbf{U}(s) = \mathbf{G}_{\mathrm{H}}\mathbf{U}(s) \tag{5}$$

$$\mathbf{G}_{\mathrm{H}} = \begin{bmatrix} Z_{\mathrm{in}} & \mathbf{T}_{\mathrm{oi}} & \mathbf{G}_{\mathrm{ci}} \\ \mathbf{G}_{\mathrm{ioL}} & \mathbf{G}_{\mathrm{oL}} & \mathbf{G}_{\mathrm{cL}} \\ \mathbf{G}_{\mathrm{io}} & -\mathbf{Y}_{\mathrm{o}} & \mathbf{G}_{\mathrm{co}} \end{bmatrix} \tag{6}$$

Hence, by selecting the inverter-side inductor current $\underline{\hat{i}}_{\mathrm{L1}}$ as the controlled output current, the control-block diagram of the system can be given as in Fig. 2. Considering the cascaded control structure required by PV applications [23], the DC-link voltage $\hat{u}_{\mathrm{o}}$ is treated as another controlled variable. Matrices $\mathbf{G}_{\mathrm{vc}}$ and $\mathbf{G}_{\mathrm{cc}}$ depict the voltage and current controllers, respectively, $\mathbf{G}_{\mathrm{del}}$ represents the system delays, $\mathbf{G}_{\mathrm{se}}$ the voltage sensing gains, and matrix $\mathbf{G}_{\mathrm{PLL}}$ contains the PLL transfer functions which are defined in Appendix B. Matrices $\mathbf{D}$ and $\mathbf{I}_{\mathrm{L1}}$ are gains for the steady state duty-ratio and inductor current.

According to the control-block diagrams and the transfer function matrix in (6), the complete closed-loop dynamics

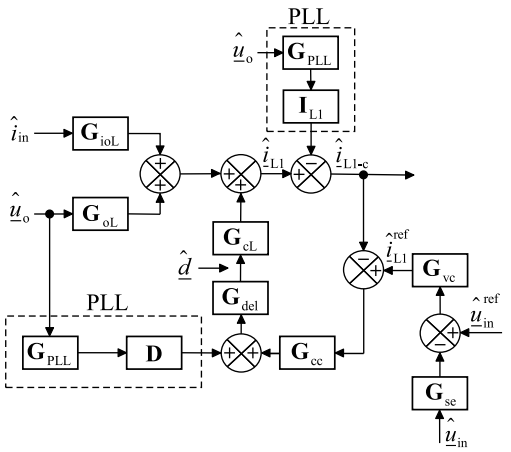

Fig. 2. Closed-loop control block diagram of a three-phase grid-connected VSI-based inverter.

for the converter can be given as in (7)-(15), where $\mathbf{L}_{\mathrm{in}} = \mathbf{G}_{\mathrm{ci}}^{\mathrm{out}}\mathbf{G}_{\mathrm{vc}}$ depicts the DC-link voltage control loop gain. Note that the transfer functions with the superscript 'out' denote that only the current control loops (i.e. the inner control loops of the cascaded control scheme) are connected, and they can be found in Appendix B. In the equations below, Eqs. (7)-(9) represent the input-voltage dynamics, Eqs. (10)-(12) are the inverter-side current dynamics, and (13)-(15) are the grid-current dynamics.

$$Z_{\mathrm{in}}^{\mathrm{tot}} = (\mathbf{I} + \mathbf{L}_{\mathrm{in}})^{-1} Z_{\mathrm{in}}^{\mathrm{out}} \tag{7}$$

$$\mathbf{T}_{\mathrm{oi}}^{\mathrm{tot}} = (\mathbf{I} + \mathbf{L}_{\mathrm{in}})^{-1} \mathbf{T}_{\mathrm{oi}}^{\mathrm{out}} \tag{8}$$

$$\mathbf{G}_{\mathrm{ci}}^{\mathrm{tot}} = (\mathbf{I} + \mathbf{L}_{\mathrm{in}})^{-1} \mathbf{L}_{\mathrm{in}} \tag{9}$$

$$\mathbf{G}_{\mathrm{ioL}}^{\mathrm{tot}} = \mathbf{G}_{\mathrm{ioL}}^{\mathrm{out}} - \mathbf{G}_{\mathrm{cL}}^{\mathrm{out}}\mathbf{G}_{\mathrm{vc}}(\mathbf{I} + \mathbf{L}_{\mathrm{in}})^{-1} Z_{\mathrm{in}}^{\mathrm{out}} \tag{10}$$

$$\mathbf{G}_{\mathrm{oL}}^{\mathrm{tot}} = \mathbf{G}_{\mathrm{oL}}^{\mathrm{out}} - \mathbf{G}_{\mathrm{cL}}^{\mathrm{out}}\mathbf{G}_{\mathrm{vc}}(\mathbf{I} + \mathbf{L}_{\mathrm{in}})^{-1} \mathbf{T}_{\mathrm{oi}}^{\mathrm{out}} \tag{11}$$

$$\mathbf{G}_{\mathrm{cL}}^{\mathrm{tot}} = -\mathbf{G}_{\mathrm{cL}}^{\mathrm{out}}\left[\mathbf{G}_{\mathrm{vc}}(\mathbf{I} + \mathbf{L}_{\mathrm{in}})^{-1}\mathbf{L}_{\mathrm{in}} - \mathbf{G}_{\mathrm{vc}}\right] \tag{12}$$

$$\mathbf{G}_{\mathrm{io}}^{\mathrm{tot}} = \mathbf{G}_{\mathrm{io}}^{\mathrm{out}} - \mathbf{G}_{\mathrm{co}}^{\mathrm{out}}\mathbf{G}_{\mathrm{vc}}(\mathbf{I} + \mathbf{L}_{\mathrm{in}})^{-1} Z_{\mathrm{in}}^{\mathrm{out}} \tag{13}$$

$$\mathbf{Y}_{\mathrm{o}}^{\mathrm{tot}} = \mathbf{Y}_{\mathrm{o}}^{\mathrm{out}} + \mathbf{G}_{\mathrm{co}}^{\mathrm{out}}\mathbf{G}_{\mathrm{vc}}(\mathbf{I} + \mathbf{L}_{\mathrm{in}})^{-1} \mathbf{T}_{\mathrm{oi}}^{\mathrm{out}} \tag{14}$$

$$\mathbf{G}_{\mathrm{co}}^{\mathrm{tot}} = -\mathbf{G}_{\mathrm{co}}^{\mathrm{out}}\left[\mathbf{G}_{\mathrm{vc}}(\mathbf{I} + \mathbf{L}_{\mathrm{in}})^{-1}\mathbf{L}_{\mathrm{in}} - \mathbf{G}_{\mathrm{vc}}\right] \tag{15}$$

Above equations determine the closed-loop dynamics of the grid-connected converter with ideal current source and voltage load (i.e., zero impedance). Next sections present the multivariable modeling procedure and analysis of both source- and load-affected small-signal models.

III. Source-affected system dynamics

Photovoltaic generator induces varying dynamical resistance (r_{pv}) connected across the input terminal of the converter. This has to be considered in the dynamical model in order to analyze the converter dynamics correctly [23]. As shown in Fig. 3, a non-ideal source with finite admittance Y_{s} is assumed here, which can be included in the open-loop dynamics of the system. Accordingly, the real input current ($\hat{i}_{\mathrm{in}}$) of the converter is affected by the non-ideal source current $\hat{i}_{\mathrm{inS}}$ as well as the parallel admittance Y_{s} and can be expressed as

$$\hat{i}_{\mathrm{in}} = \hat{i}_{\mathrm{inS}} - Y_{\mathrm{s}}\hat{u}_{\mathrm{in}}. \tag{16}$$

Consequently, the input voltage dynamics can be presented by substituting (16) into the nominal open-loop input voltage dynamics as

$$\hat{u}_{\mathrm{in}} = Z_{\mathrm{in}}\left(\hat{i}_{\mathrm{inS}} - Y_{\mathrm{s}}\hat{u}_{\mathrm{in}}\right) + \mathbf{T}_{\mathrm{oi}}\underline{\hat{u}}_{\mathrm{o}} + \mathbf{G}_{\mathrm{ci}}\underline{\hat{d}}, \tag{17}$$

$$\hat{u}_{\mathrm{in}} = \frac{Z_{\mathrm{in}}}{1+Z_{\mathrm{in}}Y_{\mathrm{s}}}\hat{i}_{\mathrm{inS}} + \frac{\mathbf{T}_{\mathrm{oi}}}{1+Z_{\mathrm{in}}Y_{\mathrm{s}}}\underline{\hat{u}}_{\mathrm{o}} + \frac{\mathbf{G}_{\mathrm{ci}}}{1+Z_{\mathrm{in}}Y_{\mathrm{s}}}\underline{\hat{d}}.$$

The source-affected input current can be expressed as in (18), which is then substituted into the open-loop dynamics of the inverter and grid currents.

$$\hat{i}_{\mathrm{in}} = \left(1 - \frac{Z_{\mathrm{in}}Y_{\mathrm{s}}}{1+Z_{\mathrm{in}}Y_{\mathrm{s}}}\right)\hat{i}_{\mathrm{inS}} - \frac{Y_{\mathrm{s}}\mathbf{T}_{\mathrm{oi}}}{1+Z_{\mathrm{in}}Y_{\mathrm{s}}}\underline{\hat{u}}_{\mathrm{o}} - \frac{Y_{\mathrm{s}}\mathbf{G}_{\mathrm{ci}}}{1+Z_{\mathrm{in}}Y_{\mathrm{s}}}\underline{\hat{d}}. \tag{18}$$

Accordingly, the source-affected dynamics for input voltage, inductor current, and grid current can be given by

$$\hat{u}_{\mathrm{in}} = \frac{Z_{\mathrm{in}}}{1+Z_{\mathrm{in}}Y_{\mathrm{s}}}\hat{i}_{\mathrm{inS}} + \frac{\mathbf{T}_{\mathrm{oi}}}{1+Z_{\mathrm{in}}Y_{\mathrm{s}}}\underline{\hat{u}}_{\mathrm{o}} + \frac{\mathbf{G}_{\mathrm{ci}}}{1+Z_{\mathrm{in}}Y_{\mathrm{s}}}\underline{\hat{d}}, \tag{19}$$

$$\begin{aligned}\underline{\hat{i}}_{\mathrm{L1}} = {} & \mathbf{G}_{\mathrm{ioL}}\left(1 - \frac{Z_{\mathrm{in}}Y_{\mathrm{s}}}{1+Z_{\mathrm{in}}Y_{\mathrm{s}}}\right)\hat{i}_{\mathrm{inS}} \\ & + \left(\mathbf{G}_{\mathrm{oL}} - \mathbf{G}_{\mathrm{ioL}}\frac{Y_{\mathrm{s}}\mathbf{T}_{\mathrm{oi}}}{1+Z_{\mathrm{in}}Y_{\mathrm{s}}}\right)\underline{\hat{u}}_{\mathrm{o}} \\ & + \left(\mathbf{G}_{\mathrm{cL}} - \mathbf{G}_{\mathrm{ioL}}\frac{Y_{\mathrm{s}}\mathbf{G}_{\mathrm{ci}}}{1+Z_{\mathrm{in}}Y_{\mathrm{s}}}\right)\underline{\hat{d}},\end{aligned} \tag{20}$$

$$\begin{aligned}\underline{\hat{i}}_{\mathrm{L2}} = {} & \mathbf{G}_{\mathrm{io}}\left(1 - \frac{Z_{\mathrm{in}}Y_{\mathrm{s}}}{1+Z_{\mathrm{in}}Y_{\mathrm{s}}}\right)\hat{i}_{\mathrm{inS}} \\ & - \left(\mathbf{Y}_{\mathrm{o}} - \mathbf{G}_{\mathrm{io}}\frac{Y_{\mathrm{s}}\mathbf{T}_{\mathrm{oi}}}{1+Z_{\mathrm{in}}Y_{\mathrm{s}}}\right)\underline{\hat{u}}_{\mathrm{o}} \\ & + \left(\mathbf{G}_{\mathrm{co}} - \mathbf{G}_{\mathrm{io}}\frac{Y_{\mathrm{s}}\mathbf{G}_{\mathrm{ci}}}{1+Z_{\mathrm{in}}Y_{\mathrm{s}}}\right)\underline{\hat{d}}.\end{aligned} \tag{21}$$

IV. Load-affected system dynamics

By considering the output terminal of the converter as the Point of Common Coupling (PCC), the grid-feeding converter observes a series input impedance with the ideal grid voltage. This grid impedance affects the voltage at the PCC by causing phase and magnitude deviation compared to the ideal grid which, in turn, affects the dynamics of the converter.

Before analyzing the effect of the load on the system dynamics, the reference frame for the analysis must be selected [22]. The converter reference frame is different than

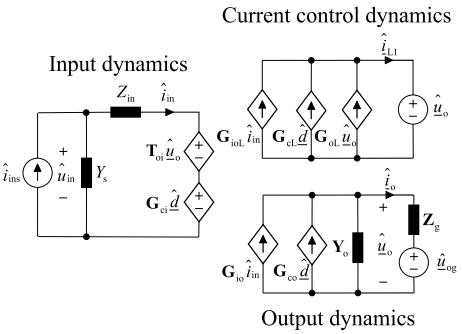

Fig. 3. Load-affected model of a grid-connected inverter at open loop.

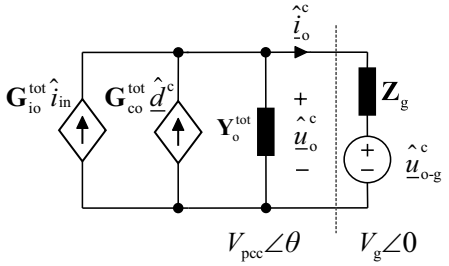

Fig. 4. The converter and grid reference frames.

the grid reference frame, which must be taken into account when deriving the model. By overlooking the aforementioned factor, the model would yield inaccurate predictions, especially considering the cross-coupling elements between the d and q-components. The effect of the load can be derived into the closed-loop dynamics by first analyzing the interface at the PCC according to Fig. 4.

In Fig. 4, the superscript 'c' in the variables denotes that the corresponding variable is inside the converter reference frame. Hereinafter, the superscript 'g' denotes that a variable is in the grid reference frame. The relation between the converter and grid reference frames can be given as

$$\underline{x}^{\mathrm{c}} = \mathbf{T}_{\mathrm{dq}}\underline{x}^{\mathrm{g}}, \tag{22}$$

where the transformation matrix $\mathbf{T}_{\mathrm{dq}}$ can be expressed as

$$\mathbf{T}_{\mathrm{dq}} = \begin{bmatrix} \cos\theta & \sin\theta \\ -\sin\theta & \cos\theta \end{bmatrix}. \tag{23}$$

The angle difference θ between the reference frames can be calculated e.g. from the steady-state values of the grid currents and grid voltages if the grid impedance is known. Alternatively, the steady-state angle difference can be obtained by simulations.

By acknowledging the aforementioned reference-frame factor, the load-affected model can be developed by first solving

the grid current under weak grid. From Fig. 4, the PCC voltage can be given as

$$\underline{\hat{u}}_{\mathrm{o}}^{\mathrm{c}} = \underline{\hat{u}}_{\mathrm{o\text{-}g}}^{\mathrm{c}} + \mathbf{Z}_{\mathrm{g}}\underline{\hat{i}}_{\mathrm{o}}^{\mathrm{c}}, \tag{24}$$

where the grid-impedance matrix is generally presented as

$$\mathbf{Z}_{\mathrm{g}} = \begin{bmatrix} Z_{\mathrm{g\text{-}d}} & Z_{\mathrm{g\text{-}qd}} \\ Z_{\mathrm{g\text{-}dq}} & Z_{\mathrm{g\text{-}q}} \end{bmatrix}. \tag{25}$$

From the closed-loop dynamics, the grid current $\underline{\hat{i}}_{\mathrm{o}}^{\mathrm{c}}$ can be further expressed as in (26). Note that the superscript 'tot' is omitted from the following equations for simplicity.

$$\underline{\hat{u}}_{\mathrm{o}}^{\mathrm{c}} = \underline{\hat{u}}_{\mathrm{o\text{-}g}}^{\mathrm{c}} + \mathbf{Z}_{\mathrm{g}}\left(\mathbf{G}_{\mathrm{io}}\underline{\hat{i}}_{\mathrm{in}} - \mathbf{Y}_{\mathrm{o}}\underline{\hat{u}}_{\mathrm{o}}^{\mathrm{c}} + \mathbf{G}_{\mathrm{co}}\underline{\hat{d}}^{\mathrm{c}}\right) \tag{26}$$

Solving the non-ideal PCC voltage from (26) yields

$$\begin{aligned}\underline{\hat{u}}_{\mathrm{o}}^{\mathrm{c}} = (\mathbf{I}+\mathbf{Z}_{\mathrm{g}}\mathbf{Y}_{\mathrm{o}})^{-1}\mathbf{Z}_{\mathrm{g}}\mathbf{G}_{\mathrm{io}}\hat{i}_{\mathrm{in}} + (\mathbf{I}+\mathbf{Z}_{\mathrm{g}}\mathbf{Y}_{\mathrm{o}})^{-1}\underline{\hat{u}}_{\mathrm{o\text{-}g}}^{\mathrm{c}} \\ +(\mathbf{I}+\mathbf{Z}_{\mathrm{g}}\mathbf{Y}_{\mathrm{o}})^{-1}\mathbf{Z}_{\mathrm{g}}\mathbf{G}_{\mathrm{co}}\underline{\hat{d}}^{\mathrm{c}},\end{aligned} \tag{27}$$

which can be substituted into the non-ideal PCC voltage denoted by $\underline{\hat{u}}_{\mathrm{o}}$. Thus, the load-affected closed-loop model, i.e. the equations for DC-link voltage, inverter-side current, and the grid current, can given by (28), (29), and (30), respectively.

$$\begin{aligned}\hat{u}_{\mathrm{in}} = \left(Z_{\mathrm{in}} + \mathbf{T}_{\mathrm{oi}}(\mathbf{I}+\mathbf{Z}_{\mathrm{g}}\mathbf{Y}_{\mathrm{o}})^{-1}\mathbf{Z}_{\mathrm{g}}\mathbf{G}_{\mathrm{io}}\right)\hat{\underline{i}}_{\mathrm{in}} \\ +\mathbf{T}_{\mathrm{oi}}(\mathbf{I}+\mathbf{Z}_{\mathrm{g}}\mathbf{Y}_{\mathrm{o}})^{-1}\underline{\hat{u}}_{\mathrm{o\text{-}g}}^{\mathrm{c}} \\ + \left(\mathbf{G}_{\mathrm{ci}} + \mathbf{T}_{\mathrm{oi}}(\mathbf{I}+\mathbf{Z}_{\mathrm{g}}\mathbf{Y}_{\mathrm{o}})^{-1}\mathbf{Z}_{\mathrm{g}}\mathbf{G}_{\mathrm{co}}\right)\underline{\hat{d}}^{\mathrm{c}}\end{aligned} \tag{28}$$

$$\begin{aligned}\hat{\underline{i}}_{\mathrm{L1}}^{\mathrm{c}} = \left(\mathbf{G}_{\mathrm{ioL}} + \mathbf{G}_{\mathrm{oL}}(\mathbf{I}+\mathbf{Z}_{\mathrm{g}}\mathbf{Y}_{\mathrm{o}})^{-1}\mathbf{Z}_{\mathrm{g}}\mathbf{G}_{\mathrm{io}}\right)\hat{\underline{i}}_{\mathrm{in}} \\ +\mathbf{G}_{\mathrm{oL}}(\mathbf{I}+\mathbf{Z}_{\mathrm{g}}\mathbf{Y}_{\mathrm{o}})^{-1}\underline{\hat{u}}_{\mathrm{o\text{-}g}}^{\mathrm{c}} \\ + \left(\mathbf{G}_{\mathrm{cL}} + \mathbf{G}_{\mathrm{oL}}(\mathbf{I}+\mathbf{Z}_{\mathrm{g}}\mathbf{Y}_{\mathrm{o}})^{-1}\mathbf{Z}_{\mathrm{g}}\mathbf{G}_{\mathrm{co}}\right)\underline{\hat{d}}^{\mathrm{c}}\end{aligned} \tag{29}$$

$$\begin{aligned}\hat{\underline{i}}_{\mathrm{o}}^{\mathrm{c}} = \left(\mathbf{G}_{\mathrm{io}} - \mathbf{Y}_{\mathrm{o}}(\mathbf{I}+\mathbf{Z}_{\mathrm{g}}\mathbf{Y}_{\mathrm{o}})^{-1}\mathbf{Z}_{\mathrm{g}}\mathbf{G}_{\mathrm{io}}\right)\hat{\underline{i}}_{\mathrm{in}} \\ -\mathbf{Y}_{\mathrm{o}}(\mathbf{I}+\mathbf{Z}_{\mathrm{g}}\mathbf{Y}_{\mathrm{o}})^{-1}\underline{\hat{u}}_{\mathrm{o\text{-}g}}^{\mathrm{c}} \\ + \left(\mathbf{G}_{\mathrm{co}} - \mathbf{Y}_{\mathrm{o}}(\mathbf{I}+\mathbf{Z}_{\mathrm{g}}\mathbf{Y}_{\mathrm{o}})^{-1}\mathbf{Z}_{\mathrm{g}}\mathbf{G}_{\mathrm{co}}\right)\underline{\hat{d}}^{\mathrm{c}}\end{aligned} \tag{30}$$

Regarding the stability analysis of the grid interface, the generalized Nyquist stability criterion is required for the assessment. However, the above equations are presented for the inverter reference frame which does not suffice when analyzing the system from the grid point-of-view. The grid current and the grid voltage in the converter reference frame must be represented in the real grid reference frame. Accordingly, the coordinate transformation can be performed by denoting

$$\hat{\underline{i}}_{\mathrm{o}}^{\mathrm{c}} = \mathbf{T}_{\mathrm{dq}}\hat{\underline{i}}_{\mathrm{o}}^{\mathrm{g}} \rightarrow \hat{\underline{i}}_{\mathrm{o}}^{\mathrm{g}} = \mathbf{T}_{\mathrm{dq}}{}^{-1}\hat{\underline{i}}_{\mathrm{o}}^{\mathrm{c}}, \quad \underline{\hat{u}}_{\mathrm{o\text{-}g}}^{\mathrm{c}} = \mathbf{T}_{\mathrm{dq}}\underline{\hat{u}}_{\mathrm{o\text{-}g}}^{\mathrm{g}}. \tag{31}$$

Note that the interpretation of the coordinate transformation should be given careful attention. In particular, it is not feasible to analyze some of the transfer functions in both reference frames, whereas in a practical setup some may not be measurable. However, considering the above, the correct dynamics of the grid-connected inverter are obtained. Note that the model is also valid for the analysis of the open-loop dynamics. Stability assessment can be, therefore, readily applied to verify the stability of the grid interface as well as its effects on the control system performance of the converter. Note that the stability analysis is not the topic of interest in this paper and, therefore, is omitted.

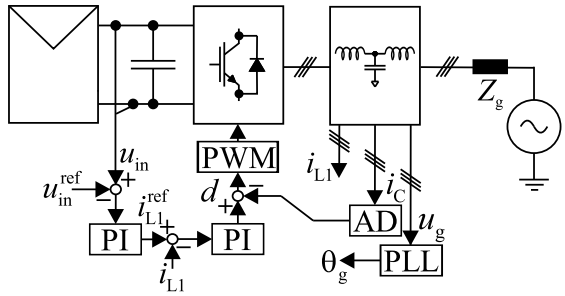

Fig. 5. Depiction of the power stage and control system configuration.

TABLE I
OPERATING POINT AND COMPONENT VALUES.

Parameter	Value	Parameter	Value
U_{in}	750 V	C_{in}	1.9 mF
I_{in}	20 A	L_1	2.5 mH
$U_{\mathrm{grid,rms}}$	230 V	r_{L1}	65 mΩ
$\omega_{\mathrm{grid}}, \omega_{\mathrm{s}}$	2π60 rad/s	C_{f}	10 μF
f_{s}	20 kHz	r_{Cf}	10 mΩ
f_{res}	2.29 kHz	L_2	0.6 mH
$f_{\mathrm{s}}/f_{\mathrm{res}}$	8.7	r_{L2}	22 mΩ
r_{sw}	10 mΩ		

V. Model Verification

This section presents the simulation results in order to validate the accuracy of the developed model. The measurements are carried with both Matlab Simulink software and with Typhoon HIL development platform. The frequency-domain data is measured by using PRBS-injection method, which can also be readily applied for experimental inverters [25] as well as by using a commercial frequency response analyzer with sine-sweep.

The overall system configuration with the power stage and the control structures is presented in Fig. 5. It consists of the PV generator, inverter bridge, a grid filter, finite grid impedance with utility grid, and the control structure. A cascaded control system is utilized as is the common practice in PV-inverter systems. Table I presents the power stage and component values used in the simulations. The superscript "tot-LS" is used to highlight that the model includes both the source and the load effects. A delay of 1.5 times the switching period was used.

In order to validate the model, the closed-loop frequency responses of the system transfer functions are presented. This is done by utilizing Matlab Simulink software and PRBS-injection method. Note that in all the following figures, the predicted transfer functions are presented by dotted lines, and solid lines represent the frequency responses identified from a MATLAB switching model. First, the input-voltage related transfer functions are verified and presented in Figs. 6-8. Then, the inverter-side current and grid current transfer functions are presented in Figs. 9 and 10-13, respectively. Based on the

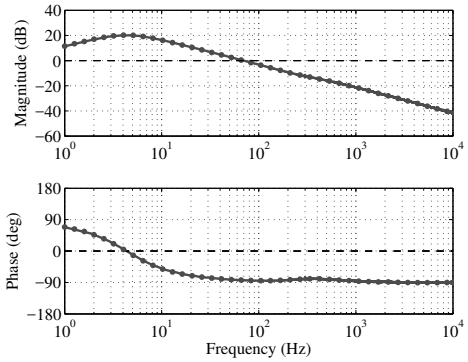

Fig. 6. Simulated (solid line) and modeled (dotted line) input impedance $Z_{\text{in}}^{\text{tot-LS}}$.

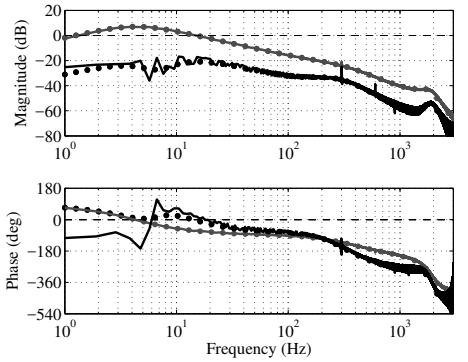

Fig. 7. Simulated (solid line) and modeled (dotted line) d-component (blue) and q-component (black) of transmittance $\mathbf{T}_{\text{oi}}^{\text{tot-LS}}$.

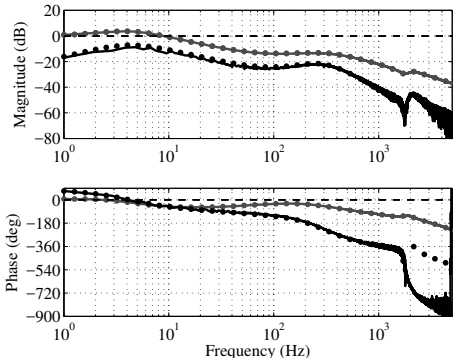

Fig. 8. Simulated (solid line) and modeled (dotted line) d-component (blue) and q-component (black) of control-to-input voltage transfer function $\mathbf{G}_{\text{ci}}^{\text{tot-LS}}$.

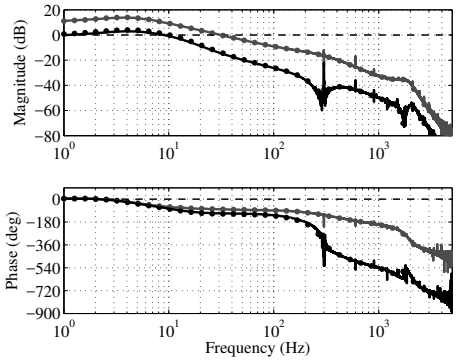

Fig. 9. Simulated (solid line) and modeled (dotted line) d-component (blue) and q-component (black) of input-to-output current transfer function $\mathbf{G}_{\text{ioL}}^{\text{tot-LS}}$.

results, the developed model is shown to be very accurate at predicting the dynamic behavior of the converter with both non-ideal source and load. Good overall accuracy is evident between the predicted and identified frequency responses.

Furthermore, to verify the accuracy of the model at different operating points and to demonstrate the effect the load and the source can have on the system dynamics, the closed-loop frequency responses of relevant transfer functions are compared regarding changes in the source and load conditions. The simulations are performed with Typhoon HIL development platform from which the frequency responses are identified using a separate frequency response analyzer with sine-sweep, except for the Fig. 17, in which Simulink was used.

In Fig. 14, the output-side admittance $\mathbf{Y}_{\text{o}}^{\text{tot-LS}}$ is shown at different PVG operating points, i.e., when the PVG is operating in constant current region (CCR), at the maximum power point (MPP), and in constant voltage region (CVR). The points of interest have been chosen as ± 10 % of the MPP voltage (here 750 V) to represent relatively small variations in the voltage under constant irradiation and temperature (STC). The chosen variations in the MPP voltage imply a reduction in the produced power of 5 % and 10 % in CCR and CVR, respectively. Under real conditions, the variations may be significantly larger depending on the MPP tracker and the irradiance fluctuation etc. The dynamic resistance of the PVG depends highly on its operating point and has an effect on the system dynamics. Accordingly, as can be seen in the figure, the transfer functions are slightly different. However, the model predicts them correctly and with good accuracy.

Fig. 15 shows the d-component of the output-side admittance $\mathbf{Y}_{\text{o}}^{\text{tot-LS}}$ when the grid inductance is decreased from 8 mH to 2 mH. Note that here the admittance is considered from the ideal grid point of view. It is clear that the grid impedance has a strong effect on the output-side admittance at higher frequencies. Adverse interaction with the grid is stronger when the grid conditions are weak, i.e., the grid impedance is high. This affects the output-side admittance by lowering the gain, as can be seen in the figure.

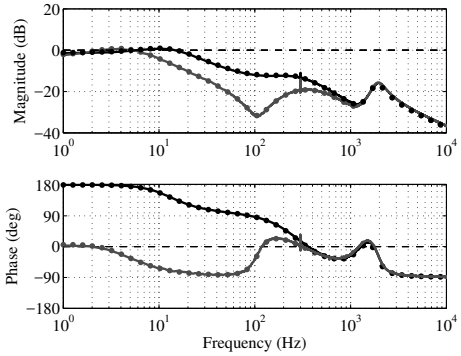

Fig. 10. Simulated (solid line) and modeled (dotted line) d-component (blue) and q-component (black) of output admittance $\mathbf{Y}_{\mathrm{o}}^{\text{tot-LS}}$.

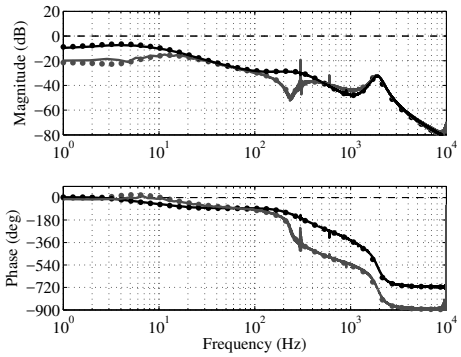

Fig. 11. Simulated (solid line) and modeled (dotted line) qd-component (blue) and dq-component (black) of output admittance $\mathbf{Y}_{\mathrm{o}}^{\text{tot-LS}}$.

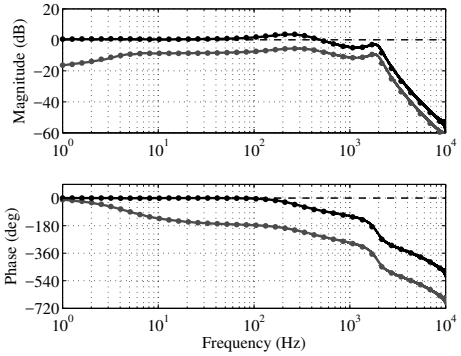

Fig. 12. Simulated (solid line) and modeled (dotted line) d-component (blue) and q-component (black) of control-to-output current transfer function $\mathbf{G}_{\mathrm{co}}^{\text{tot-LS}}$.

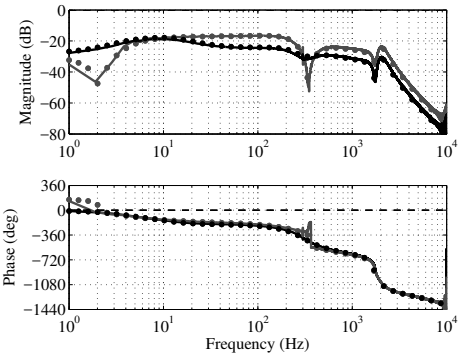

Fig. 13. Simulated (solid line) and modeled (dotted line) qd-component (blue) and dq-component (black) of control-to-output current transfer function $\mathbf{G}_{\mathrm{co}}^{\text{tot-LS}}$.

The qd-component of the output-side admittance $\mathbf{Y}_{\mathrm{o}}^{\text{tot-LS}}$ with and without the load effect is shown in Fig. 16. The difference between the two cases is significant. Thus, in order to guarantee reliable stability analysis, the effect of the load cannot be ignored, i.e., the grid cannot be estimated as ideal three-phase voltage source.

Fig. 17 presents the q-component of the control-to-output current transfer function $\mathbf{G}_{\mathrm{cL}}^{\text{tot-LS}}$ when the grid inductance is decreased from 8 mH to 2 mH. Based on the figure, the reduction in the grid inductance improves the bandwidth of the current control. The effect of the grid impedance on the control-to-output current transfer function should be taken into account especially when designing reactive power or droop control. The frequency response also reveals that the inverter may amplify noise in the kilohertz-range due to magnitude close to unity.

The figures show a good correspondence between the predicted and identified frequency responses. As a result, the model allows the effects of both the source and the load to be taken into account. Thus, the model can be used to perform reliable and deterministic control design and stability validation under varying operating conditions.

VI. Conclusion

The main contribution of this paper is the full-order small-signal model of a grid-connected PV inverter in the dq-domain which considers both the load and source effects. The model can be used to assess the effect of an arbitrary non-ideal current-type source (e.g. PV generator or PV generator with a boost converter) as well as a voltage-type load (e.g. utility grid or grid-forming inverter) on the inverter dynamics. Thus, the full dynamic analysis can be performed as e.g. the control and impedance dynamics are accurately predicted. The model is developed with the multiple-input-multiple-output modeling technique which simplifies significantly the derivation of the closed-loop model and improves the accuracy of the model [9]. Furthermore, the accuracy of the model is verified from a switching model as well as using HIL simulations.

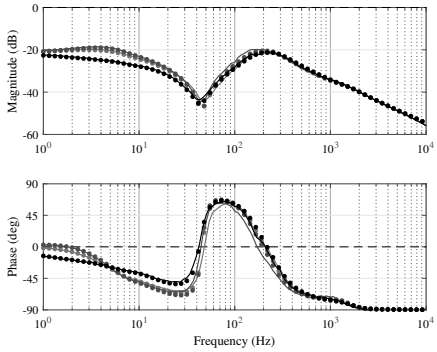

Fig. 14. HIL-simulation result (solid line) and modeled (dotted line) d-components of the output-side admittance $\mathbf{Y}_{\mathrm{o}}^{\text{tot-LS}}$ at different PVG operating points: MPP (red), CCR (blue), and CVR (black).

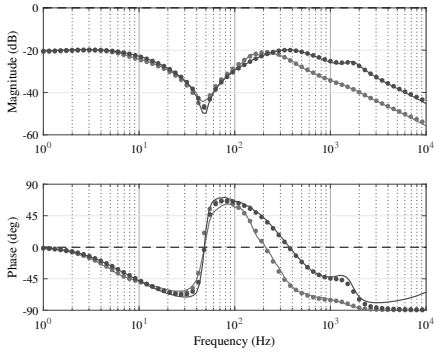

Fig. 15. HIL-simulation result (solid line) and modeled (dotted line) d-component of the output-side admittance $\mathbf{Y}_{\mathrm{o}}^{\text{tot-LS}}$ when the grid inductance is decreased from 8 mH (red) to 2 mH (blue).

APPENDIX A

The system state matrices presented in Section II in (4) are given as follows. In **A**-**D**, r_{eq} is the combined inverter-side inductor ESR and the switch on-time resistance, r_{C} is the LCL-filter capacitor ESR, r_{L2} is the grid-inductor ESR, C_{in} is the input filter capacitor, L_1 is the inverter-side inductance, L_2 is the grid-side inductance, C_{f} is the LCL-filter capacitance, U_{in} is the steady-state inverter input voltage, I_{in} is the steady-state inverter input current, D_{d} is the d-component of the steady-state duty ratio, D_{q} is the q-component of the steady-state duty ratio, and ω_{s} is the grid fundamental frequency.

$$\mathbf{A} = \begin{bmatrix} -\frac{r_{\mathrm{eq}}}{L_1} & \omega_{\mathrm{s}} & \frac{r_{\mathrm{C}}}{L_1} & 0 & -\frac{1}{L_1} & 0 & \frac{D_{\mathrm{d}}}{L_1} \\ -\omega_{\mathrm{s}} & -\frac{r_{\mathrm{eq}}}{L_1} & 0 & \frac{r_{\mathrm{C}}}{L_1} & 0 & -\frac{1}{L_1} & \frac{D_{\mathrm{q}}}{L_1} \\ \frac{r_{\mathrm{C}}}{L_2} & 0 & -\frac{r_{\mathrm{L2}}+r_{\mathrm{C}}}{L_2} & \omega_{\mathrm{s}} & \frac{1}{L_2} & 0 & 0 \\ 0 & \frac{r_{\mathrm{C}}}{L_2} & -\omega_{\mathrm{s}} & -\frac{r_{\mathrm{L2}}+r_{\mathrm{C}}}{L_2} & 0 & \frac{1}{L_2} & 0 \\ \frac{1}{C_{\mathrm{f}}} & 0 & -\frac{1}{C_{\mathrm{f}}} & 0 & 0 & \omega_{\mathrm{s}} & 0 \\ 0 & \frac{1}{C_{\mathrm{f}}} & 0 & -\frac{1}{C_{\mathrm{f}}} & -\omega_{\mathrm{s}} & 0 & 0 \\ -\frac{3}{2}\frac{D_{\mathrm{d}}}{C_{\mathrm{in}}} & -\frac{3}{2}\frac{D_{\mathrm{q}}}{C_{\mathrm{in}}} & 0 & 0 & 0 & 0 & 0 \end{bmatrix} \tag{32}$$

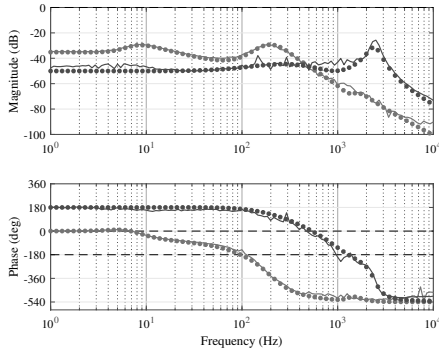

Fig. 16. HIL-simulation result (solid line) and modeled (dotted line) qd-component of the output-side admittance $\mathbf{Y}_{\mathrm{o}}^{\text{tot-LS}}$ with (red) and without (blue) the load effect.

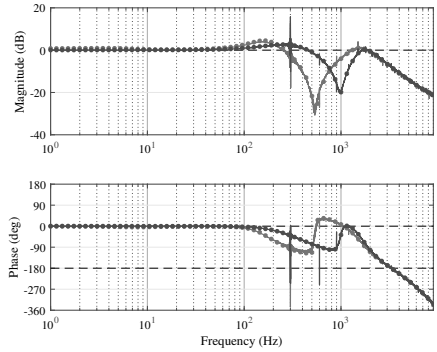

Fig. 17. Simulated (solid line) and modeled (dotted line) q-component of the control-to-output current transfer function $\mathbf{G}_{\mathrm{cL}}^{\text{tot-LS}}$ when the grid inductance is decreased from 8 mH (red) to 2 mH (blue).

$$\mathbf{B} = \begin{bmatrix} 0 & 0 & 0 & \frac{U_{\mathrm{in}}}{L_1} & 0 \\ 0 & 0 & 0 & 0 & \frac{U_{\mathrm{in}}}{L_1} \\ 0 & -\frac{1}{L_2} & 0 & 0 & 0 \\ 0 & 0 & -\frac{1}{L_2} & 0 & 0 \\ 0 & 0 & 0 & 0 & 0 \\ 0 & 0 & 0 & 0 & 0 \\ \frac{1}{C_{\mathrm{in}}} & 0 & 0 & -\frac{I_{\mathrm{in}}}{D_{\mathrm{d}}C_{\mathrm{in}}} & 0 \end{bmatrix} \tag{33}$$

$$\mathbf{C} = \begin{bmatrix} 0 & 0 & 0 & 0 & 0 & 0 & 1 \\ 1 & 0 & 0 & 0 & 0 & 0 & 0 \\ 0 & 1 & 0 & 0 & 0 & 0 & 0 \\ 0 & 0 & 1 & 0 & 0 & 0 & 0 \\ 0 & 0 & 0 & 1 & 0 & 0 & 0 \end{bmatrix} \tag{34}$$

$$\mathbf{D} = \mathbf{0} \tag{35}$$

APPENDIX B

The closed-loop transfer function matrices presented in Section II in (7)-(15) can be derived from the input and output dynamics in (5) and (6) and Fig. 2 by ignoring the input-voltage control loop and can be given as follows:

$$\mathbf{T}_{\mathrm{oi}}^{\mathrm{out}} = \mathbf{T}_{\mathrm{oi}} - \mathbf{G}_{\mathrm{ci}}\mathbf{G}_{\mathrm{del}}(\mathbf{I}+\mathbf{L}_{\mathrm{out}})^{-1}\left[\mathbf{L}_{\mathrm{out}}{\mathbf{G}_{\mathrm{cL}}}^{-1}\mathbf{G}_{\mathrm{oL}} - \mathbf{L}_{\mathrm{out}}{\mathbf{G}_{\mathrm{cL}}}^{-1}\mathbf{I}_{\mathrm{L1}}\mathbf{G}_{\mathrm{PLL}} - \mathbf{D}\mathbf{G}_{\mathrm{PLL}}\right] \quad (36)$$

$$\mathbf{G}_{\mathrm{ci}}^{\mathrm{out}} = \mathbf{G}_{\mathrm{ci}}(\mathbf{I}+\mathbf{L}_{\mathrm{out}})^{-1}\mathbf{L}_{\mathrm{out}}{\mathbf{G}_{\mathrm{cL}}}^{-1} \quad (37)$$

$$\mathbf{Y}_{\mathrm{o}}^{\mathrm{out}} = \mathbf{Y}_{\mathrm{o}} + \mathbf{G}_{\mathrm{co}}\mathbf{G}_{\mathrm{del}}(\mathbf{I}+\mathbf{L}_{\mathrm{out}})^{-1}\left[\mathbf{L}_{\mathrm{out}}{\mathbf{G}_{\mathrm{cL}}}^{-1}\mathbf{G}_{\mathrm{oL}} - \mathbf{L}_{\mathrm{out}}{\mathbf{G}_{\mathrm{cL}}}^{-1}\mathbf{I}_{\mathrm{L1}}\mathbf{G}_{\mathrm{PLL}} - \mathbf{D}\mathbf{G}_{\mathrm{PLL}}\right] \quad (38)$$

$$\mathbf{G}_{\mathrm{co}}^{\mathrm{out}} = \mathbf{G}_{\mathrm{co}}(\mathbf{I}+\mathbf{L}_{\mathrm{out}})^{-1}\mathbf{L}_{\mathrm{out}}{\mathbf{G}_{\mathrm{cL}}}^{-1}, \quad (39)$$

where the output-current loop gain $\mathbf{L}_{\mathrm{out}} = \mathbf{G}_{\mathrm{cc}}\mathbf{G}_{\mathrm{del}}\mathbf{G}_{\mathrm{cL}}$.

In Fig. 2, the matrix $\mathbf{G}_{\mathrm{PLL}}$ contains the PLL transfer functions which can be expressed as [17]

$$\mathbf{G}_{\mathrm{PLL}} = \begin{bmatrix} 0 & 0 \\ 0 & G_{\mathrm{PLL}} \end{bmatrix}, \quad (40)$$

$$G_{\mathrm{PLL}} = \frac{1}{U_{\mathrm{od}}}\frac{L_{\mathrm{PLL}}}{1+L_{\mathrm{PLL}}}, \quad (41)$$

$$L_{\mathrm{PLL}} = -G_{\mathrm{PI-PLL}}\frac{U_{\mathrm{od}}}{s}, \quad (42)$$

$$G_{\mathrm{PI-PLL}} = K_{\mathrm{p}} + \frac{K_{\mathrm{i}}}{s}. \quad (43)$$

For the PLL PI-controller, $K_{\mathrm{p}} = 0.67$ and $K_{\mathrm{i}} = 38.02$.

REFERENCES

[1] B. K. Bose, "Energy, environmental pollution, and the impact of power electronics," *IEEE Ind. Electron. Mag.*, pp. 6–17, Mar. 2010.

[2] S. Valkealahti, "Forecasting the future of renewables," in *Climate Change-Socioeconomic Effects*, Sep. 2010, pp. 425–440.

[3] M. Liserre, F. Blaabjerg, and S. Hansen, "Design and control of an LCL-filter-based three-phase active rectifier," *IEEE Trans. Ind. Appl.*, vol. 41, no. 5, pp. 1281–1291, Sep. 2005.

[4] M. Liserre, F. Blaabjerg, and A. DellAquila, "Step-by-step design procedure for a grid-connected three-phase PWM voltage source converter," *Int. J. Electron.*, vol. 91, no. 8, pp. 445–460, 2004.

[5] L. Jessen and F. W. Fuchs, "Modeling of inverter output impedance for stability analysis in combination with measured grid impedances," in *IEEE PEDG'15*, Jun. 2015, pp. 1–7.

[6] N. P. W. Strachan and D. Jovcic, "Stability of a variable-speed permanent magnet wind generator with weak ac grids," *IEEE Transactions on Power Delivery*, vol. 25, no. 4, pp. 2779–2788, Oct 2010.

[7] C. Li, "Unstable operation of photovoltaic inverter from field experiences," *IEEE Trans. Power Del.*, vol. 33, no. 2, pp. 1013–1015, April 2018.

[8] M. Rasheduzzaman, J. A. Mueller, and J. W. Kimball, "An accurate small-signal model of inverter- dominated islanded microgrids using *dq* reference frame," *IEEE Trans. Emerg. Sel. Topics Power Electron.*, vol. 2, no. 4, pp. 1070–1080, Dec. 2014.

[9] A. Aapro, T. Messo, and T. Suntio, "An accurate small-signal model of a three-phase VSI-based photovoltaic inverter with LCL-filter," in *IEEE ICPE- ECCE'15 Asia*, 2015, pp. 2267–2274.

[10] E. Figueres, G. Garcera, J. Sandia, F. Gonzalez-Espin, and J. C. Rubio, "Sensitivity study of the dynamics of three-phase photovoltaic inverters with an lcl grid filter," *IEEE Trans. Ind. Electron.*, vol. 56, no. 3, pp. 706–717, Mar. 2009.

[11] D. Boroyevich and F. Lee, "Novel reduced-order small-signal model of a three-phase PWM rectifier and its application in control design and system analysis," *IEEE Trans. Power Electron.*, vol. 13, no. 3, pp. 511–521, May 1998.

[12] Z. Liu, J. Liu, D. Boroyevich, R. Burgos, and T. Liu, "Small-signal terminal-characteristics modeling of three-phase droop-controlled inverters," in *IEEE ECCE'16*, Sep. 2016, pp. 1–7.

[13] K. M. Alawasa, Y. A. R. I. Mohamed, and W. Xu, "Active mitigation of subsynchronous interactions between pwm voltage-source converters and power networks," *IEEE Trans. Power Electron.*, vol. 29, no. 1, pp. 121–134, Jan. 2014.

[14] M. Cespedes and J. Sun, "Impedance modeling and analysis of grid-connected voltage-source converters," *IEEE Trans. Power Electron.*, vol. 29, no. 3, pp. 1254–1261, Mar. 2014.

[15] J. Sun, "Impedance-based stability criterion for grid-connected inverters," *IEEE Trans. Power Electron.*, vol. 26, no. 11, pp. 3075–3078, Nov. 2011.

[16] J. L. Agorreta, M. Borrega, J. López, and L. Marroyo, "Modeling and control of N-paralleled grid-connected inverters with LCL filter coupled due to grid impedance in pv plants," *IEEE Trans. Power Electron.*, vol. 26, no. 3, pp. 770–785, Mar. 2011.

[17] T. Messo, J. Jokipii, A. Mäkinen, and T. Suntio, "Modeling the grid synchronization induced negative-resistor-like behavior in the output impedance of a three-phase photovoltaic inverter," in *IEEE PEDG'13*, Jul. 2013, pp. 1–7.

[18] J. Puukko and T. Suntio, "Modelling the effect of non-ideal load in three-phase converter dynamics," *Electronics Letters*, vol. 48, no. 7, pp. 402–404, Mar. 2012.

[19] H. Liu, L. Yu, H. Wu, G. Liu, and W. Wang, "Small signal modeling and stability analysis on parallel photovoltaic inverters in microgrid," in *IEEE ECCE'15*, Sep. 2015, pp. 3754–3759.

[20] S. Dutta, D. Debnath, and K. Chatterjee, "A grid-connected single-phase transformerless inverter controlling two solar pv arrays operating under different atmospheric conditions," *IEEE Trans. Ind. Electron.*, vol. 65, no. 1, pp. 374–385, Jan. 2018.

[21] S. Mortazavian and Y. A. R. I. Mohamed, "Dynamic analysis and improved lvrt performance of multiple dg units equipped with grid-support functions under unbalanced faults and weak grid conditions," *IEEE Trans. Power Electron.*, vol. PP, no. 99, pp. 1–1, 2017.

[22] A. Rygg, M. Molinas, C. Zhang, and X. Cai, "On the equivalence and impact on stability of impedance modeling of power electronic converters in different domains," *IEEE Trans. Emerg. Sel. Topics Power Electron.*, vol. 5, no. 4, pp. 1444–1454, Dec. 2017.

[23] L. Nousiainen, J. Puukko, A. Maki, T. Messo, J. Huusari, J. Jokipii, J. Viinamaki, D. T. Lobera, S. Valkealahti, and T. Suntio, "Photovoltaic generator as an input source for power electronic converters," *IEEE Trans. Power Electron.*, vol. 28, no. 6, pp. 3028–3038, Jun. 2013.

[24] R. D. Middlebrook, "Small-signal modeling of pulse-width modulated switched-mode power converters," *Proceedings of the IEEE*, vol. 76, no. 4, pp. 343–354, Apr 1988.

[25] T. Roinila, J. Huusari, and M. Vilkko, "On frequency-response measurements of power-electronic systems applying MIMO identification techniques," *IEEE Trans. Ind. Electron.*, vol. 60, no. 11, pp. 5270–5276, Nov. 2013.

PUBLICATION
II

The Combined Source-Effect of Photovoltaic Generator and Bi-Directional DC-DC Battery Charger on Inverter Control Dynamics

R.-M. Sallinen and T. Messo

The Journal of Engineering 2018, pp. 5197–5201

Combined source-effect of photovoltaic generator and bi-directional dc–dc battery charger on inverter control dynamics

Roosa-Maria Sallinen[1] ✉, *Tuomas Messo*[1]

[1]*Laboratory of Electrical Energy Engineering, Tampere University, Tampere, Finland*

✉ *E-mail: roosa-maria.sallinen@tuni.fi*

Abstract: This study presents a method to solve the dynamic model of a grid-connected photovoltaic (PV) inverter with battery energy storage. A three-phase grid-connected solar-battery system is studied using small-signal state-space modelling in the synchronously rotating *dq*-reference frame. The combined effect of a PV generator and a bi-directional dc–dc battery charger (BC) on the inverter dynamic behaviour is analysed. It is shown that the characteristic right-half-plane pole in the PV inverter's dc-link voltage control dynamics shifts to a lower frequency when the BC is connected, which improves the stability of the system and allows a lower bandwidth for the dc-link voltage control.

1 Introduction

In recent years, different hybrid renewable-energy sources (RESs) have been increasingly researched and developed worldwide. The hybrid solutions aim to complement each other's weaknesses resulting in more efficient and reliable energy sources as a whole. Many types of RESs, such as photovoltaic (PV) generators, have an intermittent nature due to changing environmental factors, such as irradiation levels and temperature. Thus, predicting and controlling the energy production of these sources is more difficult compared to traditional power sources with the inertial response, such as gas turbines. As a result, these intermittent energy sources increase the overall need for regulated power reserve to keep the total production in balance with the consumption [1, 2].

To this end, battery energy storage systems (BESSs) are considered a good addition to PV generators (PVGs) and other intermittent sources due to their fast response time, reliable technology, and increasing cost-efficiency [3, 4]. The main idea of solar-battery systems is to utilise the batteries to store any excess solar energy to offer the stored energy during low irradiation levels, for example during night-time. In [5], BESS was employed for smoothing the PV power fluctuations under variations in solar irradiance. BESS can also be used for arbitrage [6], in which the charging and discharging of the BESS is chosen based on the current electricity price. Thus, there exist several promising applications for grid-connected solar-battery systems.

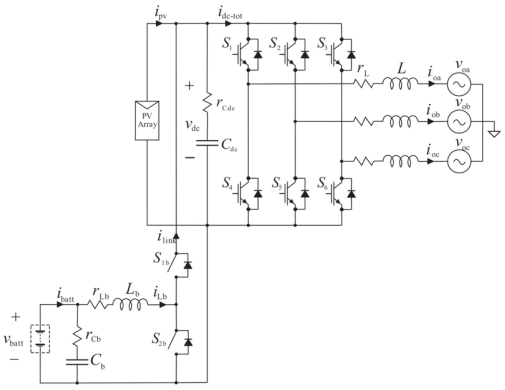

Fig. 1 *Layout of the grid-connected solar-battery system*

However, grid-connected solar-battery systems are difficult to model due to the number of different subsystems, power electronic converters and their controllers, and the variety of operating modes. The system consists of multiple different subsystems: BESS and its charge regulator (battery charger (BC)), PVG, and inverter and its output filters. The battery can be charged, discharged, or disconnected. The charging and discharging of the battery can be achieved by controlling the current and/or the voltage of the battery, depending on the chosen battery technology and its state of charge (SOC). The PVG is functioning either in the constant current region (CCR), constant voltage region (CVR) or at its maximum power point (MPP), which changes the dynamics of the PVG profoundly, as discussed in [7].

Since the stability of a power converter can be affected significantly by its operating condition, the studied system should be examined at all possible operating points. Furthermore, even though all the subsystems are stable and perform well within their own nominal operational ranges when integrated as a whole, the system may become unstable due to unexpected interactions among the subsystems. An accurate small-signal model is required to necessitate reliable controller design to guarantee the stability of the converter under varying control modes and operating points.

The effect of a PVG on the inverter dynamics has been studied previously in [7]. Bi-directional dc–dc converters have been modelled and their stability assessed in, e.g. [8, 9]. To study the dynamic behaviour of the whole system, this paper presents a small-signal model of the grid-connected solar-battery system, which can be used to analyse how the BC (i.e. bi-directional dc–dc converter) and the PVG affect the inverter dynamics. As a result, the effect of the PVG and the BESS can be taken into account in the inverter control design to guarantee stable and robust performance. Frequency domain results of the studied system under various operating conditions are presented to verify the dynamic model.

2 System configuration

Fig. 1 shows the configuration of the system under consideration: a three-phase PV inverter with a BESS connected at the dc-link through a bi-directional dc–dc converter. The dc–dc converter functions as the BC by controlling the battery current, enabling both charging and discharging modes. Note, that the battery voltage control is not considered in this paper. The inverter is connected to the grid through an L-filter.

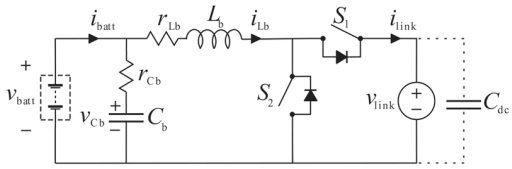

Fig. 2 *Bi-directional dc–dc converter*

2.1 Dynamic model of BC

Fig. 2 shows the schematic diagram of the bi-directional dc–dc converter for connecting the battery storage to the common dc link. Only one of the switches is active (i.e. switching) at a time: S2 when discharging (boost mode) and S1 when charging (buck mode). Note that the direction of the current in the figure is as in discharging mode; in charging mode, the flow would be the opposite. A proportional–integral (PI) controller is used to regulate the current of the BESS.

The linearised state-space representation of the BC is given in (1), where

$$R_{eq} = (r_{Lb} + r_d)(D-1) - D(r_{Lb} + r_{sw})$$
$$V_{eq} = V_d + V_{link} + I_{Lb}(r_d + r_{sw}),$$

r_{sw} and r_d are the parasitic resistances of the switches and the diode, respectively, and V_d is the voltage drop over the diode when set in the forward direction. The rest of the variables are given in Fig. 2 and D_{eq} is defined as $1-D_2$ while discharging the battery and as D_1 while charging the battery. Also, the upper signs of the plus-minus–pairs are for the discharging mode and lower signs for the charging mode. (see (1)) The transfer functions from the input variables to the output variables at open loop can be solved in the frequency-domain by utilising

$$\boldsymbol{Y}(s) = \big(\boldsymbol{C}(s\boldsymbol{I} - \boldsymbol{A})^{-1}\boldsymbol{B} + \boldsymbol{D}\big)\boldsymbol{U}(s) \tag{2}$$

where the matrices $\boldsymbol{A}$, $\boldsymbol{B}$, $\boldsymbol{C}$, $\boldsymbol{D}$, $\boldsymbol{Y}$, and $\boldsymbol{U}$ are as dictated in (1) and $\boldsymbol{I}$ is the unity matrix. As a result, the open-loop dynamics can be presented in matrix form as

$$\begin{bmatrix} \hat{i}^{bc}_{batt} \\ \hat{i}^{bc}_{link} \end{bmatrix} = \begin{bmatrix} Y^{bc}_{in-o} & T^{bc}_{oi-o} & G^{bc}_{ci-o} \\ G^{bc}_{io-o} & -Y^{bc}_{o-o} & G^{bc}_{co-o} \end{bmatrix} \begin{bmatrix} \hat{v}^{bc}_{batt} \\ \hat{v}^{bc}_{link} \\ \hat{i}^{bc}_{batt-ref} \end{bmatrix}, \tag{3}$$

where the 2×3 matrix consists of the transfer functions between the input and the output variables. Consecutively, by utilising feedback control from the battery current, the closed-loop dynamics can be presented as

$$\begin{bmatrix} \hat{i}^{bc}_{batt} \\ \hat{i}^{bc}_{link} \end{bmatrix} = \begin{bmatrix} Y^{bc}_{in-c} & T^{bc}_{oi-c} & G^{bc}_{ci-c} \\ G^{bc}_{io-c} & -Y^{bc}_{o-c} & G^{bc}_{co-c} \end{bmatrix} \overbrace{\begin{bmatrix} \hat{v}^{bc}_{batt} \\ \hat{v}^{bc}_{link} \\ \hat{i}^{bc}_{batt-ref} \end{bmatrix}}^{U_{bc}} \tag{4}$$

which is equal to (see (5)) . Moreover, the input control loop-gain is expressed as

$$L_{in-bc} = G^{bc}_{PI} G^{bc}_{ci-o} \tag{6}$$

Note, that different switches are controlled in the charging and discharging modes while the un-active switch is set to open. Furthermore, the direction of the current needs to be taken into account in the controller to make the system stable in both operating modes.

2.2 Dynamic model of PVG

The amount of current PVG can produce at a certain voltage level is correlated with the irradiance level. The PV cells are often modelled using the one-diode model presented in Fig. 3. According to the model, the current produced by the PV cell can be expressed as

$$i_{pv-cell} = i_{ph} - \underbrace{i_o\left[\exp\left(\frac{v_{pv} + r_s i_{pv}}{A v_t}\right)\right]}_{i_d} - \frac{v_{pv} + r_s i_{pv-cell}}{r_{sh}} \tag{7}$$

where i_{ph} is the light generated current, i_o the dark saturation current of the cell, v_{pv} the voltage across the cell, r_s the parasitic series resistance, r_{sh} the shunt resistance, A the ideality factor, and $v_t = kT/q$ the thermal voltage of the cell, where k is the Boltzmann constant, q the elementary charge, and T the temperature. Finally, i_d presents the diode resistance.

The PVG consists of multiple PV modules, which are built from multiple PV cells. When the PVG operates under uniform

$$\begin{bmatrix} \frac{d\hat{v}^{bc}_{Cb}}{dt} \\ \frac{d\hat{i}^{bc}_{Lb}}{dt} \end{bmatrix} = \overbrace{\begin{bmatrix} -\frac{1}{C_b r_{Cb}} & 0 \\ 0 & \frac{R_{eq}}{L_b} \end{bmatrix}}^{A} \begin{bmatrix} \hat{v}^{bc}_{Cb} \\ \hat{i}^{bc}_{Lb} \end{bmatrix} + \overbrace{\begin{bmatrix} \frac{1}{C_b r_{Cb}} & 0 & 0 \\ \pm\frac{1}{L_b} & \mp\frac{D_{eq}}{L_b} & \frac{V_{eq}}{L_b} \end{bmatrix}}^{B} \overbrace{\begin{bmatrix} \hat{v}^{bc}_{batt} \\ \hat{v}^{bc}_{link} \\ \hat{d}^{bc}_{1/2} \end{bmatrix}}^{U}$$
$$\overbrace{\begin{bmatrix} \hat{i}^{bc}_{batt} \\ \hat{i}^{bc}_{link} \end{bmatrix}}^{Y} = \overbrace{\begin{bmatrix} \mp\frac{1}{r_{Cb}} & 1 \\ 0 & D_{eq} \end{bmatrix}}^{C} \begin{bmatrix} \hat{v}^{bc}_{Cb} \\ \hat{i}^{bc}_{Lb} \end{bmatrix} + \overbrace{\begin{bmatrix} \pm\frac{1}{r_{Cb}} & 0 & 0 \\ 0 & 0 & \mp I_{Lb} \end{bmatrix}}^{D} \begin{bmatrix} \hat{v}^{bc}_{batt} \\ \hat{v}^{bc}_{link} \\ \hat{d}^{bc}_{1/2} \end{bmatrix} \tag{1}$$

$$= \begin{bmatrix} \frac{Y^{bc}_{in-o}}{1+L_{in-bc}} & \frac{T^{bc}_{oi-o}}{1+L_{in-bc}} & \frac{L_{in-bc}}{1+L_{in-bc}} \\ G^{bc}_{io-o} - \frac{G^{bc}_{co-o} G^{bc}_{PI} Y^{bc}_{in-o}}{1+L_{in-bc}} & -\left(Y^{bc}_{o-o} - \frac{G^{bc}_{co-o} G^{bc}_{PI} T^{bc}_{oi-o}}{1+L_{in-bc}}\right) & \frac{G^{bc}_{co-o} G^{bc}_{PI}}{1+L_{in-bc}} \end{bmatrix} \boldsymbol{U}_{bc}, \tag{5}$$

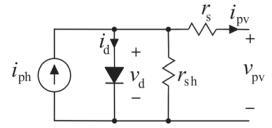

Fig. 3 *PV one-diode model*

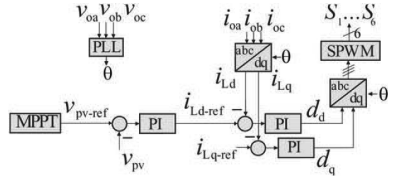

Fig. 4 *Inverter control system*

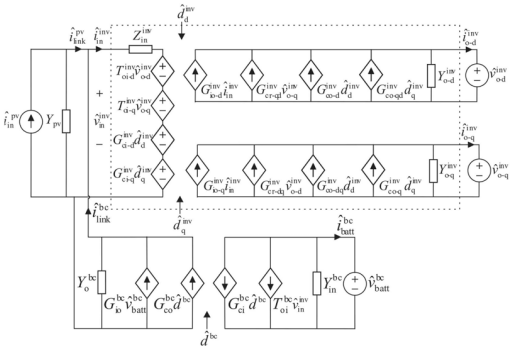

Fig. 5 *Linear equivalent circuit of the BESS-PV inverter*

irradiance, its current–voltage characteristic exhibits a unique point, the maximum power point (MPP), where the PVG produces maximum output power and which location depends on, for example the irradiance level and the cell temperature [10]. Due to the voltage–current characteristics of PVGs, when the PVG voltage is higher than the MPP voltage, the PVG is said to operate in CVR, and when the PVG voltage is lower than the MPP voltage, the PVG is said to operate in CCR. To operate the PVG efficiently, its MPP needs to be tracked continuously to yield the maximum power.

2.3 Dynamic model of grid-connected inverter

The dynamic behaviour of the three-phase inverter can be presented in matrix form as

$$\begin{bmatrix} \hat{v}_{\mathrm{in}}^{\mathrm{inv}} \\ \hat{i}_{\mathrm{o-d}}^{\mathrm{inv}} \\ \hat{i}_{\mathrm{o-q}}^{\mathrm{inv}} \end{bmatrix} = \begin{bmatrix} Z_{\mathrm{in}}^{\mathrm{inv}} & T_{\mathrm{oi-d}}^{\mathrm{inv}} & T_{\mathrm{oi-q}}^{\mathrm{inv}} & G_{\mathrm{ci-d}}^{\mathrm{inv}} & G_{\mathrm{ci-q}}^{\mathrm{inv}} \\ G_{\mathrm{io-d}}^{\mathrm{inv}} & -Y_{\mathrm{o-d}}^{\mathrm{inv}} & G_{\mathrm{cr-qd}}^{\mathrm{inv}} & G_{\mathrm{co-d}}^{\mathrm{inv}} & G_{\mathrm{co-qd}}^{\mathrm{inv}} \\ G_{\mathrm{io-q}}^{\mathrm{inv}} & G_{\mathrm{cr-dq}}^{\mathrm{inv}} & -Y_{\mathrm{o-q}}^{\mathrm{inv}} & G_{\mathrm{co-dq}}^{\mathrm{inv}} & G_{\mathrm{co-q}}^{\mathrm{inv}} \end{bmatrix} \begin{bmatrix} \hat{i}_{\mathrm{in}}^{\mathrm{inv}} \\ \hat{v}_{\mathrm{o-d}}^{\mathrm{inv}} \\ \hat{v}_{\mathrm{o-q}}^{\mathrm{inv}} \\ \hat{d}_{\mathrm{d}}^{\mathrm{inv}} \\ \hat{d}_{\mathrm{q}}^{\mathrm{inv}} \end{bmatrix}, \quad (8)$$

where the 3×5 matrix consists of the transfer functions between the input and output variables and the ac-variables are represented in the synchronously rotating *dq*-reference frame. The derivation of these transfer functions can be found, for example in [11].

The inverter is controlled using a cascaded control scheme: the output current *d*-component control acts as the inner loop and its reference is defined by the dc-link voltage controller. A PI controller is adopted in this paper due to its simple structure and easy implementation utilising the *dq*-reference frame. The control system is illustrated in Fig. 4.

2.4 Integrating the effect of BC and PVG into the inverter dynamic model

Based on (8), the linear small-signal model of the inverter at an open loop can be depicted as inside the dashed area in Fig. 5 (as a un-terminated model, without the load effect). The non-ideal characteristics of the PVG, i.e. the dynamic resistance, can be presented using an admittance term

$$Y_{\mathrm{pv}} = \frac{1}{r_{\mathrm{pv}}} \quad (9)$$

in parallel with the current source. That is, the PVG (output) current can be given as

$$i_{\mathrm{link}}^{\mathrm{pv}} = i_{\mathrm{in}}^{\mathrm{pv}} - Y_{\mathrm{pv}} v_{\mathrm{pv}}, \quad (10)$$

where the voltage over the PVG v_{pv} equals to the dc-link voltage. Based on (4) and (10), the PVG and BESS can be included as in the rest of Fig. 5 thus representing the linear equivalent circuit for the whole system: the three-phase one-stage PV inverter with the BC connected at the dc link and operated with battery current control. The controlled variables are the battery current, the voltage over the PVG, i.e. the dc-link voltage, and the inverter output current.

As can be concluded from the figure, the effect of the BC and the PVG on the inverter dynamics can be analysed by inserting the BC and PVG small-signal dynamic models into the small-signal dynamic model of the inverter. More precisely, by following Kirchhoff's current law, the inverter input current is substituted with the sum of the PVG (output) current and the BC output current as in (11), thus, taking the effect of these two sources into account.

$$\hat{i}_{\mathrm{in}}^{\mathrm{inv}} = \hat{i}_{\mathrm{link}}^{\mathrm{bc}} + \hat{i}_{\mathrm{pv}} \quad (11)$$

By presenting the inverter dynamics as in (8) and the BC closed-loop dynamics as in (4) and then following the approach, the BC and PVG -affected inverter dynamics can be given by (14). From these transfer functions, the effect of the BC and the PVG can be concluded. Thus, for example the source-affected control-related transfer functions of the inverter can be given as

$$G_{\mathrm{ci-d}}^{\mathrm{inv-S}} = \frac{G_{\mathrm{ci-d}}^{\mathrm{inv}}}{1 + Z_{\mathrm{in}}^{\mathrm{inv}} Y_{\mathrm{o}}^{\mathrm{S}}}, \quad (12)$$

$$G_{\mathrm{co-d}}^{\mathrm{inv-S}} = G_{\mathrm{co-d}}^{\mathrm{inv}} - \frac{G_{\mathrm{io-d}}^{\mathrm{inv}} G_{\mathrm{ci-d}}^{\mathrm{inv}} Y_{\mathrm{o}}^{\mathrm{S}}}{1 + Z_{\mathrm{in}}^{\mathrm{inv}} Y_{\mathrm{o}}^{\mathrm{S}}}. \quad (13)$$

Therefore, the effect of the PVG and the BC on the inverter control dynamics can be predicted based on these equations by estimating their output admittances, i.e. the dynamic behaviour between the dc-link voltage and the current fed/drawn to/from the dc link.

3 Small-signal stability analysis

By following the stated approach, the frequency responses can be evaluated for different system parameters. The small-signal stability of the chosen system can be analysed using the derived transfer functions and Bode or Nyquist plots under different operating conditions. In line with the notation in Fig. 1, the used parameters are given in Table 1.

3.1 Control loop gains

Fig. 6–8 present the source-affected inverter control-to-output current *d*-component frequency responses when the BC is operated in open- and closed-loop in discharging mode and when it is disconnected, i.e. the PVG is the only source taken into account. Changing the BC mode to charging does not change the results significantly, so they are left out of the paper. The solid black lines

Table 1 Parameter values used in the analysis

Parameter	Value	Parameter	Value
C_{dc}	1 mF	C_b	1 μF
L	1 mH	L_b	1.3 mH
f_{grid}	60 Hz	v_{batt}	200 V
v_{dc}	350…550 V	i_{batt}	± 5 A
MPP	480 V, 8 A (STC)	f_{sw}	20 kHz

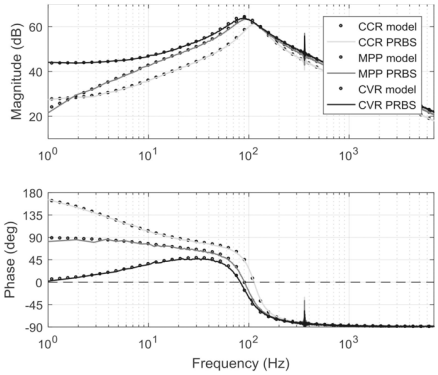

Fig. 6 *Frequency response of G_{co-d}^{inv-S} when BC is disconnected*

represent the frequency responses measured from MATLAB-Simulink model when the PVG is operated in CVR, the grey solid lines at MPP, and the light grey solid lines in CCR. The dotted lines represent the corresponding predicted frequency responses based on the derived model, i.e. Equation (13). It is clear, that in all the considered modes the model predicts the frequency response with good accuracy.

When the PVG is operated in CCR and the BC is disconnected, the control-to-*d*-channel current transfer function includes a low-frequency right-half-plane (RHP) zero that increases the phase at low frequencies to 180° instead of 0° (as when the PVG is operated in CVR). This can be seen in Fig. 6. Since the inverter is operated using a cascaded control scheme in which the outer loop controls the dc-link voltage and the inner loop the inverter current, the RHP zero becomes an RHP pole in the dc-voltage control loop.

The dc-voltage control is usually tuned for a low bandwidth due to the limitations set by the cascaded control scheme and to mitigate second harmonic ripple caused by un-balanced grid voltages. As a rule of thumb, the crossover frequency of the control loop gain should be at least two times higher than the frequency of the RHP-pole [12]. As a result, the low-frequency RHP-pole can easily cause instability. It should also be noted that the frequency of the RHP-pole also depends on the value of the dc-link capacitance and the controller tuning.

However, when the PVG is operated in CCR and the BC is added to the system and operated in closed-loop, its output admittance shifts the RHP zero to a lower frequency. This can be seen in the figures by comparing Fig. 6 with Fig. 7: at low frequencies, the phase of G_{co-d}^{inv-S} is lower when the BC is used. Due to the lower frequency of the RHP zero, the inverter dc-voltage control is less likely to become unstable. This allows a more flexible control design. Therefore, the introduction of BC has a positive effect on the inverter's stability.

Furthermore, when the BC is operated in open-loop, there exists no RHP zero in the inverter control-to-output current *d*-component transfer function, because the BC output admittance shifts the RHP zero to the LHP (left-half-plane) (see (14)) side. Consequently, in Fig. 8, the phase of the frequency response in CCR starts at 0° at low frequencies. Therefore, the RHP pole does not limit the dc-voltage control bandwidth and it can be chosen more freely. However, due to batteries' sensitivity to over-current and over-charge, open-loop control cannot be used.

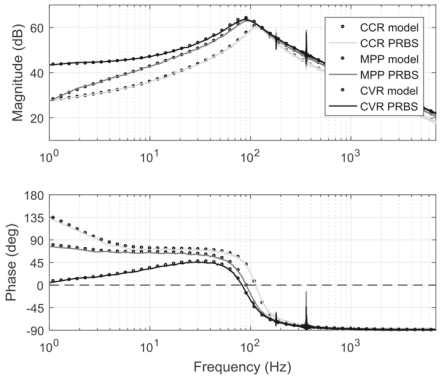

Fig. 7 *Frequency response of G_{co-d}^{inv-S} when BC is discharged in closed-loop (5 A)*

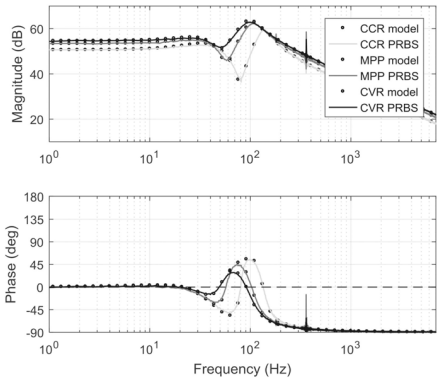

Fig. 8 *Frequency response of G_{co-d}^{inv-S} when BC is discharged in open loop (5 A)*

3.2 Root-loci analysis

In this section, root-loci plots of the real zero of the source-affected inverter control-to-output current *d*-component transfer function (i.e. G_{co-d}^{inv-S}) under a wide range of PVG voltage is analysed. The focus is only on this zero to simplify the results and to further investigate its effect on the inverter control dynamics.

Fig. 9 presents the location of the zero in the s-plane of the Laplace transform, where the parameter s represents the complex angular frequency, at different PVG voltages. As the PVG voltage increases, the zero moves along the real axis from 10.7 to −16.0 rad/s when the BESS is discharged, from 28.5 to −56.1 rad/s when the BESS is disconnected, and from 10.6 to −15.9 rad/s when the BESS is charged. In all the cases, when the PVG is operated at the MPP voltage, the zero is at the origin. However, when the PVG is operated in the CCR, the BESS limits the frequency of the RHP zero to lower frequencies (both in charging and discharging modes) compared to the situation where the BESS is disconnected.

4 Time-domain simulation results

In this section, the effect of the RHP pole in the dc-link control loop on the system stability is demonstrated in time-domain using a MATLAB-Simulink simulation. The results are shown in Fig. 10, where the dc-link voltage is controlled at 300 V so that the PVG operates in CCR, thus introducing the RHP pole in the control dynamics. The dc-voltage controller is tuned with a cross-over frequency of 10 Hz, i.e. 62.8 rad/s. When the BC is connected, the RHP pole is at a frequency of 9.2 rad/s, thus enabling a stable control.

$$\begin{bmatrix} \hat{v}_{\text{in}}^{\text{inv}} \\ \hat{i}_{\text{o-d}}^{\text{inv}} \\ \hat{i}_{\text{o-q}}^{\text{inv}} \end{bmatrix} = \frac{1}{\sigma} \begin{bmatrix} Z_{\text{in}}^{\text{inv}} & G_{\text{io-c}}^{\text{inv}} Z_{\text{in}}^{\text{inv}} & T_{\text{oi-d}}^{\text{inv}} & T_{\text{oi-q}}^{\text{inv}} \\ G_{\text{io-d}}^{\text{inv}} & G_{\text{io-c}}^{\text{bc}} G_{\text{io-d}}^{\text{inv}} & -\left(Y_{\text{o-d}}^{\text{inv}}\sigma + G_{\text{io-d}}^{\text{inv}} T_{\text{oi-d}}^{\text{inv}} Y_{\text{o}}^{\text{S}}\right) & -\left(Y_{\text{o-qd}}^{\text{inv}}\sigma + G_{\text{io-d}}^{\text{inv}} T_{\text{oi-q}}^{\text{inv}} Y_{\text{o}}^{\text{S}}\right) \\ G_{\text{io-q}}^{\text{inv}} & G_{\text{io-c}}^{\text{bc}} G_{\text{io-q}}^{\text{inv}} & -\left(Y_{\text{o-dq}}^{\text{inv}}\sigma + G_{\text{io-q}}^{\text{inv}} T_{\text{oi-d}}^{\text{inv}} Y_{\text{o}}^{\text{S}}\right) & -\left(Y_{\text{o-q}}^{\text{inv}}\sigma + G_{\text{io-q}}^{\text{inv}} T_{\text{oi-q}}^{\text{inv}} Y_{\text{o}}^{\text{S}}\right) \end{bmatrix}$$

$$\begin{bmatrix} G_{\text{ci-d}}^{\text{inv}} & G_{\text{ci-q}}^{\text{inv}} \\ G_{\text{co-d}}^{\text{inv}}\sigma - G_{\text{io-d}}^{\text{inv}} G_{\text{ci-d}}^{\text{inv}} Y_{\text{o}}^{\text{S}} & G_{\text{co-qd}}^{\text{inv}}\sigma - G_{\text{io-d}}^{\text{inv}} G_{\text{ci-q}}^{\text{inv}} Y_{\text{o}}^{\text{S}} \\ G_{\text{co-dq}}^{\text{inv}}\sigma - G_{\text{io-q}}^{\text{inv}} G_{\text{ci-d}}^{\text{inv}} Y_{\text{o}}^{\text{S}} & G_{\text{co-q}}^{\text{inv}}\sigma - G_{\text{io-q}}^{\text{inv}} G_{\text{ci-q}}^{\text{inv}} Y_{\text{o}}^{\text{S}} \end{bmatrix} \begin{bmatrix} \hat{i}_{\text{in}}^{\text{pv}} \\ \hat{v}_{\text{batt}}^{\text{bc}} \\ \hat{v}_{\text{o-d}}^{\text{inv}} \\ \hat{v}_{\text{o-q}}^{\text{inv}} \\ \hat{d}_{\text{d}}^{\text{inv}} \\ \hat{d}_{\text{q}}^{\text{inv}} \end{bmatrix} \tag{14}$$

$$Y_{\text{o}}^{\text{S}} = Y_{\text{pv}} + Y_{\text{o-c}}^{bc}, \quad \sigma = 1 + Z_{\text{in}}^{\text{inv}} Y_{\text{o}}^{\text{S}}$$

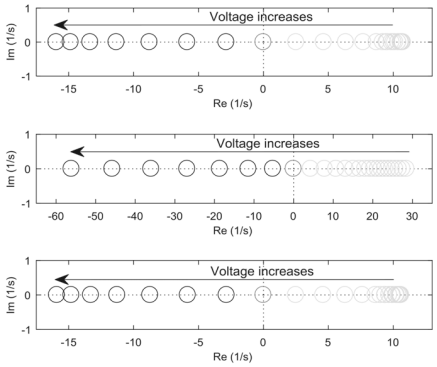

Fig. 9 *Low-frequency zero of* $G_{\text{co-d}}^{\text{inv-S}}$ *on the real-axis for different PVG voltages when the BESS is*
(a) Discharging ***(b)*** Disconnected and, ***(c)*** Charging

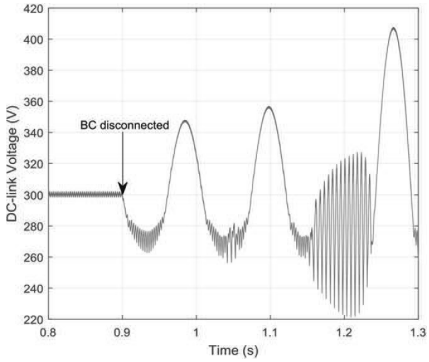

Fig. 10 *Dc-link voltage before and after the BC is disconnected while the PVG is operated in CCR*

However, at 0.9 s, the BC is disconnected from the system, and the RHP pole shifts to 28.5 rad/s, making the system unstable. This can be clearly seen in the figure as the increasing oscillation in the dc-link voltage. Due to the cascaded control loop, also the output current starts to oscillate increasingly. This instability can be predicted using the derived transfer functions to study the voltage control loop, which indicates a negative phase margin when the system is unstable.

5 Conclusion

This paper presents a method to solve the dynamic model of a grid-connected photovoltaic inverter with battery storage, thus predicting accurately, for example, the inverter's control-related transfer functions and the system's output impedance. Note, that the used method can also be applied to any type of inverter, sources, and different control schemes. The derived model has been verified through simulation studies in both time and frequency domains in all the operating modes. Using the model, the effect of PVG and the BC on the dynamics of the grid-connected inverter has been analysed.

The analysis shows that the BC has a significant positive effect on the inverter performance, and more precisely, on the dc-link voltage control, thus preventing instability arising in the CCR of the PVG. In the closed-loop operating mode, the BC operates as a constant-power source and its output admittance moves the characteristic low-frequency RHP pole of the dc-link voltage control towards the origin compared to a situation where the BC is disconnected. Consequently, either the dc-link capacitor can be selected to be smaller or more flexibility is allowed when designing the bandwidth of the dc-link voltage controller without compromising the stability of the system.

6 References

[1] Nosair, H., Bouffard, F.: 'Flexibility envelopes for power system operational planning', *IEEE Trans. Sustain. Energy*, 2015, **6**, (3), pp. 800–809

[2] Soder, L., Abildgaard, H., Estanqueiro, A., *et al.*: 'Experience and challenges with short-term balancing in European systems with large share of wind power', *IEEE Trans. Sustain. Energy*, 2012, **3**, (4), pp. 853–861

[3] Zhai, Q., Meng, K., Dong, Z.Y., *et al.*: 'Modeling and analysis of lithium battery operations in spot and frequency regulation service markets in Australia electricity market', *IEEE Trans. Ind. Inf.*, 2017, **13**, (5), pp. 2576–2586

[4] Savkin, A.V., Khalid, M., Agelidis, V.G.: 'A constrained monotonic charging/discharging strategy for optimal capacity of battery energy storage supporting wind farms', *IEEE Trans. Sustain. Energy*, 2016, **7**, (3), pp. 1224–1231

[5] Li, X., Hui, D., Lai, X.: 'Battery energy storage station (BESS)-based smoothing control of photovoltaic (PV) and wind power generation fluctuations', *IEEE Trans. Sustain. Energy*, 2013, **4**, (2), pp. 464–473

[6] Tan, X., Wu, Y., Tsang, D.H.K.: 'Pareto optimal operation of distributed battery energy storage systems for energy arbitrage under dynamic pricing', *IEEE Trans. Parallel Distrib. Syst.*, 2016, **27**, (7), pp. 2103–2115

[7] Nousiainen, L., Puukko, J., Mäki, A., *et al.*: 'Photovoltaic generator as an input source for power electronic converters', *IEEE Trans. Power Electron.*, 2013, **28**, (6), pp. 3028–3038

[8] Narasimharaju, B.L., Dubey, S.P., Singh, S.P., *et al.*: 'Modelling and stability analysis of coupled inductor bidirectional DC-DC converter'. 2010 IEEE Int. Conf. of Electron Devices and Solid-State Circuits (EDSSC), Hong Kong, 2010

[9] Ramadan, H.A., Imamura, Y., Yang, S., *et al.*: 'A new stability assessment criterion for dc power systems using multi-level virtual conductors'. 2014 IEEE 15th Workshop on Control and Modeling for Power Electronics (COMPEL), Santander, 2014

[10] Liu, S., Dougal, R.A.: 'Dynamic multiphysics model for solar array', *IEEE Trans. Energy Convers.*, 2002, **17**, (2), pp. 285–294

[11] Messo, T., Jokipii, J., Puukko, J., *et al.*: 'Determining the value of DC-link capacitance to ensure stable operation of a three-phase photovoltaic inverter', *IEEE Trans. Power Electron.*, 2014, **29**, (2), pp. 665–673

[12] Skogestad, S., Postlethwaite, I.: '*Multivariable feedback control: analysis and Design*' (John Wiley & Sons Ltd., West Sussex, England, 1996)

PUBLICATION

III

Mitigating Voltage Fluctuations in Battery Energy Storage Systems
R.-M. Sallinen, T. Messo and T. Roinila

in *Proc. IEEE Workshop on Control and Modeling for Power Electronics*, 6 pages, 2019.

Mitigating Voltage Fluctuations in Battery Energy Storage Systems

Roosa-Maria Sallinen
Faculty of Information Technology and Communication Sciences
Tampere University
Tampere, Finland
roosa.sallinen@tuni.fi

Tuomas Messo
Faculty of Information Technology and Communication Sciences
Tampere University
Tampere, Finland
tuomas.messo@tuni.fi

Tomi Roinila
Faculty of Engineering and Natural Sciences
Tampere University
Tampere, Finland
tomi.roinila@tuni.fi

***Abstract*—Battery Energy Storage Systems (BESSs) play an important role in grid-connected renewable energy systems as they provide great flexibility in the energy production. For photovoltaic (PV) energy applications, the BESS may be connected to the dc-link of the converter system to inject the deficit or to absorb the surplus of generated power. One of the main issues in such systems is the voltage variation at the dc-link, especially under grid imbalance, distorting the current fed to the grid. This paper studies a method to control the BESS to emulate a capacitance, thus mitigating the dc-link voltage fluctuation, for example, under heavy imbalance. The derived model initiates impedance-based analysis at the output of the battery charger.**

***Index Terms*—Battery energy storage system, dc-link voltage fluctuation, virtual capacitance, PV-inverter, imbalance**

I. Introduction

Battery energy storage systems (BESSs) are gaining popularity as a supplement to grid-connected photovoltaic (PV) generators as they enable using the energy when needed instead of when generated [1]. BESSs have several applications in power systems, such as peak load shaving, power outage mitigation, and frequency regulation [2], [3]. However, regardless of the advancements made in the field, they are still fairly expensive components and often have a relatively short lifespan [4]. Therefore, it should be a priority to utilize BESSs as efficiently as possible.

In PV applications, a BESS is often connected to the dc-link of an inverter that functions as the system's grid interface. In such a system, the dc-link voltage regulation is important in order to guarantee that the current fed to the grid complies with the grid codes. To this end, commonly a large capacitor per unit volume is placed on the dc-link to mitigate the voltage fluctuations. The capacitor also limits the dc-link voltage ripple, absorbs harmonics, and provides energy storage during transients [5]. However, a large capacitor increases the total cost and size of the system as well as slows down the voltage response during start-up phase [6].

To overcome these drawbacks, recent studies have proposed methods that enable the use of reduced dc-link capacitors in inverter-based systems without losing system reliability [6], [7]. The work in [6] presented an estimator-based method for a motor-drive application that stabilizes both the dc-link voltage and the motor current so that a reduced dc-link capacitor may be used. The work in [7] proposed an active power compensator in order to remove the second harmonic ripple of the dc-link voltage under imbalanced grid-voltages. However, applications involving a BESS have not been considered in these previous studies.

In order to attenuate the dc-link voltage variations in a grid-connected BESS with a reduced capacitor, a feedback/feedforward control strategy has been proposed [8]. This approach is based on the assumption that the BESS (instead of the inverter) controls the dc-link voltage. However, this may not always be the case, e.g., in PV applications [9]. For such a system, in which the inverter controls the dc-link voltage, the work in [10] proposed a method to emulate a BESS as a capacitor in order to synthesize extra inertia. However, as the main focus of the work in [10] is to compare dc-link capacitance with system inertia and to synthesize extra inertia to the system, it does not include a further analysis of the system dynamics nor address the control in the frequency-domain.

This paper analyses the method of controlling a BESS to emulate a (virtual) capacitance. The analysis is performed using small-signal models to enable reliable and straightforward investigation of the system dynamics and control design. The limitations and possible issues of the control algorithm are also emphasized. As a result, the system dynamics can be adjusted by using this controllable virtual capacitance. Special focus is given on the application where a BESS is connected to a dc-link. In this case, the BESS effectively increases the dc-link capacitance, thus, for example, mitigating the second order harmonic in the dc-link voltage during a grid imbalance. The analysis is confirmed by simulations both in the time and frequency domain.

The remainder of the paper is organized as follows. In Section II, the basic idea and analysis behind the capacitance emulation algorithm are presented. In Section III, the required small-signal models are derived. That is, the dynamics of the battery charger emulating a capacitance are determined. Section IV demonstrates and further analyses the ability of the

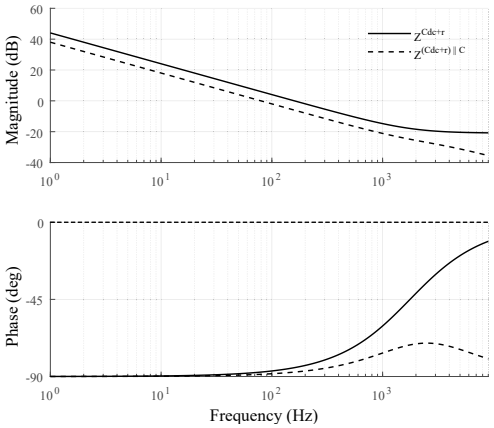

Fig. 1. The impedances of an RC circuit (solid line) and an RC circuit in parallel with a capacitor (dashed line).

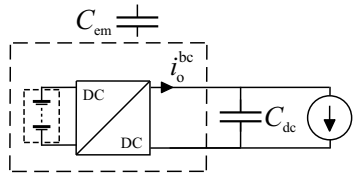

Fig. 2. Illustration of the capacitance emulation.

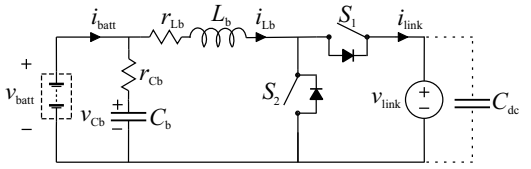

Fig. 3. Bi-directional dc-dc converter used as battery charger.

control algorithm to affect the system dynamics and to mitigate the dc-link voltage fluctuation. The paper is summarized in Section V.

II. Capacitance Emulation

The impedance of a dc-link capacitor is generally given as

$$Z^{\text{Cdc+r}} = r_{\text{Cdc}} + \frac{1}{C_{\text{dc}}s}, \tag{1}$$

where C_{dc} is the (dc-link) capacitance and r_{Cdc} its parasitic resistance. When connecting the dc-link capacitor in parallel with an ideal capacitor (that is, the parasitic resistance is ignored), their total impedance can be presented as

$$Z^{(\text{Cdc+r})\|\text{C}} = \frac{1 + r_{\text{Cdc}}C_{\text{dc}}s}{r_{\text{Cdc}}C_{\text{dc}}Cs^2 + (C_{\text{dc}} + C)\,s}, \tag{2}$$

where C is the ideal capacitance. Fig. 1 gives an example where the impedances given by (1) and (2) are shown (the parameter values are specified in Table I). The addition of the capacitor in parallel lowers the magnitude of the impedance, hence mitigating variations/disturbances in the voltage more effectively.

In order to control the BESS to emulate a capacitance (in terms of impedance), the battery charger needs to control its output current i_{o}^{bc} according to

$$i_{\text{o}}^{\text{bc-ref}} \;=\; -\,C_{\text{em}}\frac{dv_{\text{o}}^{\text{bc}}}{dt} \;=\; -\,C_{\text{em}}sv_{\text{o}}^{\text{bc}}, \tag{3}$$

where C_{em} represents the emulated capacitance and v_{o}^{bc} the output voltage of the battery charger. Note that here the positive direction of the current is defined as out of the battery charger. As impedance/admittance is (by definition) measured when the current goes into the device, it requires a minus sign. The control idea is further illustrated in Fig. 2. With this control, the output impedance of the BESS would ideally become

$$Z_{\text{C-em}} = \frac{1}{C_{\text{em}}s}. \tag{4}$$

A similar control principle has been used, e.g., in [10].

Using the Euler discretization method, the control algorithm (3) can be presented in discrete-time as

$$i_{\text{o}}^{\text{bc-ref}}(z) \;=\; -\,C_{\text{em}}\frac{z-1}{T_{\text{s}}}v_{\text{o}}^{\text{bc}}, \tag{5}$$

where T_{s} is the sampling interval.

It is emphasized, that any controller that utilizes numerical derivative is sensitive to noise. The sensitivity is inversely proportional to the magnitude of the sampling time [11]. Hence, in a practical system, a low-pass filter should be used to filter out the noise. Otherwise the output of the controller may fluctuate severely, possibly decreasing the lifetime of the switches.

III. Small-Signal Model of the Battery Charger for Capacitance Emulation

Fig. 3 presents a schematic diagram of a bi-directional dc-dc converter in which the output current i_{link} is defined as an output variable. That is, the dc-link can be modelled as a constant voltage source. Note that the direction of the current is as in discharging mode and, in this paper, will be defined as the positive current direction. In charging mode, the flow is the opposite and the current is defined as negative.

In order to derive a small-signal model for the system, the state vector, and input and output vectors are defined as

$$\hat{\mathbf{x}}(t) = \begin{bmatrix} \hat{v}_{\text{Cb}}^{\text{bc}} \\ \hat{i}_{\text{Lb}}^{\text{bc}} \end{bmatrix}, \hat{\mathbf{u}}(t) = \begin{bmatrix} \hat{v}_{\text{batt}}^{\text{bc}} \\ \hat{v}_{\text{link}}^{\text{bc}} \\ \hat{d}^{\text{bc}} \end{bmatrix}, \hat{\mathbf{y}}(t) = \begin{bmatrix} \hat{i}_{\text{batt}}^{\text{bc}} \\ \hat{i}_{\text{link}}^{\text{bc}} \end{bmatrix}, \tag{6}$$

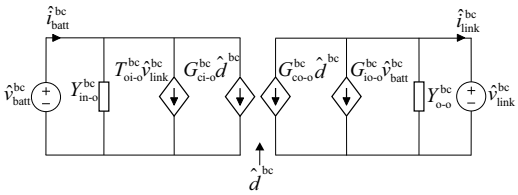

Fig. 4. Linear equivalent model of the bi-directional dc-dc converter used as battery charger.

respectively. Note that switch S_2 is controlled by duty cycle d^{bc} and switch S_1 by its opposite, $1-d^{\text{bc}}$. The linearised state-space representation of the battery charger can be given as,

$$\frac{d\hat{\mathbf{x}}(t)}{dt} = \mathbf{A}\hat{\mathbf{x}}(t) + \mathbf{B}\hat{\mathbf{u}}(t) \tag{7}$$

$$\hat{\mathbf{y}}(t) = \mathbf{C}\hat{\mathbf{x}}(t) + \mathbf{D}\hat{\mathbf{u}}(t), \tag{8}$$

where the state, input, output, and feed-through matrices $\mathbf{A}$, $\mathbf{B}$, $\mathbf{C}$, and $\mathbf{D}$, respectively, are given in the Appendix.

The transfer functions from the input variables to the output variables at open loop can be solved in the s-domain by noting that

$$\mathbf{y}(s) = \Big(\mathbf{C}(s\mathbf{I} - \mathbf{A})^{-1}\mathbf{B} + \mathbf{D}\Big)\,\mathbf{u}(s), \tag{9}$$

where $\mathbf{I}$ is the identity matrix [12]. As a result, the open-loop dynamics can be presented in matrix-form as

$$\begin{bmatrix} \hat{i}_{\text{batt}}^{\text{bc}} \\ \hat{i}_{\text{link}}^{\text{bc}} \end{bmatrix} = \begin{bmatrix} Y_{\text{in-o}}^{\text{bc}} & T_{\text{oi-o}}^{\text{bc}} & G_{\text{ci-o}}^{\text{bc}} \\ G_{\text{io-o}}^{\text{bc}} & -Y_{\text{o-o}}^{\text{bc}} & G_{\text{co-o}}^{\text{bc}} \end{bmatrix} \begin{bmatrix} \hat{v}_{\text{batt}}^{\text{bc}} \\ \hat{v}_{\text{link}}^{\text{bc}} \\ \hat{d}^{\text{bc}} \end{bmatrix} \tag{10}$$

where the 2x3 matrix consists of the transfer functions between the input and the output variables. Fig. 4 illustrates the linear equivalent model of the system. The change in the converter transient response caused by a load change can be directly seen from the output impedance $Y_{\text{o-o}}^{\text{bc}}$ (when controlled in open-loop).

By utilizing a feedback controller on the battery charger output current according to the capacitance emulation algorithm given in (3), the closed-loop dynamics can be presented as

$$\begin{aligned} \begin{bmatrix} \hat{i}_{\text{batt}}^{\text{bc}} \\ \hat{i}_{\text{link}}^{\text{bc}} \end{bmatrix} &= \begin{bmatrix} Y_{\text{in-c}}^{\text{bc-Cem}} & T_{\text{oi-c}}^{\text{bc-Cem}} \\ G_{\text{io-c}}^{\text{bc-Cem}} & -Y_{\text{o-c}}^{\text{bc-Cem}} \end{bmatrix} \overbrace{\begin{bmatrix} \hat{v}_{\text{batt}}^{\text{bc}} \\ \hat{v}_{\text{link}}^{\text{bc}} \end{bmatrix}}^{\hat{\mathbf{u}}_{\text{Cem.}}} \\ &= \begin{bmatrix} Y_{\text{in-o}}^{\text{bc}} - \dfrac{G_{\text{PI}}^{\text{bc}} G_{\text{ci-o}}^{\text{bc}} G_{\text{io-o}}^{\text{bc}}}{1 + L_{\text{out-bc}}} & T_{\text{oi-o}}^{\text{bc}} + \dfrac{G_{\text{PI}}^{\text{bc}} G_{\text{ci-o}}^{\text{bc}} Y_{\text{o}}^{\text{S}}}{1 + L_{\text{out-bc}}} \\ G_{\text{io-o}}^{\text{bc}} - \dfrac{G_{\text{PI}}^{\text{bc}} G_{\text{co-o}}^{\text{bc}} G_{\text{io-o}}^{\text{bc}}}{1 + L_{\text{out-bc}}} & -Y_{\text{o-o}}^{\text{bc}} + \dfrac{G_{\text{PI}}^{\text{bc}} G_{\text{co-o}}^{\text{bc}} Y_{\text{o}}^{\text{S}}}{1 + L_{\text{out-bc}}} \end{bmatrix} \hat{\mathbf{u}}_{\text{Cem.}}, \end{aligned} \tag{11}$$

where

$$Y_{\text{o}}^{\text{S}} = Y_{\text{o-o}}^{\text{bc}} - C_{\text{em}}s, \tag{12}$$

$$L_{\text{out-bc}} = G_{\text{PI}}^{\text{bc}} G_{\text{co-o}}^{\text{bc}}, \tag{13}$$

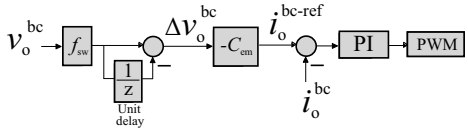

Fig. 5. Control block diagram of the battery controller for capacitor emulation.

TABLE I
PARAMETERS USED IN THE SIMULATION RESULTS

DC-DC converter		
Parameter	***Symbol***	***Value***
dc-link voltage	V_{link}	480 V
battery terminal voltage	V_{batt}	200 V
dc-link capacitance	C_{dc}	1 mF
parasitic resistance of dc-link capacitance	r_{Cdc}	90 mΩ
additional dc-link capacitance	C	1 mF
emulated dc-link capacitance	C_{em}	1 mF
switching frequency	f_{sw}	20 kHz
battery-side capacitor	C_{b}	1 μF
battery-side inductor	L_{b}	1.3 mH
PV inverter		
Parameter	***Symbol***	***Value***
MPP conditions (STC)	$V_{\text{pv-mpp}}$, $I_{\text{pv-mpp}}$	480 V, 8 A
grid voltage (RMS)	$V_{\text{a,b,c}}$	240 V
grid frequency	f_{g}	60 Hz
L-filter	L	1 mH

in which a proportional-integral (PI) controller $G_{\text{PI}}^{\text{bc}}$ is used to regulate the output current. Assuming $L_{\text{out-bc}} \gg 1$ (i.e. within the control bandwidth), the closed loop output admittance $Y_{\text{o-c}}^{\text{bc-Cem}}$ becomes equal to $-C_{\text{em}}s$, i.e. the output impedance of a capacitance (the inverse of (4)). The closed-loop dynamics can be used to evaluate the source-effect of the BESS under the capacitance emulation algorithm on other parts of the converter system and to initiate impedance-based stability analysis.

Fig. 5 illustrates the (discretized) control structure. In addition, battery safety must be guaranteed, for example, by saturation limits. The controller should be implemented to limit the current and voltage at the battery terminal to avoid extensive stress on the battery. However, for simplicity and clarity, the implementation of this has been left out in this paper. That is, the focus is only on the capacitor emulation. Furthermore, in a real application, the control function would mainly be used as a supplementary control algorithm.

IV. Analysis and Simulation Results

This section demonstrates and further analyses the ability of the control algorithm to mitigate the dc-link voltage fluctuation. First, analysis and simulations regarding only the battery charger shown in Fig. 3 are given. After this, a more practical case is considered where the battery system is connected to a PV inverter.

The parameters used in the simulations are specified in Table I. The crossover frequency of the PI-controller is chosen as 800 Hz since higher value would decrease the phase margin to $<65°$ due to control delay. The controller zero is located

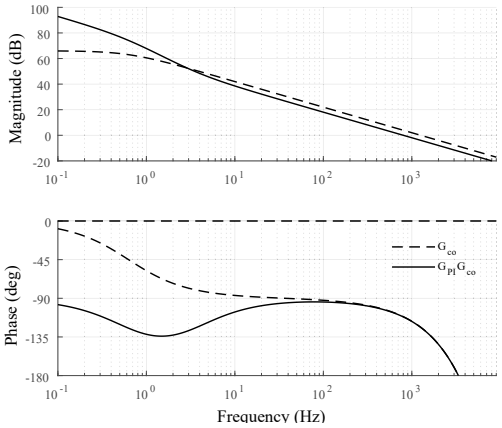

Fig. 6. Control to input transfer function (dashed line) and controller loop gain (solid line).

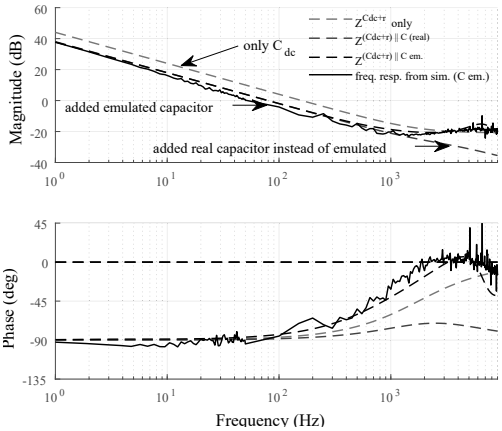

Fig. 7. Output impedance of emulated and real capacitors in parallel with dc-link capacitor.

to have -135° minimum phase at low frequencies. The system control to output transfer function $G_{\text{co-o}}^{\text{bc}}$ as well as the resulting control loop gain $L_{\text{out-bc}}$ are shown in Fig. 6.

Fig. 7 presents the frequency response of the total output impedance Z_{o} for three different cases. In the first case (dashed green line), only the output impedance of the dc-link capacitor (i.e. 90 mΩ, 1 mF) was considered (without the BESS). In the second case (dashed blue line), an additional capacitor (1 mF) was set in parallel with the dc-link. As expected, the addition of the capacitor decreases the magnitude similarly as in Fig. 1.

In the third case (dashed black line), the BESS was connected to the dc-link and set to emulate a capacitor (1 mF) instead of using the additional capacitor. This corresponds to the analysis in (11). The solid black line presents the corresponding frequency response obtained directly from MATLAB Simulink simulation model by using a nonparametric identification based on pseudo-random-binary-sequence (PRBS) injection and Fourier methods [13], [14]. The frequency response was obtained by inserting a controllable current source in parallel with the dc-link and injecting the PRBS perturbation with it. Note that the nominal output current was set to 0 A. As the figure shows, the derived output impedance of the emulated capacitor follows the measured impedance highly accurately in a wide frequency band.

With an ideal controller, the impedance with the capacitor emulation would equal to the case with the additional capacitor. However, the accuracy of the emulation depends on the controller performance; e.g, the cross-over frequency of the current controller. To demonstrate the effect of the controller cross-over frequency, Fig. 8 presents the output impedance in the case of a controller with a) 800 Hz (black solid line) and b) 500 Hz (green solid line) crossover frequency. With the higher crossover frequency, the magnitude of the emulated output

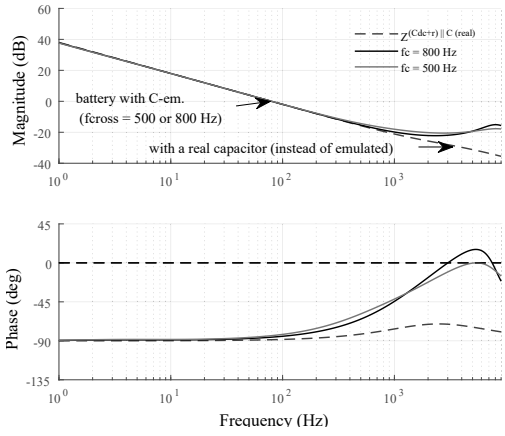

Fig. 8. The output impedance of emulated capacitor in parallel with the dc-link capacitor with different controller crossover frequencies.

impedance follows the output impedance of the additional capacitor up to higher frequencies due to the faster controller. However, the difference between them is small since the crossover frequencies are not significantly different.

To verify the correct operation of the control algorithm, a grid-connected battery-PV system illustrated in Fig. 9 was simulated under grid imbalance with and without the capacitance emulation. The imbalance is simulated by setting phase A voltage magnitude to 70 %. This introduces a second order harmonic component to the dc-link voltage, as can be seen in Fig. 10, which presents the dc-link voltage when the capacitor

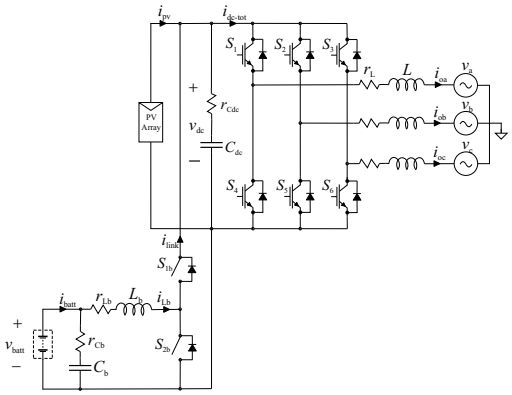

Fig. 9. The battery charger (bi-directional dc-dc converter) connected to a PV inverter.

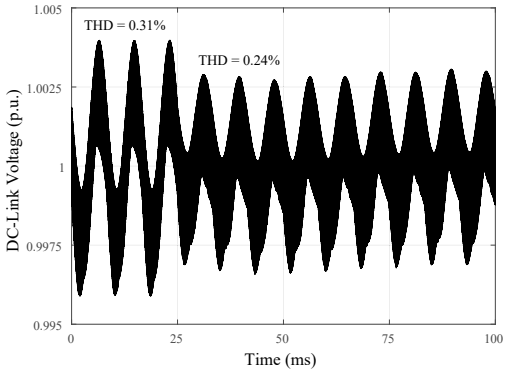

Fig. 10. Simulated dc-link voltage during grid imbalance; grid voltage phase A amplitude is set to 70 %. The capacitor emulation algorithm is set on at 25 ms.

emulation is set at 25 ms. As a result, the second harmonic component decreases from 0.24 % to 0.13 % and the total harmonic distortion (THD) from 0.31 % to 0.24 %. Hence, it is clear that the second harmonic mitigation is successful as it is within the controller bandwidth.

Furthermore, since the battery charger controls the current in an oscillatory manner such that it mitigates the second harmonic component of the dc-link voltage, the current drawn from the battery is relatively low and periodical in the sense that the average current remains at 0 A. Hence, the control scheme does not require a large battery and the state of charge (SOC) of the battery remains constant except for internal losses. However, it should be noted that due to the internal losses the battery SOC is still a limiting factor for the correct operation of the control algorithm, as the battery should not be allowed to (over- or) undercharge.

V. Conclusion

This paper has studied a method to control a BESS to emulate a capacitor so that the dc-link voltage fluctuation can be mitigated. The analysis and simulation results demonstrate that the battery can be controlled to emulate a capacitance within the battery charger's control bandwidth. As a result, the system dynamics can be adjusted by using this controllable virtual capacitance.

The analysis was performed using small-signal models to enable reliable and straightforward investigation of the system dynamics for control design. The derived model can also be used to initiate stability analysis at the output of a battery charger, e.g. at the dc-link, and to evaluate the source-effect of the BESS under the capacitance emulation algorithm on other parts of the converter system. The analysis was confirmed by simulations both in the time and frequency domain. However, it is emphasized that the battery SOC is a limiting factor for the correct operation of the control algorithm. Furthermore, the battery should not be allowed to over- or undercharge to guarantee safety and reliability of the system.

Controlling the battery to emulate a capacitor can be highly efficient, for example, if an inverter connected to the dc-link is operating under heavily imbalanced grid conditions and the dc-link capacitor is not enough to suppress the voltage fluctuation. The same effect can be achieved by increasing the dc-link capacitance. Depending on the application, the control scheme could also allow a reduced capacitance being used. However, as the control algorithm changes the system dynamics, the desired operation of the other converters in the system (e.g. inverter) must be ensured.

Appendix

The state, input, output, and feed-through matrices used in (7) are defined as

$$\mathbf{A} = \begin{bmatrix} -\dfrac{1}{C_{\mathrm{b}} r_{\mathrm{Cb}}} & 0 \\ 0 & \dfrac{R_{\mathrm{eq1}}}{L_{\mathrm{b}}} \end{bmatrix}, \ \mathbf{B} = \begin{bmatrix} \dfrac{1}{C_{\mathrm{b}} r_{\mathrm{Cb}}} & 0 & 0 \\ \dfrac{1}{L_{\mathrm{b}}} & \dfrac{D-1}{L_{\mathrm{b}}} & \dfrac{V_{\mathrm{eq}}}{L_b R_{\mathrm{eq2}}} \end{bmatrix},$$
$$\mathbf{C} = \begin{bmatrix} -\dfrac{1}{r_{\mathrm{Cb}}} & 1 \\ 0 & 1-D \end{bmatrix}, \quad \mathbf{D} = \begin{bmatrix} \dfrac{1}{r_{\mathrm{Cb}}} & 0 & 0 \\ 0 & 0 & -\dfrac{V_{\mathrm{batt}} + (D-1) V_{\mathrm{link}}}{R_{\mathrm{eq2}}} \end{bmatrix}, \tag{14}$$

respectively, where

$$\begin{aligned} R_{\mathrm{eq1}} &= (r_{\mathrm{Lb}} + r_{\mathrm{sw1}}) \ (D-1) - D \, (r_{\mathrm{Lb}} + r_{\mathrm{sw2}}) \, , \\ R_{\mathrm{eq2}} &= r_{\mathrm{Lb}} + r_{\mathrm{sw1}} + D \, (r_{\mathrm{sw2}} - r_{\mathrm{sw1}}) \, , \\ V_{\mathrm{eq}} &= (r_{\mathrm{Lb}} + r_{\mathrm{sw2}}) V_{\mathrm{link}} + (r_{\mathrm{sw1}} - r_{\mathrm{sw2}}) V_{\mathrm{batt}} , \end{aligned} \tag{15}$$

r_{sw1} is the internal on-time resistance of the switch S_1 and r_{sw2} the internal on-time resistance of the switch S_2 and the rest of the variables are as given in Fig. 3. Furthermore, the capital

letters represent steady-state values and the steady-state value of the duty cycle is defined as in Eq. 16.

$$D = \frac{V_{\text{link}} - V_{\text{batt}} + I_{\text{batt}}^{\text{ref}} \left(r_{\text{Lb}} + r_{\text{sw1}}\right)}{V_{\text{link}} + I_{\text{batt}}^{\text{ref}} \left(r_{\text{sw1}} + r_{\text{sw2}}\right)} \tag{16}$$

REFERENCES

[1] IRENA, *Electricity Storage and Renewables: Costs and Markets to 2030*. International Renewable Energy Agency, 2017.

[2] E. Telaretti and L. Dusonchet, "Battery storage systems for peak load shaving applications: Part 1: Operating strategy and modification of the power diagram," in *2016 IEEE 16th International Conference on Environment and Electrical Engineering (EEEIC)*, June 2016, pp. 1–6.

[3] R. Hidalgo-Len, D. Siguenza, C. Sanchez, J. Len, P. Jcome-Ruiz, J. Wu, and D. Ortiz, "A survey of battery energy storage system (bess), applications and environmental impacts in power systems," in *2017 IEEE Second Ecuador Technical Chapters Meeting (ETCM)*, Oct 2017, pp. 1–6.

[4] Y. Tian, A. Bera, M. Benidris, and J. Mitra, "Stacked revenue and technical benefits of a grid-connected energy storage system," *IEEE Transactions on Industry Applications*, vol. 54, no. 4, pp. 3034–3043, July 2018.

[5] H. Wang and F. Blaabjerg, "Reliability of capacitors for dc-link applications in power electronic convertersan overview," *IEEE Transactions on Industry Applications*, vol. 50, no. 5, pp. 3569–3578, Sep. 2014.

[6] W. Lee and S. Sul, "Dc-link voltage stabilization for reduced dc-link capacitor inverter," *IEEE Transactions on Industry Applications*, vol. 50, no. 1, pp. 404–414, Jan 2014.

[7] C. Ren, X. Han, L. Wang, Y. Yang, W. Qin, and P. Wang, "High-performance three-phase pwm converter with a reduced dc-link capacitor under unbalanced ac voltage conditions," *IEEE Transactions on Industrial Electronics*, vol. 65, no. 2, pp. 1041–1050, Feb 2018.

[8] D. Bazargan, B. Bahrani, and S. Filizadeh, "Reduced capacitance battery storage dc-link voltage regulation and dynamic improvement using a feedforward control strategy," *IEEE Transactions on Energy Conversion*, vol. 33, no. 4, pp. 1659–1668, Dec 2018.

[9] E. Afshari, G. R. Moradi, R. Rahimi, B. Farhangi, Y. Yang, F. Blaabjerg, and S. Farhangi, "Control strategy for three-phase grid-connected pv inverters enabling current limitation under unbalanced faults," *IEEE Transactions on Industrial Electronics*, vol. 64, no. 11, pp. 8908–8918, Nov 2017.

[10] E. Shoubaki, S. Essakiappan, M. Manjrekar, and J. Enslin, "Synthetic inertia for bess integrated on the dc-link of grid-tied pv inverters," in *2017 IEEE 8th International Symposium on Power Electronics for Distributed Generation Systems (PEDG)*, April 2017, pp. 1–5.

[11] S. Chakraverty, N. Mahato, P. Karunakar, and T. Dilleswar Rao, *Advanced Numerical and Semi-Analytical Methods for Differential Equations*. Wiley, 2019.

[12] H. H. Rosenbrock, *State-Space and Multivariable Theory*. Nelson, 1970.

[13] J. Schoukens, K. Godfrey, and M. Schoukens, "Nonparametric data-driven modeling of linear systems: Estimating the frequency response and impulse response function," *IEEE Control Systems Magazine*, vol. 38, no. 4, pp. 49–88, Aug 2018.

[14] T. Roinila, J. Huusari, and M. Vilkko, "On frequency-response measurements of power-electronic systems applying mimo identification techniques," *IEEE Transactions on Industrial Electronics*, vol. 60, no. 11, pp. 5270–5276, Nov 2013.

PUBLICATION
IV

Stability Analysis and Adaptive Resonance Damping of Multi-Converter System Applying Bidirectional Converter

R.-M. Sallinen, T. Roinila and H. Abdollahi

in *Proc. IEEE Workshop on Control and Modeling for Power Electronics*, 7 pages, 2020.

Stability Analysis and Adaptive Resonance Damping of Multi-Converter System Applying Bidirectional Converter

Roosa-Maria Sallinen
Tampere University
Tampere, Finland
roosa.sallinen@tuni.fi

Tomi Roinila
Tampere University
Tampere, Finland
tomi.roinila@tuni.fi

Hessamaldin Abdollahi
University of South Carolina
Columbia, USA
abdollh@email.sc.edu

***Abstract*—Bidirectional converters have become extensively applied in various dc power systems that contain battery energy storage systems (BESSs). Such dc power systems typically consist of several feedback-controlled converters, forming a complex power distribution system. Consequently, a number of stability issues arise due to interactions among multiple converter subsystems. Recent studies have presented adaptive control methods for guaranteeing the stability of a multi-converter system under varying operating conditions. However, most methods have not fully considered the bidirectional power-flow in BESS that significantly affects the system dynamics and stability analysis. This paper demonstrates how a bidirectional converter can be operated as an adaptive virtual impedance to improve overall system performance. In the method, an adaptive resonance term is added to the converter's voltage controller to damp resonances in the network's bus impedance, thus improving voltage damping and guaranteeing stability. The reliability and performance of the multi-converter system can be maintained under varying operating conditions by updating the bidirectional converter controller structure so that the required bus voltage damping level is guaranteed.**

***Index Terms*—adaptive stabilization, dc power systems, resonance-based controller, bidirectional converter, multi-converter system**

I. Introduction

Battery energy storage systems (BESSs) have an increasingly important role in many power-distribution systems, such as aircrafts, ships, and dc micro grids [1]–[3]. The operation of these systems often depends on a bidirectional power-electronics converter, which enables bidirectional power-flow and controls the charge and discharge processes of the energy storage.

Typically, the bidirectional converter is a part of a larger system consisting of several converters connected to a common dc bus, as shown in Fig. 1. Such a system may often experience performance degradation or instability due to impedance interactions between different converters although the converters may operate well in a standalone mode. The controller of each converter in the network is designed to track either a voltage, current, or power reference. The high bandwidth of the load converters introduces a negative incremental impedance at the point of coupling with the dc bus, and the load converters

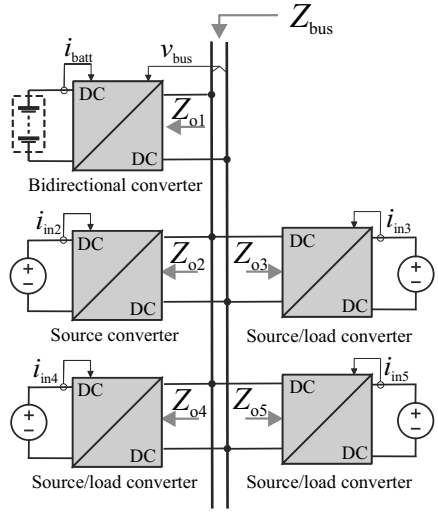

Fig. 1. Dc-dc source and load converters connected to the same bus with a bidirectional dc-dc converter.

are typically represented as constant power loads (CPLs). The negative incremental impedance of CPLs is known to present a destabilizing effect on the system [4] and it is the main reason of interaction dynamics in dc multi-converter systems [5], [6]. Therefore, in a multi-converter system, the stability cannot be reliably evaluated by only studying the operation of single converters.

Typical methods to assess the stability or performance of a converter system are based on minor-loop-gain defined as the ratio between the source subsystem output impedance and the load subsystem input impedance. Examples of such methods include Middlebrook criterion, gain-margin and phase-margin criterion, passivity criterion, and pole location visualization. These methods are, however, not directly applicable to systems including bidirectional power-flow because the methods

require that the subsystems and system grouping are clearly defined and formulated [7]. A different approach to analyze the stability of a multi-converter system is to apply the minor-loop gain based on the converter role in contributing to the current and voltage control instead of characterizing the converters as load and source converters [8]. However, as the control roles may also change based on the operating modes of the applications, this method may not be applicable for all multi-converter systems. A passivity-based stability analysis based on bus impedance was proposed in [7]. The method requires only the bus-impedance information, which is independent of the power-flow directions, the converter operation modes, and system grouping, making it suitable for multi-converter systems with bidirectional power-flow.

One method to avoid impedance-based system performance degradation caused by the CPLs is adding passive/active circuit components to the existing system [5], [9]. However, adding new components can increase both cost and size of the overall system and/or slow down the voltage response [10]. Hence, modifying the feedback loops of the individual converters without adding any extra components is a more attractive solution.

Methods that aim to mitigate the impedance-based interactions by changing the converter control structure are often separated into two groups: the load-side stabilizing methods and the source-side stabilizing methods. In the methods, either the output admittance of the CPL is reshaped using specific control solutions, [6], [10], [11], or control solutions are used to change the output admittance of a source converter, [12]–[14]. For most of the active-damping methods on the load side, the stabilizing damping controller deteriorates the converter load performance and slows down the converter output dynamics. Therefore, control solutions on the source side have been considered more efficient. In [13], a virtual negative inductor is used on the source-side converter by using the droop control method, thus enhancing the system damping effect. As the implementations are either on the source- or load-side converter, they cannot be implemented on bidirectional converters.

Different control methods that aim to mitigate the impedance-based interactions by changing the control structure of converters with bidirectional power-flow have been implemented in [5] and in [15]–[17]. In [5], a feedback control of an energy storage is used to increase the robustness of the system by mitigating the transients which occur due to temporary faults at the dc bus. In [15], a control method for multiple bidirectional power converters is proposed to reduce the circulating current and power-sharing deviation among converters of a hybrid ac/dc microgrid in island mode. Virtual impedance -based method is implemented for a multi-converter system with an AC/DC converter and a battery in [16]. Droop control with virtual impedance is implemented on bidirectional converters in [17].

An adaptive stabilization method which utilizes bus impedance measurements is implemented on a source-side converter in [18]. As the bus impedance method is based on impedance measurements, it is possible to monitor the system stability in real time and to utilize adaptive controllers [18]–[20]. However, these studies have not applied bidirectional converters for reshaping the impedance. Even though the bus impedance method allows for a straightforward stability and performance analysis of a system with bidirectional converters, the internal converter dynamics change along the changing power-flow direction. When implementing the stabilizing control on a bidirectional converter, these changes in the dynamics should be addressed to ensure that the virtual impedance design does not lead to a degradation in the bidirectional converter's internal performance, possibly leading to instability.

This paper extends the stability and performance studies of multi-converter systems presented in [18] and [19] by implementing the stabilizing control using a bidirectional converter. Such a converter can act as a source or load converter, depending on its operation mode. Specifically, the limitations of implementing the stabilizing controller on a bidirectional converter instead of a source converter are discussed. It is shown that the impedance of the bidirectional converter can be adjusted to reach a desired level of system damping in both load- and source-operation modes by applying the measured bus impedance to implement the adaptive virtual impedance. This can be achieved regardless of possible variations in the applications or operating modes.

The remainder of the work is organized as follows. In Section II, the bus impedance -based stability and performance analysis of a multi-converter system is presented. In Section III, the resonance damping control method is presented and its effect on the voltage controller is discussed. In addition, the process of obtaining bus impedance measurements and updating the resonance damping control parameters is described. In Section IV, simulations are conducted for validating the effectiveness of the resonance controller on a bidirectional converter operating both as a load and as a source. Finally, the conclusions are drawn in Section V.

II. Theory and Methods

A. Performance Assessment Based on Bus Impedance

In order to implement an adaptive controller that can guarantee a desired damping level for the system, a measurable performance assessment method is required. A straightforward method to assess the performance and stability of a multi-converter system with bidirectional power-flows and changing control modes is based on analyzing a parameter called bus impedance [21]. For a system with N converters connected to a common bus, the bus impedance Z_{bus} can be given as a parallel connection of the impedances as

$$Z_{\mathrm{bus}}(s) = \frac{1}{Z_{\mathrm{o1}}^{-1} + Z_{\mathrm{o2}}^{-1} + ... + Z_{\mathrm{oN}}^{-1}}, \tag{1}$$

where N impedances are measured on the corresponding subsystem's bus-side (indicated with subscript o in Fig. 1) and positive current direction is defined as flowing into the converter. Note that as the direction of the power-flow does not affect the definition, the method is suitable for systems with

bidirectional power-flows as well as changing operating modes and structures [7]. These terminal impedances describe the terminal behaviour of the subsystem around certain operating point.

In order to address the stability of the interconnected system, two requirements should be met in order to obtain passivity (and therefore stability) [21]:

1) $Z_{\rm bus}(s)$ has no right half plane (RHP) poles
2) $\text{Re}\{Z_{\rm bus}(j\omega)\} \geq 0, \forall\omega > 0$, i.e. $\arg\{Z_{\rm bus}(j\omega)\} \in [\pm 90^o]$

The second condition states that the system is passive (and therefore stable) if the bus impedance ($Z_{\rm bus}$) phase stays within $\pm 90^o$.

The passivity is only a sufficient but not a necessary requirement for the stability, and therefore, further concepts are required to address the performance metrics. To this end, allowable impedance region (AIR), introduced in [22], can be used. The AIR is defined as a semicircle in the right-half side of the complex plane wherein $Z_{\rm bus}(s)$ should be located to achieve a specified system damping level.

Typically, the system bus impedance is dominated by a single large resonant peak [22]. Hence, the impedance can be simplified into a form

$$Z_{\rm bus}(j\omega) = Z_{\rm o-bus}\frac{s\omega_{\rm o}}{s^2 + s\omega_{\rm o}/Q_{\rm bus} + \omega_{\rm o}^2}, \qquad (2)$$

where $Z_{\rm o-bus}$ is the characteristic impedance of $Z_{\rm bus}$ with a resonance frequency $\omega_{\rm o}$ and the quality factor $Q_{\rm bus}$ specifying the level of damping of $Z_{\rm bus}$ at $\omega_{\rm o}$. Hence, at $\omega_{\rm o}$ (i.e. at the frequency where the bus impedance phase is 0^o), $Z_{\rm bus}(j\omega_{\rm o}) = Z_{\rm o-bus}Q_{\rm bus}$, which means that the bus impedance has a real value, and it describes the resonance peak magnitude at the least damped frequency $\omega_{\rm o}$. To achieve a specified system damping level, the AIR requires that the bus impedance has to achieve a specified quality factor, $Q_{\rm max}$. In the complex plane, the AIR can be given as a semicircle with a specified radius $Z_{\rm o-bus}Q_{\rm max}$. To simplify the comparison, the results can be normalized by dividing both the bus impedance and the radius with the characteristic impedance $Z_{\rm o-bus}$, leading to a clear representation of the AIR as a semicircle with a radius $Q_{\rm max}$. Therefore, if the normalized bus impedance $Z_{\rm bus-N}(j\omega)$ stays within the AIR, the specified level of damping is achieved.

B. Typical Bus Impedance Characteristics

The dynamic behavior of a typical bus impedance based on Eq. 2 is shown in Fig. 2. Based on Eq. 1, the bus impedance increases when its denominator becomes smaller. The bus-side impedance of a CPL can be described as a negative incremental impedance within the feedback control loop bandwidth, i.e., its magnitude is resistive and phase is -180^o. On the other hand, the bus-side impedance of a voltage-controlling converter can be described as having very low impedance at low frequencies. However, the impedance has a resonance around the voltage control cross-over frequency, which causes the magnitude to peak. This peak may cause the parallel sum of the CPL impedances and the voltage controlling converter

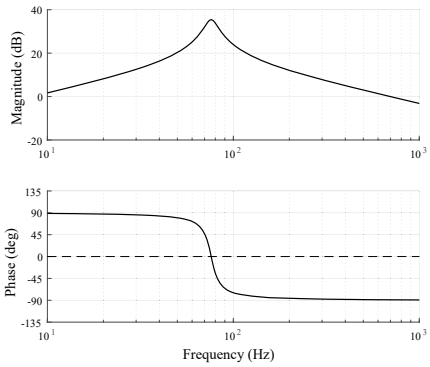

Fig. 2. Frequency response of the bus impedance as given in Eq. 2 with $Z_{\rm o-bus} = 9$, $\omega_{\rm o} = 477$ rad/s, and $Q_{\rm bus} = 6.5$.

impedance to have equal or comparable magnitudes at a frequency close to the voltage control cross-over frequency. Furthermore, if the phase difference between the impedances is greater than 180^o at this frequency, the denominator in Eq. 1 becomes very small and the bus impedance exhibits a large resonant peak. This phenomena is an example of impedance-based interactions within a multi-converter system and should be taken into account when analyzing the system stability and performance.

It is intuitive that a possible resonance or instability caused by the impedance-based interactions can be prevented by adding a virtual impedance on the voltage controlling converter's impedance, damping the resonance in the bus impedance. Even though the resonance behavior could also be smoothed by, for example, increasing the converter's bus-side capacitance, a control-oriented solution would be more desirable as extra hardware would add cost as well as slow down the dynamics, leading to a non-optimized solution under some operating points, for example, at lower powers.

It is well known that the resonance (peak) in the voltage controlling converter's impedance is caused by a resonant pole, and it occurs close to the voltage control cross-over frequency. Therefore, it is typical that the resonance of the bus impedance occurs at a frequency slightly lower than the voltage control loop bandwidth.

III. Adaptive Control of Bidirectional Converter for Resonance Damping

A. Resonance Damping Control

To prevent impedance-based interactions from degrading the system performance, the impedance(s) can be reshaped so that a specific damping level is guaranteed. As a result, the converters in the network do not interact with each other in an adverse way.

The goal is to modify the converter control so that the closed-loop impedance is further damped in a range around

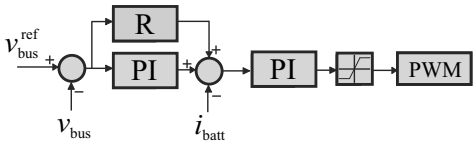

Fig. 3. Block diagram of the converter controller with a resonance term.

the resonance. Specifically, the following design requirements should be met:

- the resulting normalized bus impedance $Z_{\mathrm{bus-N}}(j\omega)$ stays within the AIR which is specified as a semicircle with a radius of maximum allowed quality factor $Q_{\max}$ on the complex plane,
- the resulting normalized bus impedance at the resonance frequency $Z_{\mathrm{bus-N}}(j\omega_{\mathrm{o}})$ has an extra separation margin K_{m} guaranteeing a safe distance from the AIR boundary $Q_{\max}$, and
- the added virtual impedance itself has a damping corresponding to the chosen quality factor Q_{d}.

Typical ranges for these parameters are $Q_{\max} = 0.7...1$, $K_{\mathrm{m}} = 0...1$, and $Q_{\mathrm{d}} = 0.7...1$. To meet these criteria, the voltage controlling converter's bus-side impedance can be reshaped by adding a damping term to its voltage control loop. To this end, a resonance gain (R-gain) is added in parallel with the voltage controller, given as [23]

$$G_{\mathrm{R}} = \frac{2K_{\mathrm{r}}\omega_{\mathrm{r}}s}{s^2 + 2\omega_{\mathrm{r}}s + \omega_{\mathrm{o}}^2}, \tag{3}$$

where K_{r} determines the amount of damping at the resonance frequency ω_{o} and ω_{r} is the bandwidth of the resonance. A block diagram of the controller structure is given in Fig. 3, where the converter is under a cascaded control with an outer voltage loop providing reference to an inner current loop, which controls the battery current i_{batt}.

Measurements of the bus impedance can be utilized to determine sufficient values for the parameters K_{r}, ω_{r}, and ω_{o} so that the design requirements are met. In [18], the relation between the parameters of the R-gain and the design requirements are derived as:

$$K_{\mathrm{r}} = \frac{Q_{\mathrm{d}}}{Z_{\mathrm{o-damp}}}; \omega_{\mathrm{r}} = \frac{\omega_{\mathrm{o}}}{2Q_{\mathrm{d}}}, \tag{4}$$

where

$$Z_{\mathrm{o-damp}} = Z_{\mathrm{o-bus}}\frac{Q_{\mathrm{d}}Q_{\mathrm{bus}}\left(Q_{\max} - K_{\mathrm{m}}\right)}{Q_{\mathrm{bus}} - \left(Q_{\max} - K_{\mathrm{m}}\right)}, \tag{5}$$

and the resonance frequency ω_{o} can be directly identified from the bus impedance.

The R-gain improves the damping of the bus-impedance, hence improving the system performance and stability. An illustrative example is given in Fig. 4, where the normalized bus impedance is presented with and without R-gain. Also the added R-gain is presented after normalizing it by multiplying the gain by $Z_{\mathrm{o-damp}}$. Without the R-gain, the bus impedance has a quality factor around 6 (out of scale). An addition of the R-gain results in a normalized bus impedance which stays within the AIR, thus guaranteeing the required damping level. At the resonance frequency, the damping equals $Q_{\max} - K_{\mathrm{m}}$, as required, to guarantee a safe distance from the AIR boundary. Furthermore, the added virtual impedance itself has a damping corresponding to the chosen quality factor Q_{d}. Hence, all the requirements have been met.

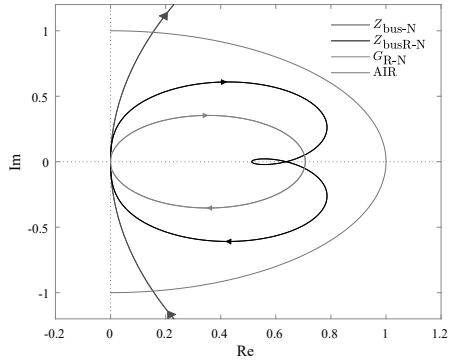

Fig. 4. Normalized bus impedance without R-gain (blue line) and with R-gain (black line), normalized R-gain (green line), and AIR boundary (red line) with Q_{d} = 0.7, $Q_{\max}$ = 1, K_{m} = 0.5. Bus impedance as given in Eq. 2 with $Z_{\mathrm{o-bus}} = 9$, $\omega_{\mathrm{o}} = 477$ rad/s, and $Q_{\mathrm{bus}} = 6.5$.

The control method based on R-gain is demonstrated in [18] for a source buck converter. When operating with a load converter, the power-flow direction is the opposite. As the bus impedance is not dependent on the power-flow direction, this does not affect the fundamental idea behind the control design. However, since the converter dynamics change, this may cause issues for the voltage controller stability or performance if the R-gain affects the voltage control loop in a degrading manner.

B. Effect of R-Gain on Voltage Control

The nominal voltage control gain (PI) is typically designed based on the desired crossover frequency f_{c} and phase-margin φ_{m}. In this work, the converter that performs the stabilization is considered to be a bidirectional dc-dc converter shown in Fig. 5. The detailed transfer functions can be found in [24]. The current controller and voltage controller are both based on PI strategy and the voltage controller is given by $G_{\mathrm{v-PI}}(s) = K_{\mathrm{p-v}} + K_{\mathrm{i-v}}/s$. When the R-gain is added to the controller, is becomes $G_{\mathrm{v-PI-R}}(s) = G_{\mathrm{v-PI}}(s) + G_{\mathrm{R}}(s)$.

An example of the effect of the R-gain on the voltage controller gain is presented in Fig. 6, where the voltage controller gain is shown with and without the R-gain. Also the R-gain is shown. The R-gain parameters are $K_{\mathrm{r}} = 0.5$, $\omega_{\mathrm{r}} = 80 * 2\pi$ rad/s, and $\omega_{\mathrm{o}} = 80 * 2\pi$ rad/s, and the PI-gain parameters are $K_{\mathrm{p-v}} = 0.55$ and $K_{\mathrm{i-v}} = 704$. It can be seen

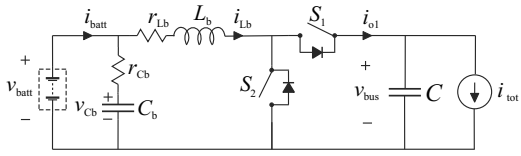

Fig. 5. Bidirectional dc-dc converter.

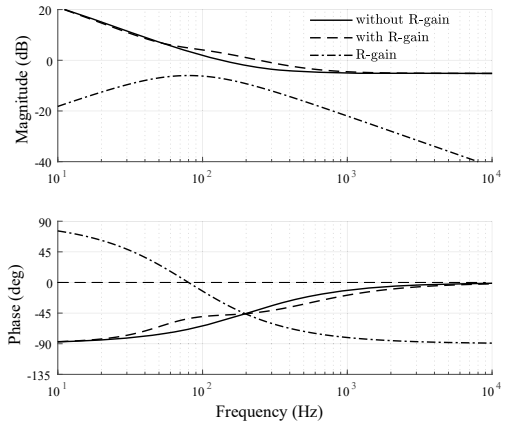

Fig. 6. Frequency response of the voltage controller without (G_{PI}) and with damping ($G_{PI\text{-}R}$) and the damping R-gain (G_R).

that the added R-gain has an effect only around the resonance frequency.

The effect of the R-gain on the original (PI) controller performance is small. However, since the R-gain increases the voltage control gain in the specified range, its effect on phase margin and cross-over frequency should be taken into account to make sure that the resonance term does not degrade the normal operation of the controller. For example, too wide R-gain bandwidth may increase the voltage control loop cross-over frequency too much because the stable operation is limited both by the inner loop control bandwidth (the inner and outer loop should be decoupled in a cascaded controller) and possible poles or zeros in the converter dynamics. In the case of a bidirectional converter, this is especially important as the system dynamics, specifically, the locations of the system poles and zeros, typically change profoundly when the power direction changes (e.g. buck vs. boost converter). By taking these restrictions into account in the design, the controller can damp possible resonances in the bus impedance without internal voltage control performance degradation.

C. Bus Impedance Measurements

Since the dynamics of the multi-converter system may change over time and can be difficult to predict, adaptive damping controller is most desired. Accordingly, bus impedance is a suitable performance assessment as it can be measured periodically by means of wideband measurement techniques [25]. By injecting a broadband excitation such as a pseudorandom binary sequence (PRBS) to the converter control (system input) signals and measuring the resulting currents and bus voltage (system output signals), and processing these input and output signals with Fourier techniques, the bus impedance can be constructed. Based on the acquired bus impedance, the controller can react to the changes in the network. This process is represented as a flowchart in Fig. 7. Note that it is often enough to measure the bus impedance only around the voltage control cross-over frequency. Furthermore, to achieve faster adaptive response from the controller, methods based on orthogonal binary sequences can be applied to speed up the bus-impedance identification procedure [19].

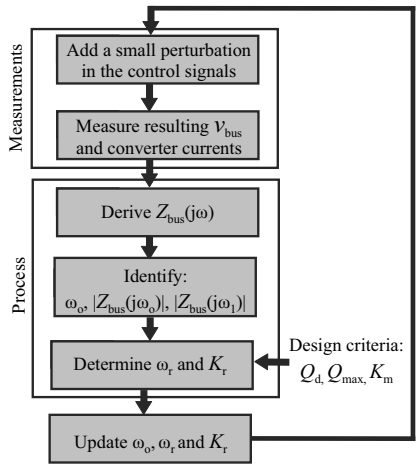

Fig. 7. Flowchart representing the adaptive resonance damping algorithm.

The greatest advantage of the impedance-based method is its black box feature: detailed knowledge of the parameters and properties of the system are not required as long as the impedance measurement can be performed [26]. The drawbacks of the impedance-based stability assessment include inability to identify the causes of the instability or resonance without further analysis. Nonetheless, the method offers enough information to adapt the virtual impedance according to the changes in the network, and hence the resonance can be prevented regardless of its root-cause.

IV. Simulation Results

This section demonstrates the ability of the control algorithm to damp the resonances caused by interactions among the different converters in a multi-converter system both in charging and discharging mode. The network corresponds to the structure given in Fig. 1. The topology of the bidirectional converter is shown in Fig. 5, where the current direction is assumed

TABLE I
CONVERTER PARAMETERS FOR THE BIDIRECTIONAL CONVERTER (BC) AND THE OTHER CONVERTERS (C2-C5) IN FIG. 1.

Parameters	Values (BC / C2-C5)	Description
V_{bus}	480 V	bus voltage
V_{in}	350 V / 200 V	battery/voltage source voltage
f_{sw}	20 kHz	switching frequency
C	85 μF / 45 μF	bus-side capacitance
r_{C}	250 mΩ / 100 mΩ	bus-side capacitor ESR
L	1 mH	inductance
r_{L}	3.6 mΩ	inductor ESR
C_{b}	1 μ F	input-side capacitance
r_{Cb}	10 mΩ	input-side capacitor ESR
r_{sw}	10 mΩ	switch on-time resistance
$f_{\mathrm{c-c}}$	2 kHz	current loop cross-over frequency
$\varphi_{\mathrm{m-c}}$	65^o / 60^o	current loop phase margin
$f_{\mathrm{c-v}}$	100 Hz / none	voltage loop cross-over frequency
$\varphi_{\mathrm{m-v}}$	55^o / none	voltage loop phase margin

TABLE II
OPERATING MODES FOR THE BIDIRECTIONAL CONVERTER (BC) AND THE OTHER CONVERTERS (C2-C5) IN FIG. 1.

BC operating mode	BC	C2	C3	C4	C5
source	30 kW	15 kW	-15 kW	-15 kW	-15 kW
load	-30 kW	15 kW	-15 kW	15 kW	15 kW

positive in discharging mode [24]. The other converters share the same topology, but are here designated as source- or load-converters. All the controllers utilize a PI control strategy. The bidirectional converter controls the battery current and the bus voltage using cascaded control with and without the damping R-gain, while the other converters control just their input side currents. The converter parameter values are given in Table I. In this example all the converters are standalone stable, and therefore, the possible degradation in system performance originates from the interactions between single converters. The R-gain parameters are chosen based on bus impedance Z_{bus} and Eq. (4) with Q_{d} = 0.5, Q_{max} = 1, and K_{m} = 0.5.

Two situations are simulated: the converter is either discharging (source mode) or charging (load mode) the battery. The converter operating modes for both cases are given in Table II, where negative power indicates that the converter operates as a load. The time-domain results are shown in Fig. 8 for the source mode and in Fig. 9 for the load mode, with and without the resonance damping R-gain. In the source mode, it is clear that without the R-gain there occurs a resonance around 70 Hz. In the load mode, the resonance is smaller but can still be identified at 70 Hz.

The corresponding bus impedances are shown in Fig. 10, with and without the resonance damping R-gain. The R-gain indeed increases the resonance damping. The resonance occurs around 70 Hz in both cases. The Nyquist contours of the corresponding normalized bus impedances are shown in Fig. 11 which indicate that the resulting normalized bus impedances stay within the AIR boundary, thus guaranteeing the desired damping level.

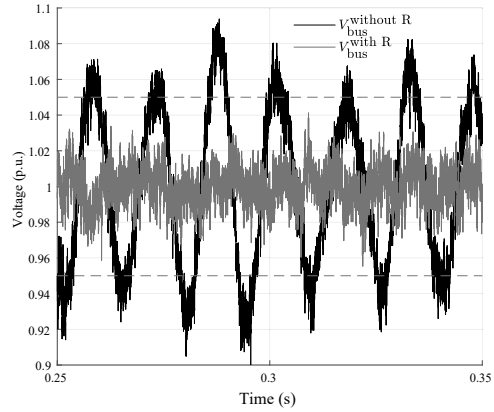

Fig. 8. Bus voltage with and without damping in discharging mode (i.e. source).

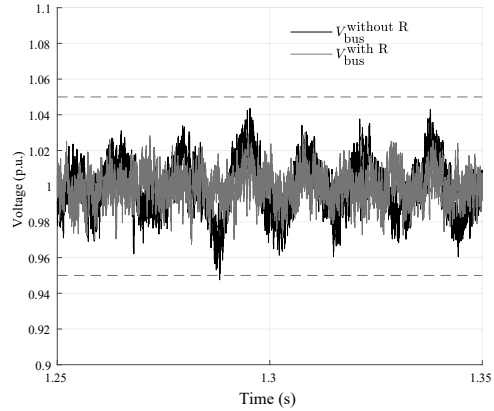

Fig. 9. Bus voltage with and without damping in charging mode (i.e. load).

V. CONCLUSION

This paper has utilized a bidirectional converter to provide adaptive damping in a multi-converter system. The adaptive tuning of the resonance controller is based on bus impedance measurements, which are used to estimate the system's stability and performance. Using the data from these bus impedance measurements, the bidirectional converter is operated as a virtual impedance, damping resonances in the bus impedance. The analysis shows that the bidirectional converter can efficiently damp the resonances in the bus impedance. As a result, the reliability and performance of the network can be maintained regardless of possible network or operating mode changes and without hardware updates or controller re-tuning.

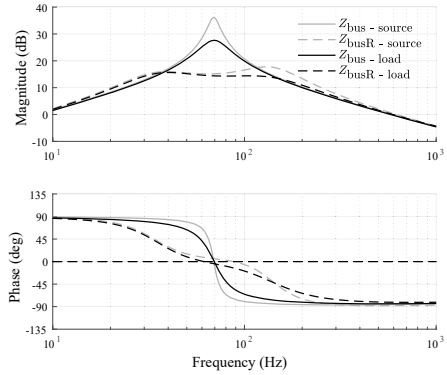

Fig. 10. Bus impedance with and without damping R-gain both in discharging (source) and charging (load) mode.

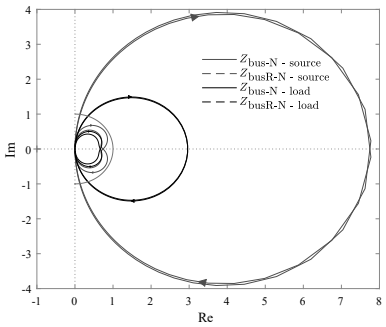

Fig. 11. Bus impedance with and without damping R-gain both in discharging (source) and charging (load) mode. AIR boundary indicated with the red line.

REFERENCES

[1] H. Zhang, F. Mollet, C. Saudemont, and B. Robyns, "Experimental validation of energy storage system management strategies for a local dc distribution system of more electric aircraft," *IEEE Transactions on Industrial Electronics*, vol. 57, no. 12, pp. 3905–3916, Dec 2010.

[2] Z. Jin, L. Meng, J. M. Guerrero, and R. Han, "Hierarchical control design for a shipboard power system with dc distribution and energy storage aboard future more-electric ships," *IEEE Transactions on Industrial Informatics*, vol. 14, no. 2, pp. 703–714, Feb 2018.

[3] T. K. Roy, M. A. Mahmud, A. M. T. Oo, M. E. Haque, K. M. Muttaqi, and N. Mendis, "Nonlinear adaptive backstepping controller design for islanded dc microgrids," *IEEE Transactions on Industry Applications*, vol. 54, no. 3, pp. 2857–2873, May 2018.

[4] Xiaogang Feng, Jinjun Liu, and F. C. Lee, "Impedance specifications for stable dc distributed power systems," *IEEE Transactions on Power Electronics*, vol. 17, no. 2, pp. 157–162, 2002.

[5] L. Herrera, W. Zhang, and J. Wang, "Stability analysis and controller design of dc microgrids with constant power loads," *IEEE Transactions on Smart Grid*, vol. 8, no. 2, pp. 881–888, 2017.

[6] X. Lu, K. Sun, J. M. Guerrero, J. C. Vasquez, L. Huang, and J. Wang, "Stability enhancement based on virtual impedance for dc microgrids with constant power loads," *IEEE Transactions on Smart Grid*, vol. 6, no. 6, pp. 2770–2783, 2015.

[7] A. Riccobono and E. Santi, "Comprehensive review of stability criteria for dc power distribution systems," *IEEE Transactions on Industry Applications*, vol. 50, no. 5, pp. 3525–3535, Sep. 2014.

[8] X. Zhang, X. Ruan, and C. K. Tse, "Impedance-based local stability criterion for dc distributed power systems," *IEEE Transactions on Circuits and Systems I: Regular Papers*, vol. 62, no. 3, pp. 916–925, March 2015.

[9] M. Cespedes, L. Xing, and J. Sun, "Constant-power load system stabilization by passive damping," *IEEE Transactions on Power Electronics*, vol. 26, no. 7, pp. 1832–1836, 2011.

[10] W. Lee and S. Sul, "Dc-link voltage stabilization for reduced dc-link capacitor inverter," *IEEE Transactions on Industry Applications*, vol. 50, no. 1, pp. 404–414, Jan 2014.

[11] B. A. Martinez-Treviño, A. E. Aroudi, A. Cid-Pastor, and L. Martinez-Salamero, "Nonlinear control for output voltage regulation of a boost converter with a constant power load," *IEEE Transactions on Power Electronics*, vol. 34, no. 11, pp. 10 381–10 385, 2019.

[12] M. Wu and D. D. Lu, "A novel stabilization method of lc input filter with constant power loads without load performance compromise in dc microgrids," *IEEE Transactions on Industrial Electronics*, vol. 62, no. 7, pp. 4552–4562, 2015.

[13] S. Liu, P. Su, and L. Zhang, "A virtual negative inductor stabilizing strategy for dc microgrid with constant power loads," *IEEE Access*, vol. 6, pp. 59 728–59 741, 2018.

[14] X. Zhang, Q. Zhong, V. Kadirkamanathan, J. He, and J. Huang, "Source-side series-virtual-impedance control to improve the cascaded system stability and the dynamic performance of its source converter," *IEEE Transactions on Power Electronics*, vol. 34, no. 6, pp. 5854–5866, June 2019.

[15] H. Xiao, A. Luo, Z. Shuai, G. Jin, and Y. Huang, "An improved control method for multiple bidirectional power converters in hybrid ac/dc microgrid," *IEEE Transactions on Smart Grid*, vol. 7, no. 1, pp. 340–347, 2016.

[16] J. He, L. Du, B. Liang, Y. Li, and C. Wang, "A coupled virtual impedance for parallel ac/dc converter based power electronics system," *IEEE Transactions on Smart Grid*, vol. 10, no. 3, pp. 3387–3400, 2019.

[17] P. Yang, M. Yu, Q. Wu, N. Hatziargyriou, Y. Xia, and W. Wei, "Decentralized bidirectional voltage supporting control for multi-mode hybrid ac/dc microgrid," *IEEE Transactions on Smart Grid*, vol. 11, no. 3, pp. 2615–2626, 2020.

[18] H. Abdollahi, S. Arrua, T. Roinila, and E. Santi, "A novel dc power distribution system stabilization method based on adaptive resonance-enhanced voltage controller," *IEEE Transactions on Industrial Electronics*, vol. 66, no. 7, pp. 5653–5662, July 2019.

[19] T. Roinila, H. Abdollahi, S. Arrua, and E. Santi, "Real-time stability analysis and control of multiconverter systems by using mimo-identification techniques," *IEEE Transactions on Power Electronics*, vol. 34, no. 4, pp. 3948–3957, April 2019.

[20] S. K. Gurumurthy, M. Cupelli, and A. Monti, "A generalized framework for synthesizing virtual output impedance control of grid integrated power electronic converters," in *2018 IEEE International Conference on Power Electronics, Drives and Energy Systems (PEDES)*, Dec 2018, pp. 1–6.

[21] A. Riccobono and E. Santi, "A novel passivity-based stability criterion (pbsc) for switching converter dc distribution systems," in *2012 Twenty-Seventh Annual IEEE Applied Power Electronics Conference and Exposition (APEC)*, Feb 2012, pp. 2560–2567.

[22] J. Siegers, S. Arrua, and E. Santi, "Stabilizing controller design for multibus mvdc distribution systems using a passivity-based stability criterion and positive feedforward control," *IEEE Journal of Emerging and Selected Topics in Power Electronics*, vol. 5, no. 1, pp. 14–27, March 2017.

[23] D. N. Zmood and D. G. Holmes, "Stationary frame current regulation of pwm inverters with zero steady-state error," *IEEE Transactions on Power Electronics*, vol. 18, no. 3, pp. 814–822, May 2003.

[24] R. Sallinen, T. Messo, and T. Roinila, "Mitigating voltage fluctuations in battery energy storage systems," in *2019 20th Workshop on Control and Modeling for Power Electronics (COMPEL)*, 2019, pp. 1–6.

[25] T. Roinila, T. Messo, R. Luhtala, R. Scharrenberg, E. C. W. de Jong, A. Fabian, and Y. Sun, "Hardware-in-the-loop methods for real-time frequency-response measurements of on-board power distribution systems," *IEEE Transactions on Industrial Electronics*, vol. 66, no. 7, pp. 5769–5777, July 2019.

[26] G. O. Kalcon, G. P. Adam, O. Anaya-Lara, S. Lo, and K. Uhlen, "Small-signal stability analysis of multi-terminal vsc-based dc transmission systems," *IEEE Transactions on Power Systems*, vol. 27, no. 4, pp. 1818–1830, Nov 2012.

PUBLICATION

V

Broadband Impedance-Measurement Methods in Dynamic Analysis of Dual Active Bridge Converters

R.-M. Sallinen and T. Roinila

in *Proc. IEEE Workshop on Control and Modelling of Power Electronics*, 6 pages, 2021.

Broadband Impedance-Measurement Methods in Dynamic Analysis of Dual Active Bridge Converters

Roosa-Maria Sallinen and Tomi Roinila
Faculty of Information Technology and Communication Sciences
Tampere University
Tampere, Finland
email: roosa.sallinen@tuni.fi; tomi.roinila@tuni.fi

***Abstract*—The output impedance of a switched-mode converter is an important parameter in the converter small-signal stability analysis and stability-enhancing control. One of the popular methods for obtaining the converter output impedance is to introduce a broadband signal such as the pseudo-random binary sequence (PRBS) to the converter duty cycle; the resulting output voltage and current are measured, and the output impedance is obtained with Fourier methods. However, such techniques have not been fully considered for dual active bridge (DAB) converters. This paper discusses the challenges of broadband impedance measurements on DAB converters, compares different implementation methods, and outlines guidelines for achieving accurate results. Unlike conventional dc-dc converters, the power of a DAB converter can be controlled by both the duty ratio and phase shift, thus allowing several methods to perform the impedance measurement. Yet, nonlinearity between the power transfer and phase shift and duty ratio introduces potential challenges to the measurement implementations. Experimental measurements based on a DAB converter are shown to demonstrate these challenges as well as the effectiveness of the proposed measurement guidelines.**

***Index Terms*—dual active bridge converter, impedance measurement, broadband methods, system identification, nonlinear power characteristics**

I. Introduction

A dual active bridge (DAB) converter is an isolated bidirectional dc-dc converter. Its advantages include flexible power flow control, zero voltage-switching, high efficiency, and modular structure, which make it useful for a wide variety of modern power-distribution systems. In particular, DAB converters play an important role in many multi-converter systems, such as dc micro grids [1], automotive power systems [2], electric ships [3], and electric aircrafts [4].

In a typical multi-converter system, several switching converters are connected to a common dc bus. Each of these interconnected converters usually has a high-bandwidth feedback control. Converters that are standalone stable may exhibit a different dynamic behavior when interconnected, which can cause undesired interactions among the interconnected converters and compromise the small-signal stability [5], [6]. As the power flow of DAB converters is bidirectional, traditional methods based on Nyquist criterion cannot be utilized directly for stability assessment [7].

In recent years, studies have presented methods such as the passivity-based stability criterion to analyze the small-signal stability of a multi-converter system [7]. This method requires measuring the system bus impedance which can be computed as a combined impedance of all the interconnected converters. Since the criterion only requires the identification of the bus impedance, the method is not dependent on the system grouping nor power flow directions. These characteristics make the technique especially suitable for stability assessment of multi-converter systems that utilize DAB converters.

Recent studies have shown broadband methods suitable for accurate and fast converter impedance measurement [8]–[10]. In these methods, a specifically designed broadband perturbation, such as the pseudo-random binary sequence (PRBS), is added on top of either the converter controller reference or duty cycle. The resulting voltage and current responses are measured at the output of the converter and Fourier analysis is applied to obtain the impedance. By applying the approach to each converter in the system, the bus impedance can be obtained as a combination of single measurements [8]–[10]. Such wideband measurement techniques can be performed online, making the method practical and suitable for various applications. In [10]–[12] the method was used to facilitate stability-enhancing adaptive controllers. In these studies, the effectiveness of the stability-enhancing control relied solely on sufficient impedance measurements.

Including a DAB converter to a multi-converter system increases the complexity of the analysis and impedance measurement. The presented broadband impedance-measurement methods rely on linearity between the perturbed parameter and converter output power. However, in a DAB converter, the relationship between the power transfer and duty ratio and phase shift is more complex and may have a nonlinear nature, depending on the chosen set-point and modulation and control strategy [13]–[17]. Furthermore, since the DAB converters can be controlled by both phase shift and duty ratio, more options for the perturbation implementation are feasible in comparison to performing the measurements on more traditional dc-dc converters in which only duty ratio can be controlled.

This paper presents methods for performing broadband

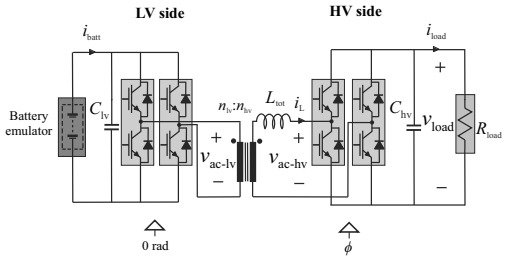

Fig. 1. Dual active bridge converter with battery emulator and resistive load.

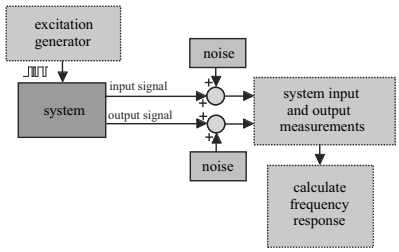

Fig. 2. Typical setup for frequency response measurement.

impedance-measurements on DAB converters. Different strategies for perturbation and measurement implementation are considered and guidelines for obtaining reliable results are outlined. Experimental measurements based on a DAB converter are shown to demonstrate the effectiveness of the proposed methods as well as to demonstrate the possible challenges caused by the nonlinear relationship between the power transfer and phase shift and duty ratio.

The remainder of the paper is organized as follows. Section II describes the relationship between the DAB converter power flow, duty ratio, and phase shift, and provides background on performing impedance measurements in general. Furthermore, guidelines for reliable impedance measurements on DAB converters are outlined. Section III presents experimental results based on a DAB converter with a resistive load. Finally, Section IV draws conclusions.

II. Theory and Methods

A. Power characteristics of dual active bridge converters

DAB converters are typically controlled by manipulating the duty ratio(s) and/or phase shift between the modulating signals of the two bridges. This differentiates DAB converters from more traditional dc-dc converters that can be controlled only by the duty ratio. Various different modulation techniques exist for DAB converters. One of the most popular methods is the phase-shift modulation, which is simple and allows for high powers but reduces the degrees of freedom to phase shift only as the duty ratios are kept constant (usually 0.5).

Fig. 1 shows a schematic diagram of a phase shift modulated and single-phase controlled DAB converter with a battery emulator and resistive load. The modulating signals of the high-voltage-side bridge are delayed by a phase shift ϕ, while the low voltage-side bridge is kept constant (0 rad). The converter power flow is controlled by adjusting the phase shift. When using phase-shift modulation and single-phase-shift control, the power transfer achieved at a certain phase shift can be given as

$$P = \frac{nV_{\mathrm{lv}}V_{\mathrm{hv}}}{2\pi f_{\mathrm{sw}}L_{\mathrm{tot}}}\phi\left(1-\frac{|\phi|}{\pi}\right) \tag{1}$$

where n is the transformer turns ratio, V_{lv} and V_{hv} are the voltages of the low- and high-voltage side, respectively (battery voltage and output/load voltage), f_{sw} is the switching frequency, and L_{tot} is the total inductance. The duty ratio has a fixed value of 0.5. Maximum power transfer is achieved when the phase shift is $\pm\pi/2$. However, due to deadtime, maximum power transfer may be achieved already at a lower phase shift.

If a different modulation and/or control strategy is used, the duty ratios (of one or both of the bridges) may be set to other values than 0.5 and/or both of the phase shifts may be varied. This adds complexity in the relationship between the power transfer and phase shift and duty ratio [13]–[16]. For example, when setting the low voltage-side duty ratio to a constant value of 0.5 and adjusting the power with the high-voltage-side duty ratio and phase shift, depending on the range of phase shift, there are two possible operation states known as inner and outer state. The power for the inner and outer states can be given by (2) and (3), respectively, as

$$P = \frac{nV_{\mathrm{lv}}V_{\mathrm{hv}}}{2\pi f_{\mathrm{sw}}L_{\mathrm{tot}}}\phi D_{\mathrm{hv}} \tag{2}$$

$$P = \frac{nV_{\mathrm{lv}}V_{\mathrm{hv}}}{2\pi f_{\mathrm{sw}}L_{\mathrm{tot}}}\left[\phi\left(1-\frac{|\phi|}{\pi}\right)-\frac{\pi}{4}\left(1-D_{\mathrm{hv}}\right)^2\right] \tag{3}$$

where D_{hv} is the high-voltage-side duty ratio [13]. Decreasing the high-voltage-side duty ratio increases the power capability. Thus, a higher maximum power can be achieved compared to the power available with both duty ratios set to 0.5. If a dual-phase-shift control strategy is used, that is, both the high and low voltage-side duty ratios are varied, the power characteristics are more complicated.

Regardless of the chosen modulation and control strategy of a DAB converter, the presence of deadtime complicates the power characteristics further due to voltage distortion phenomena, such as voltage polarity reversal, voltage sag, phase drift, and duty-cycle abnormity [17]. Especially when operating at high switching frequencies, the effect of deadtime on voltage distortion and efficiency degradation is significant and cannot be ignored. The deadtime effect on average power transfer occurs due to a voltage polarity reversal phenomenon [17]. Various methods to avoid or mitigate deadtime effects have been suggested [18]–[21] but the applicability of these methods depends strongly on the chosen application, such as the modulation and control method.

B. Broadband measurements

A switched-mode converter can be considered as a linear time-invariant (LTI) system up to half of its switching frequency. The dynamics of such a system can typically be characterized by system frequency-response functions. Fig. 2 shows a general measurement setup for obtaining the system frequency-response function. An excitation signal is introduced to the plant by, for example, applying the plant actuator/controller. The input and output signals are measured, and Fourier methods are applied to obtain the system frequency response.

The selection of an excitation signal plays an important role in measuring the system frequency response. A conventional technique is to apply sine sweeps. This technique provides the highest possible signal-to-noise ratio and hence the most reliable and accurate estimate of the frequency-response. However, sine sweeps are not well suited for online measurements due to long measurement time and difficulties in implementing the injection.

Recent studies have presented methods based on broadband perturbations to measure the frequency response(s) of various power-electronics systems [22]–[24]. One of the most popular excitation signals is the maximum-length binary sequence (MLBS). The MLBS broadband signal has a very high total energy in relation to the signal time-domain amplitude, thus minimizing the signal interference on the measured system [25]. Unlike a sine-based signal, the MLBS signal has energy at multiple frequencies. Therefore, the frequency response measurement is acquired at multiple frequencies simultaneously. Furthermore, since the MLBS consists only of two signal levels, the signal generation is straightforward: it can be easily implemented on the converter controller platform using a shift register with exclusive-or feedback [26]. The sequence length is always $N = 2^n - 1$, where n is an integer that denotes the number of bits in the shift register.

Designing the MLBS typically requires defining the following specification variables [25]:

- frequency resolution
- measurable bandwidth
- measurement time
- variance and/or SNR

Then, the sequence is generated using the following design parameters:

- sequence length
- sequence generation frequency
- perturbation amplitude
- number of averaged periods

C. Impedance measurement on DAB converters

Performing impedance measurements on a DAB converter is more complex compared to traditional dc-dc converters. First, depending on the operating point, the relationship between the transferred power and duty ratio and phase shift may be nonlinear. Yet, the MLBS-based measurement methods rely on linearity between the perturbed parameter and converter output power. Second, since the DAB converters can be controlled by both phase shift and duty ratio, an alternative option for the perturbation injection design is obtained compared to conventional dc-dc converters where only the duty ratio can be controlled.

Due to nonlinearity between the perturbed parameter and converter output power, the MLBS energy at a specific frequency may not translate to the same frequency in the converter output power, thus degrading the measurement accuracy. Some strategies can be considered to avoid or mitigate the nonlinearity [18]–[21] but the applicability of these approaches depends strongly on the chosen application.

To successfully use the MLBS for the impedance measurement of a DAB converter it is of paramount importance to appropriately define the perturbation amplitude. Depending on the effects of noise and other distortions as well as the allowable system interference, the amplitude is usually chosen so that the output deviates 1-5% from the nominal value. If the perturbation is injected on top of the controller reference, the amplitude selection is typically not very sensitive because the injection is strongly affected by the controller dynamics. However, if the perturbation is injected to the duty ratio or phase shift, the perturbation amplitude requires more careful design to ensure that the perturbation produces high enough spectral energy to the whole frequency band of interest. In the presence of nonlinearity, increasing the perturbation amplitude may not improve the measurements but yields unreliable estimates. Thus, the injection method that provides the most linear behavior between the perturbed parameter and the converter output power at the chosen set-point should be used.

Three different injection methods can be applied when implementing a broadband impedance measurement for a DAB converter.

Method 1—*Injection to output voltage or current reference*: In this method the amplitude design of the excitation is less sensitive compared to other methods because the injection is affected by the controller dynamics. The amplitude value as well as other parameters of the injection can be designed by general guidelines [25].

Methods 2 and 3—*Injection to duty ratio or phase-shift*: In this method the amplitude design is sensitive and set-point dependent due to nonlinear behavior between the perturbed parameter and output power. Hence, it is recommended to identify the nonlinear operating points and use the injection method which produces the most linear behavior around the chosen set-point. The perturbation amplitude can then be increased so that the desired SNR is reached without violating interference requirements. It is emphasized that under strong nonlinearities the measured impedance accuracy cannot be improved by increasing the injection amplitude. Instead, strategies to mitigate or to avoid nonlinear effects should be considered. The other injection parameters can be designed by general guidelines [25].

III. Experimental results

A power-converter system depicted in Fig. 3 was constructed in the laboratory. The system consists of a DAB with a battery

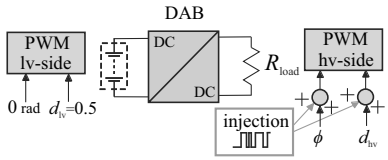

Fig. 3. Simplified schematic of the setup used for experimental results. The perturbation is injected either to the phase shift or duty ratio of the high-voltage-side switches.

TABLE I
PARAMETERS USED IN EXPERIMENTAL RESULTS.

Parameter	Value	Description
f_{sw}	50 kHz	switching frequency
t_d	2 μs	deadtime
V_{lv}	100 V	dc voltage on low-voltage side
R_{load}	150 Ω	resistive load
n	2.6	transformer turns ratio (n_{hv}/n_{lv})
C_{lv}	520 μF	capacitance on low-voltage side
C_{hv}	520 μF	capacitance on high-voltage side
L_{tot}	300 μH	equivalent/total inductance on high-voltage side
ϕ	1 rad (range $-\frac{\pi}{2}...\frac{\pi}{2}$)	phase shift between the modulating signals
D_{hv}	0.5 (range 0...1)	duty ratio for high-voltage-side bridge
D_{lv}	0.5	duty ratio for low-voltage-side bridge

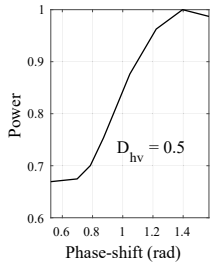

Fig. 4. Measured transferred power (normalized) as a function of the phase shift. $D_{hv} = 0.5$.

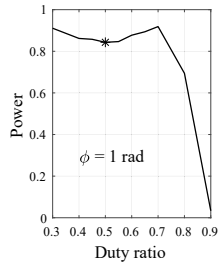

Fig. 5. Measured transferred power (normalized) as a function of the high-voltage side duty ratio. $D_{lv} = 0.5$, $\phi = 1$ rad. The nonlinear point $D_{hv} = 0.5$ has been marked.

emulator and a resistive load. The detailed system parameters are given in Table. I. The converter was operated at open-loop to bypass the effect of the controller. The perturbation was injected to the phase shift or duty ratio of the high-voltage-side bridge, depending on the chosen perturbation method. Two fundamentally different perturbation methods were used: 1) perturbation to phase shift (with a duty ratio of 0.5), and 2) perturbation to duty ratio (with a phase shift of 1 rad). This allowed for straightforward comparison between

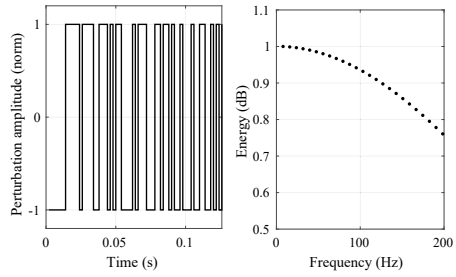

(a) MLBS in time-domain. (b) MLBS energy spectrum.

Fig. 6. MLBS signal used for perturbation.

the impedance-measurement-implementation methods as well as a basis for observing the deadtime effects.

Before measuring the impedance, the relationship between the power transfer and phase shift and duty ratio was demonstrated by measuring the output power at different set-points shown in Fig. 4 and Fig. 5. In Fig. 4, the relationship between the phase shift and power around the phase shift of 1 rad is linear. On the other hand, Fig. 5 shows strong nonlinearity between the duty ratio and power around the duty ratio of 0.5: the power increases regardless of how the duty ratio changes (see the marker in Fig. 5). The applied measurement method is based on the assumption of linearity between the perturbed parameter and converter output power. Therefore, implementing the impedance measurement with an injection to the duty ratio at the duty ratio of 0.5 is more complicated and yields unreliable results. To avoid nonlinearity at the measurement point, an additional impedance measurement was done with an *added offset* to the duty ratio. This slightly increased the converter currents and voltages (that is, changed the set-point), but allowed for greatly improved measurement accuracy as the relationship between the power and duty ratio was more linear.

The perturbation design was done with a desired frequency range of 10 Hz to 200 Hz. A 63-bit-long MLBS signal with a generation frequency of 500 Hz was chosen. Three averaging periods were used to mitigate non-systematic noise, which allowed for a measurement time less than 0.4 s. The injection amplitude was selected so that the converter output voltage and current deviated less than 2% of their nominal (average) values. Fig. 6 shows the designed MLBS both in the time and frequency domain.

The designed MLBS was injected into the system by applying three different injection methods. In the first case the phase shift was perturbed. In the second and third cases the duty ratio was perturbed without and with an added offset, respectively. More details of the perturbation parameters are given in Table II. Fig. 7 shows a sample of the perturbed parameters. The corresponding output voltages and currents are shown in Fig. 8 and Fig. 9. The figures show that the resulting waveforms are very different depending

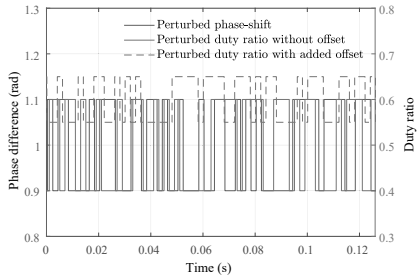

Fig. 7. Samples of perturbed signals.

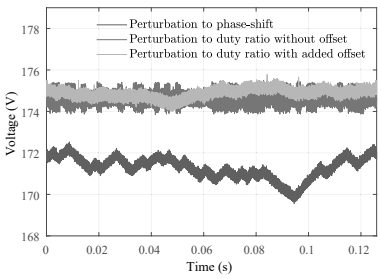

Fig. 8. Voltages for the three cases during one PRBS period.

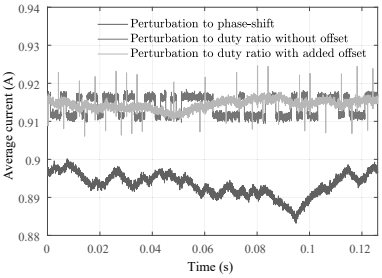

Fig. 9. Currents for the three cases during one PRBS period.

on the chosen perturbation method due to different system dynamics between the perturbed parameter and the voltage and current. The resulting converter output impedances are compared in Fig. 10. When injecting the perturbation to the phase shift the result is more accurate having less than 2.5 dB (5.5%) error in magnitude and 10 degrees in phase. On the other hand, when injecting the perturbation (without the offset) to the duty ratio, the result is not accurate at all (even if the perturbation amplitude is increased). This was expected based on the nonlinear relationship between the power and duty ratio of the DAB converter at the applied set-point. However, by adding a small dc-offset to the perturbation the power is slightly increased but the impedance is more accurately obtained, giving maximum of 3.5 dB (7.8%) error in the

TABLE II
PERTURBATIONS USED IN THE EXPERIMENTAL RESULTS AND THEIR EFFECT ON VOLTAGE AND CURRENT (AS PERCENTAGE OF AVERAGE).

injection method	average	injection amplitude	perturbation amplitude in current	perturbation amplitude in voltage
Phase shift	1.00 rad	0.10 rad	1.9 %	1.7 %
Duty ratio without offset	0.50	0.10	1.1 %	0.9 %
Duty ratio with offset	0.60	0.05	1.1 %	1.0 %

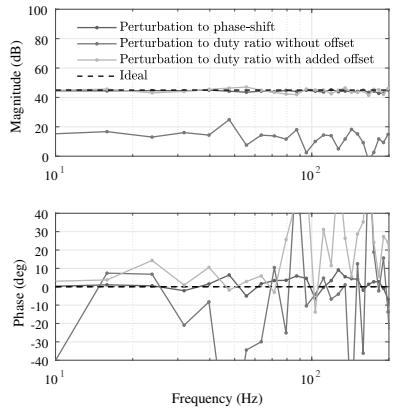

Fig. 10. Measured output impedances for the three cases and an ideal result.

magnitude response. Yet, in the phase response, the maximum error is higher and becomes significant at frequencies above 70 Hz. This phase response accuracy cannot be improved by increasing the amplitude as the relationship between the duty ratio and output power is nonlinear at both set-points $D_{\mathrm{hv}} = 0.5$ and $D_{\mathrm{hv}} = 0.7$. Fig. 11 shows the resulting impedance errors of each method in comparison to an ideal measurement (45 dB in magnitude and zero degrees in phase).

The results clearly show that system nonlinearities strongly affect the impedance measurements of DAB converters. This applies especially when injecting the perturbation to the duty ratio due to the strongly nonlinear characteristics at certain set-points. Therefore, under such nonlinearities, the perturbation should be applied to the phase shift rather than to the duty ratio. However, if the nonlinear set-points are avoided or their effects mitigated, sufficient measurements could be achieved using both perturbation methods.

IV. CONCLUSIONS

This work has presented broadband impedance-measurement methods for dual-active bridge (DAB) converters. In a DAB converter, the relationship between the power transfer and duty ratio and phase shift may be nonlinear, depending on

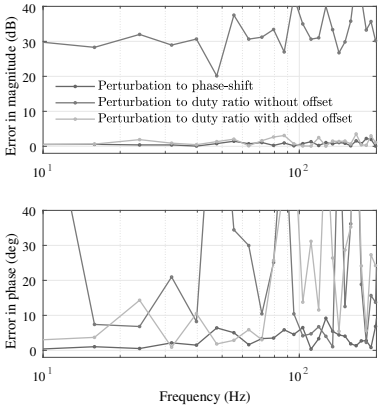

Fig. 11. Errors of the output impedance measurements compared to an ideal measurement.

the chosen set-point and modulation and control strategy. The work showed that it is vital to take into account the system dynamics at the chosen set-point before choosing the perturbation method. When injecting the perturbation on the converter duty ratio, the measurement implementation may be unfeasible at certain set-points due to strong nonlinearity between the duty ratio and output power. On the other hand, when the perturbation is injected into the phase shift, an accurate measurement implementation is more straightforward. Experimental measurements based on a DAB converter were presented to demonstrate the effectiveness of the proposed methods.

REFERENCES

[1] H. Zhou, T. Duong, S. T. Sing, and A. M. Khambadkone, "Interleaved bidirectional dual active bridge dc-dc converter for interfacing ultracapacitor in micro-grid application," in *Proc. IEEE International Symposium on Industrial Electronics*, 2010, pp. 2229–2234.

[2] L. Xue, D. Boroyevich, and P. Mattavelli, "Switching condition and loss modeling of gan-based dual active bridge converter for phev charger," in *Proc. IEEE Applied Power Electronics Conference and Exposition*, 2016, pp. 1315–1322.

[3] F. Zhang and W. Li, "An equivalent circuit method for modeling and simulation of dual active bridge converter based marine distribution system," in *Proc. IEEE Electric Ship Technologies Symposium*, 2019, pp. 382–387.

[4] R. A. Mastromauro, M. C. Poliseno, S. Pugliese, F. Cupertino, and S. Stasi, "Sic mosfet dual active bridge converter for harsh environment applications in a more-electric-aircraft," in *Proc. International Conference on Electrical Systems for Aircraft, Railway, Ship Propulsion and Road Vehicles*, 2015, pp. 1–6.

[5] Z. Jin, L. Meng, and J. M. Guerrero, "Constant power load instability mitigation in dc shipboard power systems using negative series virtual inductor method," in *Proc. Annual Conference of the IEEE Industrial Electronics Society*, 2017, pp. 6789–6794.

[6] X. Lu, K. Sun, J. M. Guerrero, J. C. Vasquez, L. Huang, and J. Wang, "Stability enhancement based on virtual impedance for dc microgrids with constant power loads," *IEEE Transactions on Smart Grid*, vol. 6, no. 6, pp. 2770–2783, 2015.

[7] A. Riccobono and E. Santi, "Comprehensive review of stability criteria for dc power distribution systems," *IEEE Transactions on Industry Applications*, vol. 50, no. 5, pp. 3525–3535, 2014.

[8] J. Siegers, S. Arrua, and E. Santi, "Allowable bus impedance region for mvdc distribution systems and stabilizing controller design using positive feed-forward control," in *Proc. IEEE Energy Conversion Congress and Exposition*, 2016, pp. 1–8.

[9] T. Roinila, H. Abdollahi, S. Arrua, and E. Santi, "Real-time stability analysis and control of multiconverter systems by using mimo-identification techniques," *IEEE Transactions on Power Electronics*, vol. 34, no. 4, pp. 3948–3957, 2019.

[10] H. Abdollahi, S. Arrua, T. Roinila, and E. Santi, "A novel dc power distribution system stabilization method based on adaptive resonance-enhanced voltage controller," *IEEE Transactions on Industrial Electronics*, vol. 66, no. 7, pp. 5653–5662, 2019.

[11] S. K. Gurumurthy, M. Cupelli, and A. Monti, "A generalized framework for synthesizing virtual output impedance control of grid integrated power electronic converters," in *Proc. IEEE International Conference on Power Electronics, Drives and Energy Systems*, 2018, pp. 1–6.

[12] R.-M. Sallinen, T. Roinila, and H. Abdollahi, "Stability analysis and adaptive resonance damping of multi-converter system applying bidirectional converter," in *Proc. IEEE Workshop on Control and Modeling for Power Electronics*, 2020, pp. 1–7.

[13] M. Jafari, Z. Malekjamshidi, and J. G. Zhu, "Analysis of operation modes and limitations of dual active bridge phase shift converter," in *Proc. IEEE International Conference on Power Electronics and Drive Systems*, 2015, pp. 393–398.

[14] H. Bai and C. Mi, "Eliminate reactive power and increase system efficiency of isolated bidirectional dual-active-bridge dc–dc converters using novel dual-phase-shift control," *IEEE Transactions on Power Electronics*, vol. 23, no. 6, pp. 2905–2914, 2008.

[15] F. Krismer and J. W. Kolar, "Closed form solution for minimum conduction loss modulation of dab converters," *IEEE Transactions on Power Electronics*, vol. 27, no. 1, pp. 174–188, 2012.

[16] H. Shi, K. Sun, H. Wu, and Y. Li, "A unified state-space modeling method for a phase-shift controlled bidirectional dual-active half-bridge converter," *IEEE Transactions on Power Electronics*, vol. 35, no. 3, pp. 3254–3265, 2020.

[17] B. Zhao, Q. Song, W. Liu, and Y. Sun, "Dead-time effect of the high-frequency isolated bidirectional full-bridge dc–dc converter: Comprehensive theoretical analysis and experimental verification," *IEEE Transactions on Power Electronics*, vol. 29, no. 4, pp. 1667–1680, 2014.

[18] K. Takagi and H. Fujita, "Dynamic control and dead-time compensation method of an isolated dual-active-bridge dc-dc converter," in *Proc. European Conference on Power Electronics and Applications*, 2015, pp. 1–10.

[19] C. Song, A. Chen, J. Chen, C. Du, and C. Zhang, "Dead-time effect analysis of dual active bridge dc-dc converter with dual-phase-shift control," in *Proc. Chinese Automation Congress*, 2017, pp. 6545–6550.

[20] J.-i. Itoh, K. Kawauchi, and H. Watanabe, "Non-linear dead-time error compensation method of dual active bridge dc-dc converter for variable dc-bus voltage," in *Proc. International Conference on Smart Grid*, 2018, pp. 208–213.

[21] S. Luo, F. Wu, and G. Wang, "Effect of dead band and transient actions on ctps modulation for dab dc–dc converter and solutions," *IEEE Transactions on Transportation Electrification*, vol. 7, no. 3, pp. 949–957, 2021.

[22] C. Fernandez, L. Ortega, M. Granda, P. Zumel, and A. Barrado, "Online impedance measurement of the batteries and loads connected to a modular multi-active bridge converter," in *Proc. IEEE Workshop on Control and Modeling for Power Electronics*, 2019, pp. 1–6.

[23] T. Roinila, T. Messo, R. Luhtala, R. Scharrenberg, E. C. W. de Jong, A. Fabian, and Y. Sun, "Hardware-in-the-loop methods for real-time frequency-response measurements of on-board power distribution systems," *IEEE Transactions on Industrial Electronics*, vol. 66, no. 7, pp. 5769–5777, 2019.

[24] H. Gong, D. Yang, and X. Wang, "Parametric identification of dq impedance model for three-phase voltage-source converters," in *Proc. IEEE International Power Electronics and Application Conference and Exposition*, 2018, pp. 1–6.

[25] A. H. Tan and K. R. Godfrey, *Industrial Process Identification*. Cham, Switzerland: Springer, 2019.

[26] A. H. Tan and K. Godfrey, "The generation of binary and near-binary pseudorandom signals: an overview," *IEEE Transactions on Instrumentation and Measurement*, vol. 51, no. 4, pp. 583–588, 2002.

PUBLICATION VI

Adaptive Bus-Impedance-Damping Control of Multi-Converter System Applying Bidirectional Converters

R.-M. Sallinen and T. Roinila

IEEE Journal of Emerging and Selected Topics in Power Electronics 2023, vol. 11, no. 1, pp. 567–575

Adaptive Bus-Impedance-Damping Control of Multi-Converter System Applying Bidirectional Converters

Roosa-Maria Sallinen, *Member, IEEE*, and Tomi Roinila, *Member, IEEE*

***Abstract*— Modern dc-power-distribution systems utilizing energy storages are often dependent on the operation of bidirectional power-electronics converters. Such distribution systems typically consist of several feedback-controlled converters prone to experience stability issues due to cross-effects among the different converters. Studies have presented adaptive control-based techniques to prevent such stability issues, but most studies have not fully considered their implementation on a bidirectional converter. The system dynamics may vary significantly depending on the operating point and particularly the direction of the bidirectional power flow. Therefore, specific care should be taken in the design of the adaptive stabilizing control to guarantee that the system's regular operation is not impeded when the stabilization is implemented on a bidirectional converter. This article proposes a procedure to implement an adaptive stabilizing control method on a bidirectional converter with minimal changes to the regular controller. We add an adaptive resonance term to the bidirectional converter's voltage controller that enhances stability and damping around the identified resonance frequency without impeding the converter's regular operation. The resonance term is adjusted periodically based on online impedance measurements and the chosen design criteria. As a result, the controller can dampen resonances and prevent adverse impedance-based interaction. Experimental measurements based on a multi-converter setup demonstrate the effectiveness of the proposed methods.**

***Index Terms*— Adaptive stabilization, bidirectional converter, dc power systems, multi-converter system, resonance-based controller.**

I. Introduction

BATTERY energy storage systems (BESSs) play an increasingly important role in many power-distribution systems, such as dc microgrids [2], electric ships [3], and electric aircraft [4]. The operation of these systems typically relies on a bidirectional power-electronics converter, which enables the bidirectional power flow and controls the charge and discharge processes of the energy storage. For such modern power-distribution systems, a dual active bridge (DAB) converter has gained prominence due to its flexible power flow control, zero voltage-switching, high efficiency, galvanic isolation, and modular structure [5], [6], [7].

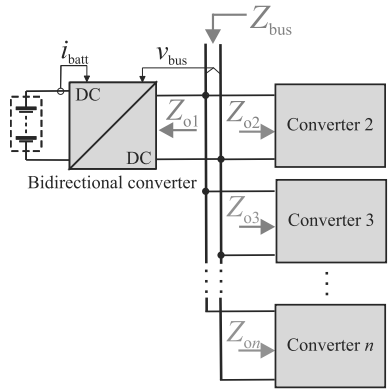

Fig. 1. Multi-converter system with a bidirectional converter.

Typically, the bidirectional converter is a part of a more complicated multi-converter system in which several converters are connected to a common dc bus, as shown in Fig. 1. Such a multi-converter system may experience performance degradation due to impedance interactions between different converters even though the converters may operate well in a standalone mode. The controller of each converter tracks either a voltage, current, or power reference. The high control bandwidth of the load converters introduces a negative incremental impedance at the point of coupling with the dc bus. These load converters act as constant power loads (CPLs). The negative incremental impedance of CPLs has a destabilizing effect on the system [8] and is the main reason for interaction dynamics in dc multi-converter systems [9], [10].

One way of avoiding impedance-based system performance degradation caused by the CPLs is to add passive/active circuit components to the existing system [9], [11]. However, the addition of new components can increase the cost and size of the overall system and slow down the voltage response [12]. Therefore, a more attractive solution is to modify the feedback loops of the individual converters based on system stability assessment [13], [14], [15].

Manuscript received 5 April 2022; revised 17 August 2022; accepted 5 October 2022. Date of publication 10 October 2022; date of current version 3 February 2023. An earlier version of this article was presented at the IEEE Workshop on Control and Modeling for Power Electronics (COMPEL) 2020 [DOI: 10.1109/COMPEL49091.2020.9265778]. Recommended for publication by Associate Editor Milijana Odavic. *(Corresponding author: Roosa-Maria Sallinen.)*

The authors are with the Faculty of Information Technology and Communication Sciences, Tampere University, 33101 Tampere, Finland (e-mail: roosa.sallinen@tuni.fi; tomi.roinila@tuni.fi).

Color versions of one or more figures in this article are available at https://doi.org/10.1109/JESTPE.2022.3213724.

Digital Object Identifier 10.1109/JESTPE.2022.3213724

Considering the stability assessment of a multi-converter system, traditional methods may not be effective with systems including bidirectional converters and varying control structures. Such methods are typically based on minor-loop gain (MLG), which is the ratio between the source subsystem output impedance and the load subsystem input impedance. Examples of such stability assessment methods include the Middlebrook criterion [16] and gain-margin and phase-margin criterion [17]. These MLG-based methods are not directly applicable to systems with bidirectional power flow because they require the subsystems and system grouping to have specific definitions and formulas [18]. A refined approach for analyzing the stability of a multi-converter system is to apply the MLG by characterizing the converters based on their role in contributing to the current and voltage control rather than assigning them as load and source converters [19]. However, because the control roles may change based on the application operating modes, this method may not be straightforward for all multi-converter systems.

Recent studies have presented passivity-based stability analysis [18], which provides an alternative approach for the stability assessment. This analysis is based on the system bus impedance, rather than the multi-converter system in MLG. The bus impedance represents the total impedance of all the bus-connected subsystems. As the passivity-based method only requires bus-impedance identification, the method is independent of the power-flow directions, the converter operating modes, and the system grouping. This makes the method especially suitable for the stability assessment of multi-converter systems with bidirectional power flow.

The stability enhancement of CPL-affected multi-converter systems on bidirectional converters is still an important problem where different approaches can be useful. Most stabilizing control designs in the literature focus on either the load- or the source-side converters rather than on bidirectional converters; these methods reshape either the output admittance of the CPL [10], [12], [20] or the output admittance of a source converter [21], [22], [23], [24]. Thus, these methods may not directly apply when implementing a stabilizing controller on a bidirectional converter. Stabilizing control designs for bidirectional converters were presented in [9], [25], [26], and [27]. However, these methods might not be suitable for all applications, as they utilize specific control methods (e.g., semidefinite programming [9]) or are mainly focused on droop-controlled inverters [25], [26], [27]. Moreover, multi-converter systems can benefit the most from adaptive, nonparametric stabilizing methods that do not require detailed information about the system variables. Such a method was used in [1], where a bus impedance-based stabilizing controller was extended to bidirectional converters, but no experimental results were used to validate the study.

This article proposes a general, adaptive, nonparametric stabilizing control design method for bidirectional converters in multi-converter systems. This method assesses the multi-converter system stability through bus-impedance identification, and then optimizes the stabilizing controller to dampen resonances within the allowable frequency range. The bus-impedance identification utilizes the existing converters of the system, and employs measurements of the bus-side voltage and currents of each converter. Based on the identification, the stabilizing controller alters the bidirectional converter impedance to provide the desired level of damping for the identified bus impedance in both load- and source-operation modes. Since the stabilizing controller adapts to transitions in the bus impedance, the variations in the operating modes do not degrade the performance. However, owing to the presented design criteria, the stabilizing controller only functions in such a way that the resonance is within the allowable frequency range. This is important because the converter dynamics, such as the current control bandwidth and poles/zeros, limit the available stabilizing controller bandwidth. Therefore, the stabilizing controller does not interfere with the regular controller operation in a degrading manner. The controller scheme is validated with experimental results on a multi-converter system with a DAB converter and two inverters.

The remainder of this article is organized as follows. Section II presents the bus-impedance-based stability and performance analysis of multi-converter systems. Section III uses this performance assessment to facilitate a resonance-damping control method for adaptive bus-voltage-damping stabilization and describes the identification of bus impedance and the resonance-damping control parameters, as well as the effect of the resonance-damping control on the voltage controller. In Section IV, experimental results validate the effectiveness of the resonance controller on a bidirectional converter operating both as a load and as a source. Conclusions are drawn in Section V.

II. Bus Impedance in Stability Analysis of Multi-Converter Systems

Consider the multi-converter system in Fig. 1; for a multi-converter system of N bus-connected converters, the system's bus impedance (i.e., single-port impedance) Z_{bus} can be given as a parallel connection of the bus-connected impedances (see [28])

$$Z_{\text{bus}}(s) = \frac{1}{Z_{\text{o1}}^{-1} + Z_{\text{o2}}^{-1} + \cdots + Z_{\text{o}N}^{-1}} \tag{1}$$

where N impedances are identified at the bus-side of the corresponding subsystem (denoted by subscript o in Fig. 1), and the positive signs for the currents correspond to the direction into the converter from the common dc bus. The interconnected multi-converter system can be shown to be passive if the following requirements are met [28].

1) $Z_{\text{bus}}(s)$ does not have right half-plane (RHP) poles.
2) $\text{Re}\{Z_{\text{bus}}(j\omega)\} \geq 0, \forall \omega > 0$.

Passivity is a sufficient but not necessary condition for stability. Additional concepts are required to assess other performance metrics (e.g., the level of damping), such as the allowable impedance region (AIR) introduced in [29]. Whereas passivity limits the bus impedance to the RHP, the AIR is defined as a semicircle within the RHP and its radius relates to the chosen attenuation level.

In the case of adverse impedance-based interaction, the bus impedance is typically characterized by a single prominent resonance peak [29]. In such a case, the bus impedance can

be expressed as

$$Z_{\text{bus}}(j\omega) = Z_{\text{o-bus}} \frac{s\omega_{\text{o}}}{s^2 + s\omega_{\text{o}}/Q_{\text{bus}} + \omega_{\text{o}}^2} \tag{2}$$

where $Z_{\text{o-bus}}$ is the characteristic impedance, ω_{o} is the resonance frequency, and the quality factor Q_{bus} specifies the level of damping. Thus, the bus impedance has a real value at the resonance frequency, $Z_{\text{bus}}(j\omega_{\text{o}}) = Z_{\text{o-bus}} Q_{\text{bus}}$. In other words, this value depicts the bus impedance peak magnitude. To achieve a chosen attenuation, the AIR demands that the bus impedance achieves a specified quality factor, Q_{max}. Therefore, the AIR can be defined in the complex plane as a semicircle with a chosen radius of $Z_{\text{o-bus}} Q_{\text{max}}$. In addition, to simplify the performance analysis, the AIR condition can be normalized by dividing the bus impedance and the AIR radius by the characteristic impedance. This normalization results in a straightforward expression for the AIR with a radius of Q_{max}. Accordingly, the chosen attenuation is achieved if the normalized bus impedance $Z_{\text{bus-N}}(j\omega)$ remains within the specified AIR.

Based on (1), the bus impedance peaks when the parallel sum of the impedances is zero, i.e., the impedances are of similar magnitude but an opposite phase. Concerning the individual converters, the shape of their impedance is strongly affected by their control structure. In the case of current controlling converters, their impedance can be described as a CPL since they have a negative incremental impedance within their feedback control loop bandwidth, i.e., the impedance magnitude is resistive with a $-180°$ phase. In contrast, the impedance of voltage-controlling converters has a relatively small magnitude except for a resonance peak around the voltage control crossover frequency. Likewise, droop control has the same characteristics as voltage control except for very low frequencies, in which the impedance magnitude is affected by the droop coefficient [30]. When converters of these different types are used together, the resonance peak in the voltage-controlling converter's impedance may cause the parallel sum of the converter impedances to have equal magnitudes at some frequency. If the impedances' phase difference is around $-180°$ at that same frequency, the denominator in (1) becomes very small, and the bus impedance exhibits significant resonance. This phenomenon is a typical example of adverse impedance-based interactions of multi-converter systems. Fig. 2 shows an example of a typical bus impedance based on (2) in which resonance occurs at 75 Hz.

Utilizing a virtual impedance is a straightforward way to prevent a resonance caused by impedance-based interactions. Essentially, the resonance in the bus impedance is caused by a resonant pole that occurs close to the voltage control crossover frequency. The resonance typically occurs at a frequency close to the voltage control loop bandwidth. Thus, a virtual impedance in the voltage-controlling converter can be designed to dampen the resonance. Even though the resonant behavior could also be smoothed with, for example, an additional capacitor, an adaptive control-oriented solution can offer a more optimized solution.

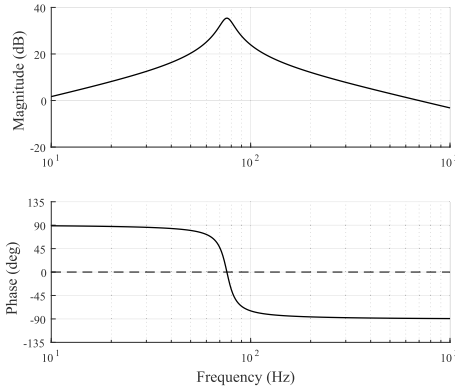

Fig. 2. Frequency response of the bus impedance as given in (2) with $Z_{\text{o-bus}} = 9$, $\omega_{\text{o}} = 477$ rad/s, and $Q_{\text{bus}} = 6.5$.

III. Impedance-Based Adaptive Stabilizing Control of Bidirectional Converters

In a multi-converter system, one of the converter impedances can be reshaped in such a way that the bus impedance achieves a chosen attenuation level. When performed adaptively, impedance reshaping can prevent impedance-based interactions from degrading the multi-converter system performance. Instead of using additional hardware, impedance reshaping can be carried out by modifying the converter control. The control can be designed to offer additional damping to the converter's closed-loop impedance, thus affecting the bus impedance. The range of this damping should be around the identified resonance frequency. For such a stabilizing control design, the following design criteria are required.

1) The added virtual impedance itself has a damping level of a chosen quality factor Q_{d}.
2) The resulting normalized bus impedance $Z_{\text{bus-N}}(j\omega)$ remains within an AIR specified by a chosen quality factor Q_{max}.
3) At the resonance frequency, the resulting normalized bus impedance $Z_{\text{bus-N}}(j\omega_{\text{o}})$ is limited to remain within an AIR specified by a chosen quality factor $Q_{\text{max}} - K_{\text{m}}$, where K_{m} is an additional margin. The quality factor of the resulting normalized bus impedance $Z_{\text{bus-N}}(j\omega_o)$ corresponds to $Q_{\text{max}} - K_{\text{m}}$ at the resonance frequency.

Typical ranges for these parameters are $Q_{\text{max}} = 0.7 \ldots 1$, $K_{\text{m}} = 0 \ldots 1$, and $Q_{\text{d}} = 0.7 \ldots 1$. One method of fulfilling the stabilizing control design criteria is to add a specific damping term to the voltage-controlling converter's voltage control loop. More specifically, a resonance gain (R-gain) can be added in parallel with the regular voltage controller, given as [31]

$$G_{\text{R}} = \frac{2\ K_{\text{r}}\omega_{\text{r}} s}{s^2 + 2\omega_{\text{r}} s + \omega_{\text{o}}^2} \tag{3}$$

where K_{r} determines the damping at the resonance frequency and ω_{r} is the resonance bandwidth. Fig. 3 shows the controller block diagram. The converter operates under cascaded control;

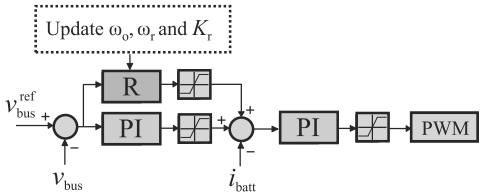

Fig. 3. Block diagram of the converter controller with a resonance term.

the outer voltage loop provides a reference to the inner current loop.

Sufficient values for the R-gain parameters K_r, ω_r, and ω_o can be determined adaptively with online bus impedance identification. First, the resonance frequency ω_o can be directly determined from the bus impedance identification. Second, the following design criteria are derived in [24]:

$$K_r = \frac{Q_d}{Z_{o\text{-}damp}}; \quad \omega_r = \frac{\omega_o}{2\ Q_d} \tag{4}$$

where

$$Z_{o\text{-}damp} = Z_{o\text{-}bus}\frac{Q_d Q_{bus}(Q_{max} - K_m)}{Q_{bus} - (Q_{max} - K_m)}. \tag{5}$$

The adaptive R-gain improves the damping of the bus impedance around the resonance frequency, which improves the multi-converter system's performance and stability. Fig. 4 presents an illustrative example of an R-gain's effect on the normalized bus impedance. The addition of the R-gain decreases the normalized bus impedance quality factor from 6 (out of scale) to within the AIR. Due to the chosen R-gain, the normalized bus impedance attenuation corresponds to $Q_{max} - K_m$ at the resonance frequency. In addition, Fig. 4 shows the normalized R-gain (i.e., R-gain multiplied by $Z_{o\text{-}damp}$). The virtual impedance itself has damping corresponding to the chosen quality factor Q_d. Accordingly, all the design criteria have been achieved. Note that if the resonance originates from two CPLs that are coupled through identical resonance frequencies, the resulting virtual impedance cannot prevent the resonance but other methods are required [21].

An R-gain-based stabilizing control is demonstrated in [24] for a source buck converter. In the case of bidirectional converters, the fundamental idea behind the control method is not affected as the bus impedance derivation is independent of the power-flow direction. However, for bidirectional converters, the converter dynamics may change profoundly depending on the operating mode and the power-flow direction. Thus, the stabilizing R-gain control may disturb the regular control performance and stability if it affects the voltage control loop in a degrading manner. The dynamic changes caused by the change in the operating mode and the power flow direction require further consideration for the successful implementation of the stabilizing controller without regular voltage control degradation or loss of stability.

A. R-Gain Effect on Voltage Control

The nominal voltage control (e.g., PI-based) is typically designed based on the desired phase-margin φ_m and crossover

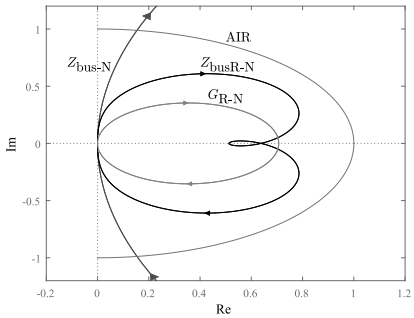

Fig. 4. Normalized bus impedance without R-gain (blue line) and with R-gain (black line), normalized R-gain (green line), and AIR boundary (red line) with $Q_d = 0.7$, $Q_{max} = 1$, $K_m = 0.5$. Bus impedance as given in (2) with $Z_{o\text{-}bus} = 9$, $\omega_o = 477$ rad/s, and $Q_{bus} = 6.5$.

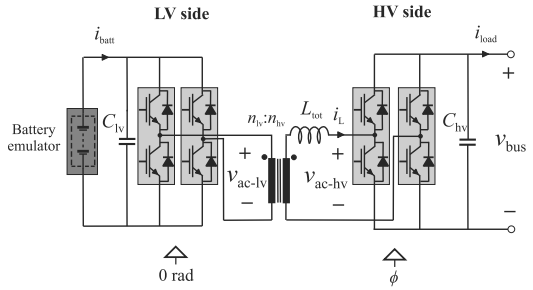

Fig. 5. DAB converter with a battery emulator.

frequency f_c. In this work, the stabilizing controller is implemented on a bidirectional DAB dc-dc converter shown in Fig. 5, but the procedure can be utilized in any bidirectional converter topology. The regular current and voltage controllers are based on PI control; the voltage controller is given by $G_{v\text{-}PI}(s) = K_{p\text{-}v} + K_{i\text{-}v}/s$. With the R-gain, the voltage controller becomes $G_{v\text{-}PIR}(s) = G_{v\text{-}PI}(s) + G_R(s)$.

Fig. 6 shows an example of the R-gain effect on the voltage controller gain. The voltage controller gain is presented with and without the R-gain. The R-gain is also shown. The chosen R-gain parameters are $K_r = 0.5$, $\omega_r = 2\pi 80$ rad/s, and $\omega_o = 2\pi 80$ rad/s; the PI-gain parameters are $K_{p\text{-}v} = 0.55$ and $K_{i\text{-}v} = 704$. As Fig. 6 shows, the R-gain only affects the area around the chosen frequency.

The R-gain effect on the original voltage (PI) controller is small but not necessarily negligible. Since the R-gain increases the voltage control gain within the chosen frequency range, its effect on the phase margin and crossover frequency should be considered to guarantee that the R-gain does not degrade the regular controller performance and stability. The converter dynamics may change profoundly depending on the operating mode and the power flow direction, which should be taken into account in the stabilizing control design and its implementation. For example, if the R-gain bandwidth is too wide, the voltage control crossover frequency may increase beyond

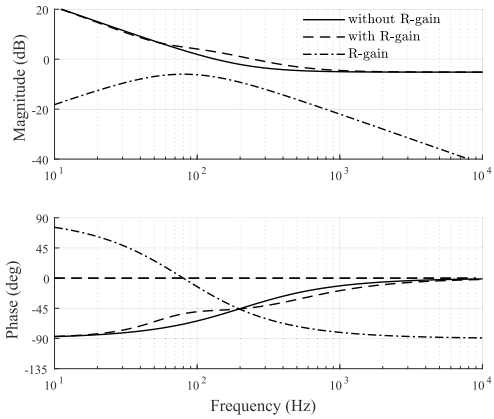

Fig. 6. Frequency response of the voltage controller without (G_{PI}) and with damping ($G_{\text{PI-R}}$) and the damping R-gain (G_{R}).

the limits of stable operation, which are restricted both by the inner control loop (i.e., the control loops should be decoupled in a cascaded controller) and possible zeros and poles in the converter dynamics. This can be especially important with bidirectional converters, as the system dynamics, specifically, the system poles and zeros, may change profoundly depending on the power direction (e.g., buck versus boost converter) and thus more easily lead to degraded control performance. Therefore, further design criteria and implementation methods are required to guarantee the proper operation of the stabilizing controller. As a general guideline, the resonance bandwidth should be limited to

$$\omega_{\text{r-max}} < \frac{2\pi f_{\text{c-innerloop}}^{\min}}{10} < \frac{2\pi f_{\text{sw}}}{10} \tag{6}$$

and

$$\omega_{\text{r-max}} < \frac{2\pi f_{\text{rhp-zero}}}{2} \tag{7}$$

where f_{sw} is the converter switching frequency, $f_{\text{c-innerloop}}$ is the inner (current) control loop crossover frequency, and $f_{\text{rhp-zero}}$ is the frequency of a possible RHP zero in the control-to-output voltage transfer function. This transfer function can be given as

$$G_{\text{cv}} = \frac{L_{\text{in}}}{1 + L_{\text{in}}} \frac{G_{\text{co-o}}}{G_{\text{ci-o}}} \tag{8}$$

where L_{in} is the inner loop gain and $G_{\text{co-o}}$ and $G_{\text{ci-o}}$ are the control-to-output voltage and control-to-input current open-loop transfer functions, respectively. Note that since the converter's internal dynamics change based on the operating point and the power direction, these restrictions should be considered in the R-gain stabilizing control design of a bidirectional converter for both power directions. Following these guidelines, the controller can dampen possible resonances in the bus impedance without regular voltage control degradation or loss of stability.

B. Bus Impedance Identification

An adaptive stabilizing controller is desirable in a multi-converter system with varying operating states and conditions. Fortunately, bus impedance identification provides a straightforward method for adjusting the stabilizing control variables because the impedance can be conveniently measured using the converter input and output currents/voltages [32].

Based on (1), the bus-impedance identification requires information about all the interconnected terminal impedances. One method of obtaining the bus impedance is to utilize broadband excitations such as pseudorandom binary sequences (PRBSs). While injecting these binary sequences into the converter controllers, the impedances can be identified from the resulting currents and bus voltage with Fourier techniques [28]. The PRBS perturbations are particularly suitable for the identification of power systems, as they have only two signal levels and they have a low crest factor, which means high signal energy in relation to the signal amplitude in the time domain [33]. Note that the PRBS signal's time-domain amplitude and frequency-domain spectrum must be carefully designed for the system under study to guarantee that the system currents and voltage stay within allowable limits and that the perturbations do not excessively degrade the power quality [34].

The impedance identification process should be as fast as possible to enable efficient use of the adaptive stabilizing control so that the system damping can be optimized and a possible distortion can be damped before reaching over-voltage or over-current conditions. For example, unnecessarily low frequencies can be excluded from the PRBS to accelerate the identification process, i.e., frequencies much lower than the voltage control crossover frequency, as specified in (6) and (7). In addition, orthogonal binary sequences can be applied to speed up further the bus impedance identification process and enable simultaneous impedance measurements rather than measuring the required impedances sequentially [35], [36].

One advantage of the impedance-based method is its black box feature; specific knowledge of the system parameters and properties is not needed [37]. Similarly, one of the drawbacks of the impedance-based stability assessment is that it cannot necessarily point the original causes of the resonance without further analysis. Nevertheless, the method offers sufficient information for adapting the virtual impedance according to changes in the multi-converter system so that a possible resonance can be dampened regardless of its root cause.

IV. Experimental Results

The proposed method is validated experimentally using a dc multi-converter system consisting of custom-built power converters. The built system and its specifications are shown in Fig. 7, in which a DAB converter is connected to two inverters. The topology of the DAB converter is shown in Fig. 5 and the inverter topologies are typical three-phase, two-level inverters; their parameters are given in Table I. The DAB converter and Inverter #2 are bidirectional and operate either as a load or as a source depending on the chosen operating point. The DAB converter and Inverter #1 operate

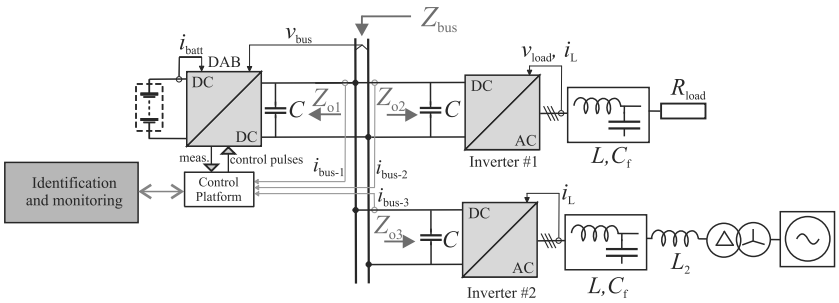

Fig. 7. Laboratory setup for the experimental tests; a multi-converter system consisting of two three-phase inverters and one DAB converter with a battery emulator.

TABLE I

CONVERTER PARAMETERS FOR THE DAB CONVERTER AND THE INVERTERS #1 AND #2 IN FIG. 7

Parameters	Values (DAB / inv #1 / inv #2)	Description
$V_{\rm bus}$	400 V	bus voltage
$V_{\rm in}$	200 V (dc) / 120 $V_{\rm rms}$ (ac) / 120 $V_{\rm rms}$ (ac)	source- or load-side voltage
$R_{\rm load}$	25 Ω	resistive load of Inverter #1 (star-connection)
$f_{\rm sw}$	50 kHz / 8 kHz / 20 kHz	switching frequency
C	1.5 mF / 1.5 mF / 1.95 mF	bus-side capacitance
$C_{\rm f}$	none / 25 μF / 10 μF	inverter ac-side filter capacitance
$L_{\rm tot}$	300 μH	DAB total inductance
L	none / 2.2 mH / 2.5 mH	inverter ac-side filter inductance
L_2	none / none / 0.6 mH	inverter grid-side filter inductance
$f_{\rm c-c}$	1 kHz / 500 Hz / 450 Hz	current loop cross-over frequency
$\varphi_{\rm m-c}$	65° / 65° / 60°	current loop phase margin
$f_{\rm c-v}$	10 Hz / 6 Hz / none	voltage loop cross-over frequency
$\varphi_{\rm m-v}$	55° / 60° / none	voltage loop phase margin

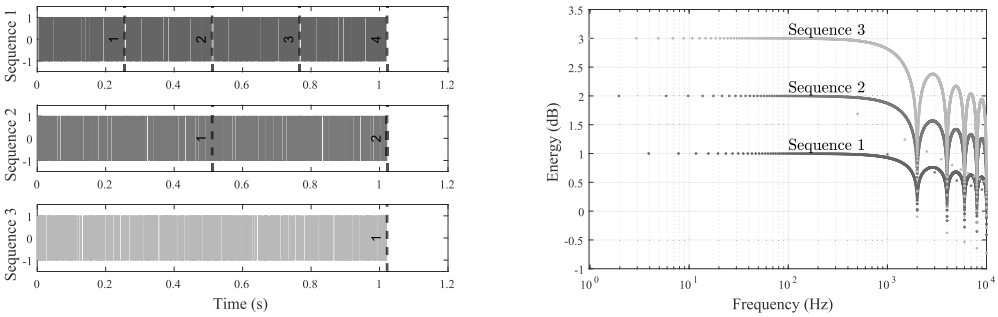

Fig. 8. MLBS signals used for perturbation for frequency response measurements (a) in time domain and (b) their energy spectrum.

under two-loop PI control and the Inverter #2 controls the grid current with PI control. Regular voltage and current measurements are marked in Fig. 7 with black arrows and orange arrows relate to the current measurements required for the stabilizing R-gain controller. The DAB controller and the Inverter #2 controller are implemented using rapid prototyping controllers by Imperix, whereas the Inverter #1 controller is implemented on the dSPACE platform. All the converters are standalone stable, so degradation in the system performance originates from the interactions between the single converters.

The perturbation sequences are implemented in all three control platforms. Three orthogonal maximum-length binary sequence (MLBS) sequences are used: Sequence 1 for DAB converter, Sequence 2 for Inverter #1, and Sequence 3 for Inverter #2. Sequence 1 is of length $N = 2^9 - 1$. Since the sequences are orthogonal, the length of Sequence 2 is $2N$, and the length of Sequence 3 is $4N$. Fig. 8 shows the three sequences in both the time and frequency domain. The sequences are generated at $f_{\rm gen} = 2$ kHz, which provides an 800-Hz bandwidth for the measured frequency responses. The frequency range of interest (i.e., around the voltage

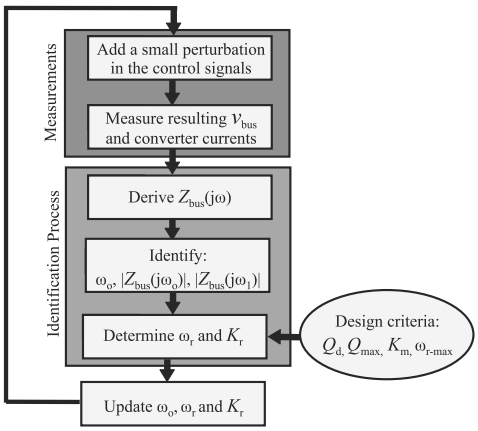

Fig. 9. Flowchart representing the adaptive resonance-damping algorithm with the chosen design criteria.

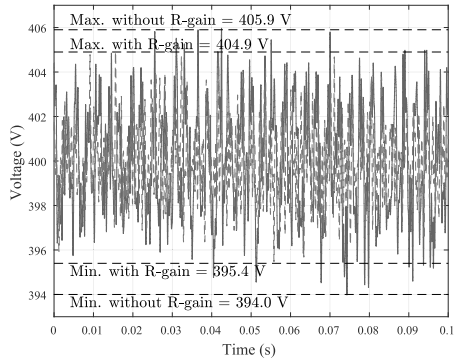

Fig. 10. Low-pass filtered (500 Hz) bus voltage without (blue) and with (orange) damping R-gain while discharging the battery.

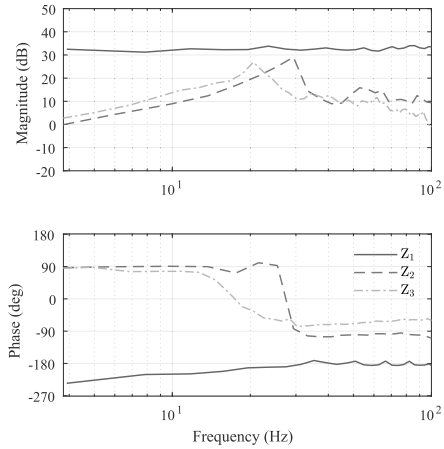

Fig. 11. Identified impedances without damping R-gain while discharging the battery.

control crossover frequency) is well within the chosen energy spectrum. As demonstrated in Fig. 8, Sequence 3 has a period length of 1.022 s, during which the other sequences are repeated periodically. The actual injection amplitudes are selected such that their values are 5%–7% of the nominal voltage/current reference values.

The designed perturbations were simultaneously placed on top of the controller reference voltages and/or currents of each converter. The first perturbation was applied with three periods, the second with six periods, and the third with 12 periods (because each perturbation length is twice compared to the previous one). The resulting bus voltage and output current of each converter were then measured using a sampling rate of 50 kHz. The measurements were averaged over the applied periods and the Fourier transform was used to obtain the output impedances of each converter. The bus impedance was then computed based on (1). After the identification process, the R-gain was added to the DAB controller and its parameters were assigned based on the identified bus impedance and (4) with $Q_d = 0.7$, $Q_{max} = 1$, and $K_m = 0.4$.

The experiments were conducted at two different operating points: the DAB converter was either feeding the dc bus with 500 W while discharging the battery or consuming 350 W while charging the battery. This change in the operating point was achieved by changing the Inverter #2 from feeding the grid with 150 W to feeding the dc bus with 700 W. Fig. 9 outlines the bus impedance identification and the controller update process. First, the discharging mode was considered. The blue line in Fig. 10 shows the bus voltage when the battery is discharging and no R-gain is applied. The minimum (394.0 V) and maximum (405.09 V) values are also marked, meaning a voltage deviation of 2.77%. Fig. 11 shows the identified impedances, and the resulting bus impedance is shown in Fig. 12 with a blue line. Without the R-gain, the bus impedance has a magnitude of 37 dB at 21 Hz, highlighted with a marker in Fig. 12. To improve stability, the proposed PI-R controller is activated so that enhanced damping is achieved around the chosen frequency. Following the aforementioned design procedure and the identified bus impedance, the values of $K_r = 0.17$ and $\omega_r = 18$ Hz are obtained for the R-gain. The resulting bus impedance with the added R-gain is shown in Fig. 12 with a red line. The R-gain increases the bus impedance damping around the identified resonance frequency (21 Hz), lowering it to 11 dB and thus improving the system damping. The resulting bus voltage is shown with the orange line in Fig. 10, and the minimum (395.4 V) and maximum (404.9 V) values are shown resulting in 2.38% voltage deviation. Since the voltage variation is lower, the added damping shows an improvement compared to the case without the R-gain.

Next, a similar study is performed while charging the battery. The voltages are comparable to Fig. 10. The identified bus impedance without the R-gain is shown in Fig. 12 with a purple line: without the R-gain, the bus impedance has a magnitude of 23 dB at 13 Hz, highlighted with a marker in

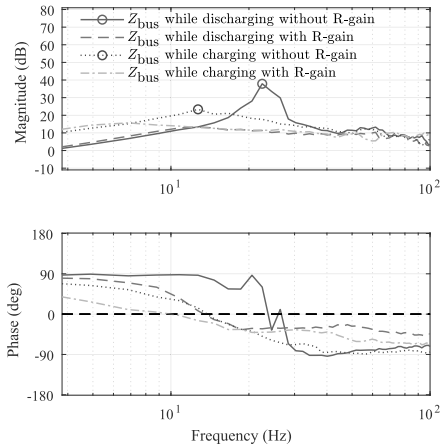

Fig. 12. Identified bus impedances with and without damping R-gain while discharging or charging the battery. Marker highlights the identified resonance.

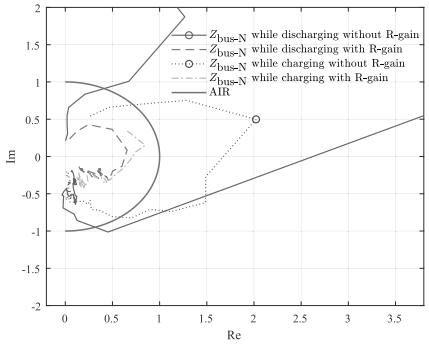

Fig. 13. Nyquist contour of the normalized bus impedance with and without damping R-gain. AIR boundary indicates with the red line. Marker highlights the identified resonance.

the figure. As before, the proposed PI-R controller is activated (now with $K_{\text{r}} = 0.25$, $\omega_{\text{r}} = 7$ Hz) and the resulting bus impedance is shown in Fig. 12 with the yellow line. The R-gain increases the bus impedance damping around 13 Hz, lowering it to 12 dB.

In both the discharging and charging experiments, the damping R-gain controller enhanced the system stability and damping around the identified resonance frequency. The R-gain controllers optimized the identified bus impedances, which were well-stabilized in both charging mode and discharging mode. Fig. 13 presents the corresponding normalized bus impedances in a complex plane. The normalized bus impedances with the R-gain have more damping and are well-confined within the AIR boundary. The Nyquist contour of the R-gain affected normalized bus impedances intersects with the real axis around the requested magnitude, indicating the achievement of the desired damping level. With the R-gain, the system damping is within the desired limits. The experimental results confirm the effectiveness of the proposed adaptive stabilization method in both power directions.

V. Conclusion

This article has implemented adaptive virtual-impedance-based stabilizing control on a bidirectional dc-dc converter. With the stabilizing resonance-damping control and the provided design guidelines, the bidirectional converter can operate as a virtual impedance that dampens resonances in the bus impedance when required without deteriorating the regular control operation. As a result, the stabilizing control can prevent adverse impedance-based interactions within a multi-converter system and optimize system stability and performance. The stabilizing controller is tuned adaptively based on an online bus impedance identification that estimates the system's stability and performance. The broadband-based identification method is well-suited for adaptive control due to its short measurement cycle. Therefore, the stabilizing control is suitable for multi-converter systems with changing operating states and conditions, such as bidirectional power flow. The analysis and experiments show that the bidirectional converter can efficiently optimize the damping in the bus impedance in both power directions. As a result, the multi-converter system performance is maintained regardless of changes (e.g., in connections or operating modes) and without hardware updates or retuning of the regular (such as PI) controller. The resonance-damping control method's simplicity (including bus impedance-based stability assessment and lack of more excessive computations) and basic requirements (such as voltage and current measurements at the bus-side of each converter) mean it can be efficiently embedded in parallel with a regular controller without disturbing its usual operation.

References

[1] R.-M. Sallinen, T. Roinila, and H. Abdollahi, "Stability analysis and adaptive resonance damping of multi-converter system applying bidirectional converter," in *Proc. IEEE 21st Workshop Control Modeling Power Electron. (COMPEL)*, Nov. 2020, pp. 1–7.

[2] T. K. Roy, M. A. Mahmud, A. M. T. Oo, M. E. Haque, K. M. Muttaqi, and N. Mendis, "Nonlinear adaptive backstepping controller design for islanded DC microgrids," *IEEE Trans. Ind. Appl.*, vol. 54, no. 3, pp. 2857–2873, May/Jun. 2018.

[3] Z. Jin, L. Meng, J. M. Guerrero, and R. Han, "Hierarchical control design for a shipboard power system with DC distribution and energy storage aboard future more-electric ships," *IEEE Trans. Ind. Informat.*, vol. 14, no. 2, pp. 703–714, Feb. 2018.

[4] H. Zhang, F. Mollet, C. Saudemont, and B. Robyns, "Experimental validation of energy storage system management strategies for a local DC distribution system of more electric aircraft," *IEEE Trans. Ind. Electron.*, vol. 57, no. 12, pp. 3905–3916, Dec. 2010.

[5] I. Alhurayyis, A. Elkhateb, and J. Morrow, "Isolated and nonisolated DC-to-DC converters for medium-voltage DC networks: A review," *IEEE J. Emerg. Sel. Topics Power Electron.*, vol. 9, no. 6, pp. 7486–7500, Dec. 2021.

[6] R. W. A. A. De Doncker, D. M. Divan, and M. H. Kheraluwala, "A three-phase soft-switched high-power-density DC/DC converter for high-power applications," *IEEE Trans. Ind. Appl.*, vol. 27, no. 1, pp. 63–73, Jan./Feb. 1991.

[7] F. Krismer and J. W. Kolar, "Efficiency-optimized high-current dual active bridge converter for automotive applications," *IEEE Trans. Ind. Electron.*, vol. 59, no. 7, pp. 2745–2760, Jul. 2012.

[8] X. Feng, J. Liu, and F. C. Lee, "Impedance specifications for stable DC distributed power systems," *IEEE Trans. Power Electron.*, vol. 17, no. 2, pp. 157–162, Mar. 2002.

[9] L. Herrera, W. Zhang, and J. Wang, "Stability analysis and controller design of DC microgrids with constant power loads," *IEEE Trans. Smart Grid*, vol. 8, no. 2, pp. 881–888, Mar. 2017.
[10] X. Lu, K. Sun, J. M. Guerrero, J. C. Vasquez, L. Huang, and J. Wang, "Stability enhancement based on virtual impedance for DC microgrids with constant power loads," *IEEE Trans. Smart Grid*, vol. 6, no. 6, pp. 2770–2783, Nov. 2015.
[11] M. Cespedes, L. Xing, and J. Sun, "Constant-power load system stabilization by passive damping," *IEEE Trans. Power Electron.*, vol. 26, no. 7, pp. 1832–1836, Jul. 2011.
[12] W.-J. Lee and S.-K. Sul, "DC-link voltage stabilization for reduced DC-link capacitor inverter," *IEEE Trans. Ind. Appl.*, vol. 50, no. 1, pp. 404–414, Jan./Feb. 2014.
[13] S. Fan, F. Wu, and H. Liu, "Unified closed-loop control and parameters design of buck–boost current-fed isolated DC–DC converter with constant power load," *IEEE J. Emerg. Sel. Topics Power Electron.*, vol. 10, no. 4, pp. 4207–4217, Aug. 2022.
[14] W. He and R. Ortega, "Design and implementation of adaptive energy shaping control for DC–DC converters with constant power loads," *IEEE Trans. Ind. Informat.*, vol. 16, no. 8, pp. 5053–5064, Aug. 2020.
[15] X. Zhang, Q. C. Zhong, and W. L. Ming, "Stabilization of cascaded DC/DC converters via adaptive series-virtual-impedance control of the load converter," *IEEE Trans. Power Electron.*, vol. 31, no. 9, pp. 6057–6063, Sep. 2016.
[16] R. D. Middlebrook, "Input filter considerations in design and application of switching regulators," in *Proc. Conf. Rec. IEEE IAS Annu. Meeting*, Jun. 1976, pp. 366–382.
[17] C. M. Wildrick, F. C. Lee, B. H. Cho, and B. Choi, "A method of defining the load impedance specification for a stable distributed power system," *IEEE Trans. Power Electron.*, vol. 10, no. 3, pp. 280–285, May 1995.
[18] A. Riccobono and E. Santi, "Comprehensive review of stability criteria for DC power distribution systems," *IEEE Trans. Ind. Appl.*, vol. 50, no. 5, pp. 3525–3535, Sep./Oct. 2014.
[19] X. Zhang, X. Ruan, and C. K. Tse, "Impedance-based local stability criterion for DC distributed power systems," *IEEE Trans. Circuits Syst. I, Reg. Papers*, vol. 62, no. 3, pp. 916–925, Mar. 2015.
[20] B. A. Martinez-Trevino, A. E. Aroudi, A. Cid-Pastor, and L. Martinez-Salamero, "Nonlinear control for output voltage regulation of a boost converter with a constant power load," *IEEE Trans. Power Electron.*, vol. 34, no. 11, pp. 10381–10385, Nov. 2019.
[21] M. Wu and D. D.-C. Lu, "A novel stabilization method of LC input filter with constant power loads without load performance compromise in DC microgrids," *IEEE Trans. Ind. Electron.*, vol. 62, no. 7, pp. 4552–4562, Jul. 2015.
[22] S. Liu, P. Su, and L. Zhang, "A virtual negative inductor stabilizing strategy for DC microgrid with constant power loads," *IEEE Access*, vol. 6, pp. 59728–59741, 2018.
[23] X. Zhang, Q. Zhong, V. Kadirkamanathan, J. He, and J. Huang, "Source-side series-virtual-impedance control to improve the cascaded system stability and the dynamic performance of its source converter," *IEEE Trans. Power Electron.*, vol. 34, no. 6, pp. 5854–5866, Jun. 2019.
[24] H. Abdollahi, S. Arrua, T. Roinila, and E. Santi, "A novel DC power distribution system stabilization method based on adaptive resonance-enhanced voltage controller," *IEEE Trans. Ind. Electron.*, vol. 66, no. 7, pp. 5653–5662, Jul. 2019.
[25] H. Xiao, A. Luo, Z. Shuai, G. Jin, and Y. Huang, "An improved control method for multiple bidirectional power converters in hybrid AC/DC microgrid," *IEEE Trans. Smart Grid*, vol. 7, pp. 340–347, Jan. 2016.
[26] J. He, L. Du, B. Liang, Y. Li, and C. Wang, "A coupled virtual impedance for parallel AC/DC converter based power electronics system," *IEEE Trans. Smart Grid*, vol. 10, no. 3, pp. 3387–3400, May 2019.
[27] P. Yang, M. Yu, Q. Wu, N. Hatziargyriou, Y. Xia, and W. Wei, "Decentralized bidirectional voltage supporting control for multi-mode hybrid AC/DC microgrid," *IEEE Trans. Smart Grid*, vol. 11, no. 3, pp. 2615–2626, Dec. 2020.
[28] A. Riccobono and E. Santi, "A novel passivity-based stability criterion (PBSC) for switching converter DC distribution systems," in *Proc. 27th Annu. IEEE Appl. Power Electron. Conf. Expo. (APEC)*, Feb. 2012, pp. 2560–2567.
[29] J. Siegers, S. Arrua, and E. Santi, "Stabilizing controller design for multibus MVdc distribution systems using a passivity-based stability criterion and positive feedforward control," *IEEE J. Emerg. Sel. Topics Power Electron.*, vol. 5, no. 1, pp. 14–27, Mar. 2017.
[30] G. Liu, P. Mattavelli, and S. Saggini, "Design of droop controllers for converters in DC microgrids towards reducing bus capacitance," in *Proc. Eur. Conf. Power Electron. Appl.*, Sep. 2018, pp. P.1–P.9.
[31] D. N. Zmood and D. G. Holmes, "Stationary frame current regulation of PWM inverters with zero steady-state error," *IEEE Trans. Power Electron.*, vol. 18, no. 3, pp. 814–822, May 2003.
[32] T. Roinila et al., "Hardware-in-the-loop methods for real-time frequency-response measurements of on-board power distribution systems," *IEEE Trans. Ind. Electron.*, vol. 66, no. 7, pp. 5769–5777, Jul. 2019.
[33] A. H. Tan and K. R. Godfrey, *Industrial Process Identification*. Cham, Switzerland: Springer, 2019.
[34] R. Pintelon and J. Schoukens, *System Identification—A Frequency Domain Approach*. Piscataway, NJ, USA: Institute of Electrical and Electronics Engineers, 2001.
[35] T. Roinila, H. Abdollahi, S. Arrua, and E. Santi, "Real-time stability analysis and control of multiconverter systems by using MIMO-identification techniques," *IEEE Trans. Power Electron.*, vol. 34, no. 4, pp. 3948–3957, Apr. 2019.
[36] T. Roinila, H. Abdollahi, and E. Santi, "Frequency-domain identification based on pseudorandom sequences in analysis and control of DC power distribution systems: A review," *IEEE Trans. Power Electron.*, vol. 36, no. 4, pp. 3744–3756, Apr. 2021.
[37] G. O. Kalcon, G. P. Adam, O. Anaya-Lara, S. Lo, and K. Uhlen, "Small-signal stability analysis of multi-terminal VSC-based DC transmission systems," *IEEE Trans. Power Syst.*, vol. 27, no. 4, pp. 1818–1830, Nov. 2012.

Roosa-Maria Sallinen (Member, IEEE) received the B.Sc. (Tech.) and M.Sc. (Tech.) degrees in electrical engineering from the Tampere University of Technology, Tampere, Finland, in 2015 and 2017, respectively. She is currently pursuing the Ph.D. degree with the Faculty of Information Technology and Communication Sciences, Tampere University, Tampere.

In 2022, she joined GE Grid Solutions, Tampere, where she is currently a Lead Control Engineer. Her main research interests include impedance-based interactions in power electronic systems and adaptive stabilization.

Tomi Roinila (Member, IEEE) received the M.Sc. (Tech.) and Dr.Tech. degrees in automation and control engineering from the Tampere University of Technology, Tampere, Finland, in 2006 and 2010, respectively.

He is currently an Associate Professor with Tampere University, Tampere. His main research interests include modeling and control of grid-connected power-electronics systems, analysis of energy-storage systems, and modeling of multiconverter systems.